NORTHWESTERN UNIVERSITY

Design and Modulation of Metal Oxo Species from Discrete to Three-Dimensional Materials and Their Applications

A DISSERTATION

SUBMITTED TO THE GRADUATE SCHOOL

IN PARTIAL FULFILLMENT OF THE REQUIREMNTS

for the degree

DOCTOR OF PHILOSOPHY

Field of Chemistry

By

Megan Cathleen Wasson

EVANSTON, ILLINOIS

June 2022

ABSTRACT

Design and Modulation of Metal Oxo Species from Discrete to Three-Dimensional Materials and Their Applications

Megan Cathleen Wasson

A unifying concept across many fields, ranging from chemistry to architecture, is the bottom-up construction of sophisticated structures from simple building blocks. Materials with long-range order allow for consistent, predictable performance throughout the resulting structure. My research focuses on building highly ordered porous materials from atomic level building blocks based on metal oxo clusters. I have synthesized and modulated the structure of atomically precise clusters as discrete entities and within multi-dimensional materials known as metal–organic frameworks (MOFs). In these studies, local techniques such as single crystal X-ray diffraction are utilized in tandem with powder X-ray diffraction, physisorption, and spectroscopic investigations of the bulk materials to fully describe the resulting structure and confidently derive property relationships.

I first demonstrated a crystal design strategy to synthesize discrete cerium oxo clusters featuring permanent porosity. Aromatic capping agents facilitated noncovalent interactions between neighboring clusters to stabilize the overall assembly. The high surface exposure of these assemblies resulted in accessible oxygen vacancy defects that facilitated a proof-of-concept photocatalytic oxidation reaction. To further capitalize on high surface area Ce oxo assemblies, I next investigated the role of the interfacial unit connecting porous Ce_{70} toroids for CO oxidation. I demonstrated the catalytic performance, surface reducibility, and oxygen vacancy formation

energetics can be varied based on the interfacial unit, highlighting the significant role of a defined atom at a specific location.

I shift in subsequent chapters to developing synthetic strategies that isolate metal oxo clusters within MOFs and probe their structural evolution. I identified the kinetic and thermodynamic MOF architectures that result during the competitive nucleation of a Zr_6 oxo cluster through two different organic linkers. In a following study, I utilized competitive nucleation as a strategy to stabilize a redox active Ce^{IV} oxo hexanuclear cluster within a MOF over a Ce^{III} oxo mononuclear cluster. In my last chapter, I demonstrate a reversible phase transition between a hexanuclear Th oxo cluster MOF building unit to a mononuclear Th-based MOF. Within these studied conditions, we observed similar transitions with an isostructural Ce_6-based MOF, yet the Zr and Hf analogues remained unchanged, highlighting differing metal oxo cluster stability.

Acknowledgments

There are many people and places to start with acknowledgments. Before I begin, I would like to first acknowledge that I was fortunate to be born into and grow up in an environment where I did not face significant barriers to chase after opportunities that came my way. Many people in this world do not have the same fortune to grow up into a safe and empowering environment, and we can only act to make the world more peaceful. With that being said, I still had to put in many painstaking, long hours, and I always tried my best to embrace, rather than squander, opportunities as they surfaced. Nonetheless, I am very happy I get the chance to acknowledge those who supported me along this journey in a multitude of ways. There are many people who I am forever indebted for, and please know the list extends far beyond who I have thanked below.

I would first like to acknowledge my Ph.D. advisor, Professor Omar Farha. From my first day in the door to my last day out the door, I felt excited by and inspired from your ambition to make the world a better place. Few graduate students are fortunate to study under someone so passionate and determined about their work, and for that, I am eternally grateful. I am indebted to the support you gave me ranging from precise scientific feedback I needed to the freedom to explore opportunities outside of my research that I became passionate about during my Ph.D. I would also like to thank my Ph.D. committee, Profs. Chad Mirkin and Eric Weitz, for providing both critical insights to my work as well as valuable advice on how to craft and present a finalized project to an audience.

Within the Farha Group, there are many people I have been fortunate to work with that have served as my greatest motivators and soundboards. To begin, thank you to Timur for always leaving your door open. You answered every question and helped with any task - no matter how big or how small, always making time for every request. Your motivation to seek perfection, even if at 4 am during an APS beamtime that we found ourselves in despite our relative inexperience, inspires me to give my all no matter the circumstance. To Jiafei, thank you for being my role model and support when I first joined the group. Simple advice and encouragement that you gave me in my first year carried enormous weight throughout my Ph.D. To Xingjie, thank you for being a source of happiness in the face of positive results and laughter in the face of negative results; your work-ethic, determination, and patience was exemplary to say the least. Thank you to Chen for being such a great example of intellectual rigor to strive for, while making space to answer anyone's questions and leading with kindness. To Riki and Lee / Lee and Riki, you taught me how to advocate for yourself and were great mentors on how to navigate graduate school uncertainties that popped up along the way. To the Argonne high pressure crew – Louis, Lee, Florencia, and Kira– thank you for some of the most enjoyable days and nights of my Ph.D. Learning to problem solve at 2 am, while critiquing the latest Kanye album on our second sugar crash of the night, made me realize that the people you're with, rather than the immediate work itself, can also fulfill you. To my fellow Farhomie cohort – Kenton, Rodrigo, Sylvia, Tim and Xinyi – thank you all for the support from the very beginning of and throughout graduate school, and the memes that sustained me in between.

And thank you to so many more Farhomies including Cornelius, Ghada, Kaikai, Ran, Yongwei, Xuan, Ken-ichi, Kent, Dahee, Deb, Haomiao, Cassandra, Yijing, Julia, Karam, Zoha, Fanrui, Madeleine, Tony, Courtney, Lauren, Mike and Seryeoung – I feel so fortunate to have overlapped and worked with you all. Additionally, thank you the undergraduate Farhomies I have directly mentored – Annabella – and those I have been fortunate to overlap with including Ian, Alyssa, Jamilla, Audrianna, Yifan, Hugo, Joshua, Kevin; your persistence and passion to learn are great reminders to us all to challenge ourselves each and every day. Thank you to the Farha Group program assistants who offered such patient help and support including Abby Rosensweig, Nick Huryk, and Greg Mandell; a special thank you to Greg for one of the most spectacular karaoke renditions of Proud Mary that I've ever seen.

Thank you to all of the helpful and intelligent scientists at Northwestern's core research facilities. In particular, thank you to Selim for your impressive scientific expertise, commitment to figuring out a way to make an experiment come to life, and eagerness to answer any question that came up along the way. Thank you for Neil for your patience in training me on new instrumentation and coming up with any set-up needed to run a variety of experiments. Lastly, thank you to Charlotte and Christos for providing a great introduction to crystallography in my first year and continuing to provide great research advice since then.

Thank you to those at Northwestern who made a Big Ten school feel a smaller place. To Megan and Meghan – thank you for ironically wearing matching shirts during our first graduate school exam and for being such caring friends. To Emily, our lunches, were always the highlight of my week and I am so grateful for our friendship. Thank you to Laura for your teamwork as we helmed the Research Safety Student Initiative. To the staff at Northwestern's Office of Research Safety – Michael, Ben, Gwen, Iwona, and others – thank you for the patience, earnest support, and biggest smile as Laura and I learned how to grow as student leaders. To Edward and Liban, thank you for the countless hours of practice case interviews; I learned so much from you both.

Thank you to those at Duquesne University who supported me in my path to reach graduate school. Thank you to Tomislav for the opportunities and invaluable support provided along the way; without your support attending Northwestern would have been only a dream. Thank you to Gabby for taking me under your wing as an undergraduate freshman and never letting go – your help and friendship all of these years has meant the world. To Ellen, I thought having a female, former D1 athlete as a freshman advisor and professor was pretty cool, but I quickly learned that your advice and support far outlasted your formal advising role. I am forever grateful for the support you gave me throughout my time at Duquesne and Northwestern. Lastly, thank you to the fearless women that surrounded me for 4 years as I played on Duquesne's varsity tennis team. I would especially like to thank Vanessa and Zuzanna. You taught me everyday what it meant to be a part of a team; I cannot thank you enough for your friendship and strength.

There are many friendships that have pushed, challenged, and inspired me to grow and for that I am ever thankful. To those that made Chicago feel like a home – especially Jess, Swara, and Weronika – thank you from the bottom of my heart. To Tierney and Wynonna, you two continuously light up my life with an excuse to celebrate any wins that come our way and for that I am forever grateful. To Noelle, I still feel like we should be haggling for $4 (instead of $5 pizza) on 10th street, but I'm so proud of what we've accomplished since leaving Duquesne; thank you for your support at all hours of the night. To Katy, thank you for agreeing to be my best friend in preschool and standing by my side since then in so many incredible ways. And to Sylvia, it's rare to find such a best friend in the exact same graduate school cohort and lab group. I am so grateful for the mutual support we have given for each other's wins, ideas bounced off each other, shopping trips made, meals shared, and spontaneous adventures in between. I cannot imagine my graduate school experience without your friendship.

Lastly, thank you to my extended family for the constant support and love for as long as I remember. I would be remiss in not including the four-legged friends in this document. Thank you to my dogs Cleo and Luna for the emotional support over the last few years; you gave me comfort and taught me humility as I picked up your waste. Of course, none of this would have been possible without my parents Janice and Bob. I feel like I won the universe's lottery to be born as your daughter, and I am indebted to you both as you worked hard to support my education and dreams, even under trying times. These past five years were far from easy, but you helped me persevere by answering every phone call, packing up coolers of frozen comfort food, and mailing newspaper clippings of every tennis comic that appeared in the Sunday edition of the Pittsburgh Post-Gazette.

Table of Contents

List of Figures

List of Tables

Chapter 1: Introduction

Portions of this chapter appear in the following manuscript:

Wasson, M. C.; Buru, C. T.; Chen, Z.; Islamoglu, T.; Farha, O. K. *Appl. Catal. A: Gen* **2019***,* 586, 117214.

1.1 Chapter Summary

This chapter begins with an overview of the structural properties of metal oxides, a class of widely utilized solid supports. I next introduce the construction of well-defined metal oxide materials instead as discrete molecular clusters or isolated within multidimensional hybrid materials known as metal–organic frameworks (MOFs). The chapter ends with an overview of my dissertation.

1.2 Overview of Structural Properties of Metal Oxides

Bulk metal oxides are a class of inorganic materials that are essential to a range of industries where their tunable surface and electronic structure facilitate their use as heterogeneous catalysts, biomedical devices, and semiconductors.[1–3] Comprised of metal cations that are coordinated to O^{2-} anions, the resulting oxide features a variety of useful reactive sites ranging from Lewis and Brønsted acid / base sites to even redox active sites.[4,5] Surface irregularities, such as kinks and terraces as well as morphology-dependent facets and edge sites, create coordinatively unsaturated metal sites with vastly different surface energies.[6–9] Within redox active metals, the ability to selectively store and release lattice oxygen in their oxide is highly dependent on the exposed surface.[10] Moreover, reducing nanoxide size significantly lowers the formation energy required to form an oxygen defect site by exposing a higher percentage of the oxides' atoms to the surface.[11,12] Thus, structure and function are closely tied through exposed surface sites and the population of oxygen vacancy sites within metal oxides. Any structural polydispersity within metal oxide materials complicates the confident delineation of structure activity relationships .[13–16]

Considerable work has lessened this dilemma of structural heterogeneity through the careful synthetic development to yield shape and size specific metal oxides to enable more consistent reactivity within metal oxides.[17–21] However, access to total structural knowledge is still complicated within these systems given they feature a distribution of grafting sites required for further functionalization of the support. For example, loading an active catalyst onto a support containing a variety of anchoring sites can create multiple active catalysts, leading to inconsistent catalyst performance at the different sites.[22] Furthermore, the precise identification of grafted active site is convoluted on metal oxides, often precluding the use of diffraction methods to determine atomic level bonding and garner interfacial insights.[23] Thus, efforts toward correlating structure with activity to enable rational design of next-generation metal oxide materials are impeded by structural irregularities.

1.3 Introduction of Metal Oxo-Based Molecular Clusters

Molecular clusters have ushered in a new era of study bridging the gap between atomic and bulk structures by containing a finite number of atoms.[24] By definition, each molecular cluster in a particular sample exhibits the same size and composition.[25] Molecular clusters can serve as simplified subsets to target reactivity found within complex molecules, such as active sites in enzymes.[26] Beyond the atomic precision offered by clusters, they can offer unique properties vastly differing from their bulk materials. For example, a discrete gold thiol cluster <2 nm was oxidized under ambient conditions despite the inertness of bulk gold and larger gold nanoparticles under the same conditions.[27] Thus, one can envision the unique properties that can be accessed in reactive bulk supports such as metal oxides when discretized within molecular clusters.

Discrete metal oxo clusters are comprised of metal cations coordinated to charge-balancing monodentate O-donor ligands.[28] Surface and electronic modification of the cluster is readily achieved through the judicious selection of the capping agent. The resulting inorganic and organic interface can then be precisely identified through atomically precise techniques like single crystal X-ray crystallography.[29]

Often, metal oxo clusters crystallize in densely packed lattices with limited surface accessibility as solid-state structures.[30,31] This creates a conundrum of dead weight in that interior clusters are "wasted" with only exposed metal atoms on the surface of the crystal can participate in surface chemistry. Thus, there is a need for hierarchically ordered metal oxide materials with highly exposed surface atoms (**Figure 1.1**). Within molecular level clusters, the capping agent can serve as a handle to induce supramolecular interactions or unique cluster shapes to reduce the resulting density. Chapter 1.4 discusses another strategy of incorporating the clusters as structural building units to create multidimensional materials.

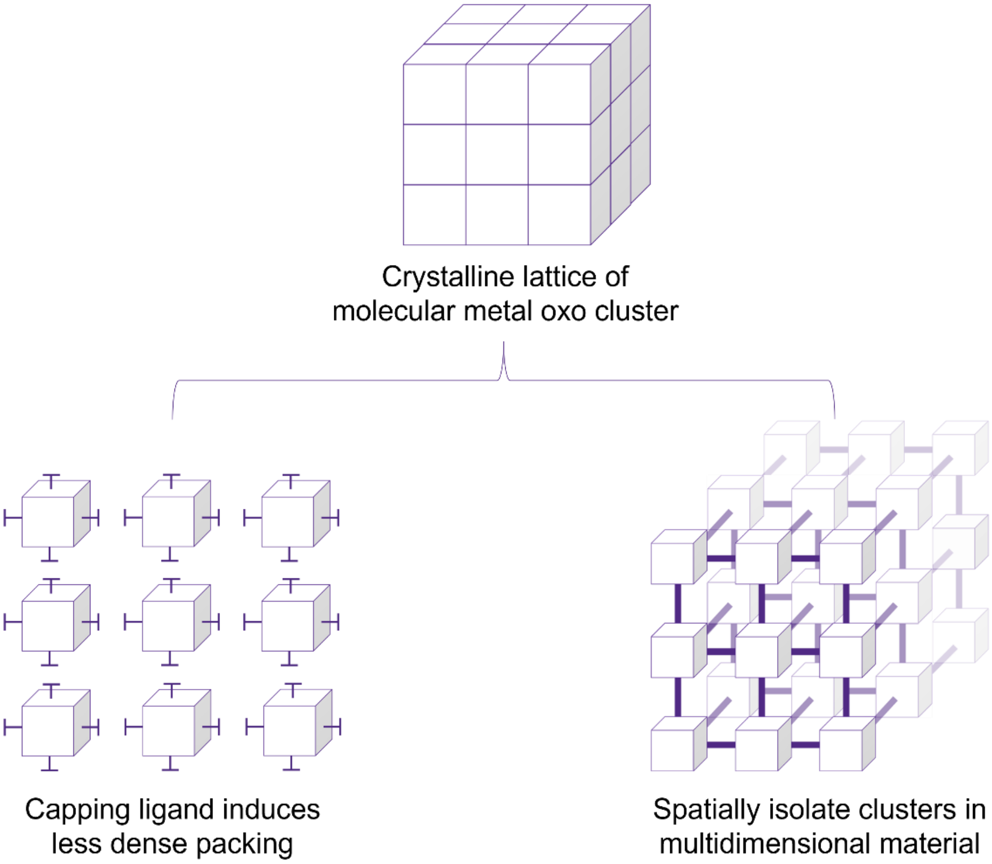

Figure 1.1 Depiction of structural design concepts to increase the accessible surface of metal oxo clusters.

1.4 Metal–Organic Frameworks and Their Growth Strategies

Metal–organic frameworks (MOFs) are an emerging class of highly porous, well-defined crystalline materials that have attracted considerable interest for catalysis, gas storage/separation, and chemical sensing, among other applications.[32–36] These materials are composed of inorganic nodes and multidentate organic linkers that assemble into multidimensional lattices through coordination bonds.[37–40] Available nodes and linkers access a vast number of framework connectivities and offer precise control of chemical functionality. MOF periodicity eliminates the structural variability present in traditional solid-phase supports, providing a platform to delineate structure-property relationships.[41] Thus, a suite of post-synthetic modifications can impart additional functionality onto the MOF support through the deposition of reactive species on the MOF structural building units, exchange of MOF structural building units inaccessible *de novo*, and the incorporation of guests within the MOF pore (**Figure 1.2**). Ultimately, MOFs offer a platform to create systematic atomic level changes while eliminating all other variability to derive more confident assignments of structure activity relationships.

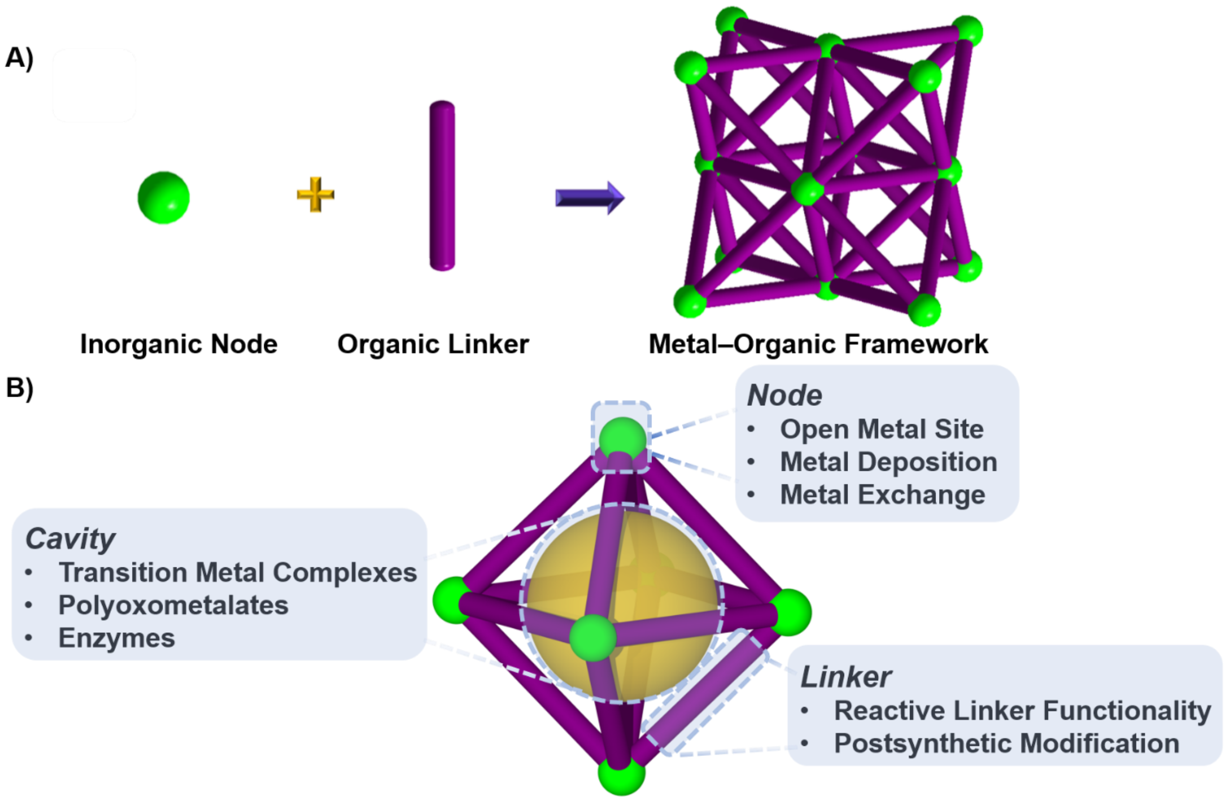

Figure 1.2 A) Metal–organic frameworks (MOFs) consist of inorganic nodes and organic linkers. 12-c **fcu** net is used for illustration. B) Accessible sites on MOFs available for modification include the node, linker, and content of the cavity.

The first reported MOFs with permanent porosity were based on divalent metals such as Zn^{II} and Cu^{II} forming coordination bonds with carboxylate linkers.[37,42] However, higher valent metals (Zr^{IV}, Hf^{IV}, Ce^{IV}, Th^{IV}) exhibit a higher charge density and stronger metal-carboxylate bonds, enabling more chemically and thermally robust frameworks.[43–46] Tetravalent species' can more readily accommodate a higher coordination sphere and consequently more structurally interesting MOF topologies.[43,47] However, within M^{IV}-based MOFs, identical MOF nodes and linkers can readily form different phases, which complicates the pure-phase synthesis of targeted frameworks (**Figure 1.3**).[48–50] Thus, it is imperative to study the formation and evolution of MOFs to discover strategies to better control the framework architecture.

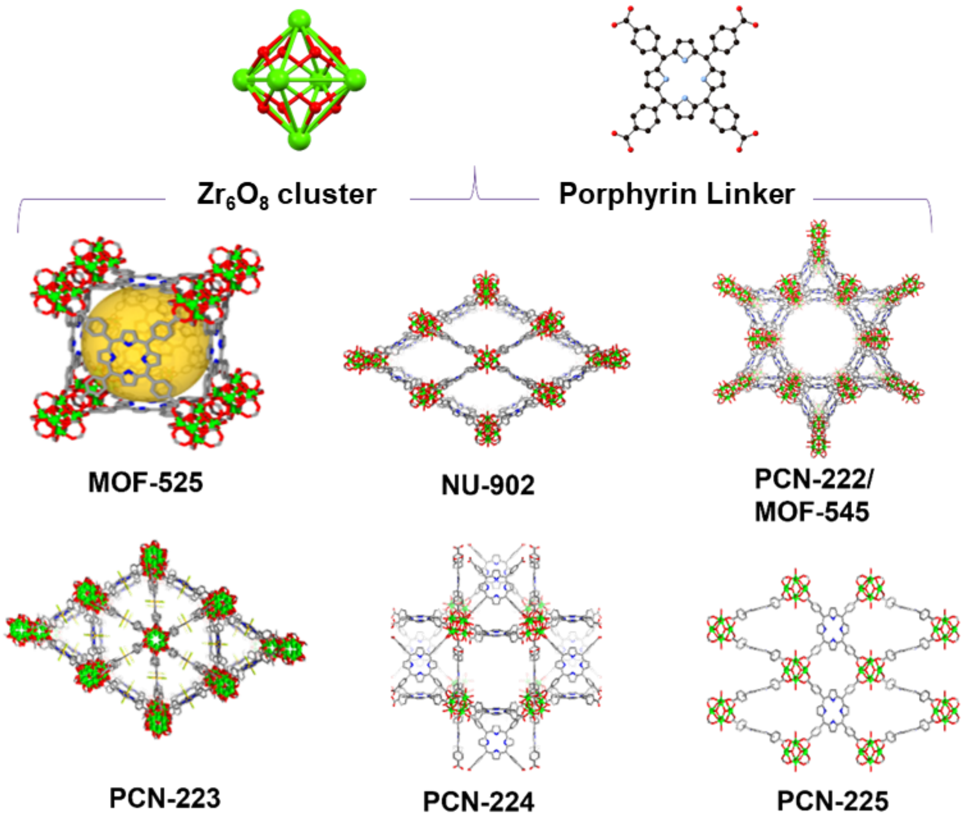

Figure 1.3 Overview of reported multiple MOF products containing the same Zr_6 oxo cluster and in the presence of tetrakis(4-carboxyphenyl)porphyrin (TCPP) organic ligands.

Another challenge often encountered in attempted M^{IV}-based MOF syntheses is the rapid crystallization of the material due to the favorable formation of exceptionally strong M^{IV}-O bonds, often yielding intergrown particles, polycrystalline materials, or even amorphous products. Materials that crystallize instead in a single domain are more desired because they can be structurally characterized through precise X-ray and three-dimensional electron diffraction methodologies.[51,52] Additives, referred to now as modulators within the MOF community, were discovered as a strategy to alter the coordination equilibria and control the growth processes first within Cu^{II}-based MOFs.[53] These modulating species contain the same monotopic functionality as the MOF ligand in solution and undergo transient binding node to slow down and modulate the MOF node and linker crystallization (**Figure 1.4**). The introduction of carboxylate-based modulators within Zr-MOF synthesis expanded the library of available Zr-MOFs for applications requiring high chemical stability including water remediation, toxic chemical degradation, and drug delivery.[54–56] However, few generalizable modulation rules exist and are less commonly explored within other M^{IV}-containing MOFs, limiting the library of available frameworks.[48,57]

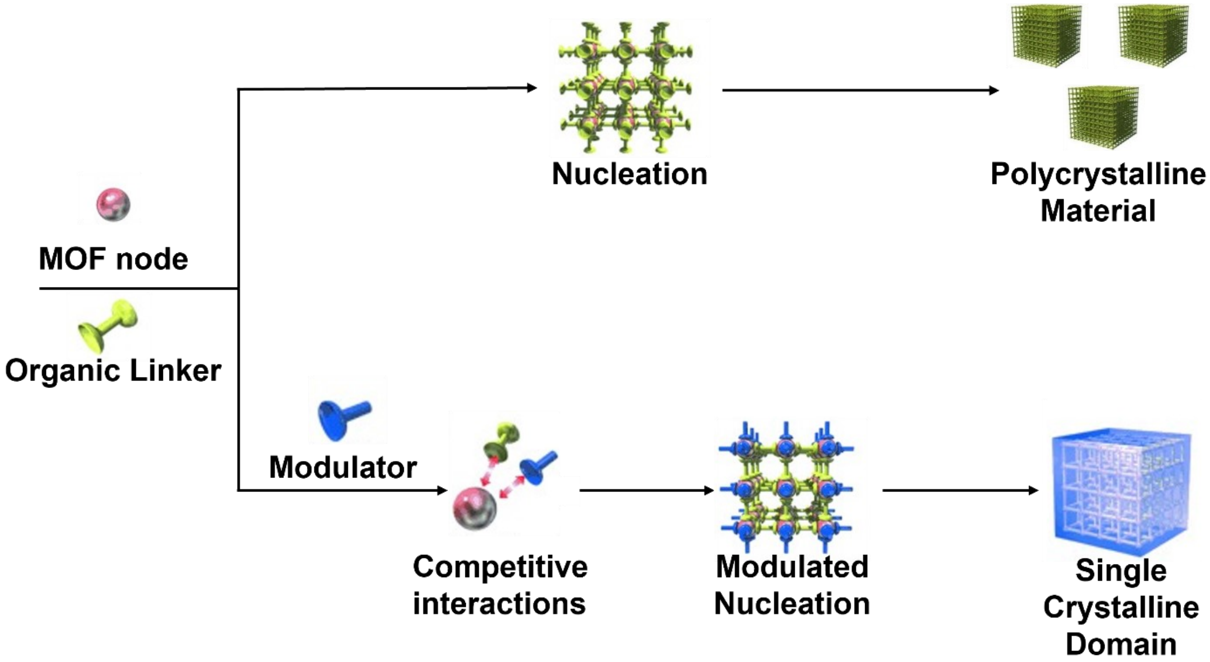

Figure 1.4 Overview of MOF crystallization processes in the presence of just MOF node and linker (top) or MOF node, linker, and modulator (bottom). Figure adapted with permission from ref 53.

Reticular chemistry is a powerful strategy that has expanded the available MOF library by utilizing molecular building blocks with pre-selected geometries to form architectural arrangements dictated by geometry.[58] This concept has enabled ultra-high surface area of MOFs with some reports of MOF surface areas exceeding 7000 m^2/g, well-surpassing accessible surface areas offered by traditional oxide-based supports.[59,60] However, reticular chemistry principles break down when individual MOF building units deviate from their expected structure in solution, often a consequence of the labile coordination bonds that make up the inorganic metal oxo building units.[61] Thus, predictive MOF design and exploratory parameter space have often been applied to lower nuclearity metal nodes with simpler geometries, such as binuclear metal paddlewheels, trinuclear trigonal prismatic units, and hexanuclear cuboctahedron building units.[61,62] However, it is predicted that stabilizing higher connected metal oxo clusters within MOF self-assembly can expand the available networks and topologies of these multidimensional materials.[62] Thus, MOF structural diversity can be accelerated by both the discovery of new metal oxo clusters as well as studying the evolution of metal oxo clusters during MOF self-assembly.

1.5 Dissertation Outline

The work in this thesis discusses the structural design and modulation of atomically precise metal oxo species focusing primarily on 1) forming discrete clusters or 2) spatially isolating the clusters as building units to build highly porous MOF multidimensional materials. My research leverages X-ray diffraction to determine the structure which is correlated to functions identified through physisorption and spectroscopic techniques. In some instances, the atomic precision of these materials facilitated collaborative theoretical work to probe energetic questions related to structure and function.

Chapter 2 describes a supramolecular strategy to induce permanent porosity within assemblies of two cerium oxide clusters through the organic, aromatic-based capping ligands used. Through single-crystal X-ray crystallography, we observed unique non-covalent interactions that enabled accessible channels in the zero-dimensional cluster materials, further confirmed through adsorption isotherms supported with density functional theory calculations. We explored the unique structural assemblies with variable pressure and temperature diffraction studies and characterized the electronic state of the bulk materials with X-ray photoelectron spectroscopy, electron paramagnetic resonance spectroscopy, and Raman spectroscopy. We benchmarked catalytic activities of these cluster families with other reported atomically precise materials through the photooxidation of 2-propanol.

Within Chapter 3, we shift to studying another series of porous Ce cluster-based assemblies that feature toroid like structures linked through interfacial sulfate and monomeric cation units (M = Cd, Ce, Co, Cu, Fe, Ni, and Zn). The more stable capping sulfate groups within this family enabled us to shift from studying photocatalytic activity in chapter 2 to studying CO oxidation, a more thermally challenging gas-phase reaction highly relevant for Ce oxo-based materials. This chapter demonstrates that a single ion-based linkage unit between neighboring clusters can serve as an active interface that readily tunes the reducibility and defect formation energetics of the Ce_{70} ring, and consequently the catalytic activity.

Chapter 4 highlights the structural complexities within 3-Dimensional MOF materials containing metal oxo species. Specifically, we explore the synthesis of kinetic and thermodynamic MOF products based on isostructural $[Zr_6(\mu_3\text{-}O)_4(\mu_3\text{-}OH)_4]^{12+}$ metal oxo building units through competitive nucleation. We present a novel *in situ* linker competition for MOF nucleation as a strategy to distinguish between kinetic and thermodynamic MOF products and to yield previously inaccessible thermodynamic Zr MOF products.

Chapter 5 extends the concept of competitive nucleation studied within Chapter 4 to further stabilize and dictate the structure of Ce oxo clusters isolated within MOF materials. We compare the identities and concentrations of different carboxylate based modulating species to slow down the nucleation of a pre-formed Ce_6O_8 cluster. Low modulator concentrations yielded a mononuclear Ce^{III} MOF through single-crystal X-ray diffraction studies, while higher modulator concentrations yielded a pure phase Ce_6-based MOF featuring instead a Ce^{IV} node. Beyond just offering competitive nucleation to yield more crystalline materials, this chapter suggests a new function for modulators to limit the reduction of highly redox active inorganic nodes during MOF self assembly.

Chapter 6 describes a serendipitous discovery of the phase transition observed within a Th-based MOF without added external stimuli. We report the transition of a 3-Dimensional Th_6-based MOF to a mononuclear 2-Dimensional Th MOF that we attribute to the evaporation of solvent during the synthesis. Upon exposing the 2-D material to water, it partially converted back into to the 3-D MOF, highlighting the complex equilibrium. We explored the possible transitions within other isostructural $M^{IV}{}_6$-based MOFs and propose that Ce could also exhibit the same behavior with isolated products we characterize with single crystal X-ray diffraction.

Chapter 2. Supramolecular Porous Assemblies of Atomically Precise Catalytically Active Cerium-Based Clusters

Portions of this chapter appear in the following manuscript:

Wasson, M.C.; Zhang, X.; Otake, K.; Rosen, A.; Alayoglu, S.; Krzyaniak, M.D.; Chen, Z.; Redfern, L.R.; Robsion, L.; Son, F.A.; Chen, Y.; Islamoglu, T.; Notestein, J.M.; Snurr, R.Q.; Wasielewski, M.R.; Farha, O.K. *Chem. Mater.* **2020**, *32*(19), 8522–8529.

2.1 Chapter Summary

Atomically precise metallic clusters offer total structural information lacking in metal oxide and nanoparticle catalysts. However, their use as heterogeneous catalysts requires accessible and robust catalytic sites, yet directing clusters into ordered and porous assemblies through functional control remains elusive. In this chapter, we present a supramolecular strategy to induce permanent porosity within assemblies of two cerium oxide clusters through the capping ligands used. Single-crystal X-ray crystallography and density functional theory calculations revealed cluster assemblies with accessible channels, while adsorption isotherms showed permanent porosity. The clusters exhibited a bulk modulus >5 GPa in variable pressure diffraction studies. X-ray photoelectron spectroscopy, electron paramagnetic resonance spectroscopy, and Raman spectroscopy demonstrated mixed valency (Ce^{3+}/Ce^{4+}) and oxygen vacancies in the clusters. We benchmarked catalytic activities through the photooxidation of 2-propanol.

2.2 Targeted Design Strategies of Atomically Precise Clusters

In the past several decades we have witnessed a surge in the design of nanomaterials tailored in porosity, size, and morphology that give rise to tremendous chemical and/or physical functionality.[59,63–67] Targeting high surface area of materials to enhance the accessibility of active sites for analyte adsorption and subsequent catalysis has been well-studied through synthetic modulation of bulk oxides,[68–70] structure-directing agents or templates in zeolites[71–73], and more recently, reticular chemistry in tunable, crystalline materials like metal–organic frameworks (MOFs).[74,75] Balancing the accessibility of active sites to substrates and ensuring material robustness in industrially relevant catalytic conditions is very important within these novel porous materials. Beyond the porosity of nanomaterials, synthetic control to access a desired size domain or surface facet has tuned metallic nanoparticles and metal oxides for a myriad of applications including drug delivery, photovoltaics, and catalysis.[76–78] However, it remains challenging to synthesize monodisperse nanoparticles or structurally well-defined nano-sized oxides, which complicates the study of fundamental reactivity.

If atomically precise metal clusters are available, it is much easier to develop structure-property relationships at the molecular level. For example, Jin and co-workers[29,79] synthesized and designed sophisticated gold thiol-based clusters. Crystallography facilitates the study of ligand coordination interfaces to probe the role imparted by organic capping agents on clusters' structures. In one study, two thiolate capped Au_{28} clusters exhibited ligand-induced reversible isomerization, which resulted in different efficacies in the catalytic oxidation of CO over a CeO_2 support.[80] In addition to thiol groups, carboxylate based capping groups can stabilize metallic clusters.[81–89] Recent work by Chatelain *et al.* isolated a series of U_6, U_{10}, U_{13}, U_{16},U_{24}, and U_{38} -oxo clusters, which suggested the thermodynamically assisted condensation of isolated U_{24} and U_6 clusters can access a large nuclearity U_{38} motif.[89]

The reactivity of cerium oxide compels the targeted synthesis of cerium-based clusters to serve as simplified subsets of the bulk material. Highly utilized and well-studied within heterogenous catalysis, the metal oxide features porosity and unique reactivity toward CO oxidation, thermochemical water splitting, and photocatalytic oxidation.[90–96] Depending on reaction conditions, bulk ceria selectively stores and releases lattice oxygen atoms.[94,97] The abstraction of oxygen and charge balancing reduction of two lattice Ce^{4+} atoms to Ce^{3+} generates highly reactive defect sites, known as oxygen vacancy defects (OVDs).[98] OVDs facilitate oxidation and reduction processes in ceria through a Mars-van Krevelen mechanism; in some cases, vacancy sites form as a result of lattice oxygen mobility,[99] whereas in other reports they can then directly participate in catalytic reactions. [7,100] Due to varying surface energies and propensity to form OVDs, changes in ceria morphology and nanoparticle size dramatically impart a difference in oxidative reactivity.[92,101] OVD themselves can differ in their local structure within CeO_2 as Esch *et al.* previously observed a distribution of single layer and double layer surface vacancies as well as subsurface vacancies.[102]

A library of cerium clusters synthesized to date includes several Ce_6O_8-based clusters[103,104] as well as larger Ce_{10} and Ce_{22} clusters, resulting from the condensation of cerium carboxylate coordination polymers.[105] Christou and coworkers put forth pioneering work in accessing larger nuclearity Ce_{38} and Ce_{40} oxide clusters through the room-temperature self-assembly of ammonium cerium nitrate and propionic or acetic acid, respectively.[31] These clusters provide an elegant, atomically precise structural introduction to bulk ceria through the shared fluorite packing. However, the densely packed structures of the pristine clusters are in stark contrast to the porosity present in cerium dioxide targeted for catalytic reactions, often within the range of 50-100 m^2/g.[106] A *de novo* strategy to induce porosity and impart assembly control within a cluster's packing, while maintaining atomically precise structural knowledge, has yet to be developed for colloidal metallic nanoparticles. Moreover, the redox behavior of such large cerium oxo clusters reported to date remains mostly unexplored, although there is recent work on Ce_6 clusters. Estes *et al.* reported the reduction potential of Ce^{4+} decreased inside a Ce_6 cluster capped with glycine by ~0.8 V.[103] More recently, Mashima and coworkers generated hexanuclear cerium carboxylate clusters that photocatalyzed the decarboxylative oxygenation of aliphatic carboxylic acids and the lactonization of 2-isopropylbenzoic acid.[107] However, in these hexanuclear Ce-oxo clusters, OVDs were not directly observed, and a gap in reactivity between Ce clusters and bulk ceria still persists. Therefore, a porous cerium cluster with high nuclearity that can accommodate accessible OVDs could combine the atomic precision of a cluster with ceria's porosity and redox activity.

Herein, we sought to devise a strategy to introduce permanent porosity within high-nuclearity cerium oxo cluster materials through the judicious selection of capping organic ligands. To develop such systems, we utilized benzoic acid and 2-naphthoic acid, rigid aromatic moieties capable of undergoing favorable noncovalent interactions and providing steric bulk, as capping agents to stabilize high nuclearity clusters. Single crystal X-ray diffraction (SCXRD) provided structural data with lattice constants in good agreement with density functional theory (DFT) calculations. Crystallographic refinement suggested discrete channels that are accessible in this assembly, while adsorption isotherms supported bulk porosity. Variable temperature powder X-ray diffraction (VT-PXRD) studies explored the thermal stability; variable pressure X-ray diffraction studies within a diamond anvil cell (DAC) probed the mechanical stability. A mixed valency oxidation state was observed in the materials by X-ray photoelectron spectroscopy (XPS) and further suggested by electron paramagnetic resonance (EPR) spectroscopy. Raman spectroscopy revealed the presence of oxygen vacancy defects within the clusters. Following structural and electronic characterization, the porous cerium cluster assemblies exhibited a proof-of concept catalytic activity as benchmarked through the photooxidation of 2-propanol.

2.3 Experimental Methods and Material Characterization

To target the synthesis of high nuclearity Ce clusters, a solvothermal reaction of a stabilized Ce^{4+} source, a Ce_6O_8-glycine cluster (Ce_6 precursor), was exposed to either excess benzoic acid or 2-naphthoic acid in a diethylformamide/water mixture for 18 h at 120 °C. Indeed, with single crystal X-ray diffraction confirmed the synthesis of two Ce_{38} clusters capped with benzoic acid, **Ce_{38}-BA**, and 2-naphthoic acid, **Ce_{38}-NA**. Through interactions between phenyl rings on adjacent clusters (**Figure 2.1C**), the discrete clusters pack into a supramolecular porous, crystalline lattice (**Figure 2.1D**). A parallel displaced motif and displaced T-shaped motif between phenyl rings were observed in **Ce_{38}-BA**. The distances between the benzene centroids of the orthogonal interacting phenyls were ~5.5 Å, comparable to prior experimental and computational observations for benzene-benzene interactions in a T-shaped motif.[108,109] Thus, it is suggested that aromatic interactions could facilitate the observed packing of the assemblies. The directed packing renders discrete pores of roughly ~1 nm within the **Ce_{38}-BA** structure with accessible -OH/H_2O ligands directed into the pores. While data resolution of **Ce_{38}-NA** limited structural refinement to resolve only the Ce_{38} core, the slight enlargement of the unit cell parameters of **Ce_{38}-NA** from **Ce_{38}-BA** (*vide supra*) and an increase in cluster-cluster distance by ~1.4 Å suggest that **Ce_{38}-NA** features a similar packing direction motif directed by a larger capping agent. Periodic DFT calculations were conducted with the charge-neutral **Ce_{38}-BA** structure to optimize the atomic positions and Niggli-

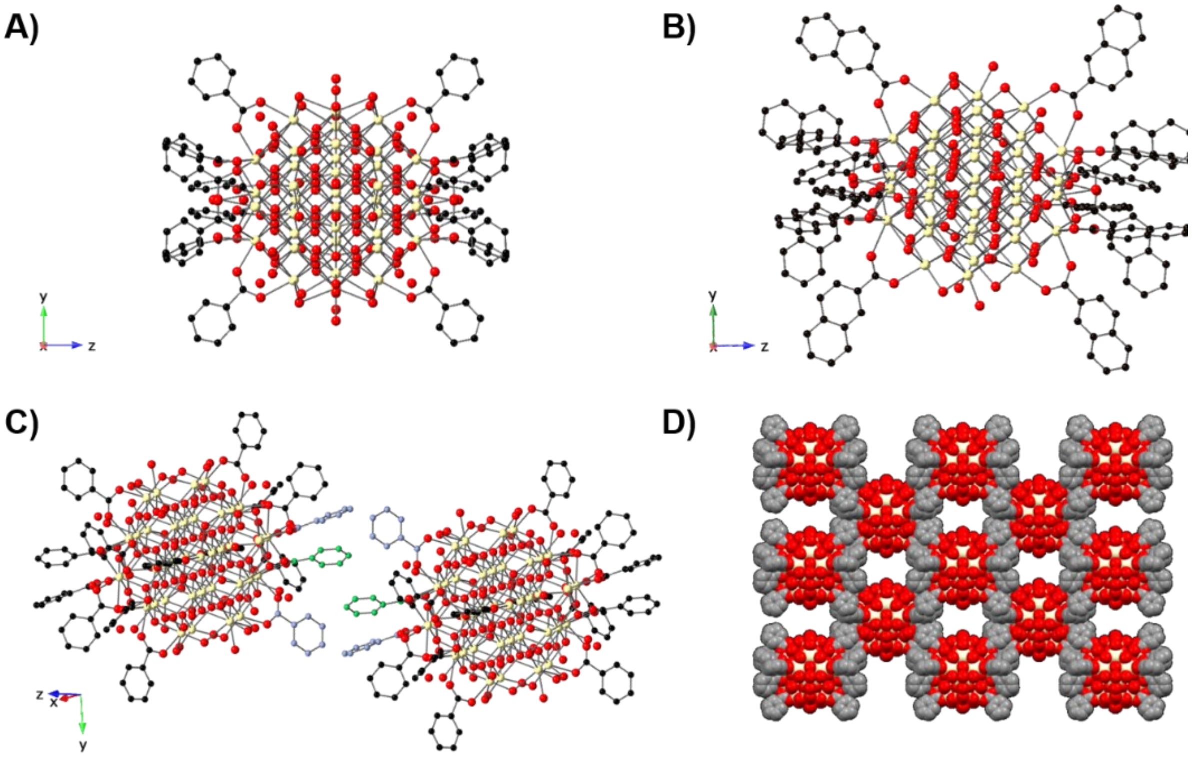

Figure 2.1 A) View of **Ce_{38}-BA** with 16 capped benzoate ligands. B) Simulated structure of **Ce_{38}-NA** with naphthoate ligands. C) Interacting phenyl groups between neighboring cluster in T-shaped (phenyls in pastel blue) or displaced parallel (phenyls in pastel green). D) Space-filled model **of Ce_{38}-BA** showing accessible pores. Unless otherwise indicated, C, black; O, red; Ce, pale yellow. H atoms are omitted for clarity.

reduced primitive cell lattice parameters using the rev-vdW-DF2 functional,[110–112] as implemented in VASP 5.4.1.[113,114] As shown in Figure S3A, the capping ligand-induced packing of the **Ce_{38}-BA** clusters is energetically plausible, and the overall structure is consistent with experiments. The capping ligands for **Ce_{38}-NA** are also able to stack in a similar manner as **Ce_{38}-BA** based on the theoretical calculations (**Figure 2.9B**).

Phase-purity of the bulk materials was first probed through powder X-ray diffraction (PXRD). Good agreement between the PXRD patterns of the synthesized structures and simulated structures was observed. Unit cell expansion with larger d_{101} and d_{110} of **Ce_{38}-NA** with respect to **Ce_{38}-BA** was indicated by a decrease of ~ 0.4° 2θ in the first two peaks (**Figure 2.2A**). To probe the extent of bulk porosity suggested by the crystallographic packing of **Ce_{38}-BA** and hypothesized to also exist within **Ce_{38}-NA**, N_2 physisorption isotherm measurements were conducted following activation procedures (**Figure 2.2B**). Indeed, permanent porosity was demonstrated with BET areas of 60 m^2/g and 65 m^2/g, respectively, for **Ce_{38}-BA** and **Ce_{38}-NA**, while the nonlocal density functional theory (NLDFT) derived pore model revealed respective pore sizes of 13 and 15 Å (**Figure 2.10**). We anticipate higher BET areas and pore volumes can be achieved with more complete activation methods (see *2.9.2 Methods for Material Characterization*).[115] Moreover, negligible N_2 adsorption within the previously reported propionic acid capped Ce_{38} cluster (**Ce_{38}-PA**) confirms its nonporous nature, in accordance with its densely packed crystal structure.[31] To the best of our knowledge, these are the first examples of non-covalent porous assemblies of cerium clusters.

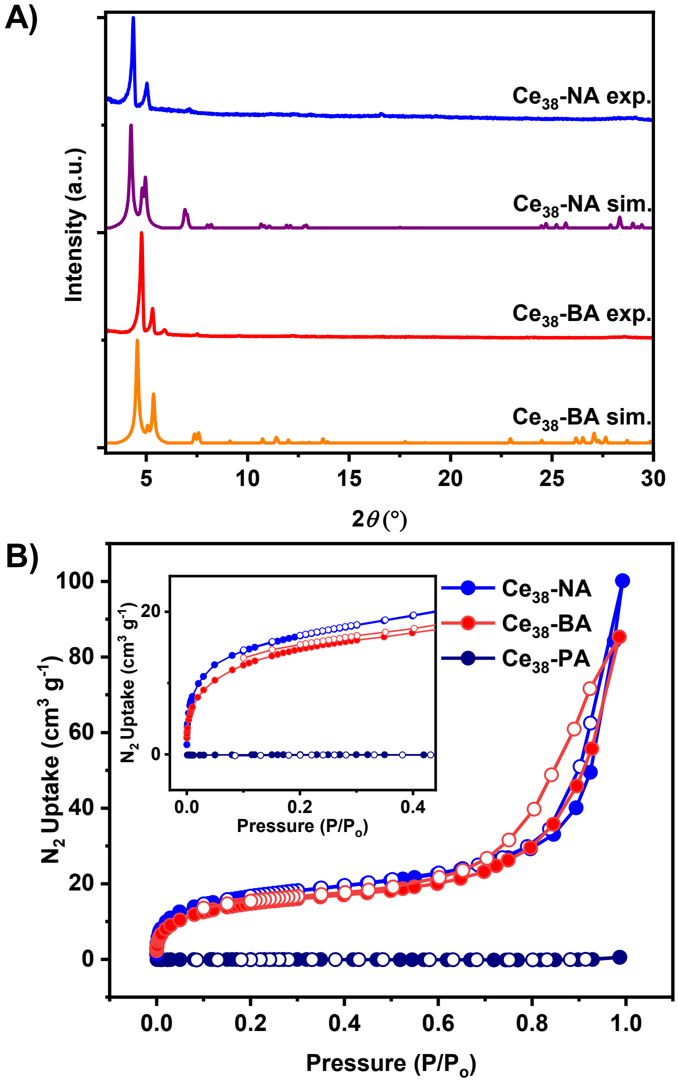

Figure 2.2 A) PXRD patterns of experimental **Ce$_{38}$-BA** and **Ce$_{38}$-NA** with simulated patterns. B) N_2 isotherms collected at 77 K of **Ce$_{38}$-BA**, **Ce$_{38}$-NA**, and **Ce$_{38}$-PA**. Inset highlights N_2 uptake from 0.0 to 0.4 P/P_0.

2.4 Thermal and Mechanical Stabilities of Porous Ce$_{38}$ Clusters

After establishing bulk phase purity of **Ce$_{38}$-BA** and **Ce$_{38}$-NA**, their respective thermal and mechanical stabilities were investigated. The thermal stabilities of **Ce$_{38}$-BA** and **Ce$_{38}$-NA** were probed with *in situ* VT-PXRD, and pure-phase crystallinity was maintained until 150 °C within each cluster (**Figures 2.11-2.14**). Beyond thermal stability, recent focus within porous frameworks has turned to also investigating frameworks' resistance to compression from external pressure to probe their physical robustness.[116–119] However, studies investigating the mechanical stability within non-covalent porous frameworks are rare. We were motivated to investigate how noncovalent interactions present in **Ce$_{38}$-BA** and **Ce$_{38}$-NA** would behave under applied pressure. The clusters' resistance to mechanical compression was measured in a diamond anvil cell under moderate pressure (< 1.5 GPa) with *in situ* powder X-ray diffraction from a synchrotron radiation source at the 17-BM beamline of the Advanced Photon Source following previously reported methodology.[120,121] The unit cell parameters of the sample in each pressure environment were extracted with Le Bail analysis. A second-order Birch–Murnaghan equation of state modeled the decrease in lattice volume to measure the bulk modulus (**Figure 2.3**), a term that is inversely related to the material's compressibility. Bulk moduli of 5.2(2) GPa and 6.3(3) GPa were determined for **Ce$_{38}$-BA** and **Ce$_{38}$-NA**, respectively. Notably, these non-covalent materials feature bulk moduli comparable to those of mineral clay (6.2 GPa)[122] or even greater than what is reported for some MOFs, PCN-57 (4.6 GPa).[121]

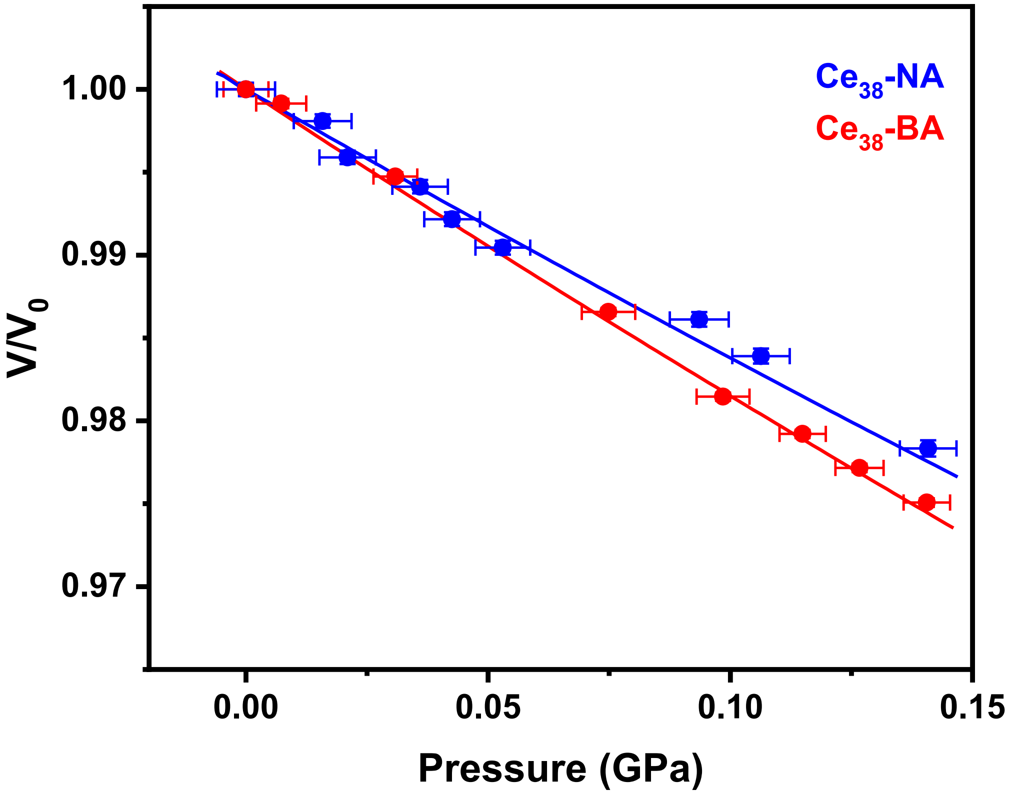

Figure 2.3 Relative lattice compression of **Ce_{38}-BA** and **Ce_{38}-NA**. Lines denote the second-order Birch–Murnaghan equation-of-state fits to the collected data.

2.5 Electronic Characterization of Ce_{38} Clusters

As a preliminary methodology to probe the valency of the cerium clusters, X-ray photoelectron spectroscopy (XPS) was performed. Within the Ce 3d XPS spectra of **Ce_{38}-BA** and **Ce_{38}-NA**, Ce^{3+}-related peaks appeared at 885.9/903.3 eV and 886.6/905.0 eV for each respective sample, totaling ~10% of Ce^{3+} present in each sample (**Figure 2.4**). In comparison, nearly quantitative Ce^{4+} was observed in the **Ce_6 precursor** utilized in the syntheses as well as in **Ce_{38}-PA**, in agreement with previous literature reports.[31,103] The intriguing mixed valency of **Ce_{38}-BA** and **Ce_{38}-NA** suggested in XPS was further explored through continuous wave electron paramagnetic resonance (EPR) spectroscopy at 10 K. Observation of an EPR signal attributed to a $S = \frac{1}{2}$ species, presumably Ce^{3+}, was observed for both **Ce38-BA** and **Ce38-NA** in agreement with XPS data, while one was not detected for **Ce38-PA** (**Figure 2.18**).

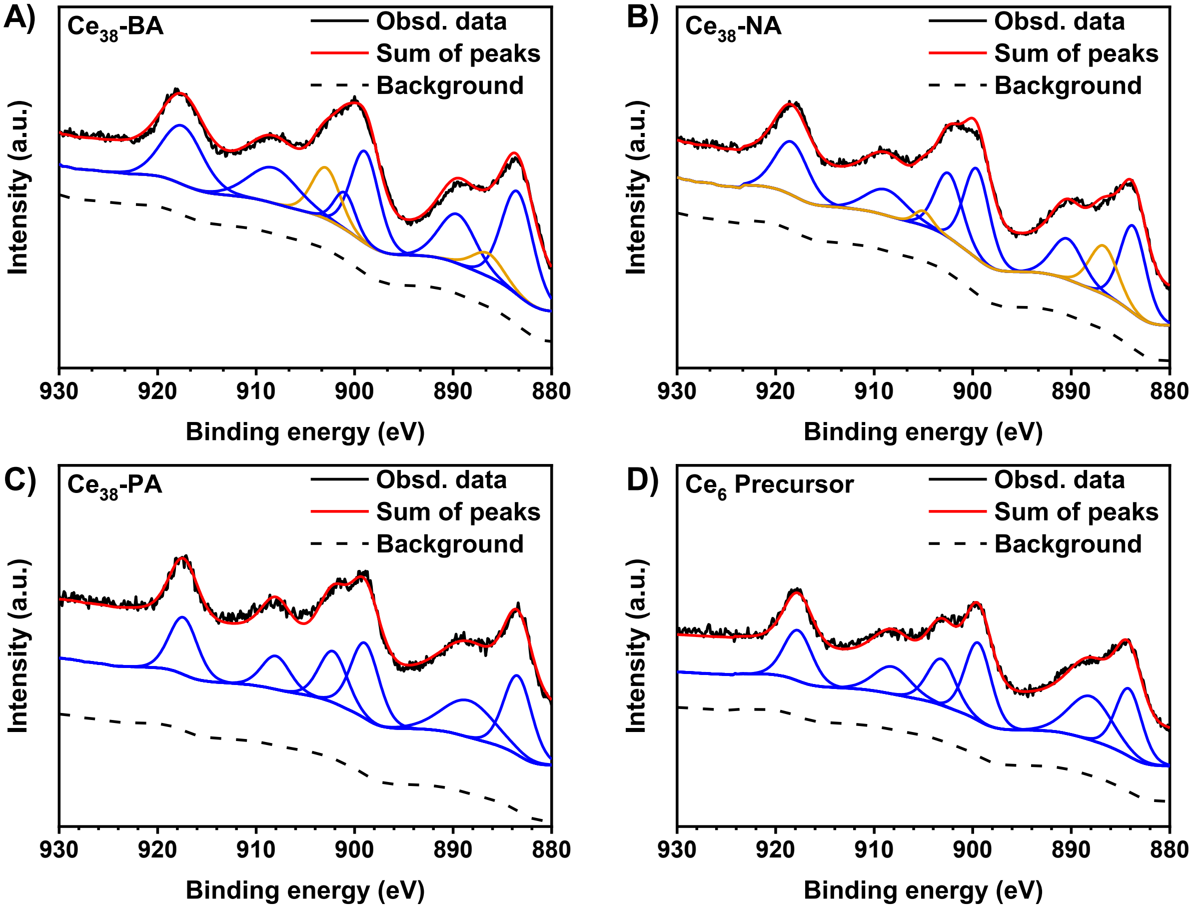

Figure 2.4 Observed Ce 3d XPS (solid black line) and sum of fitted data (red line) for A) **Ce38-BA**, B) **Ce38-NA**, C) **Ce38-PA,** and D) **Ce6 precursor**. The observed data were fitted by Gaussian/Lorentzian functions with deconvoluted peaks in blue corresponding to Ce^{4+} and orange deconvoluted peaks corresponding to Ce^{3+}.

2.6 Raman Spectroscopy

Motivated by the prevalence of OVDs in bulk ceria, Raman spectroscopy was utilized to probe the lattice defect environment in **Ce38-BA**, **Ce38-NA**, **Ce38-PA**, and commercial CeO_2. All of the samples featured two prominent peaks in the Raman spectra (**Figure 2.5**): a strong peak at

465 cm^{-1}, which is assigned to the Ce-O vibration with F_{2g} symmetry of the fluorite phase, and a weak peak (D) at about 620 cm^{-1}, which is well-established as arising from structural defects (oxygen vacancies and Ce^{3+} sites).[123] The three different Ce_{38} clusters F_{2g} peaks are broader and shifted >5 cm^{-1} to lower frequencies than that of the CeO_2 standard, suggesting more structural disorder. In agreement with this observation, D peaks for each Ce_{38} cluster are also more prominent, indicating defect rich structures. A ratio of the D/F_{2g} peak can be utilized as a simplified method of quantifiably comparing defect densities throughout cerium oxide materials. **Ce_{38}-BA** and **Ce_{38}-NA** both exhibited D/F_{2g} ratios of 0.28 and 0.25 respectively, while **Ce_{38}-PA** yielded a ratio of 0.08. The nanostructured CeO_2 reference was less defective with a ratio of 0.02. The intriguing difference in defects observed through Raman for **Ce_{38}-BA** and **Ce_{38}-NA** compared to

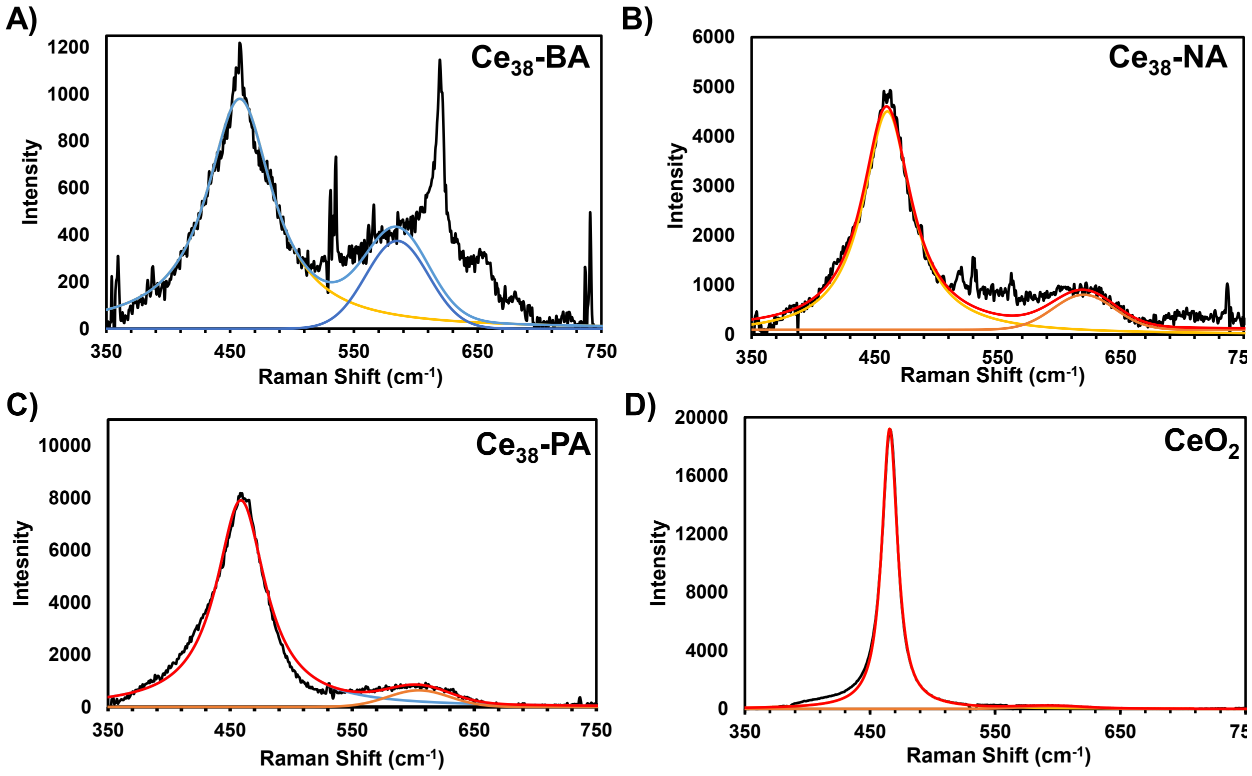

Figure 2.5 Raman spectra collected (black lines) and fitted data (colored lines) for A) **Ce_{38}-BA**, B) **Ce_{38}-NA**, C) **Ce_{38}-PA,** and D) commercial CeO_2.

Ce_{38}**-PA** was rationalized through ligand stoichiometry as well as overall void spaces in the materials. 36 propionic acid ligands cap the Ce_{38}**-PA** cluster, while 16 carboxylate linkers chelate to Ce_{38}**-BA** (through SCXRD) and Ce_{38}**-NA** (estimated through elemental analysis). Subsequently, the surface -OH/-H_2O ligands that replace any missing carboxylate linkers in Ce_{38}**-BA** and Ce_{38}**-NA** render the Ce_{38}-oxo core more accessible. Moreover, the surfaces of the Ce_{38}**-PA** clusters are all directly touching each other yielding a denser environment than the porous assemblies of Ce_{38}**-BA** and Ce_{38}**-NA**. Subsequently, we rationalize the higher defect ratios present in Ce_{38}**-BA** and Ce_{38}**-NA** as a result of the heightened accessibility of the Ce_{38}-oxo clusters. This is the first observation of lattice oxygen defects observed within a cerium oxo-based cluster to the best of our knowledge. Moreover, the full width at half maximum values of the F_{2g} peak, can be used to extrapolate average grain sizes of 2.2 nm, 3.2 nm and 3.1 nm, respectively, for Ce_{38}**-BA**, Ce_{38}**-PA**, and Ce_{38}**-NA**, consistent with the theoretical size estimates for these clusters.[123]

2.7 Photocatalytic Reactivity

To benchmark the catalytic activity of the synthesized clusters, we explored the photooxidation of 2-propanol under aerobic conditions with 3 mol% of catalyst. ^1H nuclear magnetic resonance (NMR) monitored reaction progress through the disappearance of the starting material (**Figure 2.6**). Liquid products were quantified through NMR, while CO and CO_2 present in the head space were detected through manual injections in a gas-tight syringe into a gas chromatograph equipped with a flame ionization detector (GC-FID). After 1 hour of reaction progress, 45% and 46% of 2-propanol was consumed by Ce_{38}**-BA** and Ce_{38}**-NA** respectively, while 25% was converted by Ce_{38}**-PA** and 14% by Ce_6 **precursor**. A kinetic profile up to 6 hours was collected (**Figure 2.19**) and a distribution of oxidation products were observed (**Figures 2.26-2.28**, **Tables 2.5-2.8**). However, liquid-phase products accounted for only <25% of the total product yield, while the remaining product formed was attributed to the detected major gaseous product, CO (**Figure S29**). Negligible conversion was observed when the reaction proceeded in absence of light as well as in the absence of catalyst. Filtration studies suggested the heterogeneity of all four catalysts investigated (**Figure 2.20**). After catalysis, the crystallinity of **Ce38-BA** and **Ce38-NA** was retained as demonstrated through PXRD (**Figure 2.21**). These results suggest that the high porosity and rich OVDs of **Ce38-BA** and **Ce38-NA** can facilitate the photooxidation of 2-propanol. This preliminary benchmark of catalytic activity demonstrates the utility of the large nuclearity Ce-oxo based clusters for future studies.

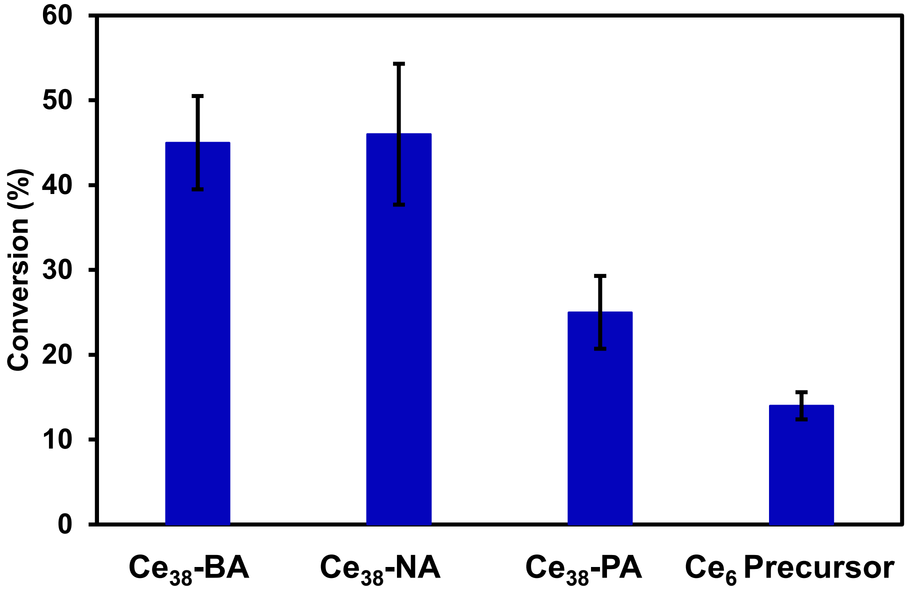

Figure 2.6 Reaction progress after 1 hour for the photooxidation of 2-propanol catalyzed by cerium clusters at 390-400 nm as monitored by ^{1}H NMR. Average of three trials.

2.8 Conclusions

We demonstrated a supramolecular strategy to access bulk porosity within an assembly of well-defined cerium oxo clusters through the use of rigid, aromatic capping agents—benzoic acid and 2-napthoic acid—to yield **Ce38-BA** and **Ce38-NA**. Single-crystal X-ray diffraction analyses of

Ce_{38}-BA and **Ce_{38}-NA** suggested discrete channels that are accessible in this assembly, while gas adsorption isotherms supported permanent porosity. To the best of our knowledge, these are the first examples of non-covalent porous assemblies of cerium clusters. Despite the absence of coordination bonds between clusters, *in situ* variable pressure powder X-ray diffraction experiments highlighted the robustness of these systems with the bulk moduli extracted. **Ce_{38}-BA** and **Ce_{38}-NA** contained appreciable amounts of Ce^{3+} in the bulk product and demonstrated Raman signatures of lattice oxygen vacancy defects. The photocatalytic oxidation of 2-propanol benchmarked the catalytic activity of the cerium clusters, featuring a 3-fold increase in conversion over the **Ce_6 precursor** and a 2-fold increase in conversion over **Ce_{38}-PA**. The strategy developed herein to design porous cluster assemblies through the judicious selection of capping agents is a promising step toward imparting atomic level control of metal-oxide materials. We are hopeful that additional properties present in well-studied nanoparticle and coordination frameworks can be similarly targeted in periodic clusters through such bottom-up design strategies.

2.9 Additional Information

2.9.1 Materials

All chemicals and solvents were obtained from commercial suppliers and used without further purification. Ammonium cerium nitrate (≥98.5%), glycine (≥99%), sodium chloride (≥99.5%), benzoic acid (≥99.5%), N,N-diethylformamide (99%), ammonium iodide (≥99%), propionic acid, cerium oxide nanopowder (<50 nm particle size (BET), 99.95% trace rare earth metals basis), acetonitrile - d_3 (99.8 atom % D), and 1-bromo-3,5-difluorobenzene (98%) were purchased from Sigma-Aldrich. 2-naphthoic acid (98%) was purchased from Combi-Blocks. Pyridine (≥99 %), acetonitrile (99.9%), 2-propanol (≥99.5 %), and ethanol (histological) were purchased from Fischer Chemical. Deionized water was used as the water source.

2.9.2 Methods for Material Characterization and Catalytic Experiments

Single Crystal X-Ray Diffraction Analysis: Single-crystal X-ray structure analysis of ***Ce$_{38}$-BA*** was carried out using a Bruker Kappa APEX II CCD/ detector equipped Mo Kα (λ = 0.71073) microsource with MX optics. Single-crystal X-ray diffraction (SC-XRD) data of ***Ce$_{38}$-NA*** was collected at 250 K on a 'Bruker APEX-II CCD' diffractometer with a CuKα (λ = 1.54184 Å) microfocus X-ray source. The single crystals were mounted on MicroMesh (MiTeGen) with paratone oil. The structures were determined by intrinsic phasing (SHELXT 2018/2) and refined by full-matrix least-squares refinement (SHELXL-2018/3) using the Olex2 software packages. Due to the small size and weak diffraction of the single crystals (best resolution of 1.3 Å), only the Ce$_{38}$ core of the Ce$_{38}$-NA structure was resolved and refined. The arrangement of Ce atoms were similar to Ce$_{38}$-BA. The rest of the structures was completed through computational modeling as detailed below. Refinement results are summarized in **Table 2.1**. Crystallographic data in CIF format have been deposited in the Cambridge Crystallographic Data Centre (CCDC) under deposition number 2000674 (**Ce$_{38}$-BA**) and 2003383 (**Ce$_{38}$-NA**). The data can be obtained free of charge via www.ccdc.cam.ac.uk/data_request/cif (or from the Cambridge Crystallographic Data Centre, 12 Union Road, Cambridge CB2 1EZ, U.K.).

*Refinement Details of **Ce$_{38}$-BA**:* Coordinating benzoate and water/hydroxyl sites were refined using some thermal and structural restraints (ISO, RIGU, SIMU). On the benzoate sites, AFIX66 was also used to model the benzene rings. The disordered non-coordinated solvents were removed using the PLATON SQUEEZE program after the determining all assignable atoms of Ce$_{38}$ clusters. Refinement results are summarized in Table 2.1.

Table 2.1: Crystallographic details of **Ce$_{38}$-BA**

Empirical formula	$C_{114}H_{80}Ce_{38}O_{114}$
Formula weight	8598.33
Temperature/K	100
Crystal System	Tetragonal
Space Group	$I\,4/m$
***a*/Å**	23.2865(8)
***b*/Å**	23.2865(8)
***c*/Å**	34.8183(4)
***α*/°**	90
***β*/°**	90
***γ*/°**	90
Volume/Å^3	18880.6(15)
Z	2
ρ_{calc}g/cm^3	1.512
μ/mm^{-1}	4.522
F(000)	7760
Crystal size/mm^3	0.05×0.10×0.25
Radiation	MoKα (λ = 0.71073)
2θ range for data collection/°	1.237 to 23.409
Index ranges	$-24 \leq h \leq 26$, $-22 \leq k \leq 25$, $-38 \leq h \leq 38$,
Reflections collected	42638
Independent reflections	6980
Data/restraints/parameters	6980/313/306
Goodness-of-fit on F^2	1.329($I \geq 2\sigma(I)$), 1.322 (all data)
Final R indexes [I ≥ 2σ (I)]	0.1092 (R_1), 0.3307 (wR_2)
Final R indexes [all data]	0.1589 (R_1), 0.4052 (wR_2)
CCDC deposition number	2000674

*Response to A level check cif alerts for **Ce$_{38}$-BA** single crystal:*

Alert level A

PLAT973_ALERT_2_A Check Calcd Positive Resid. Density on Ce1 7.74 eA-3

PLAT973_ALERT_2_A Check Calcd Positive Resid. Density on Ce2 6.92 eA-3

PLAT973_ALERT_2_A Check Calcd Positive Resid. Density on Ce3 6.75 eA-3

PLAT973_ALERT_2_A Check Calcd Positive Resid. Density on Ce4 5.59 eA-3

PLAT973_ALERT_2_A Check Calcd Positive Resid. Density on Ce5 5.36 eA-3

PLAT973_ALERT_2_A Check Calcd Positive Resid. Density on Ce6 5.31 eA-3

Response: The atom type is correct, and there is no evidence of twinning. The crystals showed strong diffuse scattering between Bragg peaks probably because of the oxygen defects. This is believed to be the source of the high electron density on the Ce. Inefficient absorption correction and an anomalous dispersion effect may also cause this problem.

Computational Methods

Constructing the **Ce$_{38}$-BA** System: A Niggli-reduced primitive cell of the experimentally resolved crystal structure for the **Ce$_{38}$-BA** clusters was constructed such that there is only one Ce$_{38}$ cluster per unit cell. The disorder in the experimental structure was refined by removing half of the O atoms with occupancies of 0.5. Protons were then added to the cluster such that the resulting structure was charge-neutral under the assumption that the Ce atoms are in the 4+ oxidation state. This yields a formula unit of $Ce_{38}(C_6H_5COO)_{16}(\mu_4\text{-}O)_{34}(\mu_4\text{-}OH)_2(\mu_3\text{-}O)_{24}(\mu_2\text{-}OH)_8(\mu_1\text{-}OH)_{10}$ per cerium oxide cluster, including the BA capping agent. While the exact proton topology of the synthesized **Ce$_{38}$-BA** cluster may differ, this is not expected to significantly alter the predicted geometric properties. Water molecules were not included in the model since these are also not expected to notably alter the geometric properties. The atomic positions and cell volume were relaxed using periodic density functional theory (DFT), as described below.

Constructing the **Ce_{38}-NA** System: Unlike the **Ce_{38}-BA** system, the capping agents of the **Ce_{38}-NA** crystal structure are not crystallographically resolved. We also note that the space group and placement of the Ce_{38} clusters in the unit cell of **Ce_{38}-NA** are different from that of **Ce_{38}-BA,** such that the smallest unit cell for **Ce_{38}-NA** contains two Ce_{38} cluster per unit cell rather than the one Ce_{38} cluster in **Ce_{38}-BA**. To generate a physically plausible crystal structure of **Ce_{38}-NA** with capping agents included, we first replaced the two partially resolved Ce_{38} clusters of the **Ce_{38}-NA** structure with two copies of the charge-neutral, DFT-optimized **Ce_{38}-BA** cluster, ensuring the centers of mass and orientation of the Ce_{38} clusters were roughly unchanged. Then, the BA capping agents were converted to NA in a manual fashion to provide a physically reasonable initial structure for the **Ce_{38}-NA** system. The NA capping agents are not rotationally symmetric; therefore, the exact packing of the crystal structure depends on the orientation of the capping agents. We ensured that the NA capping agents were oriented in such a way to prevent overlapping atoms or close-contacts within the constraints of the experimentally resolved **Ce_{38}-NA** crystal structure. Given the large number of atoms in the **Ce_{38}-NA** system (912 atoms/cell), a DFT relaxation could not be performed. Instead, as a means of refining the manually constructed capping agents, a partial geometry optimization of the atomic positions was carried out using molecular mechanics, as described below.

Structure Relaxations: Periodic DFT calculations were carried out using the Vienna *ab initio* Simulation Package (VASP) v.5.4.1[114,124] with v.5.4 of the VASP-recommended projector-augmented wave (PAW) pseudopotentials. The rev-vdW-DF2 exchange-correlation functional was employed,[110–112] as it accounts for dispersion interactions and is known to yield accurate lattice constants.[110] As benchmarked in prior work,[125] the DFT calculations were carried out using a 520 eV plane-wave kinetic energy cutoff with k-point sampling at the Γ-point. Symmetry constraints were disabled, and the accurate precision keyword was enabled in VASP. The geometry was considered converged once the net force on each atom was less than 0.05 eV/Å. The conjugate gradient algorithm was used to relax the structures. A mixture of the Davidson and Residual Minimization/Direct Inversion in the Iterative Subspace (RMM-DIIS) algorithms was used to converge the self-consistent field, and non-spherical contributions from the gradient corrections inside the PAW spheres were included. Gaussian smearing of the band occupancies with a smearing width of 0.2 eV and fully automatic optimization of projection operators were used. Structural relaxations were carried out by first optimizing all the atomic positions with a fixed unit cell, followed by a full volume relaxation of the atomic positions, lattice constants, and cell shape. VASP calculations were carried out and analyzed using the Atomic Simulation Environment (ASE) v.3.18.1.[126] Pymatgen v.2019.8.4[127] was used to construct the Niggli-reduced primitive cell.

Geometry optimizations using molecular mechanics were carried out using the Forcite module in Materials Studio v.5.0.0 with manually confirmed bond-typing for each atom and the Universal Force Field (UFF).[128] Since UFF does not properly describe several of the key parameters related to the Ce_{38} clusters, we defined all the Ce and O atoms as being part of a fixed motion group. The atomic positions of the remaining atoms were then relaxed, at fixed cell volume, using the default "Medium" optimization settings in Materials Studio until convergence was achieved.

Powder X-ray Diffraction Analysis: Powder X-ray diffraction (PXRD) patterns of the samples were measured by a STOE-STADI MP powder diffractometer operating at 40 kV voltage and 40 mA current with Cu-Kα1 X-ray radiation (λ = 1.5406 Å) in transmission geometry.

Variable Temperature In Situ Powder X-Ray Diffraction Analysis: Variable temperature PXRD patterns ranged from 1.75° to 20° were taken on a STOE STADI MP instrument using a

Mo-Kα1 source (λ = 0.7107 Å). Prior to being mounted on the instrument, the VT samples were loaded into a capillary (O.D. 1.5mm) and flame sealed. The activated samples were heated from 30 °C to 400 °C in 10°C/min increments with a 3-minute hold.

Variable Pressure In Situ Powder X-Ray Diffraction Analysis: Each sample was mixed with an internal standard, CaF_2 (~10% by volume). The powders were evenly mixed and any larger crystals were broken up with gentle grinding in a mortar and pestle. The mixture was loaded into a 250 μm diameter hole in a 250 μm thick stainless-steel gasket pre-indented to 100 μm thickness using a membrane-driven diamond anvil cell (DAC) equipped with 500 μm culet anvils. The cell was closed without applied pressure to collect the diffraction pattern for the sample under ambient conditions. The cell was opened and a drop of FluorinertTM FC-70 was added as a non-penetrating pressure transmitting fluid. The cell was sealed and *in situ* powder X-ray diffraction data were collected using the monochromatic X-rays (λ = 0.45390 Å, 100 μm beam size) at the 17-BM-B beamline at the Advanced Photon Source, Argonne National Laboratory in combination with a Perkin Elmer a-Si Flat Panel PE1621 area detector. Data were collected with 6 s exposures (1 min per image) as the pressure was varied from 0-1.5 GPa. After completion of a pressure campaign, the pressure within the cell was released and a final measurement was made at ambient pressure. Raw images were processed with GSAS-II, utilizing sample-to-detector distance and tilt parameters based on data obtained for a LaB_6 standard.[129] Representative examples of powder diffraction data for **Ce_{38}-BA** and **Ce_{38}-NA** are presented in **Figures 2.15** and **2.16** respectively. The pressure-dependent lattice parameters were extracted from Le Bail fits of reported structural models to the diffraction data using GSAS-II.[130] The unit cell parameters extracted from the ambient pressure PXRD pattern in the DAC differ from those observed during single crystal X-ray diffraction: **Ce_{38}-BA** (a=b= 23.19280 Å, c=29.16064 Å) in I4/m and **Ce_{38}-NA** (a=b= 24.20509

Å, c=34.8422 Å) in $P4_2/n$. These unit cell parameters were utilized to determine the initial unit cell volume for variable pressure powder X-ray diffraction analysis. Equations of state were fit to the P vs. V_0/V data using EOS-FIT7c and EOS-FIT7-GUI with the 2nd-order Birch-Murnaghan equation of state.[131,132] While diffraction data was collected up to ~ 1.3 GPa, the 2nd-order Birch-Murnaghan equation of state could only effectively model the lower pressure regimes.

N_2 Sorption Isotherm Measurements: N_2 adsorption and desorption isotherms on activated materials were measured on a Micromeritics Tristar (Micromeritics, Norcross, GA) instrument at 77 K. Around 30 mg of sample was used in each measurement and the specific surface areas were determined using the Brunauer−Emmett−Teller model from the N_2 sorption data in the region P/P_0 = 0.005–0.05. Pore size distributions were obtained using DFT calculations using a carbon slit-pore model with a N_2 kernel.

X-ray Photoelectron Spectroscopy: X-ray photoelectron spectroscopy measurements were carried out on a Thermo Scientific ESCALAB 250 Xi equipped with an electron flood gun and a scanning ion gun. Analysis used the Thermo Scientific Avantage Data System software, and C1s peak (284.8 eV) peak was used as the reference. Oxidation states of Ce were assigned by comparison to previously published data.[133]

Nuclear Magnetic Resonance (NMR) Spectroscopy: NMR spectra were collected on a Bruker Avance III 500 MHz system equipped with DCH CryoProbe and automated with a BACS-60 autosampler.

Electron Paramagnetic Resonance Spectroscopy: EPR measurements were performed at X-band (~9.6 GHz) using a Bruker Elexsys E580-X EPR spectrometer outfitted with a pulsed ENDOR resonator (EN 4118X-MS5). The temperature was maintained at 10 K with an Oxford

Instruments CF935 continuous-flow cryostat using liquid helium. The continuous wave (CW) EPR spectra were collected using non-saturating microwave power and 0.5 mT field modulation at 60 kHz.

Raman Spectroscopy: Raman measurements were carried out on a custom-built system equipped with a Lexel SHG deep UV and visible Ar ion laser and a Horiba IHR 550 spectrometer. Fundamental 488 nm excitation was employed for all Raman measurements. Laser power by the sample was 50 mW; and spot size by the sample was estimated at a few hundred micrometers. Raman signal was collected by using an off-axis parabolic mirror with a through pinhole. Powder samples were placed in the fluidized bed reactor and fluidized during laser illumination by a flow of simulated air (100 sccm, 20% O_2 in balance N_2). An average of four spectra were collected for all the samples. Exposure time per spectrum was 150 s for the Ce_{38} samples, and 15 s for the CeO_2 nanopowder reference (Aldrich, 50 nm particles).

Photooxidation of 2-propanol: The catalyst (3 mol %, entire cluster considered as active catalyst) and 1 mL of aceotonitrile was added to a Biotage microwave vial with a stir bar. The vial was cringe-capped and purged with O_2 for 15 min. 2-propanol (11.5 μL, 0.15 mmol) and 1-bromo-3,5-difluorobenzene (10 μL, 0.15 mmol) were added to the vial with a glass syringe. A 10 μL aliquot was taken prior to irradiation as a time zero point. Samples were then irradiated, stirring at 500 rpm at room temperature. 10 μL aliquots were taken at designated time points and diluted with 600 μL of acetonitrile-d_3 prior to NMR analysis. LED irradiation was performed using solderless LEDs, purchased from RapidLED, which were then mounted on aluminum to give a homemade irradiation setup. The LEDs were hooked up in series to a Mean Well LPC-35-700 constant current driver also purchased from RapidLED. The irradiation setup contains two UV LEDs (λ_{max} = 390-400 nm) that are mounted facing each other ~1.5 cm apart. The set-up was covered with aluminum foil to limit the escape of the light. To test the gaseous headspace of the reaction vial for product generation, 1 mL of headspace was collected in an airtight gas syringe and manually injected into an Agilent 7890A GCA gas chromatograph equipped with a flame ionization detector (GC-FID), Activated Research Company Jetanizer, and an Agilent HP-PLOT Q column. A 25:1 ratio of CO: CO_2 (see **Figure 2.29**) was typically observed. Filtration studies were completed by filtering the catalyst from the reaction mixture after 1 hour of reaction. The resulting filtrate was re-purged with O_2 prior to further 2-hour irradiation with stirring.

2.9.3 Materials Synthesis and Powder X-Ray Diffraction Characterization

Synthesis of Ce_{38}-BA: Benzoic acid (500 mg, 4 mmol) was placed in an 8-dram vial containing 5 mL of diethylformamide. The vial was sonicated until the contents solubilized. Next, Ce_6 precursor (120 mg, 0.05 mmol) and 2.5 mL of water were added to the vial, which was sonicated until the cluster solubilized. The vial was placed in an oven overnight at 120 °C for 18 h. Solutions were removed from the oven and cooled to room temperature. The tan-brown product and supernatant were placed in a centrifuge tube and were centrifuged for five minutes to remove the supernatant. Then, the resultant powder was washed with N,N-diethylformamide (10 mL×2) and acetone (10 mL×2), soaking in each solvent for 20 minutes prior to 5 minutes of centrifugation. The material was then washed in ethanol (10 mL x2), soaking each time for 20 minutes, prior to 5 minutes of centrifugation. The material was soaked in ethanol overnight, and then washed two more times with ethanol and centrifuging the solvent off in between washes. The material was dried for 30 minutes in a vacuum oven at 80 °C prior to overnight (18 hr) treatment under high vacuum at 30 °C on a Micromeritics Smart Vacprep. Of note, super critical-CO_2 activation [134] was also explored as an alternative activation procedure to increase surface area of materials, yet comparable surface areas were obtained with room temperature high vacuum treatment. Further optimization of activation procedures is likely needed fully access the greatest extent of the nanoclusters' apparent surface area if any capping agent is trapped as a guest in the pores.

Synthesis of Ce_{38}-NA: 2-naphthoic acid (700 mg, 4 mmol) was placed in an 8-dram vial containing 5 mL of diethylformamide. The vial was sonicated until the contents solubilized. Next, Ce_6 precursor (120 mg, 4 mmol) and 2.5 mL of water were added to the vial, which was sonicated until the cluster solubilized. The vial was placed in an oven overnight at 120 °C for 18 h. Solutions were removed from the oven and cooled to room temperature. The yellow-orange product and supernatant were placed in a centrifuge tube and centrifuged for five minutes to remove the supernatant. Then, the resultant powder was washed with N,N-diethylformamide (10 mL×2) and acetone (10 mL×2), soaking in each solvent for 20 minutes prior to 5 minutes of centrifugation. The material was then washed in ethanol (10 mL×2)), soaking each time for 20 minutes prior to 5 minutes of centrifugation. The material was soaked in ethanol overnight, and then washed two more times with ethanol and the solvent removed with centrifugation between washes. The material was dried for 30 minutes in a vacuum oven at 80 °C prior to overnight (18 hr) treatment under high vacuum at 30 °C on a Micromeritics Smart Vacprep.

$[Ce_6(\mu_3\text{-}O)_4(\mu_3\text{-}OH)_4(NH_3CH_2COO)_8(NO_3)_4(H_2O)_6]Cl_8\cdot 8H_2O$ **(Ce_6 precursor)** and $[Ce_{38}O_{54}(OH)_8(CH_3CH_2CO_2)_{36}(C_5H_5N)_8]$ **(Ce_{38}-PA)** were synthesized according to literature procedures.[31,103,135]

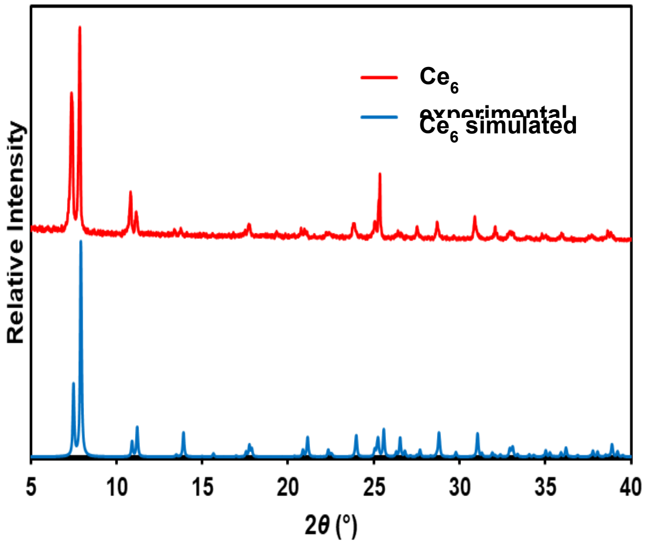

Figure 2.7: PXRD patterns (λ = 1.5406 Å) of experimentally synthesized and simulated patterns of **Ce_6 precursor**.

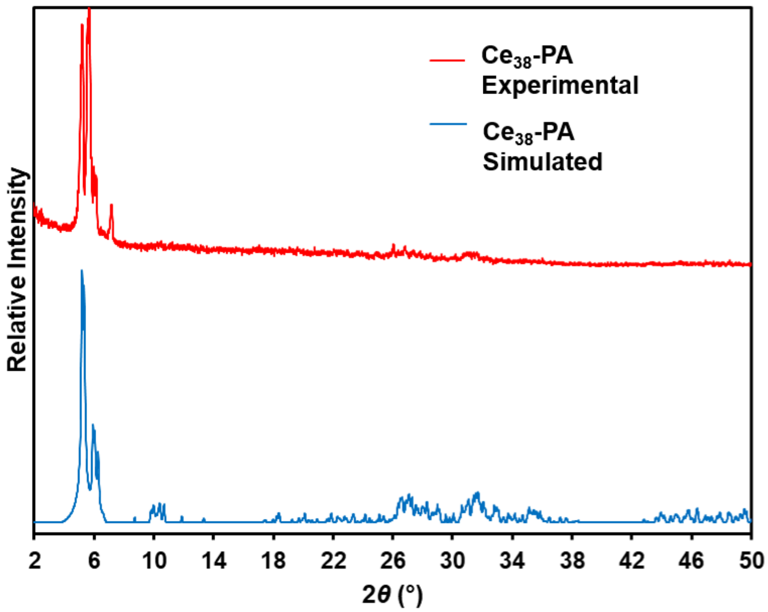

Figure 2.8: PXRD patterns (λ = 1.5406 Å) of experimentally synthesized and simulated patterns of **Ce_{38}-PA.**

2.9.4 Structural Relaxations

The VASP-optimized structure of **Ce$_{38}$-BA** is shown in **Figure 2.9A**. Consistent with the experimental results shown in **Figure 2.1C**, the structure is stabilized by interactions between nearby phenyl groups. The DFT-optimized lattice constants using the aforementioned settings are $a = 23.23$ Å, $b = 23.23$ Å, $c = 23.93$ Å, $\alpha = 119.07°$, $\beta = 119.06°$, and $\gamma = 89.98°$, which are within 0.25% of experiment ($a = b = 23.29$ Å, $c = 23.97$ Å, $\alpha = \beta = 119.07°$, $\gamma = 90.00°$). As such, the DFT calculations confirm that the packing of the clusters is energetically plausible. We note that the potential energy surface is extremely flat with respect to unit cell volume, and additional reduction to the cell volume lowers the energy further. Nonetheless, the aforementioned DFT-optimized structure can likely be thought of as a meta-stable state due to the low forces on all the atoms, lending confidence to the feasibility of the capping ligand arrangement. If there are any molecules that remain within the pores of **Ce$_{38}$-BA**, then this would also be expected to influence the exact equilibrium volume. The partially optimized **Ce$_{38}$-NA** structure is shown in **Figure 2.9B**. Even though the capping ligands of **Ce$_{38}$-NA** could not be resolved crystallographically, the optimized structure indicates that the capping ligands of **Ce$_{38}$-NA** can be arranged in an energetically favorable manner that is comparable to that of **Ce$_{38}$-BA**.

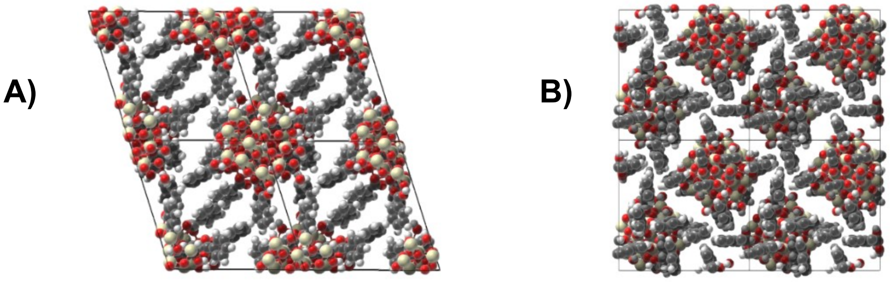

Figure 2.9 Relaxed structures of A) **Ce$_{38}$-BA** and B) **Ce$_{38}$-NA**. 2 × 2 × 2 simulation unit cells are shown. Color key: Ce (yellow), O (red), C (gray), H (white).

2.9.5 Pore Size Distributions

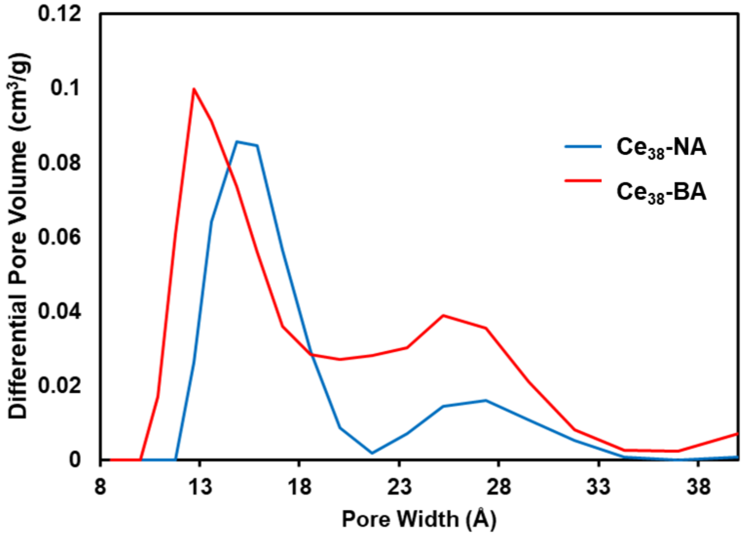

Figure 2.10: Pore size distributions for **Ce38-BA** and **Ce38-NA**.

2.9.6 Variable Temperature and Pressure Powder X-Ray Diffraction Patterns

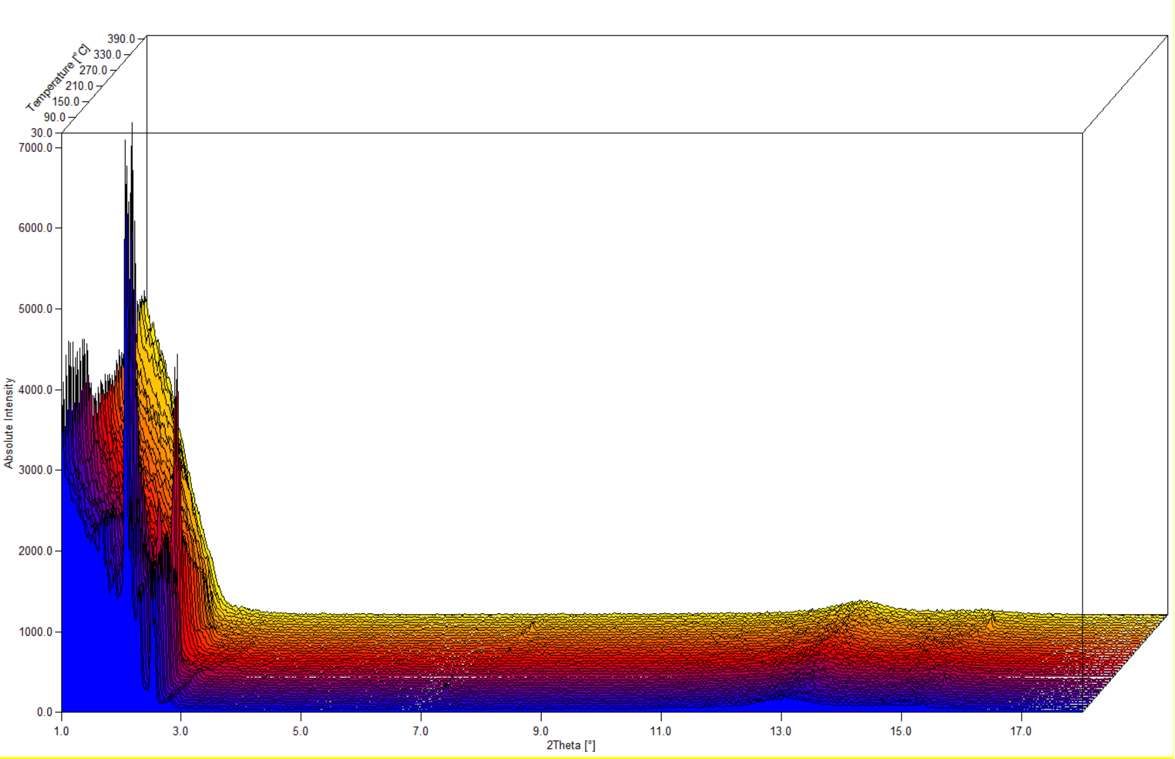

Figure 2.11: Variable temperature PXRD patterns for **Ce$_{38}$-BA** collected with Mo wavelength (0.7107 Å).

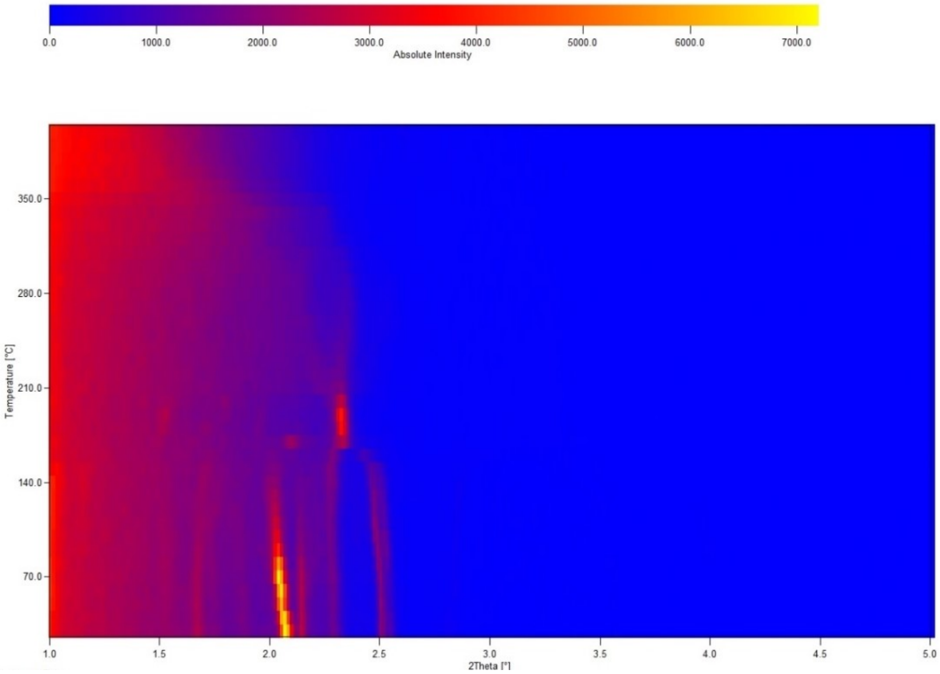

Figure 2.12: Variable temperature PXRD patterns for **Ce$_{38}$-BA** collected with Mo wavelength (0.7107 Å) with top down view from 0 to 5 2θ (°) to emphasize phase transition around 150 °C.

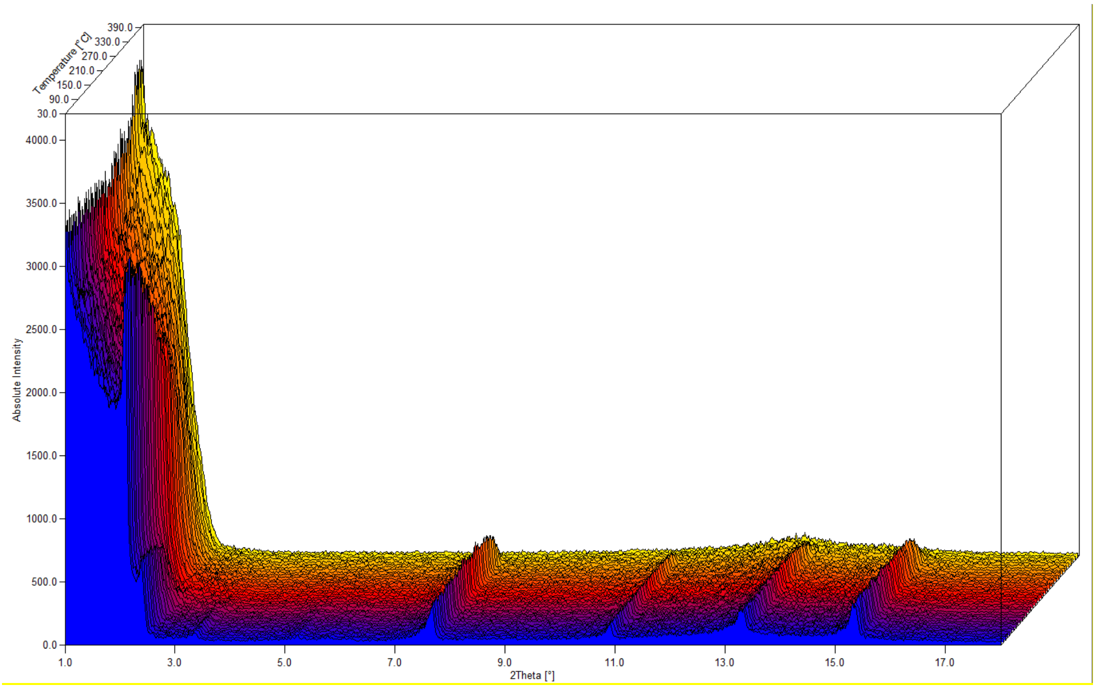

Figure 2.13: Variable temperature PXRD patterns for **Ce$_{38}$-NA** collected with Mo wavelength (0.7107 Å).

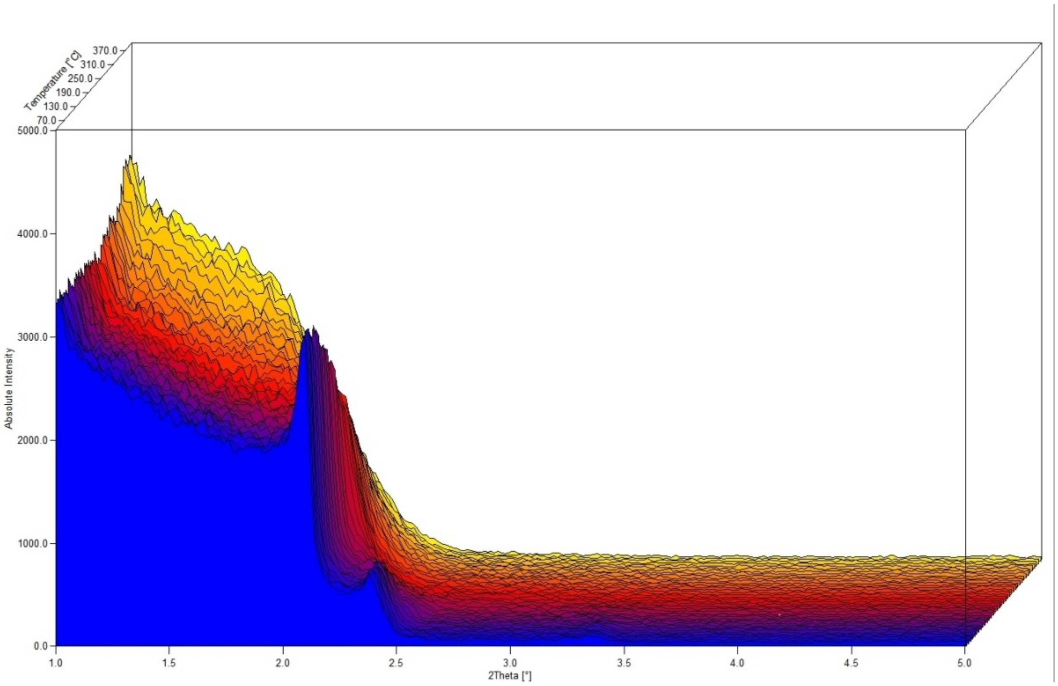

Figure 2.14: Variable temperature PXRD patterns for **Ce$_{38}$-NA** collected with Mo wavelength (0.7107 Å) from 0 to 5 2θ (°) to emphasize phase crystallinity until ~150 °C.

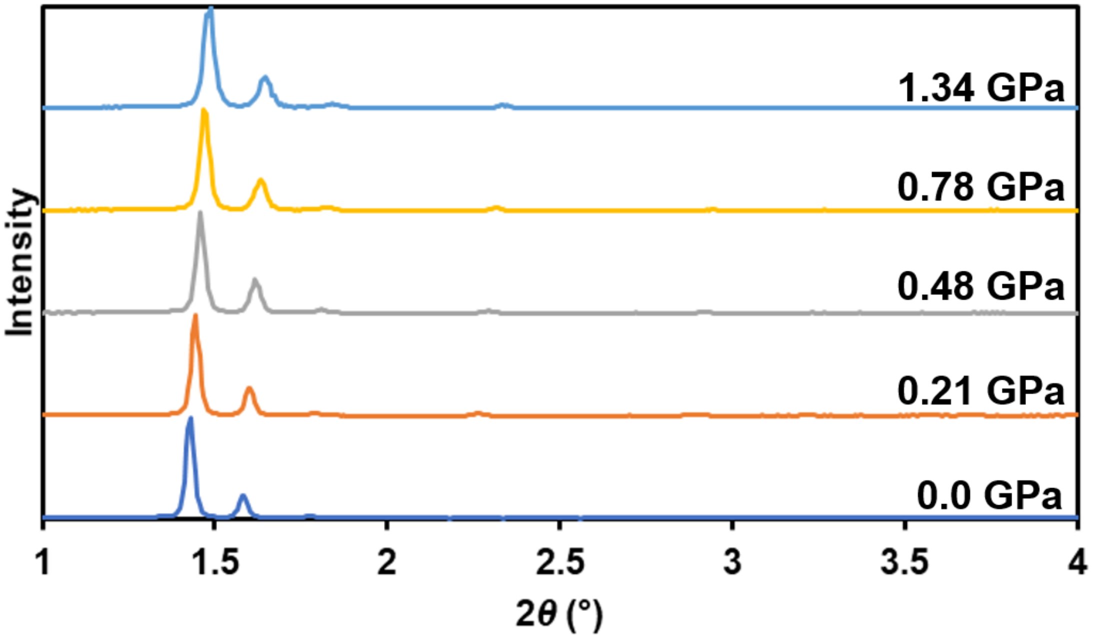

Figure 2.15: Representative powder diffraction data collected for **Ce38-BA** as pressure increases.

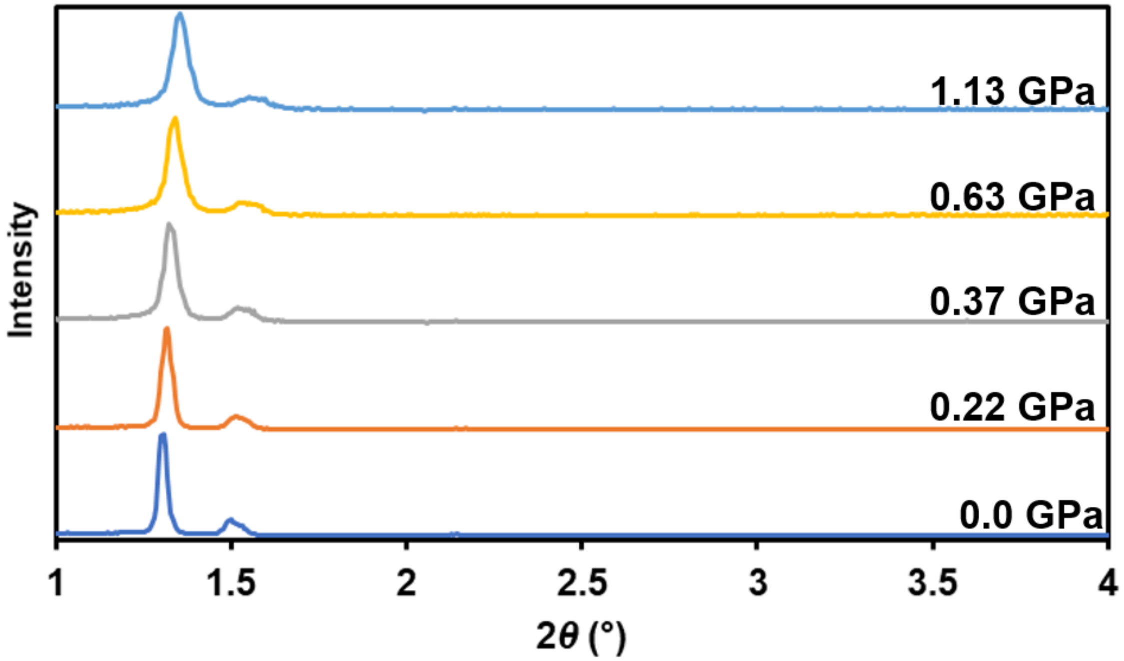

Figure 2.16: Representative powder diffraction data collected for **Ce38-NA** as pressure increases.

Table 2.2: Parameters for LeBail fits to Variable Pressure Powder Diffraction Data for **Ce_{38}-BA**

P (GPa)	V CaF_2 (Å^3)	*a* = *b* Ce_{38}-BA (Å)	*c* Ce_{38}-BA (Å)	V Ce_{38}-BA (Å^3)	R_{wp} %
0.00	163.47679	23.2083	29.26735	15764.14071	10.645
0.007	163.45485	23.20106	29.26085	15750.80093	13.779
0.03	163.40909	23.16435	29.22401	15681.23255	10.094
0.07	163.3237	23.10067	29.14408	15552.46999	9.849
0.10	163.27781	23.05769	29.1012	15471.85375	9.765
0.12	163.24597	23.03965	29.08004	15436.42907	10.063
0.13	163.2232	23.02302	29.06094	15404.02914	10.258
0.14	163.1963	23.01559	29.01668	15371.17525	10.641

Table 2.3: Parameters for LeBail fits to Variable Pressure Powder Diffraction Data for **Ce_{38}-NA**

P (GPa)	V CaF_2 (Å^3)	*a* = *b* Ce_{38}-NA (Å)	*c* Ce_{38}-NA (Å)	V Ce_{38}-NA (Å^3)	R_{wp} %
0.00	162.9967	24.05901	34.79391	20139.965	8.497
0.020	162.9582	24.04633	34.7642	20101.561	8.551
0.03	162.9193	23.9983	34.76473	20021.658	8.52
0.03	162.9065	23.9821	34.74325	19982.271	8.834
0.05	162.8862	23.9766	34.699	19947.676	9.017
0.09	162.8078	23.96014	34.67179	19860.377	9.271
0.11	162.7831	23.91759	34.64001	19815.848	10.018
0.14	162.7165	23.87469	34.56784	19703.688	11.467

2.9.7 X-Ray Photoelectron Spectroscopy Data

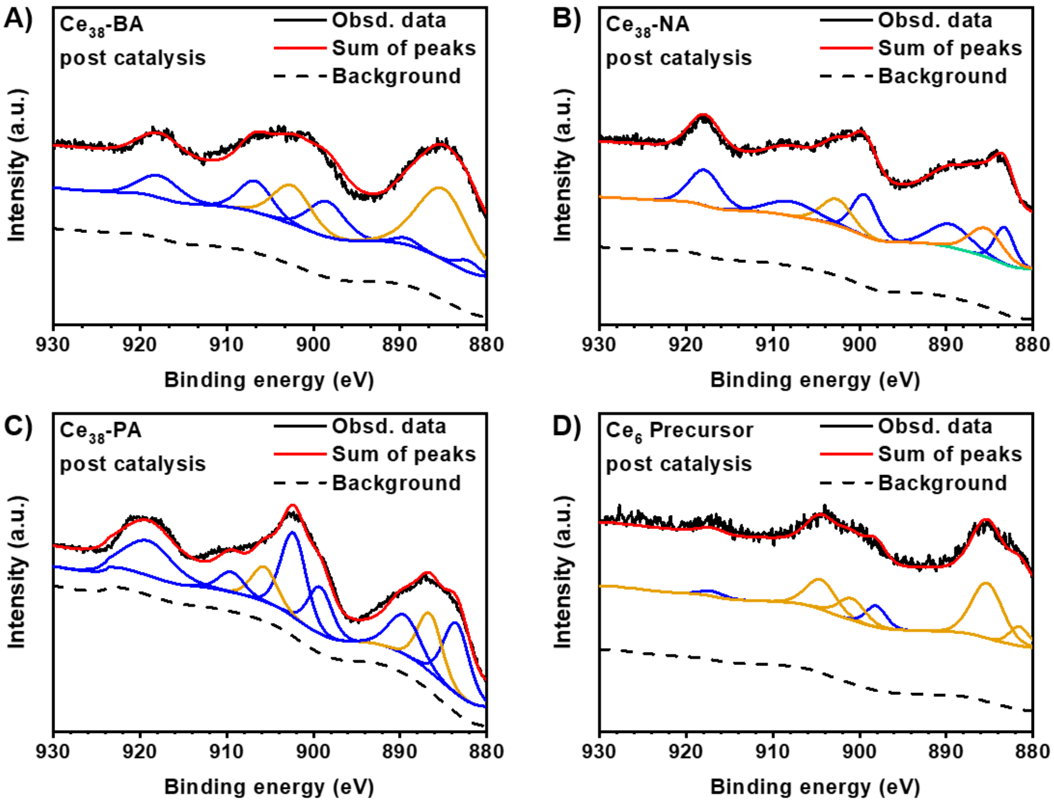

Figure 2.17: Observed Ce 3d XPS (solid black line) and sum of fitted data (red line) for A) **Ce_{38}-BA**, B) **Ce_{38}-NA**, C) **Ce_{38}-PA**, and D) **Ce_6 precursor** after 1 hour of catalysis. The observed data were fitted by Gaussian/Lorentzian functions with deconvoluted peaks in blue corresponding to Ce^{4+} and orange deconvoluted peaks corresponding to Ce^{3+}.

2.9.8 Electron Paramagnetic Resonance Spectra

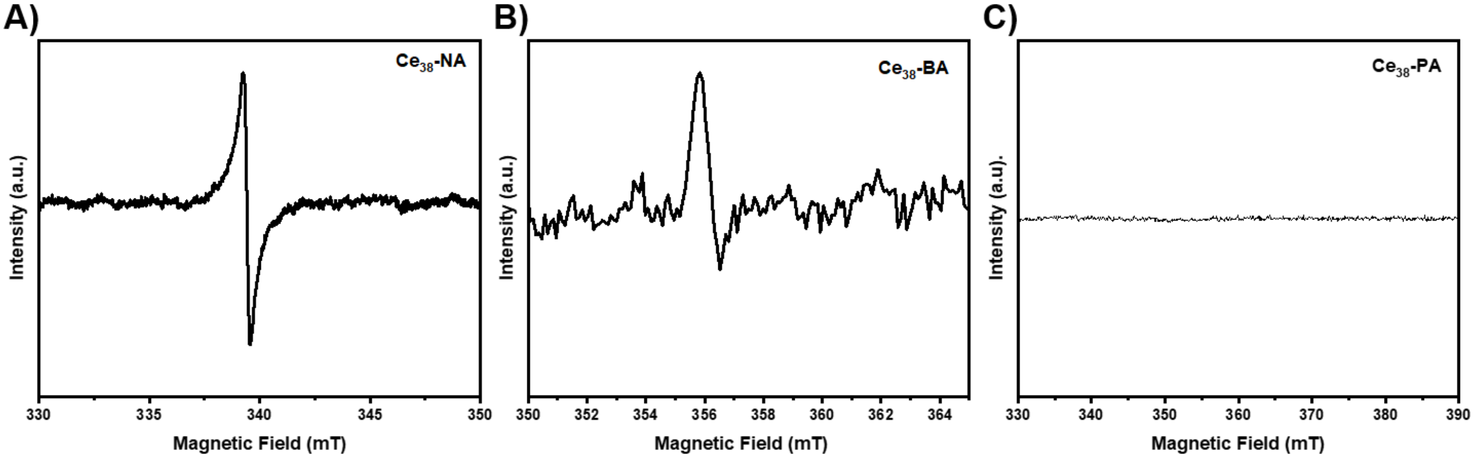

Figure 2.18: Continuous Wave EPR Spectra collected at 10 K of A) **Ce_{38}-NA**, B) **Ce_{38}-BA**, and C) **Ce_{38}-PA**.

2.9.9 Raman Spectroscopy Details

Table 2.4: Raman details of Ce oxo clusters

	Size (nm)	**F_{2g} Peak Position (cm^{-1})**	**D/F_{2g} Peak Area Ratio**
CeO_2 Nanospheres	30.2	465.6	0.02
Ce_{38}-NA	3.2	459.7	0.25
Ce_{38}- BA	2.2	457.7	0.28
Ce_{38} -PA	3.1	458.7	0.08

(Grain) size is calculated by using the equation, Γ (cm^{-1})=10+124.7/d_g(nm), where Γ is the FWHM of the F_{2g} peak.[123]

2.9.10 Catalytic Data

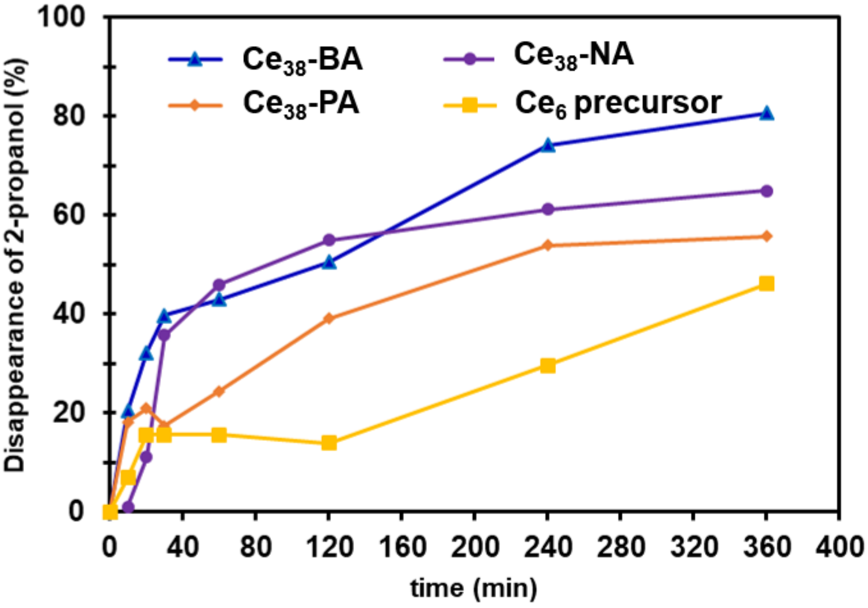

Figure 2.19: Reaction profile for photooxidation of 2-propanol catalyzed by cerium oxo clusters as monitored by ^1H NMR.

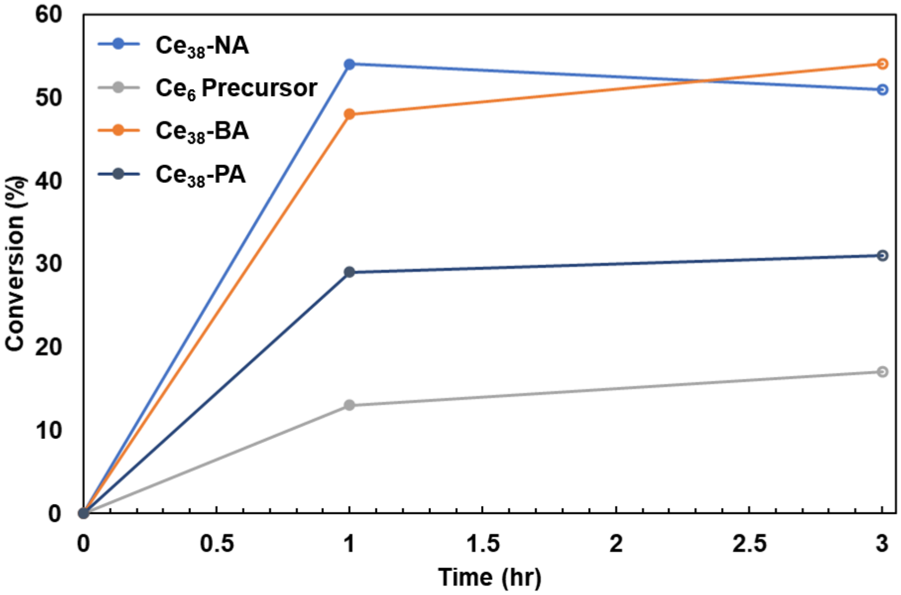

Figure 2.20: Conversion after 1 hour of reaction (closed circles), followed by filtration and subsequent re-purging the residual filtrate with O_2. Reaction progress after filtrate indicating by the open circles.

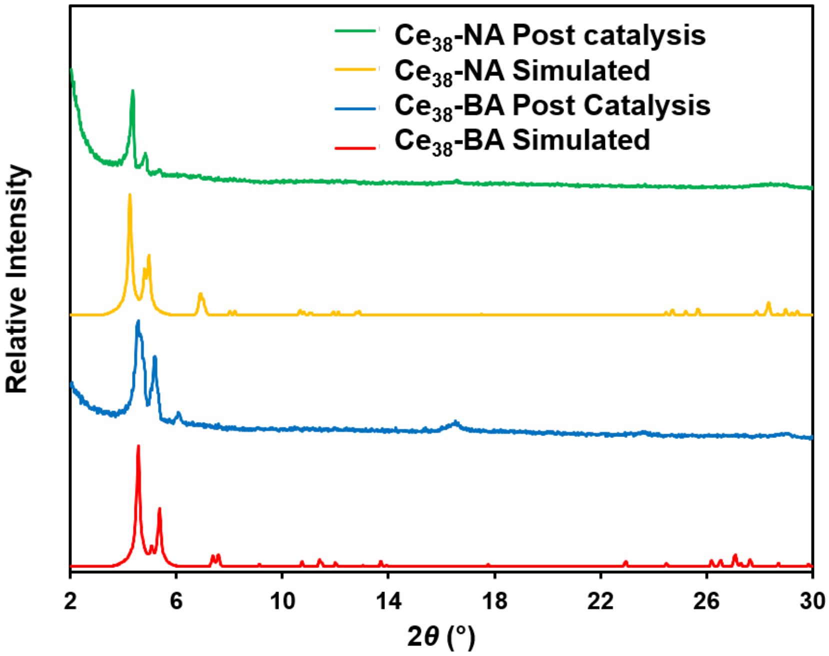

Figure 2.21: PXRD patterns of Ce_{38} samples after catalysis and their respective simulated patterns.

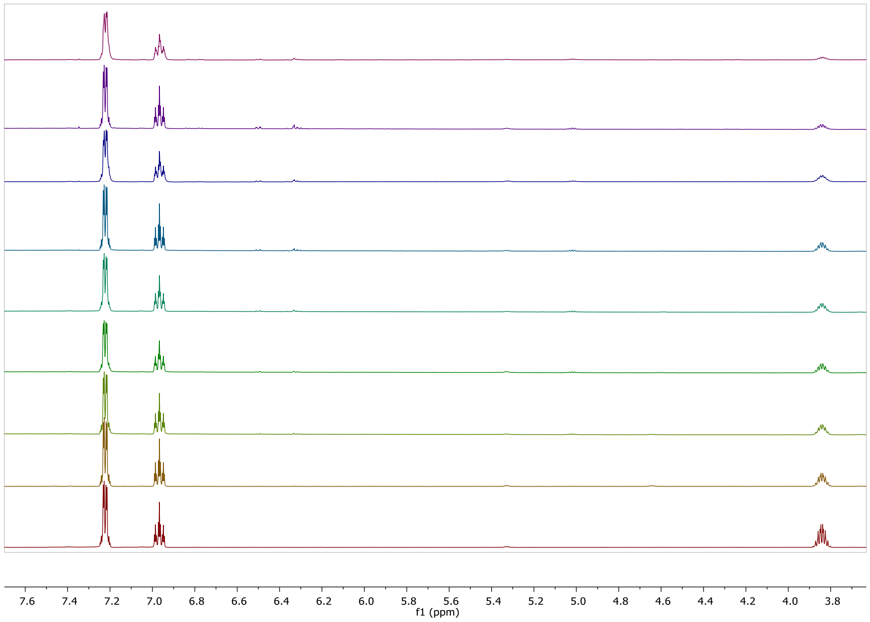

Figure 2.22: Stacked ^{1}H NMR of **Ce$_{38}$-BA** catalyzed photooxidation of 2-propanol with increasing time (0 min to 6 hr) from bottom to top spectra. 2-propanol seen at ~3.8 ppm while internal standard (1-bromo-3,5-difluorobenzene) ~6.9 – 7.3 ppm.

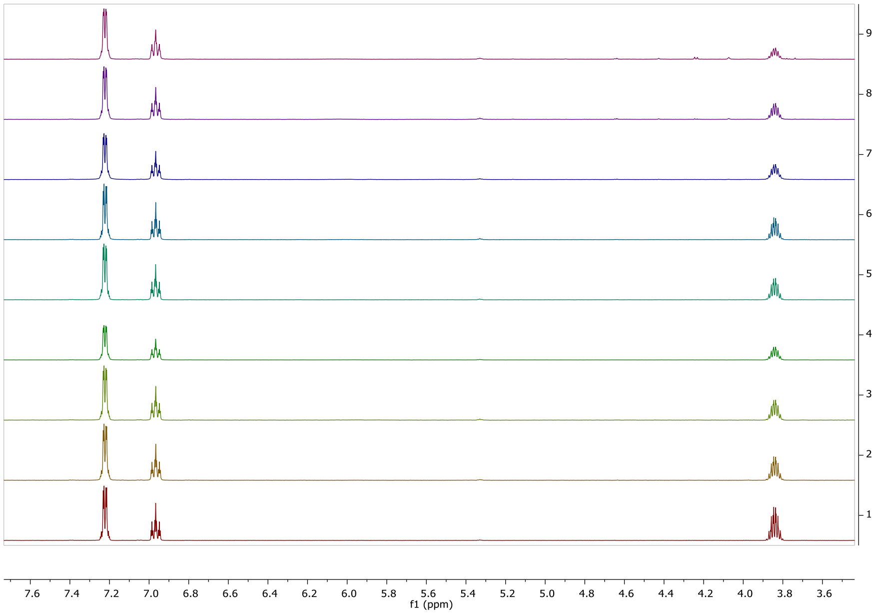

Figure 2.23: Stacked ^{1}H NMR of **Ce$_{38}$-NA** catalyzed photooxidation of 2-propanol with increasing time (0 min to 6 hr) from bottom to top spectra. 2-propanol seen at ~3.8 ppm while internal standard (1-bromo-3,5-difluorobenzene) ~6.9 – 7.3 ppm.

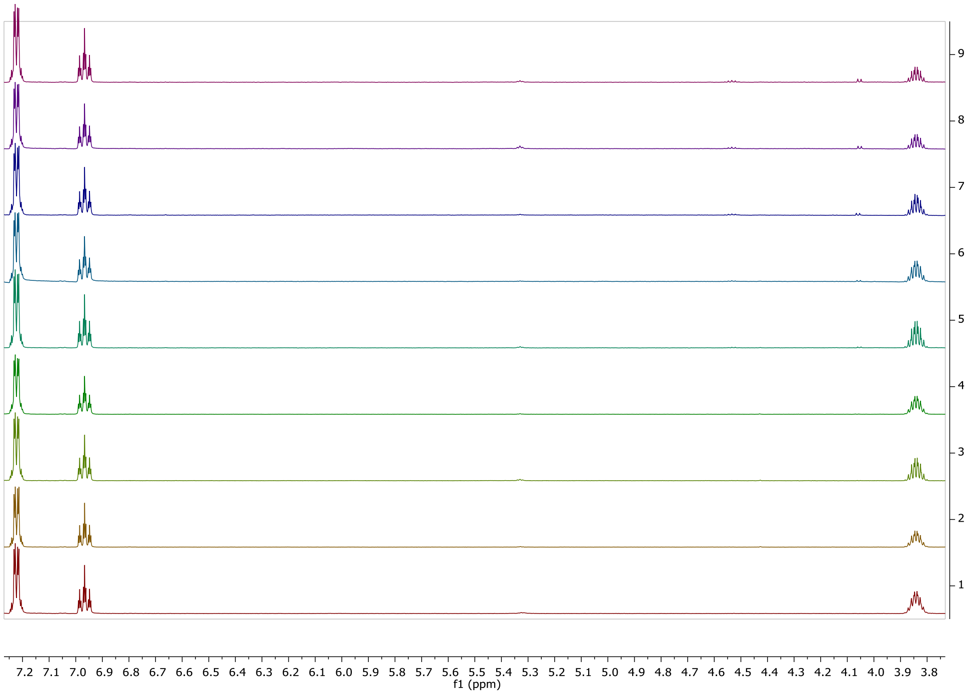

Figure 2.24: Stacked ^{1}H NMR of **Ce$_{38}$-PA** catalyzed photooxidation of 2-propanol with increasing time (0 min to 6 hr) from bottom to top spectra. 2-propanol seen at ~3.8 ppm while internal standard (1-bromo-3,5-difluorobenzene) ~6.9 – 7.3 ppm.

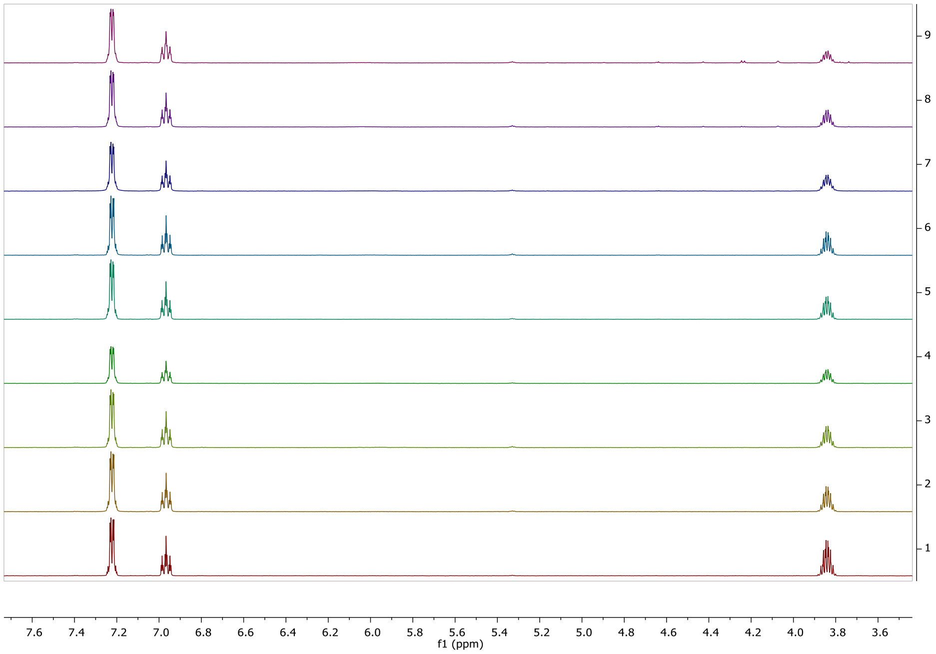

Figure 2.25: Stacked ^{1}H NMR of **Ce$_{6}$ precursor** catalyzed photooxidation of 2-propanol with increasing time (0 min to 6 hr) from bottom to top spectra. 2-propanol seen at ~3.8 ppm while internal standard (1-bromo-3,5-difluorobenzene) ~6.9 – 7.3 ppm.

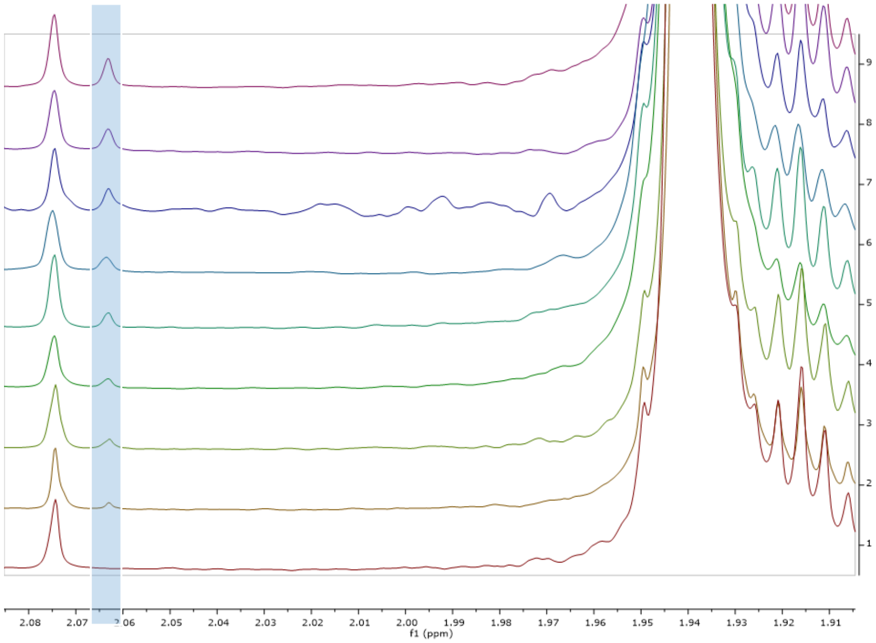

Figure 2.26: Stacked ^{1}H NMR of detected acetone (highlighted region) at δ 2.06 in the photooxidation of 2-propanol in CD_3CN.

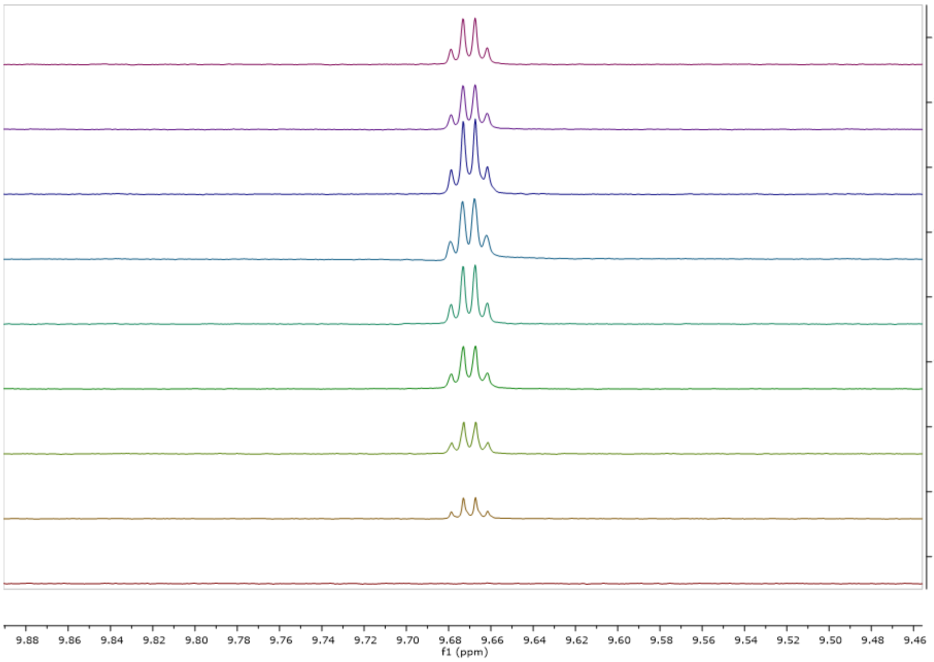

Figure 2.27: Stacked ^{1}H NMR of detected formaldehyde at δ 9.67 in the photooxidation of 2-propanol in CD_3CN.

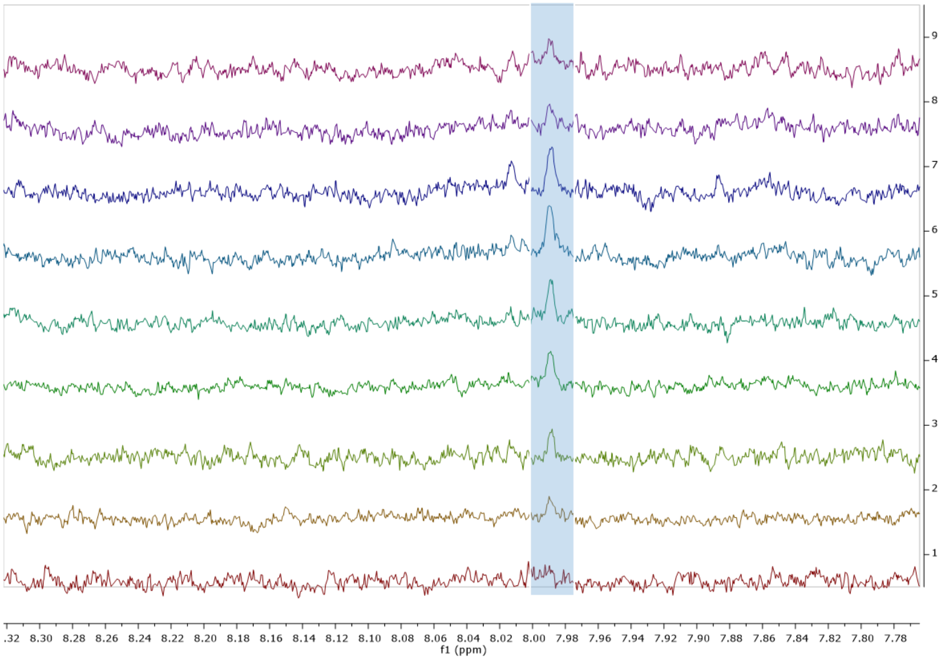

Figure 2.28: Stacked ^{1}H NMR of detected formic acid (highlighted region) at δ 7.99 in the photooxidation of 2-propanol in CD_3CN.

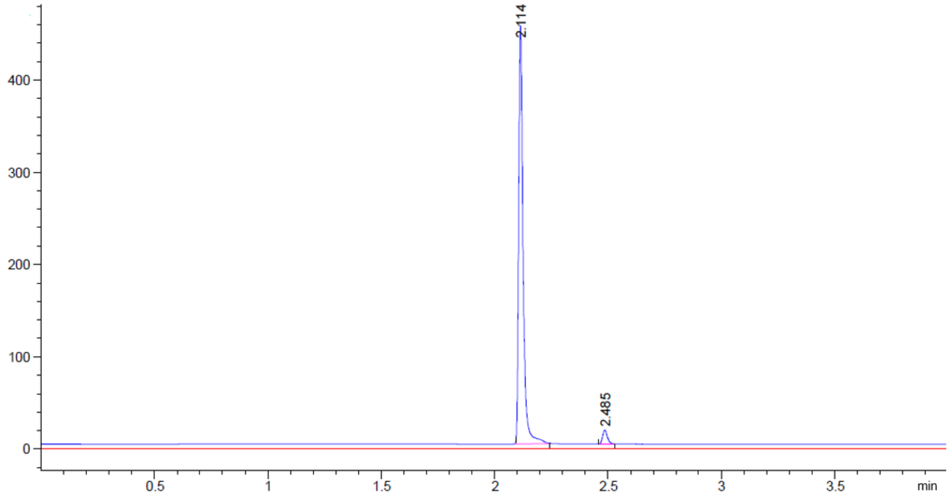

Figure 2.29: Example gas chromatogram of headspace observed above a **Ce_{38}-NA** catalyzed isopropanol oxidation. The peak at 2.114 min corresponds to CO while the peak at 2.485 min corresponds to CO_2.

Table 2.5: **Ce_{38}-BA** liquid product profile as quantified by ^1H NMR. Remaining product presumed to be gaseous product.

Time (min)	2-propanol disappearance (%)	Total Liquid Product Yield (%)	Acetone yield (%)	Formic acid yield (%)	Acetaldehyde yield (%)
0	-	-	-	-	-
10	20	13	4	2	7
20	32	15	3	6	6
30	40	15	3	7	5
60	43	14	3	6	5
120	51	14	7	6	4
240	74	17	6	7	4
360	81	16	6	7	3

Table 2.6: **Ce_{38}-NA** liquid product profile as quantified by ^1H NMR. Remaining product presumed to be gaseous product.

Time (min)	2-propanol disappearance (%)	Total Liquid Product Yield (%)	Acetone yield (%)	Formic acid yield (%)	Acetaldehyde yield (%)
0	-	-	-	-	-
10	>1	-	-	-	-
20	11	< 6	2	3	< 1
30	36	< 6	2	3	< 1
60	46	9	4	3	2
120	55	8	3	2	3
240	61	11	4	3	4
360	65	12	5	3	4

Table 2.7: **Ce_{38}-PA** liquid product profile as quantified by ^{1}H NMR. Remaining product presumed to be gaseous product.

Time (min)	2-propanol disappearance (%)	Total Liquid Product Yield (%)	Acetone yield (%)	Formic acid yield (%)	Acetaldehyde yield (%)
0	-	-	-	-	-
10	18	7	2	0	5
20	21	13	5	0	8
30	17	20	7	0	13
60	24	22	7	0	15
120	39	25	8	0	17
240	54	18	8	0	10
360	56	20	10	0	10

Table 2.8: **Ce_{6} Precursor** liquid product profile as quantified by ^{1}H NMR. Remaining product presumed to be gaseous product.

Time (min)	2-propanol disappearance (%)	Total Liquid Product Yield (%)	Acetone yield (%)	Formic acid yield (%)	Acetaldehyde yield (%)
0	0	-	-	-	-
10	7	7	0	0	0
20	16	13	0	0	0
30	16	20	0	0	0
60	16	22	3	0	0
120	14	25	7	0	0
240	30	18	7	0	<1
360	46	20	15	0	<1

Chapter 3: Interfacial Unit-Dependent Catalytic Activity for CO Oxidation over Cerium Oxysulfate Cluster Assemblies

Portions of this chapter appear in the following manuscript:

Wasson, M.C.;* Wang, X.;* Melix, P.; Alayoglu, S.; Wolek, A.T.Y.; Colliard, I.; Son, F.A.; Xie, H.; Weitz, E.; Islamoglu, T.; Nyman, M.; Snurr, R.Q.; Notestein, J.M.; Farha, O.K. *Under Revision.*

3.1 Chapter Summary

Atomically precise cerium oxo clusters offer a platform to investigate structure-property relationships that are much more complex in the ill-defined bulk material cerium dioxide. We investigated the activity of the MCe_{70} torus family (M = Cd, Ce, Co, Cu, Fe, Ni, and Zn), a family of discrete oxysulfate-based Ce_{70} rings linked by monomeric cation units, for CO oxidation. $CuCe_{70}$ emerged as the best performing MCe_{70} catalyst among those tested, prompting our exploration of the role of the interfacial unit on catalytic activity. Temperature programmed reduction (TPR) studies of the catalysts indicated a lower temperature reduction in $CuCe_{70}$ as compared to $CeCe_{70}$. *In situ* diffuse reflectance infrared Fourier transform spectroscopy (DRIFTS) indicated that $CuCe_{70}$ exhibited a faster formation of Ce^{3+} and contained CO bridging sites absent in $CeCe_{70}$. Isothermal CO adsorption measurements demonstrated a greater uptake of CO by $CuCe_{70}$ as compared to $CeCe_{70}$. The calculated energies for the formation of a single oxygen defect in the structure significantly decreased with the presence of Cu at the linkage site as opposed to Ce. This study revealed that atomic level changes in the interfacial unit can change the reducibility, CO binding / uptake, and oxygen vacancy defect formation energetics in the MCe_{70} family to thus tune their catalytic activity.

3.2 Cerium Oxo-based Heterogeneous Catalysts

Bulk metal oxides are essential to a range of industries where their tunable surface and electronic structure facilitate their use as heterogeneous catalysts, in biomedical devices, and as semiconductors.[1–3] In recent years, efforts have shifted to capitalizing on surface atoms and how the change in chemical environment, i.e. fewer nearest neighboring atoms, can increase their catalytic properties as compared to their bulk counterparts.[136] Such strategies have included isolating a smaller nanooxide size regime to increase the amount of surface atoms or a specific morphology to access desired surface facets with higher surface energies to increase their catalytic activity.[137,138] However, great care is needed to minimize the polydispersity in these systems to confidently assign structure-property relationships given the surface heterogeneity.[18] Other emerging strategies to access nano-sized bulk oxides tailored in size or shape include the growth of nano-sized oxides with templating mesoporous materials[139] or on substrates such as thin films.[140] Another strategy to access discrete nanooxide materials is their incorporation into structural building units in highly ordered hybrid materials, such as metal–organic frameworks (MOFs).[23] Shifting to a smaller size regime with discrete, crystallographically-defined clusters enables more confident assignments of structure activity relationships.[141] Thus, it is imperative to expand and subsequently interrogate the available library of metal oxo clusters.[28]

Of the well-studied metal oxides, metal-oxo clusters that resemble cerium dioxide present a fascinating platform for further research given the facile storage and release of oxygen within ceria to form reactive oxygen vacancy defects.[106] Enabled by the favorable redox couple of Ce^{4+} / Ce^{3+}, surface O atoms can readily be abstracted depending on reaction conditions and directly participate in reactions through a Mars-Van Krevelen mechanism.[97,98] Moreover, subsurface atoms can facilitate the transport of O vacancies through the lattice, rather than remaining innocent to chemistry occurring at the surface.[102] The reducibility of Ce^{4+} is greatly affected by and can be readily tuned through its local environment[142] and geometry[143]. Thus, ceria-based catalysts and catalyst supports have become indispensable within heterogeneous catalysis.[144] Inspired by their ubiquity, a library of Ce-oxo clusters have been reported in recent years, often focusing on the synthesis to control size and/or surface accessibility.[31,103,145–147] Most recently, the Christou group modified a solvent used to facilitate the growth of intermediate Ce species to access a Ce_{100}-baesd oxo cluster, the highest nuclearity Ce oxo cluster reported to date.[148]

Additionally, work from the Nyman group expanded the metal oxysulfate torous motif, first reported in U and Zr,[149,150] to Ce while providing insights to their asssembly.[151,152] In these crystallographically defined systems, every Ce atom is exposed to the surface in a donut-like structure (**Figure 3.1**) with a range of monomeric metal linkage moieties interconnecting the clusters to form 1-D channels. Recent work from the Farha and Nyman teams further expanded the series to include a Ce_{70} torus structure interconnected by Ce monomers and examined the photocatalytic and radical scavenging character of these clusters.[153] To date, most discrete Ce oxo species have been studied in photocatalytic settings, given that the monodentate alkyl or aromatic capping agents present in other reported Ce oxo clusters limit their thermal stability.[107,147] However, the limited reports of utilizing discrete Ce oxo clusters for thermal-based catalysis starkly contrasts the substantial volume of studies investigating bulk ceria as a catalyst and/or catalyst support in applications such as CO oxidation or CO_2 hydrogenation.[92,154] Thus, the Ce_{70} torus family, which instead features capping sulfates, is more amenable to interrogate as catalysts for more thermally demanding conditions. The unique surface architecture prompted us to further explore the efficacy of these clusters within gas-phase oxidation reactions.

In this study, we report the oxidation of CO over a range of MCe_{70} oxysulfate clusters differing in the linkage cation between the clusters (M= $Ce^{3+/4+}$, Cd^{2+}, Co^{2+}, Cu^{2+}, $Fe^{2+/3+}$, Ni^{2+}, Zn^{2+}). We demonstrate that the identity of this interfacial unit can alter the catalytic activity of the MCe_{70} cluster family. The higher catalytic activity of $CuCe_{70}$ was corroborated with enhanced reducibility as observed through TPR-MS and *in situ* DRIFTS studies. Furthermore, DRIFTS and CO isothermal physisorption measurements suggested stronger CO binding and enhanced CO uptake respectively by $CuCe_{70}$. Following the experimental observation of oxygen vacancy defects through Raman spectroscopy, density functional theory (DFT) calculations indicated that oxygen vacancy defect formation energetics differ among the bridging chain sites, with Cu interfacial sites exhibiting the lowest energy of formation, which further rationalizes its superior catalytic activity.

3.3 Experimental Methods and Material Characterization

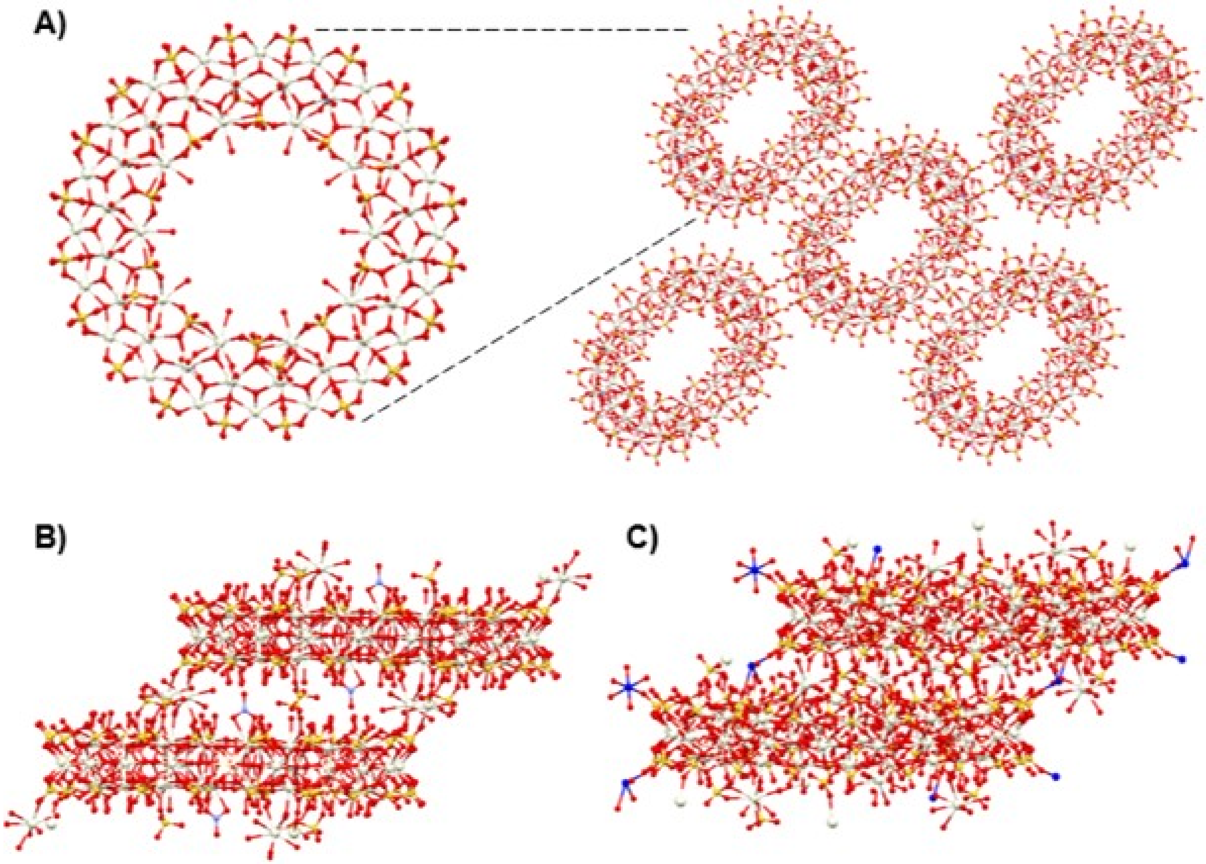

Figure 3.1 A) $CeCe_{70}$ assembly with enlarged repeated unit. B) Interfacial linkage sites between two connected $CeCe_{70}$ rings. C) Linkage sites between two connected $CuCe_{70}$ sites. Color scheme: Light yellow, Ce; red, O; golden yellow, S; N, light blue, Cu, royal blue. H atoms omitted for clarity.

The family of MCe_{70} torus clusters (M= $Ce^{3+/4+}$, Cd^{2+}, Co^{2+}, Cu^{2+}, $Fe^{2+/3+}$, Ni^{2+}, Zn^{2+}) were synthesized according to published procedures.[151,153] Notably, the MCe_{70} clusters feature the shared formula of repeating Ce_{70} toroids as previously reported through single crystal X-ray diffraction (SC-XRD): $[Ce_{70}(OH)_{36}(O)_{64}(SO_4)_{60}(H_2O)_{10}]^{4-}$ (see **Table 3.1** for detailed formula listings).[151] The toroid clusters are linked through sulfate and monomeric cation-based interfacial units (Figure 1). Powder X-ray diffraction (PXRD) measurements of the clusters resulted in patterns consistent with prior reports and exhibited long-range order (**Figure 3.6**). Inductively coupled plasma-optical emission spectrometry (ICP-OES) demonstrated the successful incorporation of the linkage metal with a Ce: M ratio ranging from (6.1: 1) to (7.6:1) in addition to a consistent Ce:S ratio throughout all clusters (**Table 3.2**). The higher ratio of M in the powder samples as compared to the Ce: M ratio derived from SC-XRD (74:3) has been previously observed and documented. Interestingly, the lower concentration of M used to form MCe_{70} clusters increased the rate of assembly and M incorporation.[151] The synthetic procedures used to create microcrystalline MCe_{70} samples in this study used a smaller concentration of M as compared to the procedures previously reported to generate MCe_{70} single crystals.[151–153] Nitrogen physisorption measurements were performed at 77 K to measure the apparent surface areas of all clusters (**Figure S8**), which are in agreement with previously reported surface areas of MCe_{70} clusters.[153]

3.4 Catalyst Reactivity Data

Following the characterization of the MCe_{70} cluster family, we explored the clusters' performance in CO oxidation in a packed bed reactor across a selected temperature regime (**Figures 3.9-3.15**). Additionally, we investigated CeO_2 (commercially obtained) to contextualize the conversions of the MCe_{70} materials (**Figure 3.16**). CeO_2 achieved a 2.5% conversion at 200 °C, which is in the same range of most of the studied MCe_{70} catalysts and ~2-fold lower than $CuCe_{70}$ before increasing to as high as 36% at 300 °C. All MCe_{70} catalysts were stable up to 200 °C, so the discussion is restricted to these temperatures. Conversion profiles at 200 °C indicated comparable conversions among all the clusters, except the $CuCe_{70}$ cluster, which exhibited a 3-fold higher conversion than $CeCe_{70}$ and nearly 2-fold higher than that of the other MCe_{70} clusters (**Figure 3.2**). Post-catalysis PXRD patterns demonstrated a retention in crystallinity without detectable formation of CeO_2 (**Figure 3.7**). Thus, we determined that the family of the clusters remained intact, and there is a difference in catalyst reactivity with ($CuCe_{70}$) > ($CdCe_{70}$, $CoCe_{70}$, FeCe$_{70}$, NiCe$_{70}$, ZnCe$_{70}$) > (CeCe$_{70}$). Moving forward, we elected to focus on CuCe$_{70}$ and CeCe$_{70}$ to interrogate the effect of linkage cation on the catalytic activity.

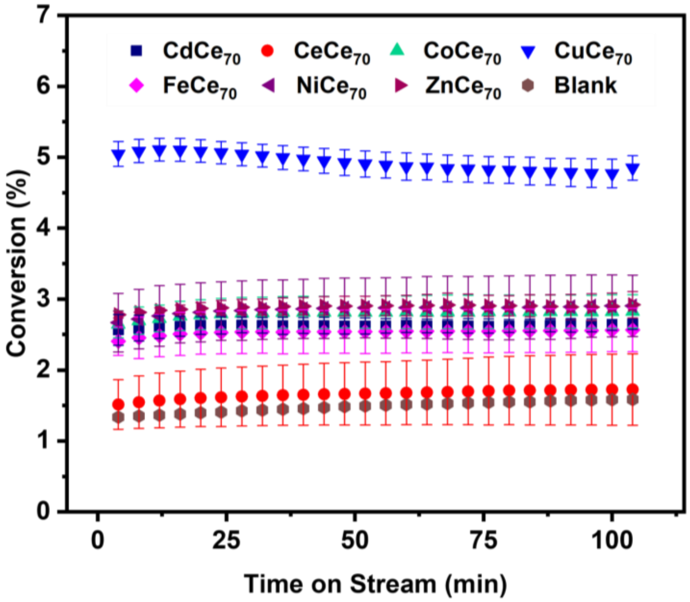

Figure 3.2 CO oxidation profiles at 200 °C of MCe$_{70}$ clusters averaged over 3 trials. See Chapter 3.9.2 for further experimental setup details.

Next, we investigated the conversion profiles of CeCe$_{70}$ and CuCe$_{70}$ at 200 °C for 16 hr on stream (**Figure 3.17**) to probe the catalyst stability. In these studies, CeCe$_{70}$ exhibited constant reactivity, suggesting it does not undergo an initial inductive effect that could have resulted in a lower conversion than CuCe$_{70}$. CuCe$_{70}$ suffered a loss of ~20% catalytic activity after 3 hr but remained constantly higher than CeCe$_{70}$. Moreover, through X-ray photoelectron spectroscopy (XPS), we determined that CeCe$_{70}$ and CuCe$_{70}$ both contained similar amounts of Ce^{3+} (45%) post-catalysis (**Figures 3.18-3.19**).

3.5 Temperature Programmed Reduction Data of Catalysts

We further explored the effect of Cu as a linkage element, hypothesizing that the Cu$^{2+/1+}$ redox couple affects the overall reducibility of our catalysts given the literature precedence that the Cu^{2+} to Cu^{1+} redox couple served as a potent redox promoter on CeO_2-based catalysts.[155] We investigated the temperature programmed reduction (TPR) of the $CeCe_{70}$ and $CuCe_{70}$ catalysts under 5% CO/He while connected to a mass spectrometer (MS). We monitored the formation of detected CO_2 and SO_2 to distinguish between the reduction of Ce^{4+} to Ce^{3+}, a process that must be coupled with the oxidation of CO to CO_2, as well as the reduction of surface sulfates on the clusters to SO_2. For $CeCe_{70}$, we observed TCD signals centered at 322 °C and 498 °C, whereas $CuCe_{70}$ exhibited TCD signals at lower temperatures of 288 °C and 480 °C (**Figure 3.3A/B**). We therefore determined that $CuCe_{70}$ is more reducible at lower temperatures. Within this temperature regime, TPR-MS traces demonstrated $[CO_2] >> [SO_2]$ for the two sets of lower temperature peaks for both catalysts (**Figures 3.3A/B**). However, the low conversion of CO to CO_2 in the TPR-MS precludes definite conclusions about the reducibility of specifically Ce^{4+} within this particular experiment; only 1.1 μmol and 1.8 μmol of CO_2 were generated in $CeCe_{70}$ and $CuCe_{70}$ respectively in the 290-350 °C range, corresponding to less than 1% of total moles of Ce reduced. The third TPR peak that appears ~650 °C in both catalysts features an equivalent production of CO_2 and SO_2, which complicates any conclusions that can be made about Ce^{4+} reduction at this temperature regime (**Figure 3.21**). Nonetheless, the TPR-MS data of the lower temperature TPD signals suggests the identity of the cation in the bridging unit affects reduction within MCe_{70} clusters. Furthermore, the more reducible nature of $CuCe_{70}$ at lower temperatures coincides with its higher activity in the CO oxidation experiments as compared to $CeCe_{70}$. We were motivated to further investigate the evolution of Ce^{3+} within $CeCe_{70}$ and $CuCe_{70}$ to elucidate the effect of the linking cation on the reduction of Ce^{4+}.

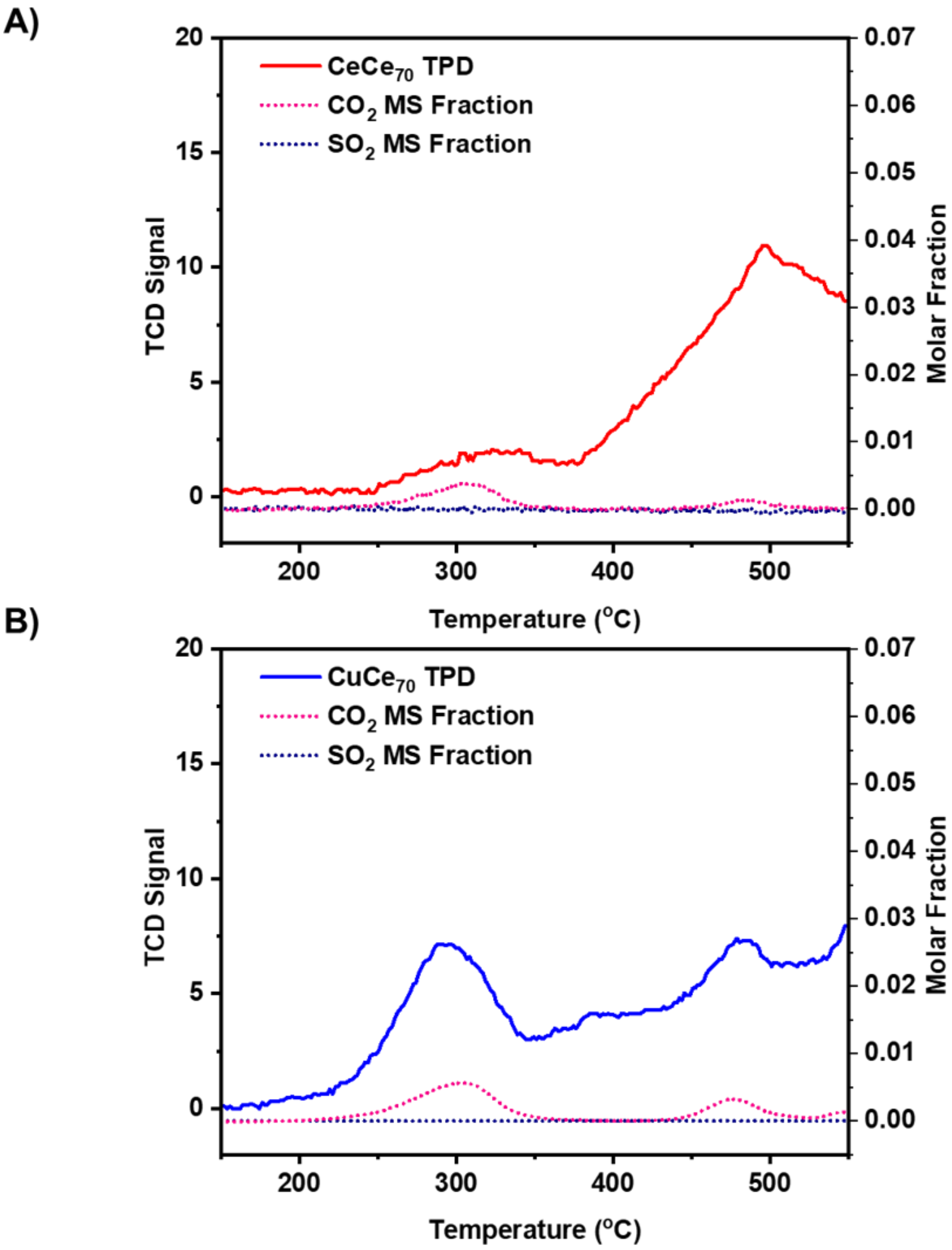

Figure 3.3 TPR-MS profiles of A) CeCe70 and B) CuCe70 under CO within 150 – 550 °C range. Remaining molar fraction corresponds to He, the carrier gas for the experiments.

3.6 *In situ* Diffuse Reflectance Infrared Fourier Transform Spectroscopy Data and Data Deconvolutions

An available tool to study Ce^{3+} formation in CeO_2-based catalysts is monitoring the spin-orbit transition peak of Ce^{3+} appearing ~2150 cm^{-1},[156,157] as demonstrated by Wu *et al.* [158] Thus, we conducted *in situ* DRIFTS measurements of recirculated ^{13}CO in the presence of an $^{18}O_2$ rich atmosphere flowed over $CeCe_{70}$ and $CuCe_{70}$. See Chapter 9.9.2 for more experimental details. Labeled ^{13}CO was used to further separate the spectrum of the reagent gas from the 2150 cm^{-1} region of interest.[159] We intentionally collected spectra with a resolution lower than that of the rotational coupling constants of CO (2 cm^{-1}) to remove the vibrational-rotational peaks of gas phase CO to enable more facile data fitting.[160] As shown in **Figure 3.4B**, we detected a more noticeable shoulder around 2150 cm^{-1} in the DRIFTS of $CuCe_{70}$, suggesting a greater evolution of

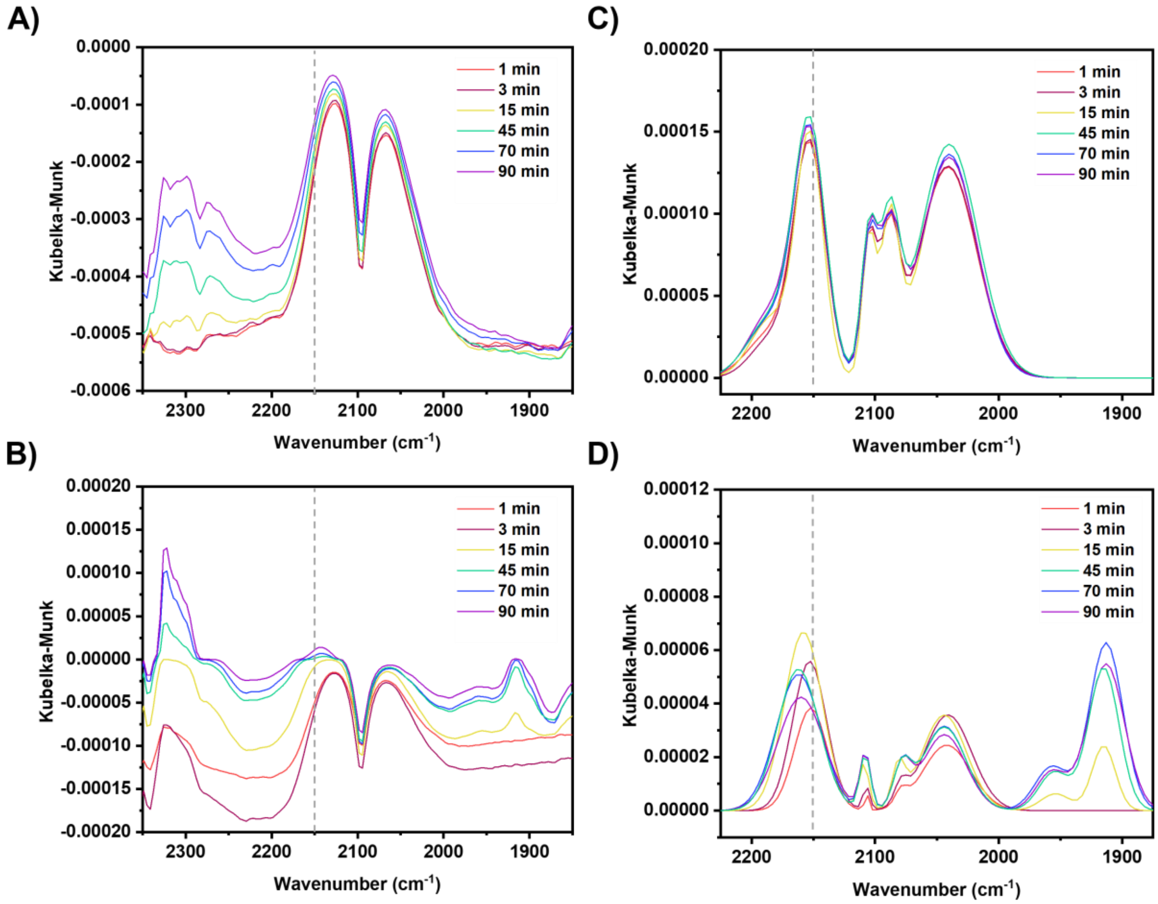

Figure 3.4 ^{13}CO DRIFTS data of a) $CeCe_{70}$ and b) $CuCe_{70}$ in selected region collected at 200 °C. Time in legend corresponds to duration of DRIFTS cell exposure to ^{13}CO / $^{18}O_2$. Residual DRIFTS data shown in c) of $CeCe_{70}$ and d) of $CuCe_{70}$ Grey dotted line added to aid visualization of 2150 cm^{-1}.

Ce^{3+} in $CuCe_{70}$ as compared to $CeCe_{70}$ (**Figure 3.4A**). Both catalysts demonstrated the formation of CO_2 with peaks appearing between 2250-2320 cm^{-1}. Interestingly, a strong peak at around 1915 cm^{-1} and a broader peak around 1955 cm^{-1} appeared during the DRIFTS experiment in $CuCe_{70}$ and not in $CeCe_{70}$.

To identify the contributions of the Ce^{3+} peak at 2150 cm^{-1} and explore the unexpected features between 1915 - 1960 cm^{-1}, we removed the gas phase ^{13}CO signal and deconvoluted the resulting residual spectra between 1875 cm^{-1} and 2225 cm^{-1}. Details of background treatment and the deconvolution procedure are located in Chapter 3.9.9. The residual peaks of $CeCe_{70}$ and $CuCe_{70}$ are plotted in **Figures 3.4C/D**. Peaks assigned to adsorbed CO were observed at 2040 cm^{-1}, 2078-2088 cm^{-1}, and 2105 cm^{-1}. In the $CuCe_{70}$ system, the second peak appeared slightly redshifted to 2078 cm^{-1}, indicating a weaker C–O bond and suggesting a stronger CO interaction as compared to the peak centered around 2088 cm^{-1} in $CeCe_{70}$. Importantly, with the data deconvolution, we determined the amplitude of the Ce^{3+} peak at 2150 cm^{-1} (**Tables 3.4-3.5**). In order to follow the rate of formation of Ce^{3+} in each catalyst, we normalized the 2150 cm^{-1} peak to the adsorbed CO peak at 2040 cm^{-1} (**Figure 3.36).** With these data, we concluded that there is a faster rate of Ce^{3+} formation and likely neighboring oxygen vacancy formation in $CuCe_{70}$ despite the ~5% fitting error associated with fits and surface site fluctuations too fast to appear on this timescale. This more facile Ce^{3+} formation aligns with the higher catalytic activity of $CuCe_{70}$ in CO oxidation.

Additionally, from the deconvolution of the $CuCe_{70}$ spectra, we observed a clear increase in the intensity of the lower frequency peaks (1915 cm^{-1} and 1955 cm^{-1}) while the 2040 cm^{-1} and the 2150 cm^{-1} peaks proportionally decreased. We reasoned that the Cu must be contributing to this interaction given the absence of these low frequency peaks in $CeCe_{70}$. We determined that the lower frequency peaks are unlikely to result from CO linearly bonding solely to Cu species, as prior reports indicate shifts >2055 cm^{-1} for Cu^{x+}- ^{13}CO species (>2100 cm^{-1} correlates to Cu^{x+}-^{12}CO species).[161] Since this region is where bridging CO stretches are expected,[162] the peaks assigned at 1915 cm^{-1} and 1955 cm^{-1} can likely be attributed to 1) bridging CO forming a Cu-CO-Ce dimer and/or 2) bridging CO forming a Ce-CO-Ce dimer that is facilitated by nearby Cu. The ability to form bridging CO in $CuCe_{70}$ as opposed to $CeCe_{70}$ implied a higher CO uptake in $CuCe_{70}$ given this bridging motif is more energetically challenging to access at lower CO concentrations, as previously reported through Monte Carlo simulations.[163] To further explore this hypothesis, we conducted CO isothermal adsorption measurements at 87 K, and we observed an almost 2-fold increase in CO uptake by $CuCe_{70}$ as compared to $CeCe_{70}$, consistent with its higher N_2 uptake (**Figure 3.37**). The higher CO uptake, which likely enables the unique bridging CO stretches observed in the $CuCe_{70}$ DRIFTS spectra, is consistent with the observed superior reactivity of $CuCe_{70}$.

3.7 Oxygen Vacancy Defect Formation

After detecting the evolution of Ce^{3+} in our DRIFTS data, we further explored the formation of neighboring O vacancies, species known to directly participate in oxidative or reduction processes,[98,106] using Raman spectroscopy. Measurements under ambient conditions indicated vacancies are present in the pristine $CeCe_{70}$ and $CuCe_{70}$ clusters, in agreement with prior studies by Wang *et al.* (**Figure 3.38**).[153] Both catalysts demonstrated a signal around 400 cm^{-1} that is attributed to surface Ce-O vibrations with a larger intensity than the peak around 465 cm^{-1} associated with bulk Ce-O vibrations.[164] Herman and co-workers previously demonstrated that a shoulder in Raman spectra of ceria nanoparticles as small as 6 nm at ~400 cm^{-1} is due to combined effects of strain and photon confinement.[165] However, more intense surface than bulk features is highly unusual, even among CeO_2 nanoparticles, further highlighting their cluster-like nature as opposed to a nanostructured solid-state character. The intensities found between 500-700 cm^{-1} indicate a rich defect character for both clusters.[166] Given that both clusters are able to accommodate oxygen defects, we conjectured that the ability to form the defects in the Ce_{70} toroid system could be affected by the linkage element present.

To further investigate the formation of oxygen vacancy defects within $CeCe_{70}$ and $CuCe_{70}$, we calculated and compared the defect formation energy in these systems using density functional theory. Based on previously published structural data of Colliard *et al.* and Wang *et al.*, we first manually created an idealized cluster model of a Ce_{70} toroid with D_{10h} symmetry.[151–153] Due to the missing/disordered hydrogen atoms in the experimental structure solutions, we rigorously tested all reasonable hydrogen placements adhering to the D_{10h} symmetry. See Chapter 3.9.12 for a detailed discussion of possible hydrogen placements. The resulting 22 hydrogen patterns were optimized at the PBE level of theory and the resulting relative energies were compared. We found two hydrogen placements within a range of 9 kJ/mol of each other, while all other placements are found to be more than 450 kJ/mol higher in energy. We therefore chose the hydrogen placement with the lowest energy for our further investigations. The second lowest energy configuration can also be expected to occur, in line with -O/OH disorder observed in the bond valence sum calculations of Colliard *et al.*[151] A comparison of all hydrogen placements and their relative energies is given in Chapter 3.9.12.

Using the selected hydrogen placement scheme, we investigated the formation energy (ΔE_{defect}) for a defect consisting of a single missing neutral oxygen atom using the formula $\Delta E_{\text{defect}} = E(\text{toroid w. defect}) + E\left(\frac{1}{2}\text{O}_2\right) - E(\text{toroid})$. The selected hydrogen placement scheme allows for five distinct neutral oxygen vacancies. The resulting defective toroid was modeled in a triplet spin state, as the spin coupling between Ce atoms adjacent to the defect site is expected to be small and the accuracy of the calculation setups is expected to be lower than possible effects observable by employing the broken symmetry approach to describe a singlet antiferromagnetic (AFM) spin state.[167] To validate the triplet state, we also calculated the defect formation energies using a singlet spin state of the defective cluster. Absolute energies of the clusters as well as defect formation energies are significantly lower in the triplet state, confirming our spin state choice. See **Figure S.43** for more details. We note here that the defect formation energies calculated using the singlet state of the defective cluster and bulk ceria are surprisingly close to some values reported in the literature where no spin state is specified.[168–170] Our results underline the importance of investigating different spin states (and reporting what spin state was used) when modeling defective ceria using DFT. All calculated defect energies are given in Chapter 3.9.12.

We calculated the defect formation energies of the five possible defect sites in the Ce_{70} cluster (labeled A to D and F, see **Figure 3.5A/B**). The average value is 0.48 eV, with a minimum value of 0.38 eV and one outlier at 0.75 eV (**Figure 3.5C**). For comparison, we also calculated the bulk defect energies of bulk CeO_2 and a $Ce_6O_8(O_2CH)_8$ cluster (an often-used precursor in Ce-oxo cluster synthesis[103] or building block in metal–organic frameworks[171] and comparable to the Ce_6 octahedron unit in the toroid) using the same methodology to be 2.32 eV and 0.42 eV, respectively (computational details are given in Chapter 3.9.12). We therefore observe the same trend of decreasing ΔE_{defect} with decreasing particle size that is also observed experimentally.[172,173] Our ΔE_{defect} of bulk ceria is slightly lower than previously reported values calculated using DFT+U (e.g. 3.2 eV by Chen *et al.* using $U_f = 6.2$ eV).[174] Ziemba *et al.* calculated ΔE_{defect} for ceria surfaces using DFT+U ($U_f = 4.5$ eV) to be in the range of 1.1 to 2.1 eV.[175,176] This clearly shows the overall trend of a decreasing ΔE_{defect} for a decreasing dimensionality and extension of the ceria particles and agrees well with our results. Our Ce_{70} cluster model furthermore exhibits no significant deviation in ΔE_{defect} from the isolated $Ce_6O_8(O_2CH)_8$ cluster even though it is an extended system.

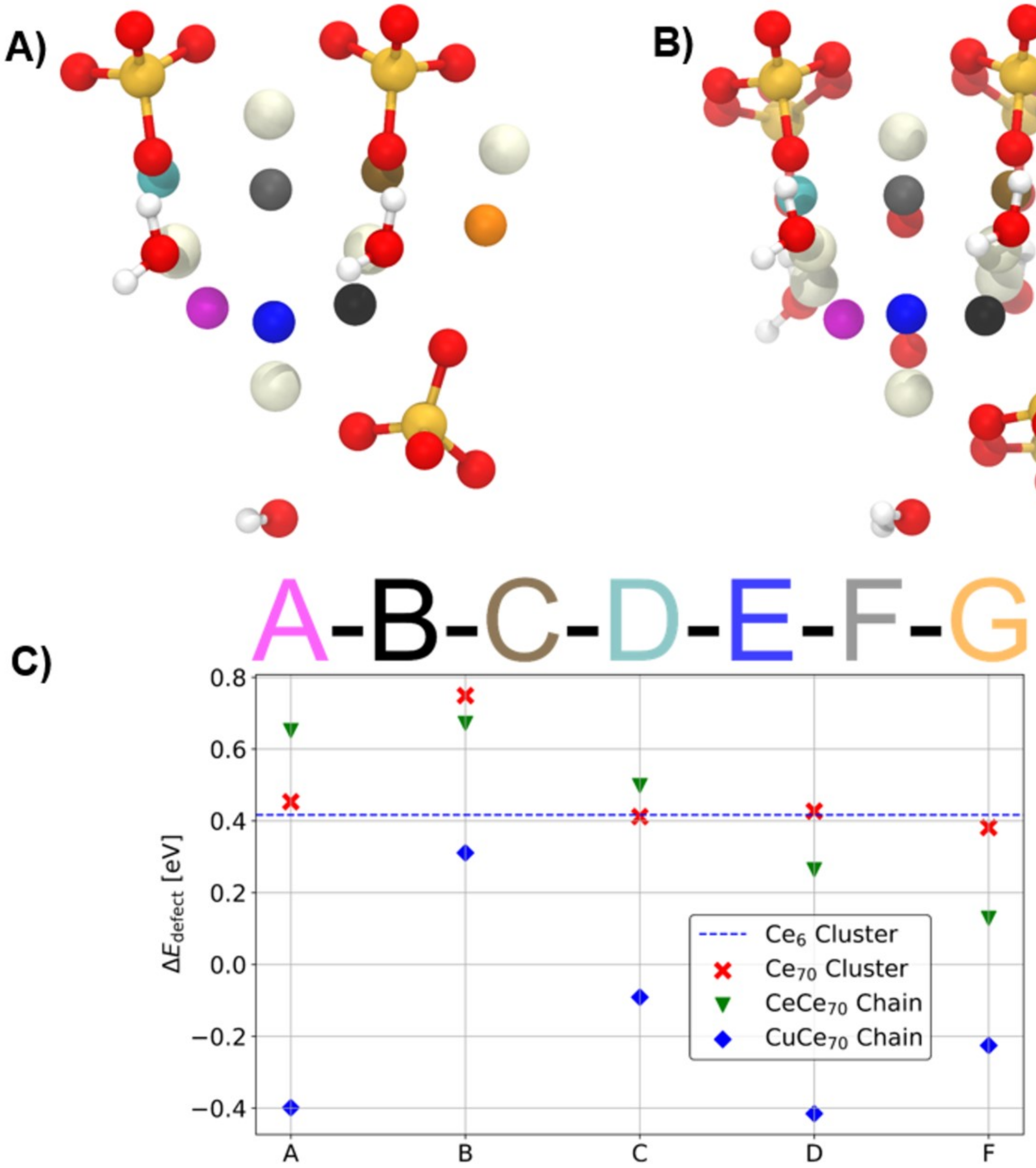

Figure 3.5 Visualization (A) and alternate perspective (B) of the $[Ce_7O_{10}(SO_4)_6(H_2O)_5]^{4-}$ fragment used for constructing initial configurations. Atoms colored by element: Ce light yellow, H white, S yellow, O red. The seven unique oxygens for hydrogen placement possibilities are color coded following the naming scheme below **Figures 3.5A/ B**. C) Calculated single oxygen vacancy formation energies (ΔE_{defect}) in the Ce_{70} cluster (red crosses), the $CeCe_{70}$ chain (green triangles) and the $CuCe_{70}$ chain (blue diamonds). The calculated defect formation energy in an isolated $Ce_6O_8(O_2CH)_8$ cluster is plotted as a blue dashed line.

To investigate the influence of the bridging Ce and Cu units in the experiment, we extended our model into a one-dimensional chain by adding the bridging CeO_4 or CuO_4 unit from the single crystal-derived structure solution to the DFT+U optimized cluster and applying one dimensional periodic boundary conditions (1D PBC). In the case of Ce, two oxygens were saturated with two H atoms each. For the Cu bridge, two oxygens were saturated with two H atoms each, and the remaining two oxygens were saturated with one H atom each. After relaxation of the unit cell length and subsequent geometry optimization, the same methodology as for the cluster model was applied to obtain ΔE_{defect} for the five possible defect sites (labeled A to D and F, see **Figure 3.5A/B**). The resulting defect formation energies of the Ce-bridged chain (**Figure 3.5C**) are in good agreement with the Ce_{70} cluster model values. The average ΔE_{defect} is 0.44 eV for the $CeCe_{70}$ chain, while the spread is significantly larger than in the Ce_{70} cluster model (minimum of 0.13 eV and maximum of 0.67 eV). **Figure 3.5C** compares all three model systems and the Ce_6 cluster. More details and a comparison of the effect of varying U_d values on the resulting defect formation energies in the Cu-bridged chains are given in Chapter 3.9.12.

From **Figure 3.5C** it is clearly visible that the substitution of Ce with Cu in the bridging unit results in a significant decrease of ΔE_{defect}. This conclusion agrees well with the experimental observation of increased activity for the Cu system but is still surprising. The chemical nature of the system would, in our opinion, suggest a highly localized nature of the defect formations. The Ce_{70} cluster model also suggests a highly localized electron redistribution upon formation of the oxygen vacancy, with the two free electrons localizing in the Ce f orbitals of two adjacent Ce atoms. In the case of the Ce-bridged periodic model, we also observe no significant charge transfer upon formation of the oxygen vacancy beyond the two adjacent Ce atoms. In the Cu-bridged chain, however, a significant charge transfer towards the Cu atom in the bridge is observed (decrease of

Mulliken charge on Cu from 0.47 to 0.18). The previous doublet spin state on the Cu transforms into a singlet state in our calculations, suggesting a reduction of the Cu. The defective system, however, still favors the anticipated quartet state, and the three unpaired electrons localize on the three Ce atoms adjacent to the oxygen vacancy. This charge transfer is unexpected, and we are at this stage unable to determine whether this is an artifact of the level of theory applied here or if this is indeed close to the true electronic ground state of the system. Further computational and experimental investigations are needed to better model the effects of the bridge on the nearby defect sites. Nonetheless, we are hopeful that our initial systematic study into modeling defect energetics within experimentally derived Ce-oxo clusters will motivate future investigations among other cluster shapes and compositions given the rarity of such inquiries.

While Cu/CeO_2 based catalysts have been well-studied for CO oxidation, they often are in the form of polydisperse oxides, hindering the understanding of the real active sites.[177] Our inquiry into highly crystalline, discrete clusters provides an alternative approach to derive meaningful insights relating structure and reactivity with increased confidence of the atomic level structure. Our results indicated that even a single ion-based linkage unit between neighboring clusters can serve as an active interface that readily tunes the reducibility and defect formation energetics of the Ce_{70} ring, and consequently the catalytic activity. We envision that our study can further motivate the creation of single / few ion[178] or ultrathin[179] interfaces within ceria-containing nanostructures.

3.8 Conclusions

In summary, we have established a correlation between higher catalytic activity for CO oxidation and the identity of the bridging cationic units linking the Ce_{70} toroids within the MCe_{70} cluster assemblies. We observed the highest CO conversion with $CuCe_{70}$, containing Cu in the bridging units. Through CO-TPR studies, we observed that $CuCe_{70}$ is more reducible than $CeCe_{70}$. *In situ* DRIFTS data suggested a faster formation of Ce^{3+} and identified unique CO bridging adsorption bands within $CuCe_{70}$, while CO isotherms confirmed higher CO uptake in $CuCe_{70}$ as compared to $CeCe_{70}$. Lastly, calculations determined that the presence of Cu in the bridging unit can substantially lower the energetic requirements to form a single oxygen vacancy in $CuCe_{70}$ compared to $CeCe_{70}$. Thus, we conclude that the incorporation of Cu in the bridging chain of the Ce_{70} torus family results in superior catalytic activity for CO oxidation due to its higher reducibility, enhanced CO binding and uptake, and more favorable oxygen vacancy defect formation. This investigation into gas-phase reactivity and cluster chemistry demonstrates that subtle atomic changes can affect the assemblies' properties. We are hopeful that this study will inspire further inquiry into this fascinating array of species as well as the expansion of further metal oxo cluster or bulk metal oxide architectures with unique interfaces.

3.9 Additional Information

3.9.1 Materials

Cerium ammonium nitrate ($Ce(NH_4)_2(NO_3)_6$), cerium sulfate ($Ce(SO_4)_2$), copper nitrate ($Cu(NO_3)_2$), cobalt nitrate ($Co(NO_3)_2$), iron nitrate ($Fe(NO_3)_3$), nickel nitrate ($Ni(NO_3)_2$), zinc nitrate ($Zn(NO_3)_2$), cadmium acetate ($Cd(CH_3COO)_2 \cdot 2H_2O$), sulfonic acid, tetrabutylammonium chloride ($[CH_3(CH_2)_3]_4NCl$), potassium bromide (KBr), quartz sand (trace-metal grade) were purchased from Sigma Aldrich. Deionized water was used as the water source for cluster synthesis. Ethanol (99%) was used as received from Fisher Scientific. For ICP measurements, all ICP standards (including Cd, Ce, Co, Cu, Fe, Ni, S, Zn) were purchased from Sigma Aldrich. Concentrated nitric acid was used to digest the sample and was purchased from VWR Scientific, LLC. (Chicago, IL). Ultrapure deionized water was obtained from a Millipore Milli-Q-Biocel A10 instrument used for ICP digestion. N_2, CO_2, and CO (99.999%) tanks were purchased and received from Airgas for sorption measurements. 5% CO / 20% O_2 / He, 20% O_2 / He, and N_2 were used as received from Airgas for reactivity measurements. ^{13}CO and $^{18}O_2$ were also purchased and received from Airgas for DRIFTS measurements. <25 nm CeO_2 was purchased from Sigma Aldrich and used as received.

3.9.2 Synthesis and Experimental Procedures

MCe_{70} Syntheses: $CeCe_{70}$, $CoCe_{70}$, $CuCe_{70}$, $FeCe_{70}$, $NiCe_{70}$ were synthesized according to published procedures for microcrystalline samples.[153] $CdCe_{70}$ was synthesized according to published procedure for CdCe70 – standard, yet was left to sit undisturbed for 5 days.[151] $ZnCe_{70}$ was synthesized according to modifications from published procedure and is detailed below.[151]

87 mg of $Zn(NO_3)_2$ and 110 mg of $Ce(SO_4)_2$ were placed in 2 mL of water with 20 µL of a 1.0 M aqueous solution of tetrabutylammonium chloride. The clusters were left for 36 hr undisturbed at room temperature.

After synthesis, all clusters underwent the following washing procedure:

The as-synthesized cluster solutions were centrifuged to decant the collected solid from the mother solution. The isolated cluster was then washed twice more with DI water, followed by centrifugation and then twice with ethanol. After the second ethanol wash and centrifugation, the isolated powder dried overnight on the benchtop.

The corresponding formulas for the MCe_{70} clusters are comprised in Table S1 below determined from SC-XRD unless otherwise indicated:

Table 2.1: Summary of MCe_{70} formulas.

Cluster	Formula	Reference
$CdCe_{70}$	$Cd_7Ce_{70}(OH)_{36}(O)_{64}(SO_4)_{65}(H_2O)_{72}$	Ref. 151
$CeCe_{70}$	$Ce_{50}^{IV}Ce_{22}^{III}(OH)_{64}(NO_3)_2(O)_{36}(SO_4)_{64}(H_2O)_{62}$	Ref. 153
$CoCe_{70}$	$Ce_{55}^{IV}Ce_{20}^{III}Co_2^{II}(OH)_{72}(O)_{42}(SO_4)_{64}(H_2O)_{63}$	Ref. 153
$CuCe_{70}$	$Ce_{53}^{IV}Ce_{21}^{III}Cu_3^{II}(OH)_{73}(O)_{36}(SO_4)_{68}(H_2O)_{108}$	Ref. 153
$FeCe_{70}$	$Ce_{52}^{IV}Ce_{22}^{III}Fe_x^{II}Fe_y^{III}(OH)_{72}(O)_{36}(SO_4)_{68}(H_2O)_{63}$	Ref. 153 (XPS / ICP-OES)
$NiCe_{70}$	$Ce_{55}^{IV}Ce_{20}^{III}Ni_2^{II}(OH)_{72}(O)_{36}(SO_4)_{66}(H_2O)_{108}$	Ref. 153
$ZnCe_{70}$	$[Zn(H_2O)_6]_{0.5}Ce_{4.5}Ce_{70}(OH)_{36}(O)_{64}(SO_4)_{67.5}(H_2O)_{64.75}$	Ref 151

Powder X-ray Diffraction (PXRD) Measurements: PXRD measurements were recorded at room temperature on a STOE-STADI P powder diffractometer equipped with an asymmetric curved Germanium monochromator (CuKα1 radiation, $\lambda = 1.54056$ Å) and one-dimensional silicon strip detector (MYTHEN2 1K from DECTRIS). The generator was set to be 40 kV and 40 mA. The activated powder was measured in transmission geometry in a rotating holder with the intensity data from 1 to 40 degrees. The scan step was set to be $2\theta = 4.005°$ while the scan time was 30 s.

Inductively-coupled plasma optical emission spectroscopy (ICP-OES): The analyses were completed on a Varian Vista-MDX model ICP-OES spectrometer (Varian, Walnut Creek, CA) with a CCD detector and Ar plasma that covers 175-785 nm range. To prepare the sample, 2-4 mg mg of each material was digested in 2 mL concentrated HNO_3 by heating in a 2-5 mL of Biotage (Uppsala, Sweden) SPX microwave reactor (software version 2.3, build 6250) at 150 °C for 10 minutes. After that, 400 µL of the solution was taken out and then diluted to a final volume of 10 mL with Millipore H_2O.

N_2 Physisorption Measurements: Prior to isotherm measurements, around 100 mg of sample was degassed on a Micrometritics ASAP 2420 for 18 hr at 30 °C. Then, N_2 sorption isotherms were measured using a Micrometritics ASAP 2420 surface area analyzer at 77 K.

Catalyst Reactivity Studies: In a typical experiment, ~40 mg of catalyst (based on ~0.3 mmol of Ce_{70}) was diluted with 1 g of quartz sand (trace-metal grade) and packed in a quartz tube plugged with quartz wool. The height of the bed was approximately 1 in. The sample was pretreated with at 200 °C for 2 hr with a flow rate of 20 sccm of 20% O_2/He. After pretreatment, the catalyst was immediately exposed to reactant gases of 20 sccm of 0.5% CO/ 20% O_2/ He and 20 sccm of 20% O_2/ He co-fed with 50 sccm of N_2. For a typical temperature ramp-up and ramp down profile, the reactor was first cooled to 150 °C at a rate of 10 °C / min and held for 2 hr, then ramped to 200 °C at a ramp rate of 10 °C / min and held for 2 hr, then ramped to 250 °C at a ramp rate of 10 °C / min and held for 2 hr, then ramped to 300 °C at a ramp rate of 10 °C / min and held for 4 hr, then cooled to 250 °C at a rate of 10 °C / min and held for 2 hr, then cooled to 200 °C at a rate of 10 °C / min and held for 2 hr, then cooled to 150 °C at a rate of 10 °C / min and held for 2 hr before a final cool down to 40 °C. To generate the 200 °C conversion data to gather triplicate data points (**Figure 3.2**), a typical experiment repeated the pretreatment protocol of heating the reactor tube at 200 °C for 2 hr with a flow rate of 20 sccm of 20% O_2/He. To remain consistent with the prior temperature ramp profile described above, the catalyst was first cooled to 150 °C and held for 2 hr under the reactant conditions described above before ramping to 200 °C at 10 °C/min and held for 2 hr to generate the additional trials used for catalyst comparisons. For the stability studies of $CeCe_{70}$ and $CuCe_{70}$, each catalyst was again pre-treated at 200 °C for 2 hr with a flow rate of 20 sccm of 20% O_2/He. Then, the catalyst was heated at 200 °C for over 16 hr under the reactant conditions mentioned above to remain consistent with the other studies.

XPS Measurements: X-ray photoelectron spectroscopy (XPS). The oxidation states of the metals in the cluster before and after the catalysis were tested at the KECKII/NUANCE facility at Northwestern University on a Thermo Scientific ESCALAB 250 Xi instrument equipped with an electron flood gun and a scanning ion gun. XPS data was analyzed using Thermo Scientific Avantage Data System software and all spectra were referenced to the C1s peak (284.8 eV) and Ce peaks were assigned according to literature references.[133] The $CuCe_{70}$ sample post catalysis was transferred from the BenchCAT reactor in an air-free manner to an Ar glovebox where it was then placed into an air-free chamber attachment that connects to the XPS instrument.

CO Temperature Programmed Reduction Experiments: Approximately 70 mg of material was placed in quartz reaction tube plugged between quartz wool and quartz sand. Temperature programmed experiments were performed on an Altamira AMI-200 instrument equipped with a thermal conductivity detector (TCD). In a typical experiment, catalysts were pretreated at 200 °C for 2 hr under 30 cc/min under 10% O_2/He and then cooled to 40 °C in 30 sccm He. Then, the system was heated to 900 °C at a ramp rate of 10 °C/min under 25 sccm of 5% CO/He with a carrier gas flow of 5 cc/min of He. Then, the system was cooled to 40 °C at a ramp rate of 30 °C/min under 30 cc/min of N_2.

In situ DRIFTS Measurements: *In situ* ^{13}CO DRIFTS measurements were carried out using a Nicolet iS50 FT-IR spectrometer equipped with a Harrick Scientific Praying Mantis DRIFTS accessory and a high temperature reaction chamber. Each sample (12 mg of each) was crushed using a mortar and pestle and placed in the sample cup of the DRIFT reaction chamber on top a bed of KBr. The temperature was raised to 200 °C under 10% O_2/ Ar (Airgas, UHP grade) flowing at 50 sccm. A background spectrum was collected after 200°C for 2 hr and used as a reference for the subsequent spectra. Then, a gaseous mixture of ^{13}CO (20.0 mbar) and $^{18}O_2$ (50 mbar) in He

(1000 mbar) was recirculated through a custom-built system equilibrated at 820 mbar. IR spectra were acquired over the course of ~2 hr until spectral changes in the CO and CO_2 stretch region (~2200–1900 cm^{-1}) were negligible. The spectra resolution was 3.857 cm^{-1}. The system was evacuated under Ar as the reaction chamber cooled back down.

CO Isothermal Adsorption Measurements: Carbon monoxide (99.999%) was purchased from Airgas. CO isotherms were measured on a Micromeritics 3Flex. MOF samples were activated overnight under vacuum at 30 °C using a Micromeritics ASAP 2420. The CO isotherms were collected at 87 K and collected on a Micromeritics 3Flex Instrument. **Note: CO is a higly toxic gas, and special precautions should be taken for isotherm collection. The instrument should be placed in a fumehood equipped with CO sensors. We recommend users to install a excess flow shut off valve and a flashback arrestor. Here the isotherms are collected at 87 K, however, if the users desire to collect isotherms at 77 K, the pressure must be limited to 0.5 bar as the CO can condense in the analysis tube pressures at higher than 0.57bar at 77 K.**

Raman Spectroscopy: Raman measurements were carried out on a custom-built system equipped with a visible Ar ion laser and a Horiba IHR 550 spectrometer. Fundamental 532 nm excitation was employed for all Raman measurements. Laser power by the sample was 26 mW; and spot size by the sample was estimated at a millimeter. Raman signal was collected by using an off-axis parabolic mirror with a through pinhole. Powder samples were placed in the fluidized bed reactor and fluidized during laser illumination by a flow of 35 sccm of 10% O_2/Ar. An average of four spectra were collected for all the samples. Exposure time per spectrum was 600 s per sample.

3.9.3 PXRD Patterns

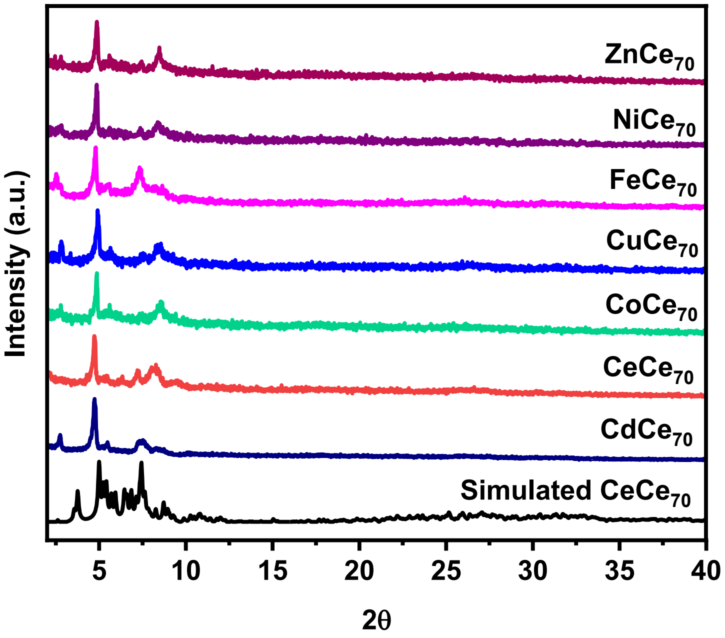

Figure 3.6 PXRD patterns of MCe_{70} clusters taken after solvent exchange and evacuation procedures detailed in Chapter 3.9.2 stacked above the simulated PXRD pattern of $CeCe_{70}$.

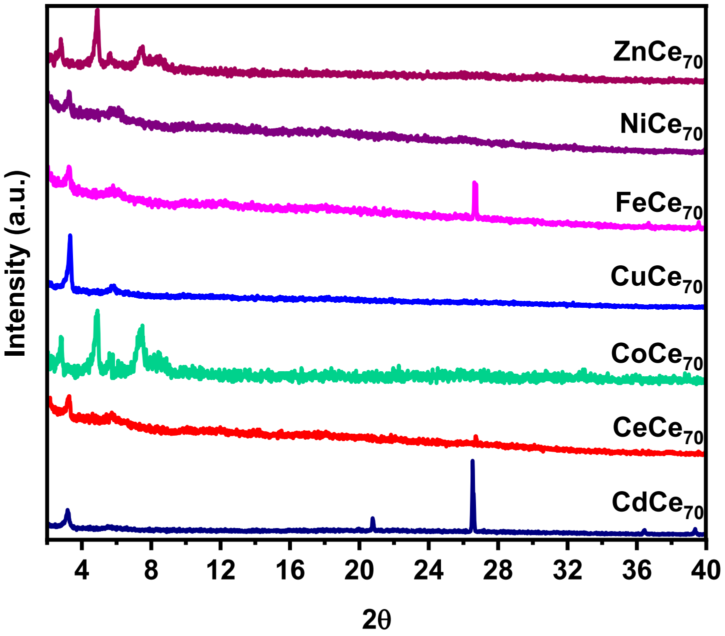

Figure 3.7 PXRD patterns of MCe_{70} clusters post catalysis. No peaks attributed to CeO_2 were detected after 16 hr on stream. Quartz sand impurities found in some samples near 21° and 26°.

3.9.4 ICP-OES Data

Table 3.2 ICP-OES data of digested MCe_{70} clusters.

Sample	Ce:M Ratio	Ce:S Ratio
$CdCe_{70}$	6.3: 1	1.2: 1
$CeCe_{70}$	-	1.3: 1
$CoCe_{70}$	7.5: 1	1.2: 1
$CuCe_{70}$	6.3: 1	1.2: 1
$FeCe_{70}$	7.6 :1	1.2: 1
$NiCe_{70}$	7.2: 1	1.2: 1
$ZnCe_{70}$	6.1: 1	1.2: 1

3.9.5 N_2 Physisorption Measurements

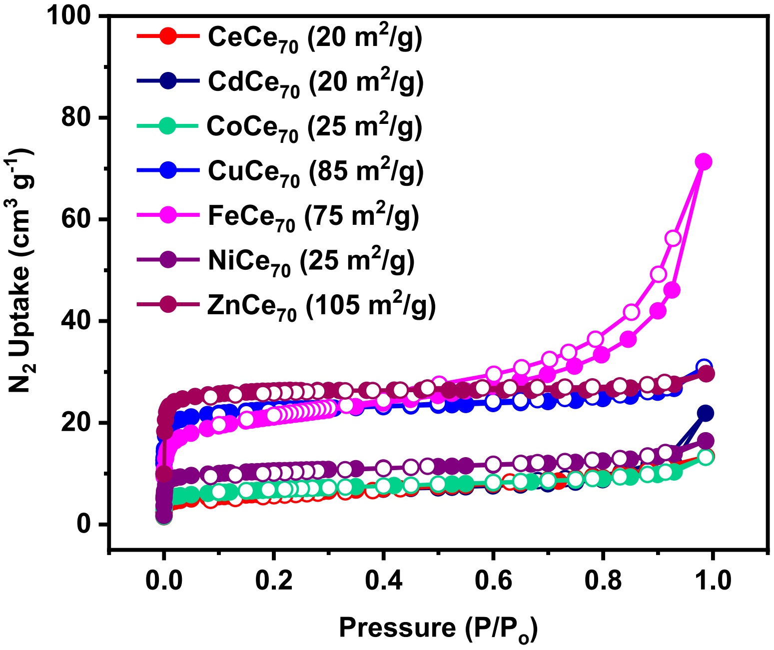

Figure 3.8 N_2 physisorption data collected at 77 K. BET areas indicated in parentheses.

3.9.6 Catalyst Reactivity Data

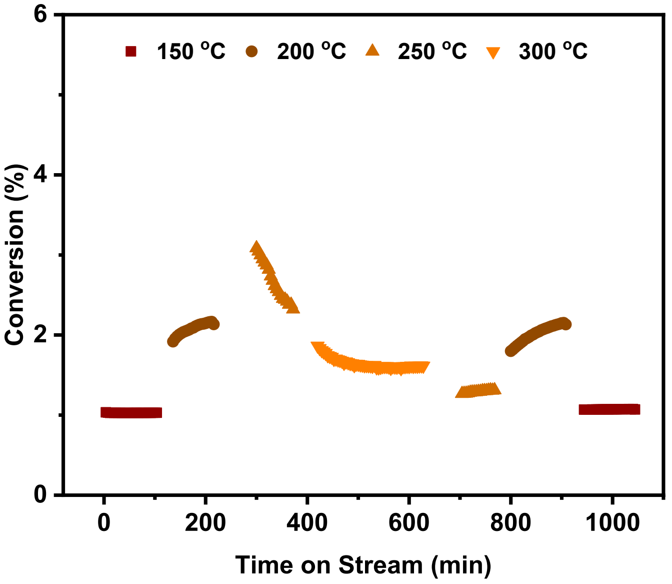

Figure 3.9 CeCe$_{70}$ temperature profile. Conditions described in Chapter 3.9.2; time on stream refers to exposure to reactant gases. Catalyst heated at 200 °C for 2 hr under O_2/He prior to catalysis.

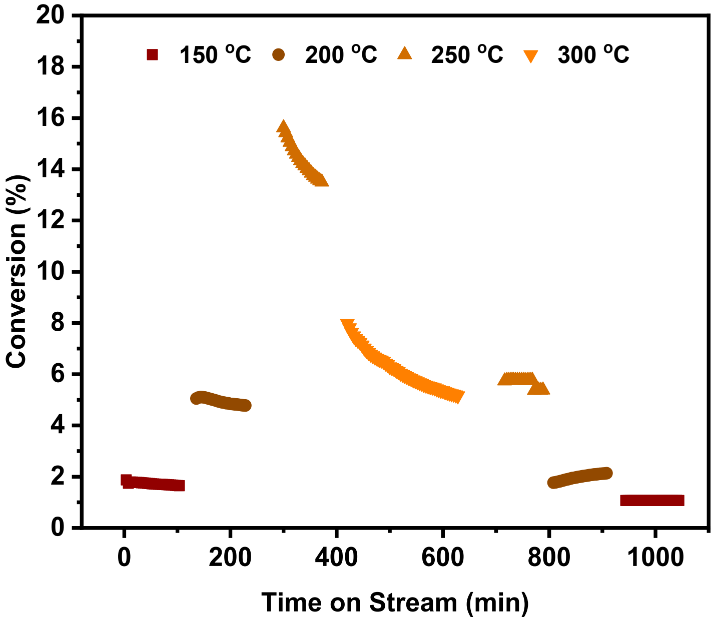

Figure 3.10 CuCe$_{70}$ temperature profile. Conditions described in Chapter 3.9.2; time on stream refers to exposure to reactant gases. Catalyst heated at 200 °C for 2 hr under O_2/He prior to catalysis.

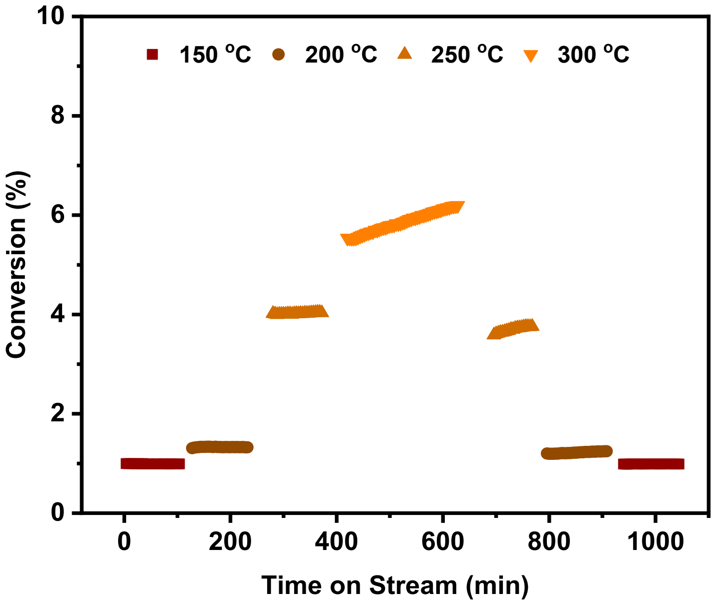

Figure 3.11 $CdCe_{70}$ temperature profile. Conditions described in Chapter 3.9.2; time on stream refers to exposure to reactant gases. Catalyst heated at 200 °C for 2 hr under O_2/He prior to catalysis.

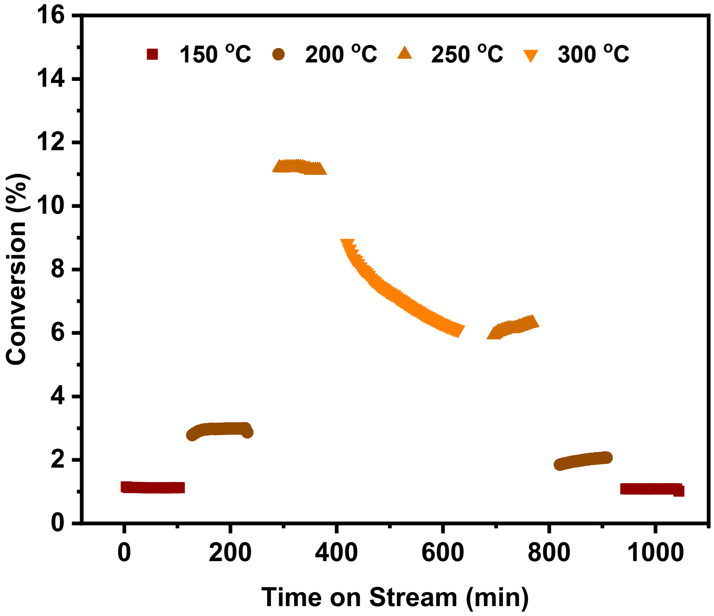

Figure 3.12 $CoCe_{70}$ temperature profile. Conditions described in Chapter 3.9.2; time on stream refers to exposure to reactant gases. Catalyst heated at 200 °C for 2 hr under O_2/He prior to catalysis.

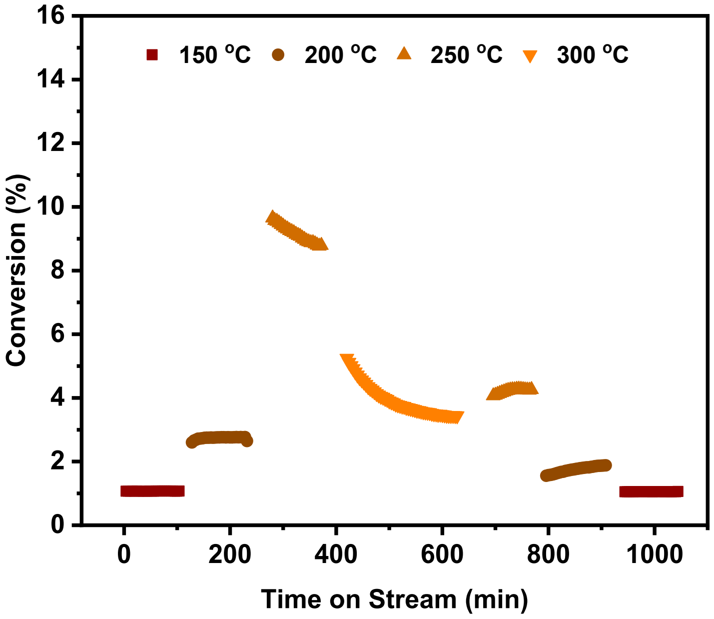

Figure 3.13 $FeCe_{70}$ temperature profile. Conditions described in Chapter 3.9.2; time on stream refers to exposure to reactant gases. Catalyst heated at 200 °C for 2 hr under O_2/He prior to catalysis.

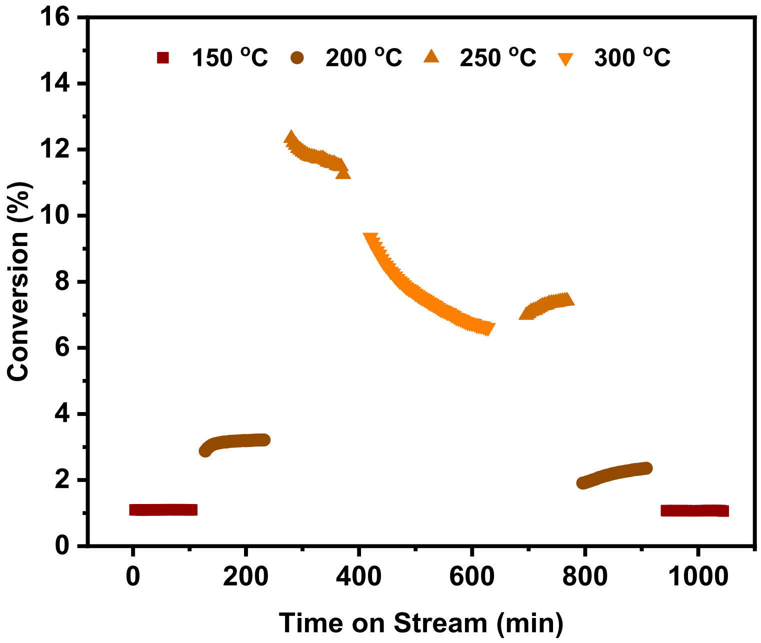

Figure 3.14 $NiCe_{70}$ temperature profile. Conditions described in Chapter 3.9.2; time on stream refers to exposure to reactant gases. Catalyst heated at 200 °C for 2 hr under O_2/He prior to catalysis.

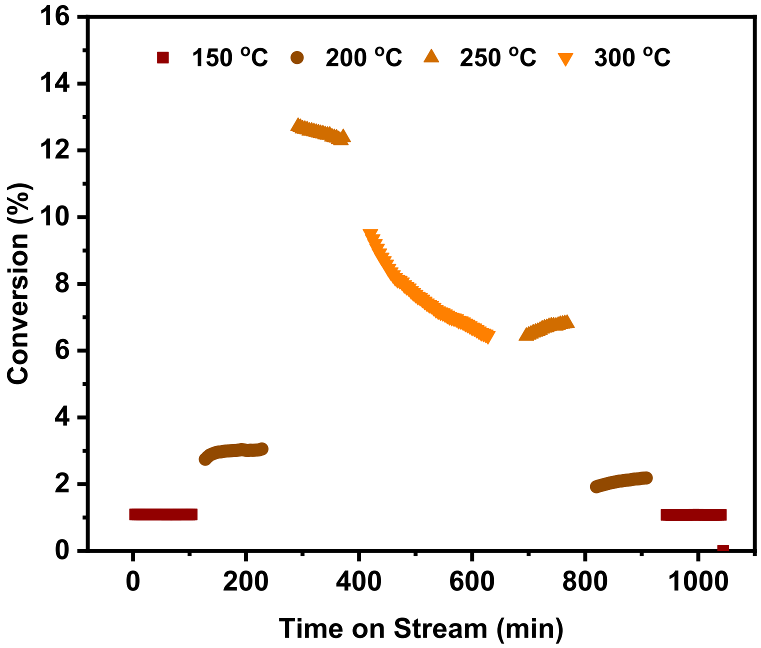

Figure 3.15 $ZnCe_{70}$ temperature profile. Conditions described in Chapter 3.9.2; time on stream refers to exposure to reactant gases. Catalyst heated at 200 °C for 2 hr under O_2/He prior to catalysis.

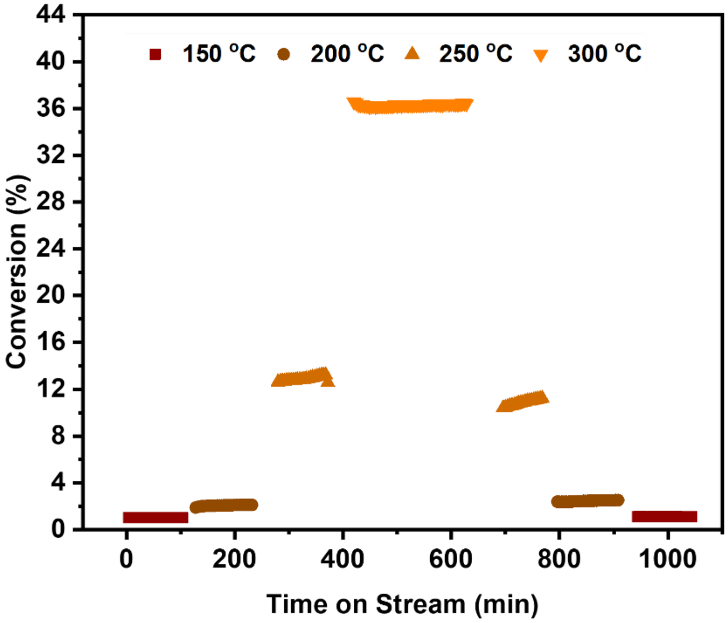

Figure 3.16 CeO_2 (commercially obtained) temperature profile. Conditions described in Chapter 3.9.2; time on stream refers to exposure to reactant gases. Catalyst heated at 200 °C for 2 hr under O_2/He prior to catalysis.

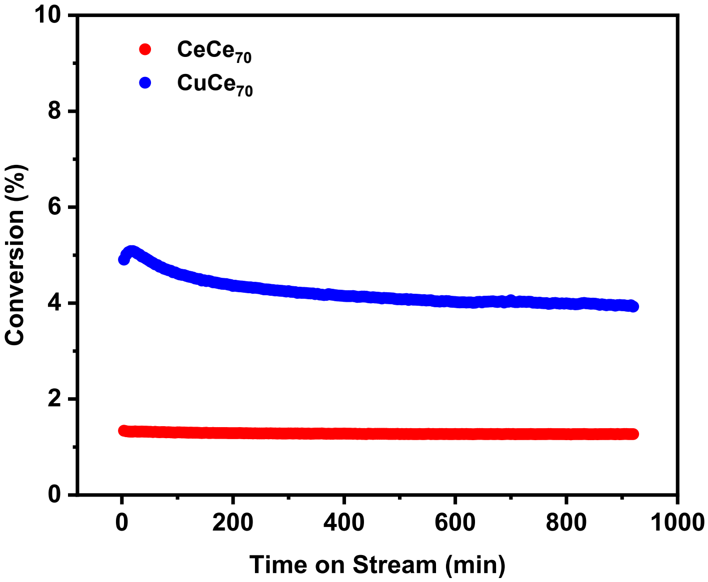

Figure 3.17 $CeCe_{70}$ and $CuCe_{70}$ stability test conducted at 200 °C. Conditions described in Chapter 3.9.2; time on stream refers to exposure to reactant gases. Catalyst heated at 200 °C for 2 hr under O_2/He prior to catalysis.

3.9.7 XPS Data

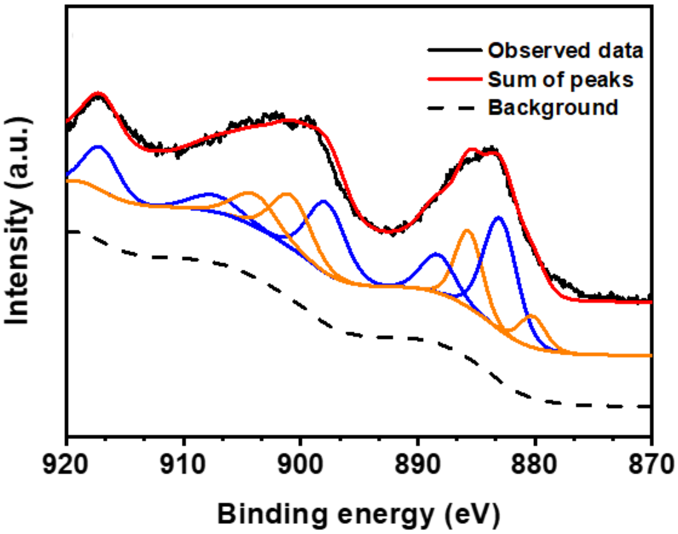

Figure 3.18 $CeCe_{70}$ Ce 3d spectrum post-catalysis (collected after 2 hr on stream with reactants) at 200 °C. The observed data were fitted by Gaussian/Lorentzian functions with deconvoluted peaks in blue corresponding to Ce^{4+} and orange deconvoluted peaks corresponding to Ce^{3+}.

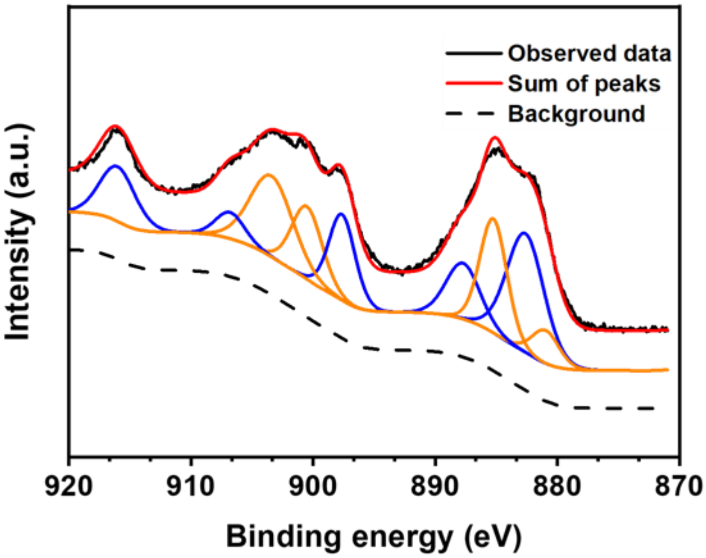

Figure 3.19 $CuCe_{70}$ Ce 3d spectrum post-catalysis (collected after 2 hr on stream with reactants) at 200 °C. The observed data were fitted by Gaussian/Lorentzian functions with deconvoluted peaks in blue corresponding to $Ce4^+$ and orange deconvoluted peaks corresponding to Ce^{3+}.

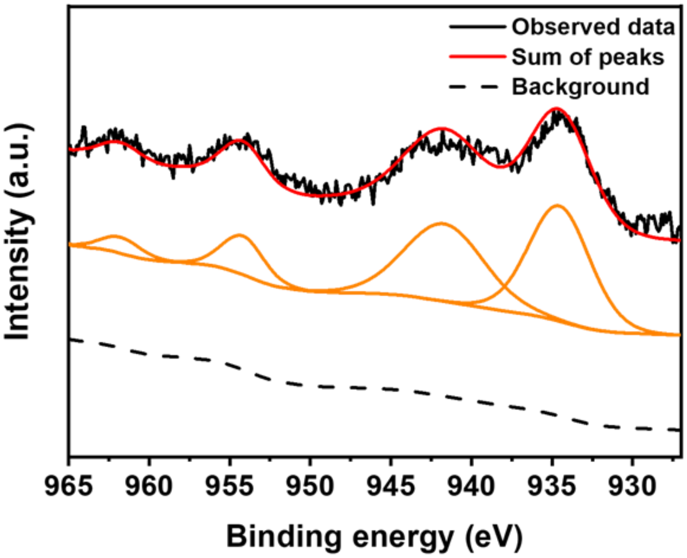

Figure 3.20 $CuCe_{70}$ Cu 2p spectrum post-catalysis (collected after 2 hr on stream with reactants) at 200 °C. The observed data were fitted by Gaussian/Lorentzian functions. To investigate the presence of Cu^{1+} in $CuCe_{70}$ post catalysis, we handled our spent $CuCe_{70}$ in an air-free manner to investigate the Cu 2p XPS, but we observed a spectrum that suggested the presence of either Cu^{2+} or a mixture of Cu^{1+}/Cu^{2+}.[180]

3.9.8 TPR-MS Data

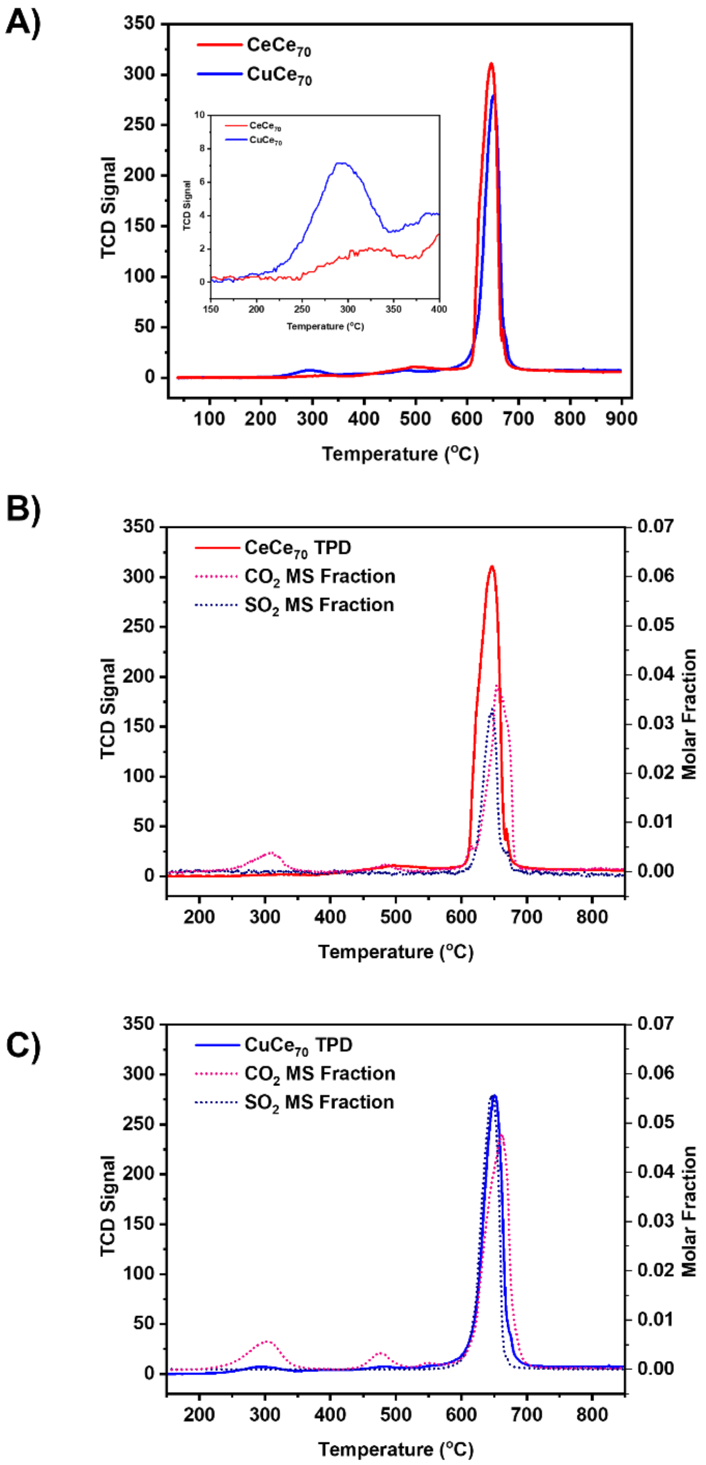

Figure 3.21 A) Overlaid TPR profile of CeCe$_{70}$ and CuCe$_{70}$ collected under CO/He with inset showing 150-400 °C range. B) CeCe$_{70}$ TPR-MS profile and C) CuCe$_{70}$ TPR-MS profile.

3.9.9 DRIFTS Data and Fitting Details

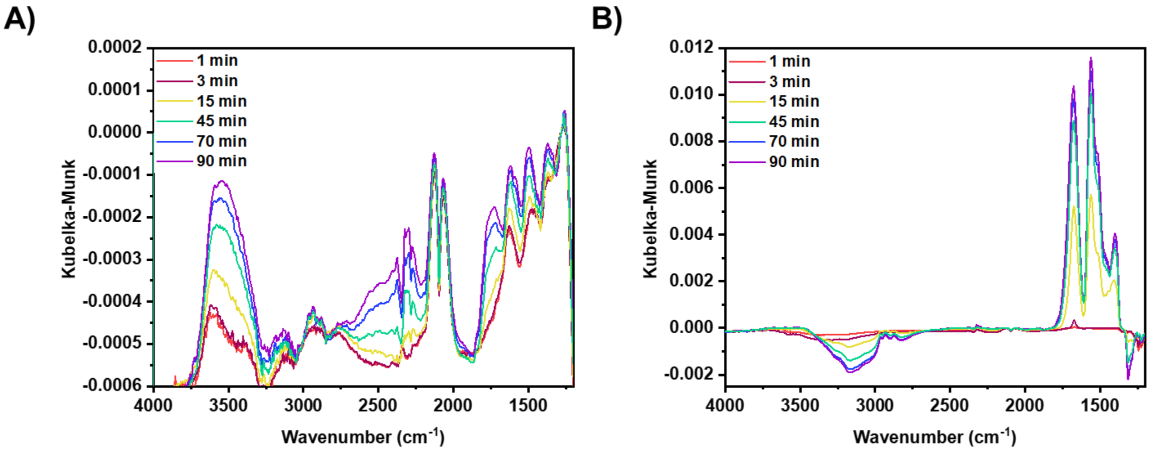

Figure 3.22 DRIFTS data collected at 200 °C under ^{13}CO and $^{18}O_2$ flowed over a) CeCe$_{70}$ b) CuCe$_{70}$.

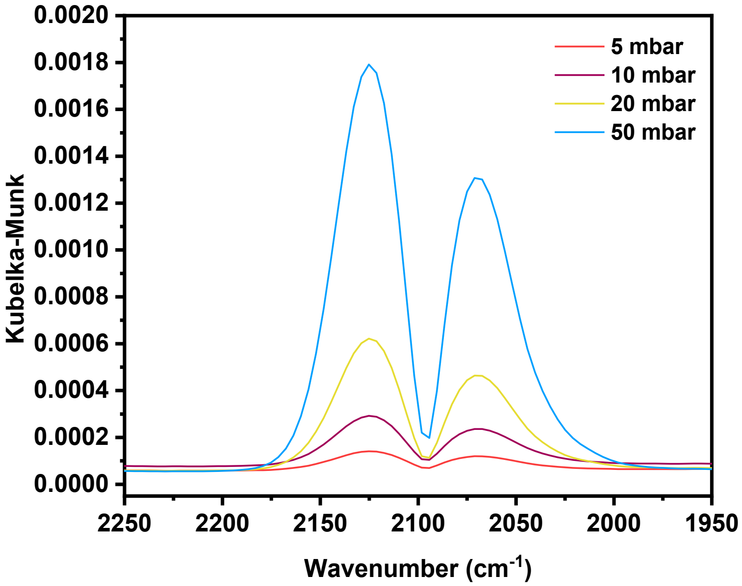

Figure 3.23 DRIFTS data collected of ^{13}CO of varying partial pressures used for data deconvolution as discussed below.

DRIFTS Data Deconvolution Details: We deconvoluted the region of the spectra between 1875 cm^{-1} and 2225 cm^{-1}. While shifted relative to gas phase ^{12}CO features, the gas phase ^{13}CO features are still dominant in this region. Control experiments indicated a linear relationship between the ^{13}CO partial pressure and the magnitude of the asymmetric gas phase signal (**Figure 3.23**). To process the data, background were applied and the signal due to the ^{13}CO asymmetric stretching mode was subtracted using a linear combination of ^{13}CO gas phase spectra. A linear background was applied to the CeCe$_{70}$ sample, while a more appropriate shape-preserving cubic spline (pchip) background was applied to the CuCe$_{70}$. The linear combination was constructed from ^{13}CO gas phase spectra shown in Figure S16 and was normalized to the background corrected CeCe$_{70}$ and CuCe$_{70}$ spectra using the magnitude of the R branch at 2125 cm^{-1}. Peak heights and widths are summarized in **Tables 3.3-3.4** and outputs from Matlab are included below. For the peak deconvolution, we used a code for MatLab published by reference 181.[181] This yielded a number of features attributed to Ce^{3+} and bound CO to various sites.[182,183]

Table 3.3 Deconvolution results summarized for CeCe$_{70}$ DRIFTS data; time refers to the amount of exposure to reactant gases.

Time	Peak Number	Peak Center (cm^{-1})	Peak Height	Peak Width	Peak Area
1 min	1	2041	1.29E-04	5.44E+01	7.46E-03
	2	2088	8.28E-05	1.81E+01	1.59E-03
	3	2105	8.06E-05	1.40E+01	1.20E-03
	4	2155	1.39E-04	3.55E+01	5.26E-03
3 min	1	2041	1.29E-04	5.54E+01	7.62E-03
	2	2088	8.40E-05	1.72E+01	1.54E-03
	3	2105	8.43E-05	1.40E+01	1.26E-03
	4	2155	1.42E-04	3.43E+01	5.17E-03
15 min	1	2038	1.35E-04	5.18E+01	7.45E-03
	2	2089	9.52E-05	1.89E+01	1.92E-03
	3	2105	7.66E-05	1.16E+01	9.46E-04
	4	2156	1.46E-04	3.13E+01	4.88E-03
45 min	1	2041	1.42E-04	5.58E+01	8.44E-03
	2	2088	9.05E-05	1.76E+01	1.70E-03
	3	2105	8.85E-05	1.43E+01	1.34E-03
	4	2156	1.54E-04	3.70E+01	6.05E-03
70 min	1	2041	1.36E-04	5.21E+01	7.56E-03
	2	2088	8.93E-05	2.09E+01	1.98E-03
	3	2106	7.76E-05	1.34E+01	1.10E-03
	4	2156	1.50E-04	3.64E+01	5.80E-03
90 min	1	2042	1.34E-04	5.45E+01	7.77E-03
	2	2088	8.58E-05	1.82E+01	1.67E-03
	3	2105	8.54E-05	1.39E+01	1.27E-03
	4	2156	1.49E-04	3.78E+01	6.01E-03

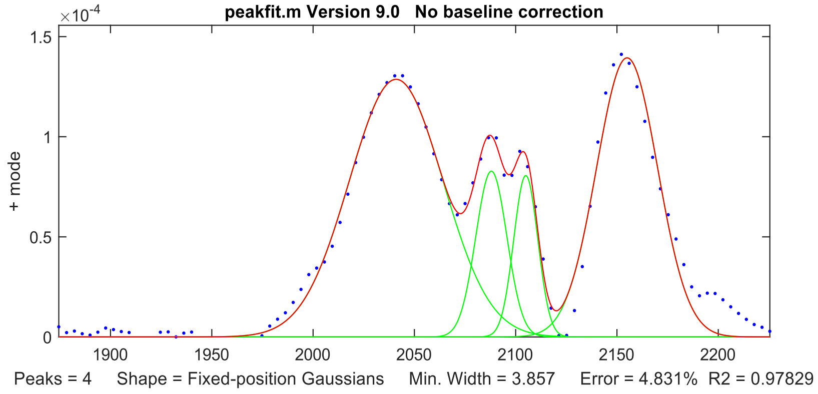

Figure 3.24 Data deconvolution output from Matlab for CeCe$_{70}$ after 1 min of exposure to reactant gases.

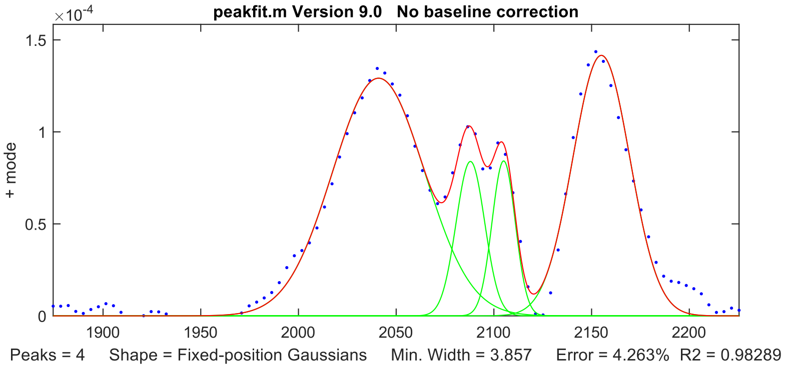

Figure 3.25 Data deconvolution output from Matlab for $CeCe_{70}$ after 3 min of exposure to reactant gases.

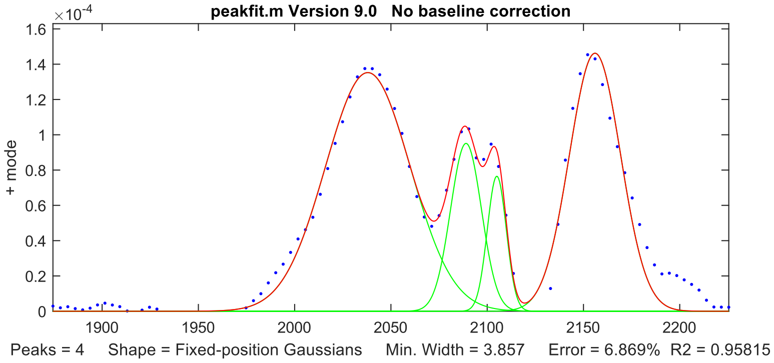

Figure 3.26 Data deconvolution output from Matlab for $CeCe_{70}$ after 15 min of exposure to reactant gases.

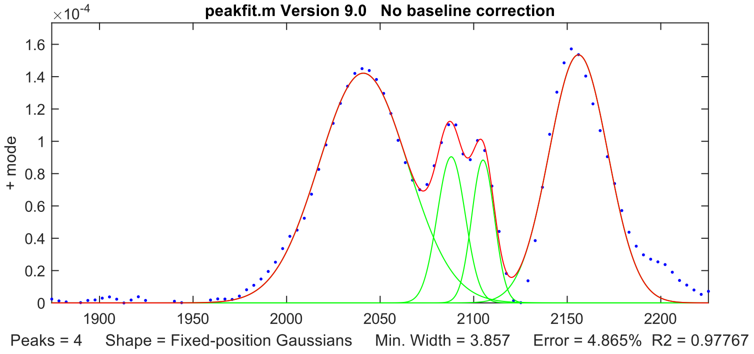

Figure 3.27 Data deconvolution output from Matlab for $CeCe_{70}$ after 45 min of exposure to reactant gases.

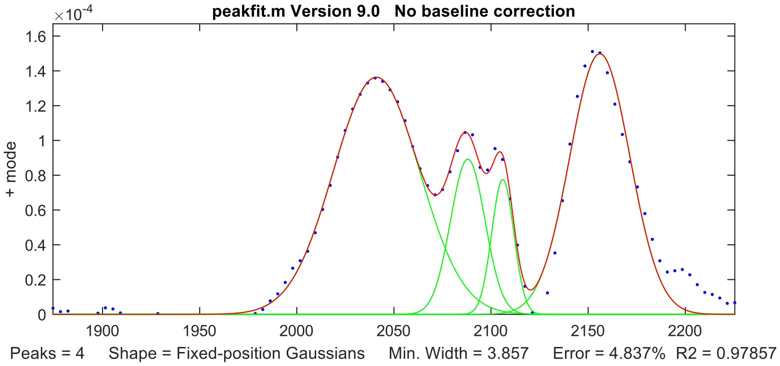

Figure 3.28 Data deconvolution output from Matlab for $CeCe_{70}$ after 70 min of exposure to reactant gases.

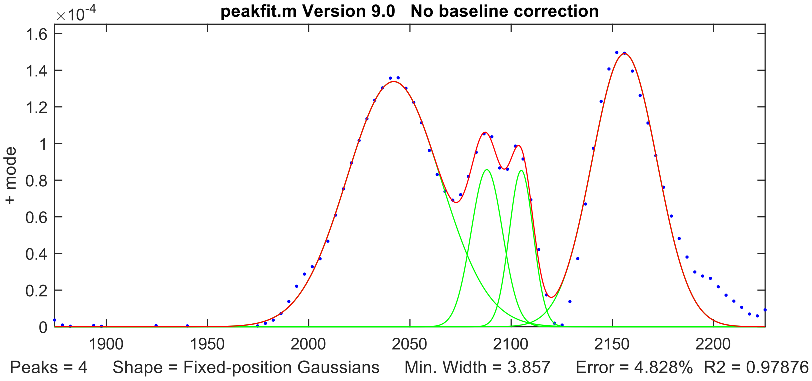

Figure 3.29 Data deconvolution output from Matlab for $CeCe_{70}$ after 90 min of exposure to reactant gases.

Table 3.4 Deconvolution results summarized for $CuCe_{70}$ DRIFTS data; time refers to the amount of exposure to reactant gases.

Time	Peak Number	Peak Center (cm^{-1})	Peak Height	Peak Width	Peak Area
1 min	1	2042	2.45E-05	4.57E+01	1.19E-03
	2	2079	5.29E-06	1.14E+01	6.44E-05
	3	2107	6.72E-06	3.86E+00	2.76E-05
	4	2152	3.83E-05	3.12E+01	1.27E-03
3 min	1	2041	3.58E-05	4.53E+01	1.73E-03
	2	2079	7.77E-06	1.22E+01	1.01E-04
	3	2107	8.76E-06	6.63E+00	6.18E-05
	4	2153	5.59E-05	3.22E+01	1.92E-03
15 min	1	1915	2.43E-05	2.23E+01	5.75E-04
	2	1954	6.32E-06	2.80E+01	1.88E-04
	3	2044	3.57E-05	4.26E+01	1.62E-03
	4	2081	1.52E-05	1.24E+01	2.01E-04
	5	2109	1.69E-05	9.63E+00	1.74E-04
	6	2158	6.69E-05	3.64E+01	2.59E-03
45 min	1	1915	5.35E-05	2.91E+01	1.66E-03
	2	1955	1.44E-05	2.93E+01	4.50E-04
	3	2044	3.13E-05	4.15E+01	1.38E-03
	4	2078	1.54E-05	1.65E+01	2.71E-04
	5	2108	2.08E-05	1.03E+01	2.28E-04
	6	2162	5.30E-05	3.97E+01	2.24E-03
70 min	1	1913	6.27E-05	3.18E+01	2.12E-03
	2	1957	1.64E-05	3.19E+01	5.56E-04
	3	2044	3.16E-05	4.11E+01	1.38E-03
	4	2078	1.58E-05	1.65E+01	2.77E-04
	5	2108	2.16E-05	1.05E+01	2.40E-04
	6	2162	5.10E-05	4.22E+01	2.29E-03
90 min	1	1913	5.49E-05	3.47E+01	2.02E-03
	2	1957	1.45E-05	2.95E+01	4.57E-04
	3	2044	2.84E-05	4.15E+01	1.26E-03
	4	2078	1.58E-05	1.68E+01	2.83E-04
	5	2108	2.10E-05	1.03E+01	2.30E-04
	6	2160	4.24E-05	4.42E+01	1.99E-03

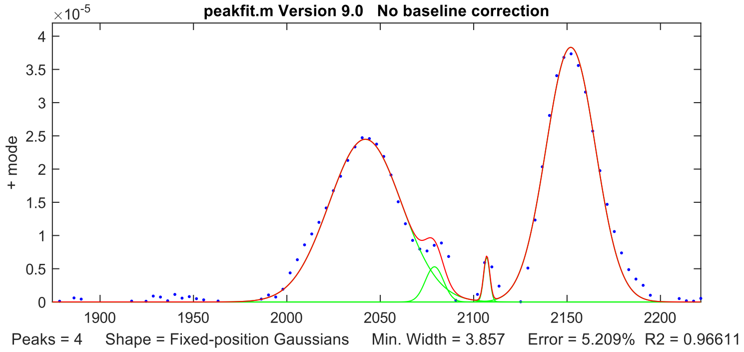

Figure 3.30 Data deconvolution output from Matlab for $CuCe_{70}$ after 1 min of exposure to reactant gases.

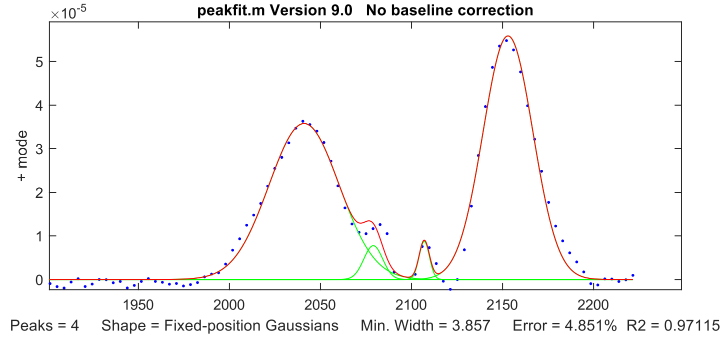

Figure 3.31 Data deconvolution output from Matlab for $CuCe_{70}$ after 3 min of exposure to reactant gases.

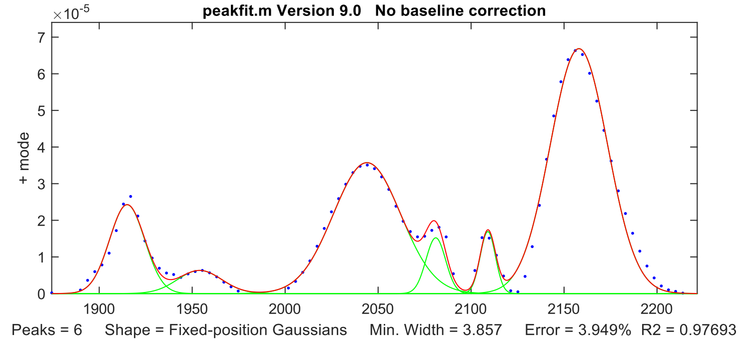

Figure 3.32 Data deconvolution output from Matlab for $CuCe_{70}$ after 15 min of exposure to reactant gases.

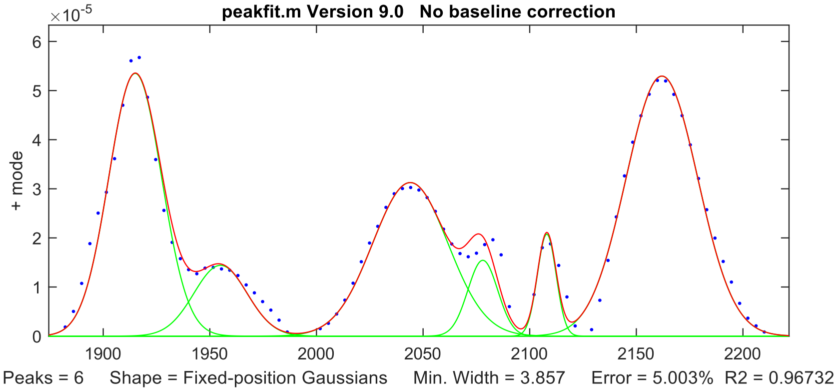

Figure 3.33 Data deconvolution output from Matlab for $CuCe_{70}$ after 45 min of exposure to reactant gases.

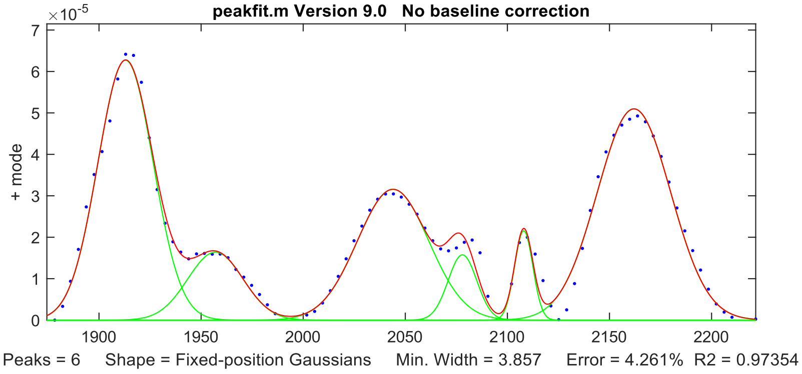

Figure 3.34: Data deconvolution output from Matlab for $CuCe_{70}$ after 70 min of exposure to reactant gases

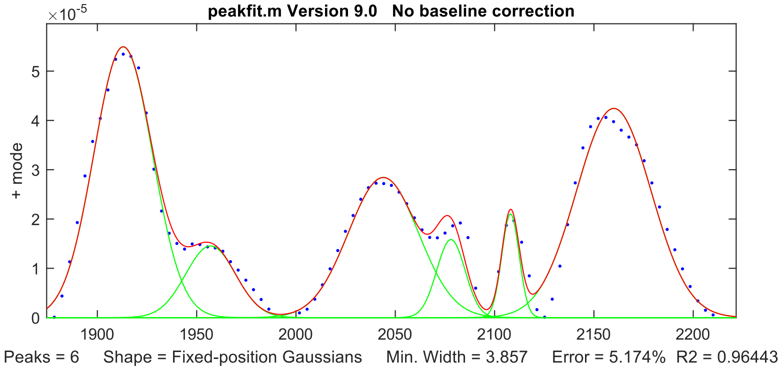

Figure 3.35 Data deconvolution output from Matlab for $CuCe_{70}$ after 90 min of exposure to reactant gases.

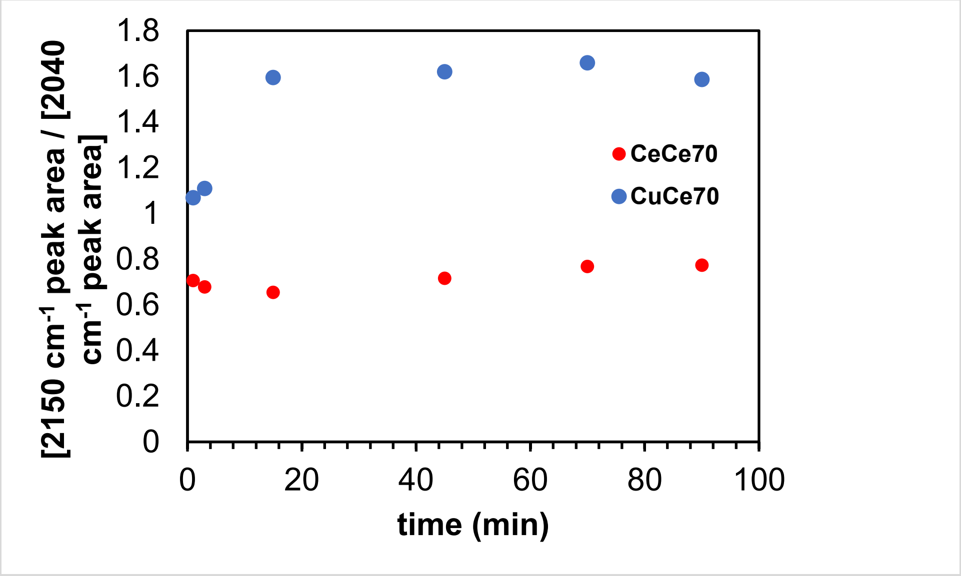

Figure 3.36 Ratio of Ce^{3+} peak area (~2150 cm^{-1}) to CO adsorbed peak area (2040 cm^{-1}) in $CeCe_{70}$ and $CuCe_{70}$ over the experiment duration.

3.9.10 CO Physisorption Measurements

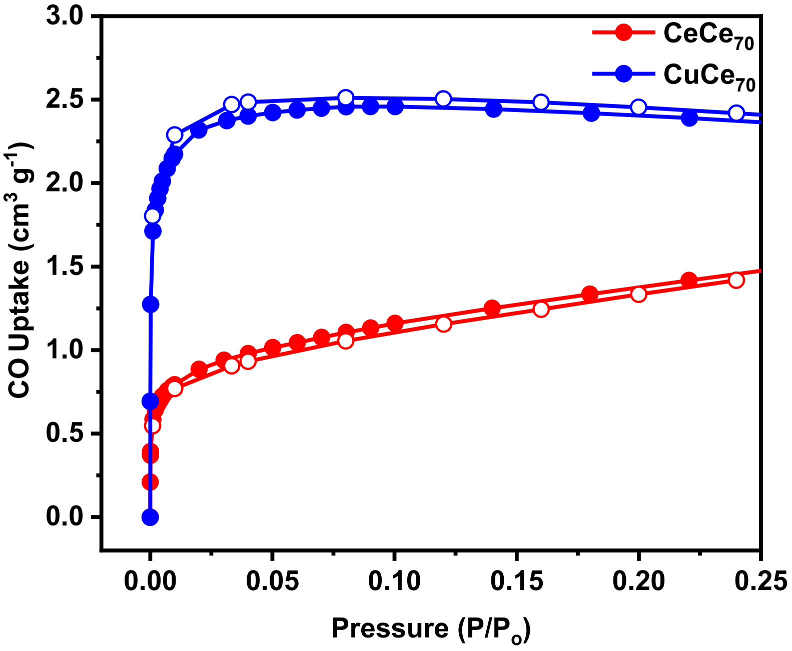

Figure 3.37 CO adsorption isotherms conducted at 87 K of $CeCe_{70}$ and $CuCe_{70}$.

3.9.11 Raman Spectroscopy

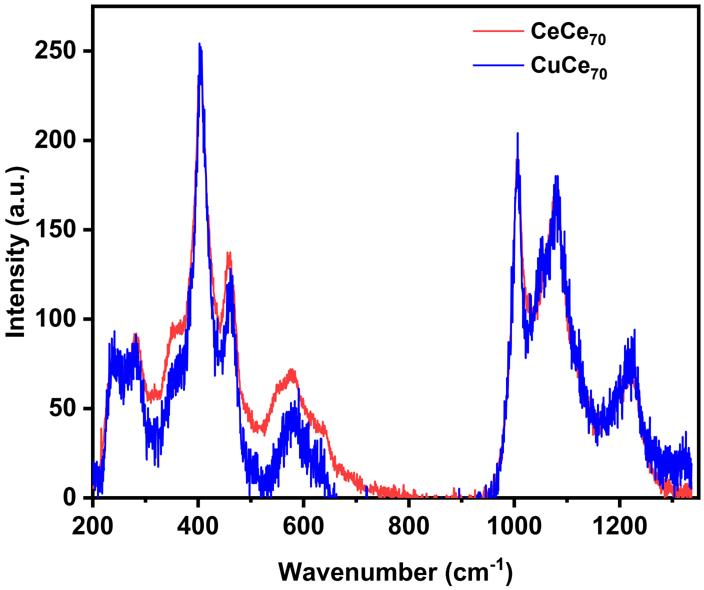

Figure 3.38 Raman spectra of CeCe$_{70}$ and CuCe$_{70}$ collected at 23 °C under 10% O_2/Ar.

3.9.12 Computational Methodology and Results

Computational Details: Raw data of input and output files, as well as pre- and postprocessing scripts and figures, are published online on Zenodo.[184] Plots were produced using Matplotlib (version 3.3.0)[185] and graphical representations of structures using VMD (version 1.9.3).[186] PLAMS was used for pre- and postprocessing of jobs.[187]

General Simulation Setup: Restricted open shell Kohn-Sham (ROKS) density functional theory (DFT) calculations, employing the PBE[188] functional with Grimme's D3(BJ) dispersion correction (no ATM/C_9 terms nor long range correction),[189,190] were performed using the Quickstep module in CP2K version 8.1.[191,192,201,193–200] The DZVP MolOpt short range basis set was used in conjunction with the GTH pseudopotentials for all elements except Ce, for which a DZV basis was used in conjunction with the GTH-LnPP1 pseudopotentials.[189,200,202–204] Four multigrids were used with a cutoff value of 400 Ry and a relative cutoff value of 50 Ry (values chosen based on convergence tests, see **Figure 3.39**). The SCF was converged using the orbital transformation (OT) method[191] with a DIIS minimizer and additional variables for rotations of the occupied subspace (needed for ROKS calculations). The convergence criterion of the outer and inner SCF was set to 10^{-6}.

Cluster calculations made use of the Martyna-Tuckermann (MT)[205] Poisson solver using no periodicity. Periodic calculations were performed using the analytic Poisson solver with periodicity in X direction. If needed, the diagonal of the stress tensor for the periodic systems was calculated numerically. Optimizations employed the BFGS algorithm and default convergence criteria.

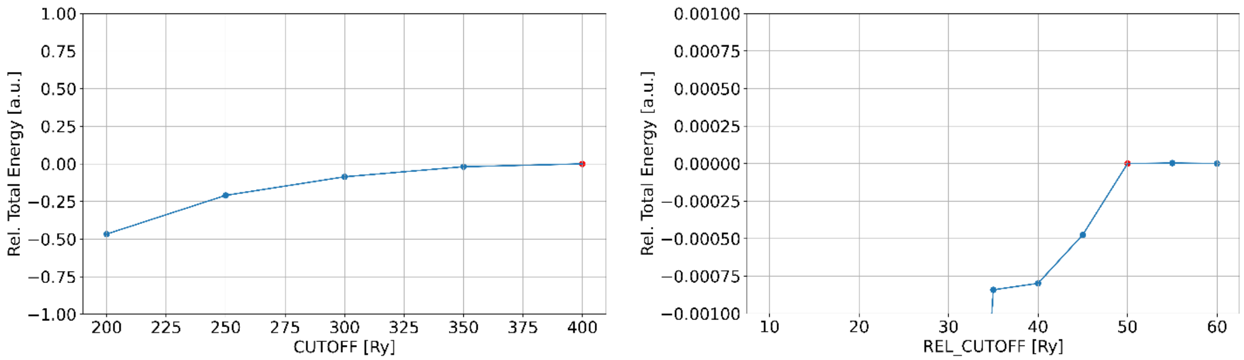

Figure 3.39 Convergence of multigrid cutoff (left) and relative cutoff (right) with respect to the total energy. Chosen values are highlighted in red.

An effective Hubbard parameter (+U_{eff} correction) was added in calculations denoted with PBE+U.[206,207] For the Ce f orbitals, a value of $U_f = 4.5$ eV[175,176,208,209] and for the Cu d orbitals, a value of $U_d = 7$ eV[210] was used, based on the references given.

Cluster Hydrogen Placement:

To reduce complexity of the model structure used, we imposed a hypothetical D_{10h} symmetry on the initial cluster model. Based on the experimental structure solutions of Colliard *et al.*[151,152] and this work, we manually built an approximate $[Ce_7O_{10}(SO_4)_6(H_2O)_5]^{4-}$ fragment to be repeated ten times using the imposed C_{10} axis through the center of mass of the final ring. We chose this initial fragment, as the bond valence sum calculations of Colliard *et al.*[151,152] suggest that the terminal oxygens in the center of the toroid, as well as the terminal oxygens on the corners of the Ce_6 octahedrons belong to water molecules. A graphical representation of the initial fragment is given in **Figure 3.40**. The fragment was prepared using the AMS GUI[211] by manually editing cartesian coordinates to ensure full D_{10h} symmetry of the resulting toroid after repetition around the C_{10} axis. The resulting symmetry was validated using the GaussView6 software.[212]

In the fragment, two groups of oxygen atoms (without the already saturated water oxygens) can be distinguished. The first group ("**A**") consists of four oxygen atoms located in the σ_h plane (labeled A to D). The second group ("**B**") consists of three oxygen atoms located above the σ_h mirror plane. These three oxygens of group **B** are identical to their mirror images below the plane, resulting in a total of six oxygen atoms in group **B**. See **Figure 3.40** for a colored representation of the two groups of oxygen atoms. To balance the charge of our fragment, we added four hydrogen atoms in all possible combinations, resulting in 22 unique hydrogen placements. To distinguish the hydrogen placement, we introduce a naming scheme containing 7 unique locations, corresponding to the four oxygen atoms of group **A** and the three unique atoms of group **B**. The location of a hydrogen atom is denoted by "1", the absence by "0". The name "0-0-0-0-1-0-1" therefore represents no hydrogen atoms on group **A** oxygens and one hydrogen on the first and third oxygen atom of group **B**, respectively. Since group **B** is subject to duplication by the mirror plane, the two hydrogens appear "on the top" and "on the bottom" of the ring. **Figure 3.40** provides a visual correlation of the naming scheme with the atoms. Hydrogens were placed manually for the 22 unique hydrogen placements using the AMS GUI and the resulting $Ce_7O_6(OH)_4(SO_4)_6(H_2O)_5$ fragments were extended into full toroid structures by rotation around the C_{10} axis using the ASE python package.[126]

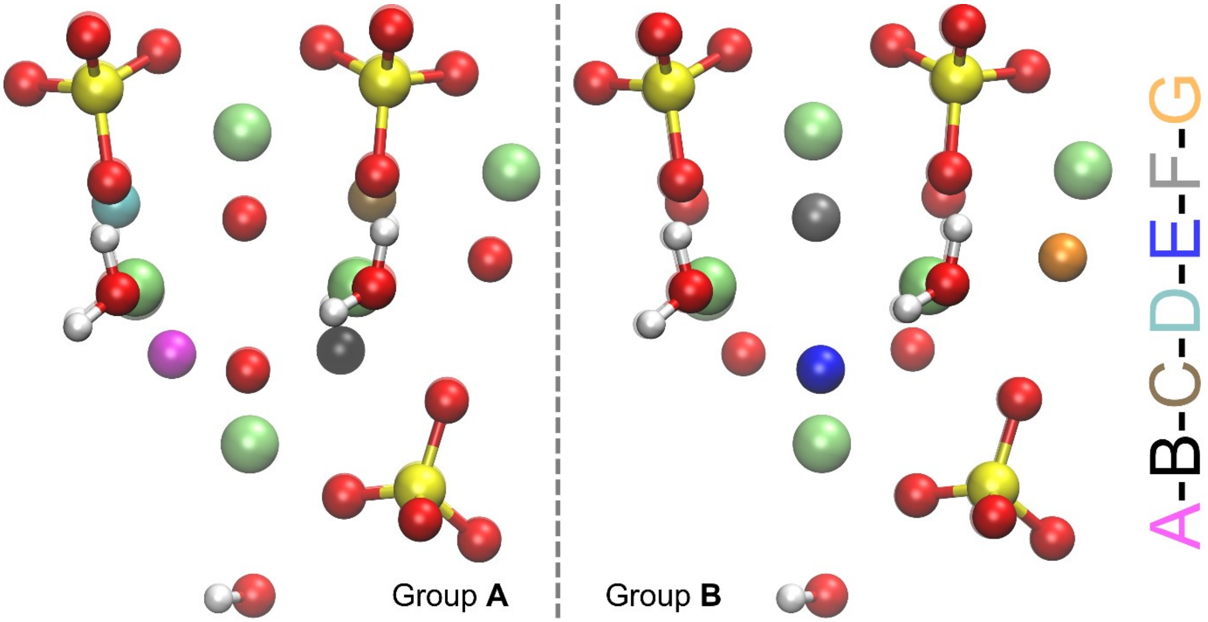

Figure 3.40 Naming scheme for hydrogen placement. Visualization of the $[Ce_7O_{10}(SO_4)_6(H_2O)_5]^{4-}$ fragment used for constructing initial configurations. Atoms colored by element: Ce lime, H white, S yellow, O red. Left: Group **A** of oxygen atoms; Right: Group **B**. The seven unique oxygens for hydrogen placement possibilities are color coded following the naming scheme given on the far right.

We ran DFT geometry optimizations without any constraints on all 22 hydrogen placements (for details see Section General Simulation Setup). The D_{10h} symmetry is therefore not exactly retained during the geometry optimization. We compare the relative absolute energies of all 22 fully optimized structures in **Figure 3.40**. We observe that the two hydrogen placements with the lowest energies are within 9 kJ/mol of each other. All other hydrogen placements exhibit a relative energy of more than 450 kJ/mol higher than the lowest energy structure, although all structures remain intact (based on visual inspection of all optimized geometries). It is noteworthy that both low-energy structures have hydrogens placed only in group **B**. Since the two most favorable structures are within 9 kJ/mol of each other, it can be expected that both occupation patterns will occur under realistic conditions. This also fits well with the O/OH disorder observed in the bond valence sum calculation of Colliard *et al.*[151] To reduce computational efforts and complexity of the defect energetics calculations, we chose system “0-0-0-0-1-0-1” (the lowest

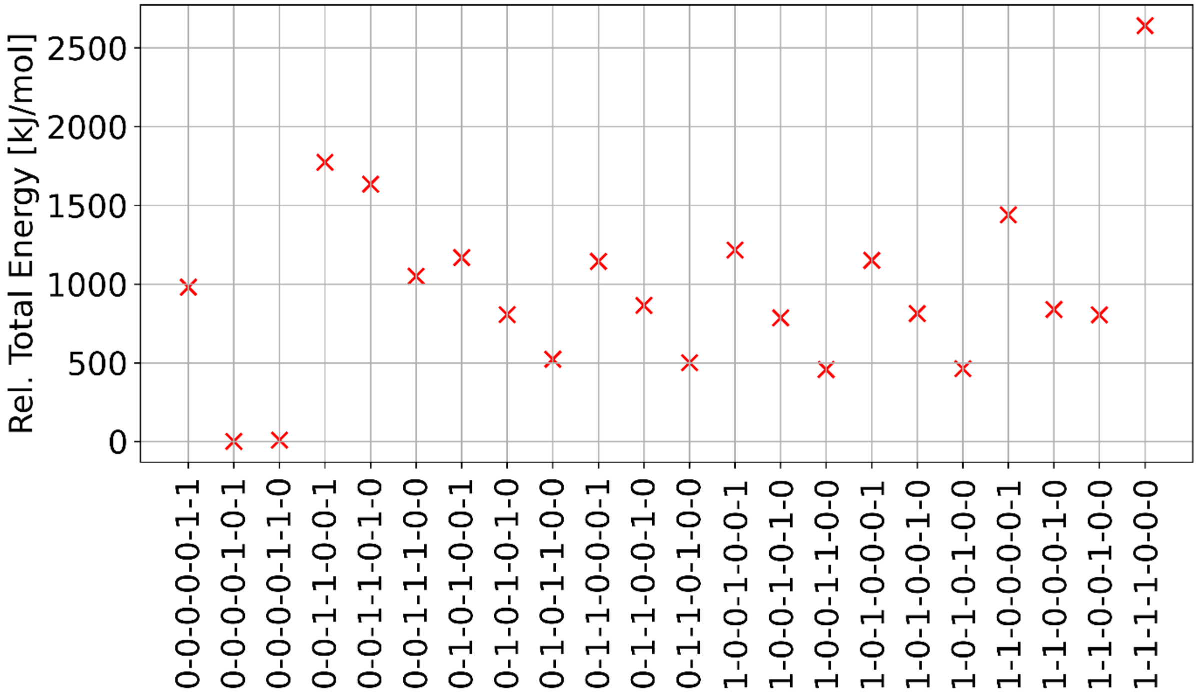

Figure 3.41 Relative total energies of the 22 hydrogen placements after geometry optimization.

energy isomer) as the basis for all further calculations. A visual representation of this system is shown in **Figure 3.42**.

Cluster Defect Energies: The defect formation energy (ΔE_{defect}) for a single neutral oxygen vacancy defect was calculated using the formula $\Delta E_{\text{defect}} = E(\text{toroid w. defect}) + E\left(\frac{1}{2}\text{O}_2\right) - E(\text{toroid})$. All energies are taken from optimized geometries. The O_2 calculations were performed using the same simulation setup as the full cluster. The O_2 molecule is expected to be in a triplet spin state and therefore optimized as such. The defect-free toroid structure is expected to be a singlet system.

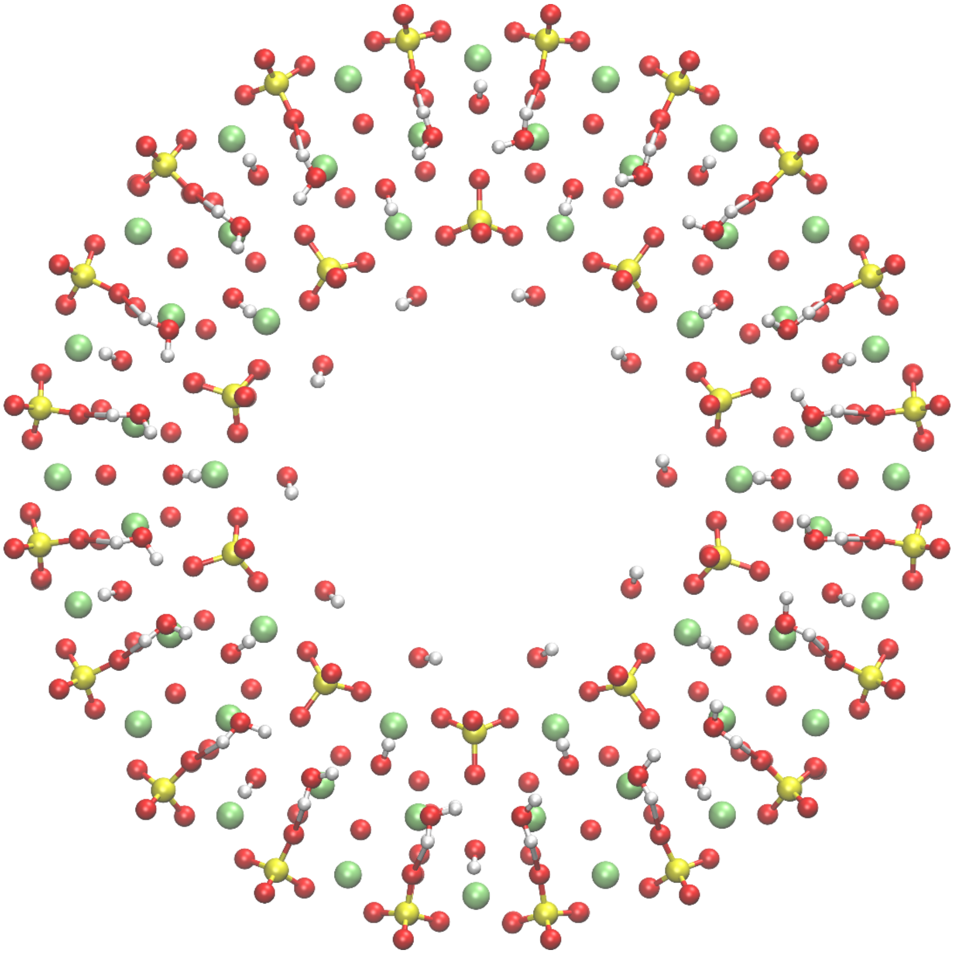

Figure 3.42 Graphical representation of the optimized system "0-0-0-0-1-0-1".

The defective toroid systems were created based on the “0-0-0-0-1-0-1” system as described above. We created the five possible pure oxygen defects. The position of the defect is described by replacing 0 with X in our nomenclature. Removing e.g., the second oxygen of group **A** is denoted as “0-X-0-0-1-0-1”. In our plots, a short notation is used with the letters A (“X-0-0-0-1-0-1”) to F (“0-0-0-0-1-X-1”) based on the nomenclature defined in **Figure 3.40**. Note that only one defect was created in the entire toroid. For the defective toroid (one missing oxygen), we compared the singlet and triplet states.

For comparison, bulk CeO_2 (2x2x2 supercell, Γ only) and a $Ce_6O_8(O_2CH)_8$ cluster (an often-used precursor in ceria cluster synthesis and comparable to the Ce_6 octahedron unit in the toroid) and their defective counterparts were also optimized.

To further refine the obtained defect formation energies, all systems outlined above were also optimized using DFT+U (see Section General Simulation Setup).

All calculated defect energies are plotted in **Figure 3.43**. For both DFT and DFT+U calculations, absolute energies as well as defect formation energies are lower in the triplet state than in the singlet state. Therefore, the triplet state should be chosen for interpretation even though the bulk singlet defect energy is closer to the experimental value of 4-5 eV.[213] The inclusion of the +U correction on the Ce f orbitals results in the expected increase in defect formation energy and is used from here on, even though the exact value of the U parameter remains a matter of debate and the defect formation energy can be freely tuned by increasing the U parameter.

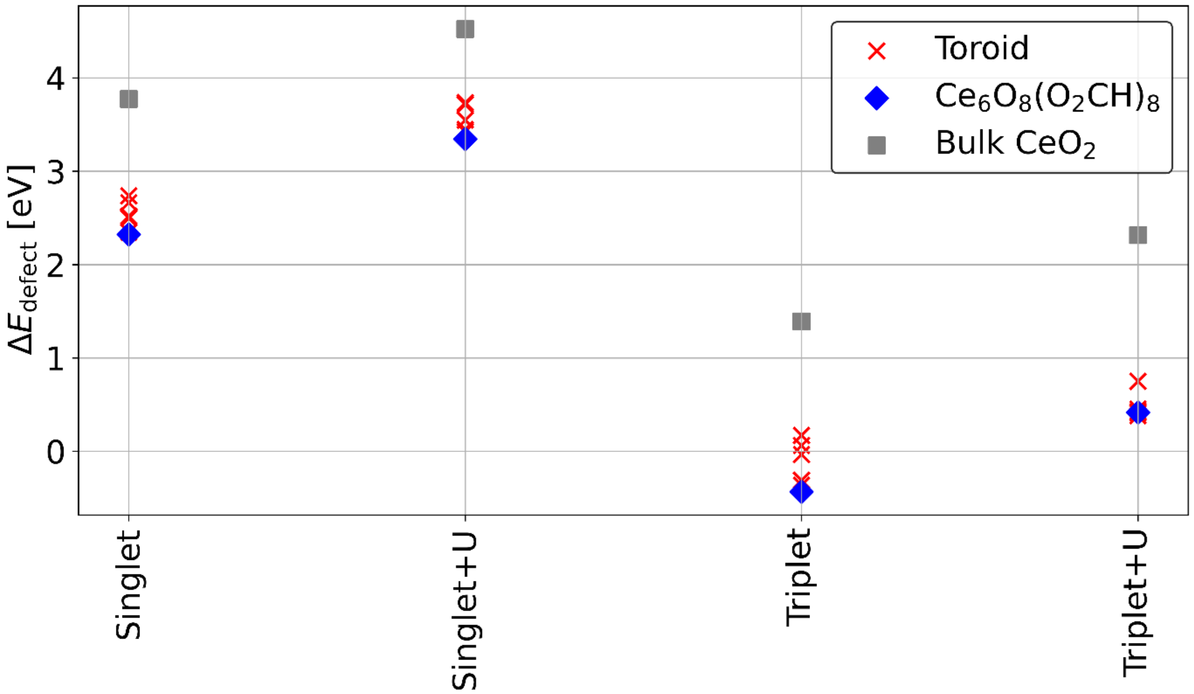

Figure 3.43 Calculated defect energies using DFT and DFT+U with the defective toroid using singlet or triplet spin states. Defect energies of the toroid systems (red crosses), the $Ce_6O_8(O_2CH)_8$ cluster (blue diamonds) and bulk CeO_2 (grey squares).

Chain Optimization: A one-dimensional chain to model bridging Cu or Ce sites was created using the optimized clusters and the experimental bridging [MO_4] fragment. The bridging unit was saturated with hydrogen atoms to achieve charge neutrality. Two of the oxygen atoms in the Ce-bridge were saturated with two H atoms each. In the Cu-bridge, two oxygens were saturated with two H atoms each and the remaining two oxygens with one H atom each. The oxidation state of the Cu was determined to be +2 from prior reports and the system was therefore modeled in a doublet spin state.[153] See **Figure 3.44** for a graphical representation of the two bridging units. The cell length (PBC along x) was initialized using the atomic distances in the experimental $CeCe_{70}$ bridge and subsequently optimized using analytical gradients while fixing the y and z coordinates of the ring atoms. The convergence of the cell length for the $CuCe_{70}$ and $CeCe_{70}$ systems is plotted in **Figure 3.45**. The convergence for the $CeCe_{70}$ chain is satisfactory, and the last cell vector length was chosen for subsequent relaxation of the atomic coordinates. For the $CuCe_{70}$ system, the optimization procedure failed. The optimization step closest to convergence (three of five convergence criteria, step 37) was therefore chosen for subsequent relaxation of atomic coordinates.

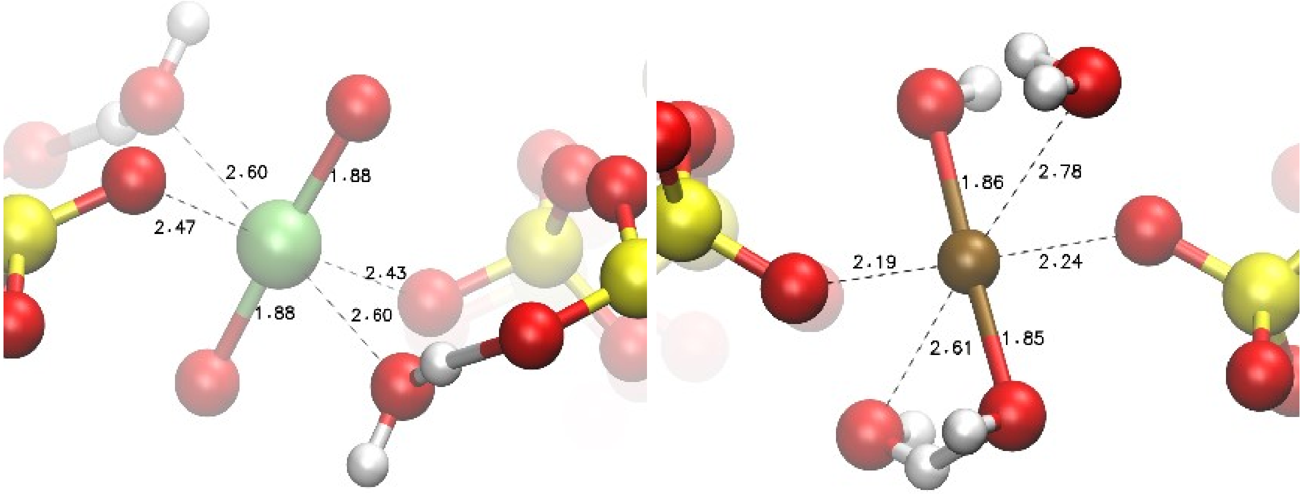

Figure 3.44 Graphical representation of the optimized $CeCe_{70}$ (left) and $CuCe_{70}$ (right) bridging unit.

Chain Defect Energies: Defect calculations were performed by removing one of the unique oxygen atoms closest to the bridge according to the same naming scheme as in the cluster model. Defective $CuCe_{70}$ systems were modeled in a quartet spin state, as the Cu provides an additional unpaired electron compared to the Ce bridged system. To estimate the effect of the +U correction on the Cu atom, defect formation energies were calculated with and without an effective U_d parameter of 7 eV (see **Figure 3.46**). For system A, two more literature U values were used to estimate the effects of the magnitude of U_d. Wang *et al.* suggest a value of 4.5 eV based on fitting to experimental data.[214] Mann *et al.* calculate a value of 10.4 eV for use in metal–organic frameworks (MOFs).[215] System A shows a defect formation energy of -0.66 eV when using a U_d value of 4.5 eV and therefore exactly between the value of -1.22 eV without U correction and the

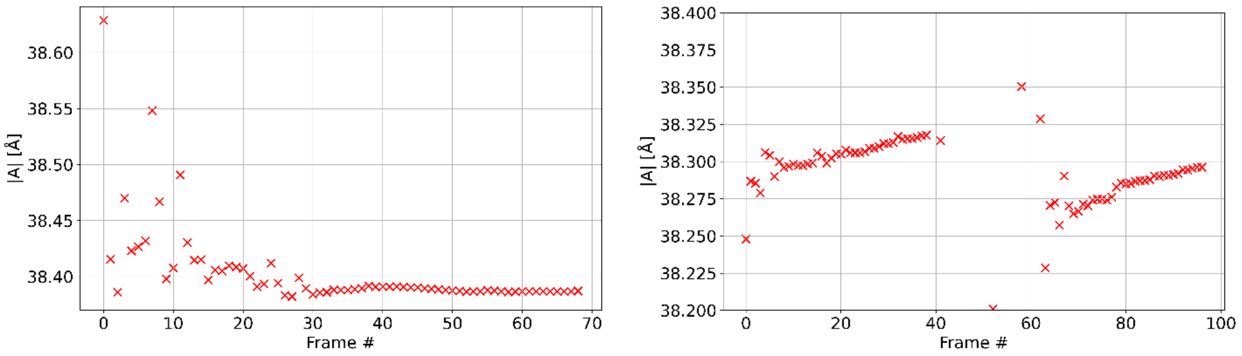

Figure 3.45 Convergence of the cell length with respect to the optimization step of the $CeCe_{70}$ chain (left) and the $CuCe_{70}$ chain (right).

value of -0.23 eV using a U_d value of 7 eV. When employing a U_d value of 10.4 eV, unphysical Mulliken charges arise during the calculations; we therefore suggest that this value is unrealistically large for the systems under investigation. As can be clearly seen, application of U_d shifts $\Delta E_{\mathrm{defect}}$ towards larger values with increasing magnitude. Based on these results we chose the U_d value of Mishra *et al.* for the discussion in the main text.[210] Values of $\Delta E_{\mathrm{defect}}$ for the $CeCe_{70}$ systems are shown and discussed in the main text.

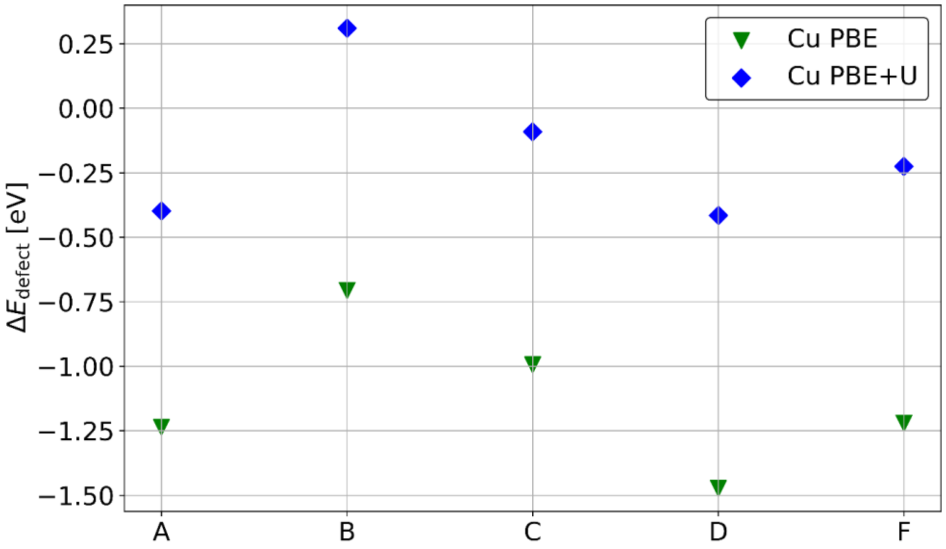

Figure 3.46 Defect formation energies of the $CuCe_{70}$ system with (blue diamonds) and without (green triangles) +U correction.

Chapter 4. Linker Competition within a Metal–Organic Framework for Topological Insights

Portions of this chapter appear in the following manuscript:

Wasson, M. C.; Lyu, J.; Islamoglu, T.; Farha, O. K. *Inorg. Chem.* **2019**, *58*, 1513-1517.

4.1 Chapter Summary

Efforts toward predictive topology within the design and synthesis of metal-organic frameworks (MOFs) have been extensively studied. Herein, we report an investigation of a linker competition for the nucleation of a Zr_6 based mixed linker MOF. By varying the relative additions of two linkers and introducing prior seeding to the system, we discern that the **scu** topology is the kinetic product of the two competing linkers. Elemental mapping analysis indicates that the competing linkers are uniformly distributed throughout the MOF. The final ratios of the linkers in the dissolved MOFs align well with the initial synthetic ratio. Through the introduction of a prior nucleation phase to seed the system, the thermodynamic **csq** product is more readily achieved. The results reported will enhance the understanding of MOF growth process. This chapter served as a training exercise in synthesizing and characterizing coordination frameworks.

4.2 Predictive Topology within Metal-Organic Frameworks

An emerging class of highly porous, crystalline materials known as metal-organic frameworks (MOFs) has attracted much interest throughout the past two decades.[33,37,216] Composed of inorganic atom(s) as the node that form coordination bonds in three dimensions to multidentate organic linkers, MOFs provide a seemingly infinite combination of unique connectivities. The inherent tunability of MOF substituents provides the ability to strategically tailor frameworks for a myriad of applications including gas storage and separations,[217–221] chemical sensing,[222,223] drug delivery,[224] and catalysis.[32,225,226]

Since first reported in 2008, the interest in Zr^{4+} based cluster MOFs has ever been increasing due to exceptionally strong Zr−O bonds to carboxylate linkers which subsequently affords highly stable and robust materials.[44] The meticulous selection of linker topicity and geometry thus far has accessed connectivities of 4, 6, 8, 10, and 12 carboxylates per Zr_6 node.[44,227–

[231] While di- and tritopic based linkers have been extensively employed to synthesize Zr-MOFs with different topologies, tetratopic linkers are far more interesting from a structural point of view because the same components can result in MOFs with different topologies which offers a great platform to study the effect of topology.[232,233] Specifically, topology diversity is prominent amongst the 8-connected Zr_6 series that form coordination bonds to tetratopic linkers.

Existence of multiple topologies in a bulk framework imparts different physical and chemical properties of the system. Consequently, the careful design and development pure-phase MOFs has received much attention.[234,235] Fundamental guidelines for provided by Matzger and co-workers enable topology prediction in Zr-based MOFs through tuning the linker geometry, yet **csq**, **scu**, and **sqc** topologies are indistinguishable following this approach.[49] Another judicious strategy for topology control was employed by our group as well as the Zhou group with the design of linkers with bulky substituents to force a conformational change and subsequent topology change in an 8-connected Zr_6 MOF.[236,237] While rational linker selection can preferentially target one topology over another, there are well-documented instances of MOFs of identical linkers and nodes that form different topologies which can synthetically be controlled.[48,236] The structural diversity of the TCPP (tetrakis(4-carboxyphenyl)porphyrin) linker in conjunction with a Zr_6 node is evident in the possible MOFs products: MOF-525, MOF-545/PCN-222, PCN-223, PCN-224, PCN-225, and NU-902.[233,238–242] Another canonical example includes Zr_6 nodes in the presence of the TBAPy (1,3,6,8-tetrakis(p-benzoate)pyrene) linker that form either microporous NU-901 or mesoporous NU-1000.[48,228,243] Effective methods to favor the phase pure growth of NU-1000 and prevent the more dense NU-901 phase include the use of more rigid modulators or highly acidic co-modulators.[48,244] Moreover, computational insights show that modifying the pyrene based ligand with bulky substituents can perturb a favorable arrangement of Zr_6 nodes for **scu** formation to ensure a clean NU-1000 **csq** framework instead.[245] Alternative strategies for pure-phase MOF synthesis have been explored such as the seed-mediated methodology developed by the Zhou group.[246] By adding a small sample of a pure-phase MOF to seed a solution of reactants, they achieved a bulk synthesis of a pure phase MOF. Identical synthetic conditions conducted in a traditional homogenous nucleation instead afforded a mixed phase product.

Topological studies have been largely fixated thus far on the synthesis of pure-phase MOFs. However, valuable insights can be extrapolated in a mixed phase MOF regarding the kinetic or thermodynamic driving topologies in a system. A fundamental comparison of two linkers that favor different topologies in direct synthetic competition with one another has been overlooked. Aforementioned, our group has recently shown the introduction of two sterically demanding bromo groups can force a tetratopic organic linker to undergo conformational change to favor a **csq** topology (NU-1008) while its nonfunctionalized analogue yields a **scu** topology (NU-903).[231,237] With this system in mind, we set out to directly compare the competition between the linkers to become the leading seeding agent in a MOF and determine the overall system topology. In this work, we investigate the thermodynamic and kinetic products of the competing linkers that prefer csq or scu topologies in a mixed linker system.

4.3 Simultaneous Linker Nucleation Studies of a Zr_6O_8 Metal Oxo Cluster

To first probe the degree of linker competition, we explored the simultaneous nucleation of a Zr_6 node by two tetratopic linkers prior to solvothermal treatment. As we have previously shown, a Zr_6 node and **L1** (1,2,4,5-tetrakis(4-carboxyphenyl)benzene (TCPB)) linker can form the **scu** topology NU-903 while **L2**, a dibromo substituted TCPB, favors the **csq** topology NU-1008.[231,237] The judicious introduction of bulky substituents ortho to one another increases the dihedral angle from 69.8° in **L1** to 77.7° in **L2**. As the dihedral angle expands, the symmetry of

L2 is lowered to C_{2v} as two pairs of phenyl arms rotate toward each other and favors the crystallization of a **csq** topology framework over **scu** (**Figure 4.1**).

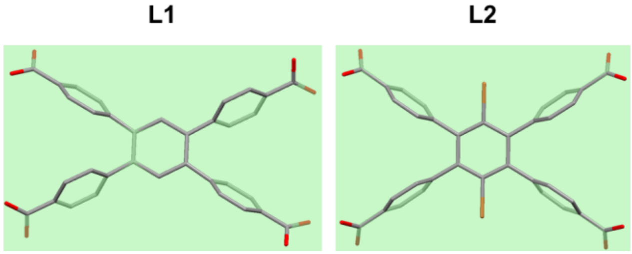

Figure 4.1 Conformations of the linkers in **scu** (**L1**) and **csq** (**L2**) topology MOFs.

With the knowledge of how linker symmetry can dictate bulk topology, different ratios of the C_{2h} L1 linker relative to C_{2v} **L2** were simultaneously introduced into a Zr_6 node solution to observe anticipated phase changes (**Figure 4.2**). Upon the simultaneous addition of both linkers, the solutions were heated overnight. PXRD was used to provide initial topology insight into the in-situ competition.

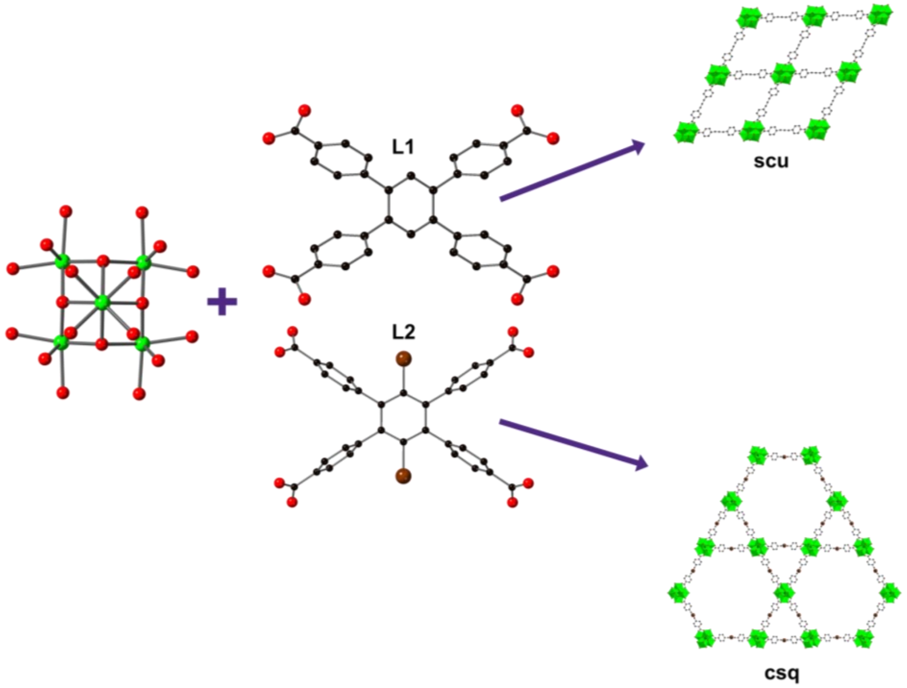

Figure 4.2 Schematic representation of **scu** and **csq** topology MOFs synthesized with **L1** and **L2**, respectively. Green: Zirconium, red: oxygen, black: carbons, and burgundy: bromine. Hydrogen atoms omitted for clarity.

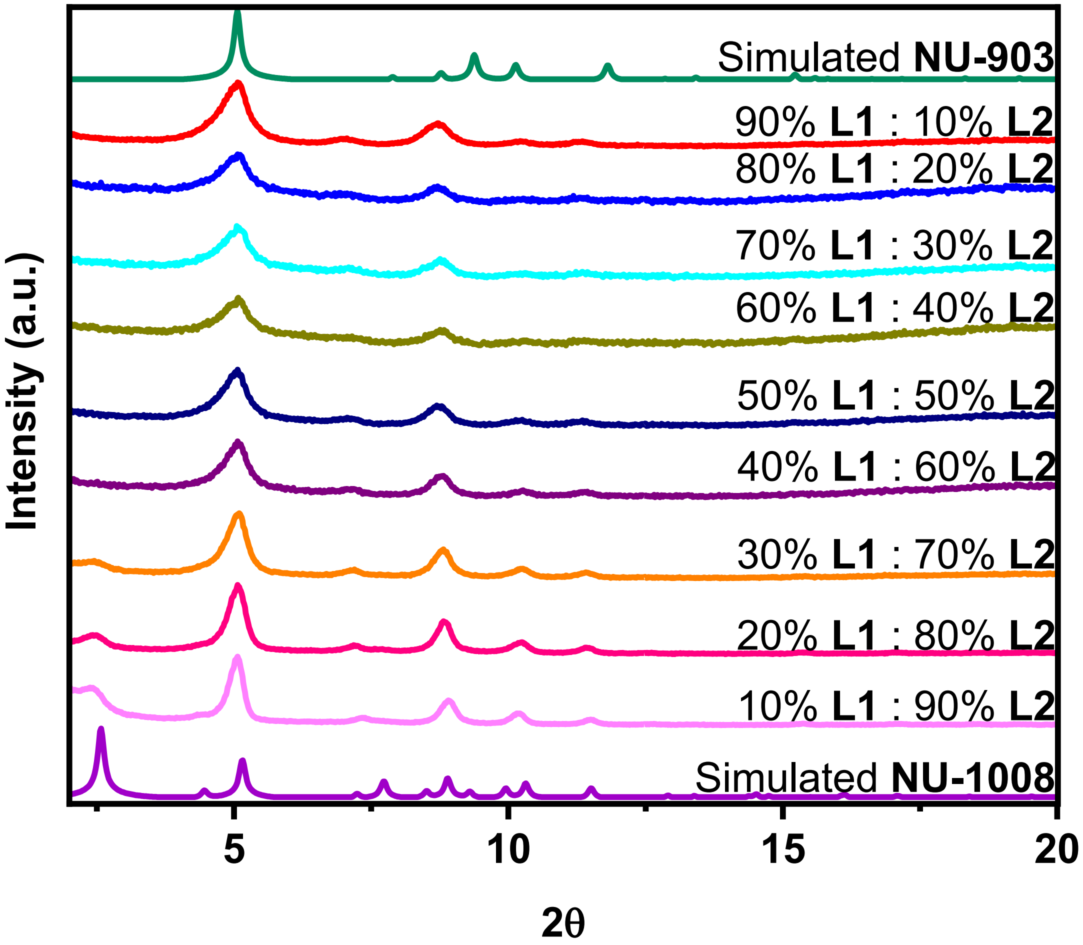

Figure 4.3 PXRD patterns of MOFs synthesized under simultaneous addition of L1 and L2 linkers in variable amounts as indicated.

In **Figure 4.3**, the 2.5 2θ peak, indicative of the mesopore in a csq topology, is absent until 70% **L2**: 30% **L1**, rendering a pure **scu** pattern in all other conditions. From this observation, we inferred that the **L1** linker can outcompete **L2** to provide the initial seeding of the MOF to yield a **scu** topology as the kinetic product. To better understand the porosity of the competition products, nitrogen isotherm measurements of selected ratios were conducted. Isotherm measurements confirm that the presence of mesopores is only observed when **L2** is in excess in the system with a characteristic mesopore step between 0.2 to 0.25 P/P_0 in **Figure 4.4C**, which is also evident from pore size distribution (**Figure 4.4F**, **Figure 4.13**). Upon equimolar additions of **L1** and **L2**, the observed adsorption isotherm (**Figure 4.4B**) exhibits negligible N_2 uptake in the mesopore region (**Figure 4.4E**) to support a microporous material, as with **L1** in excess (**Figures 4.4A** and **4.4D**). Thus, the **scu** topology outcompetes the **csq** topology during the initial MOF seeding process to form the kinetically favored product.

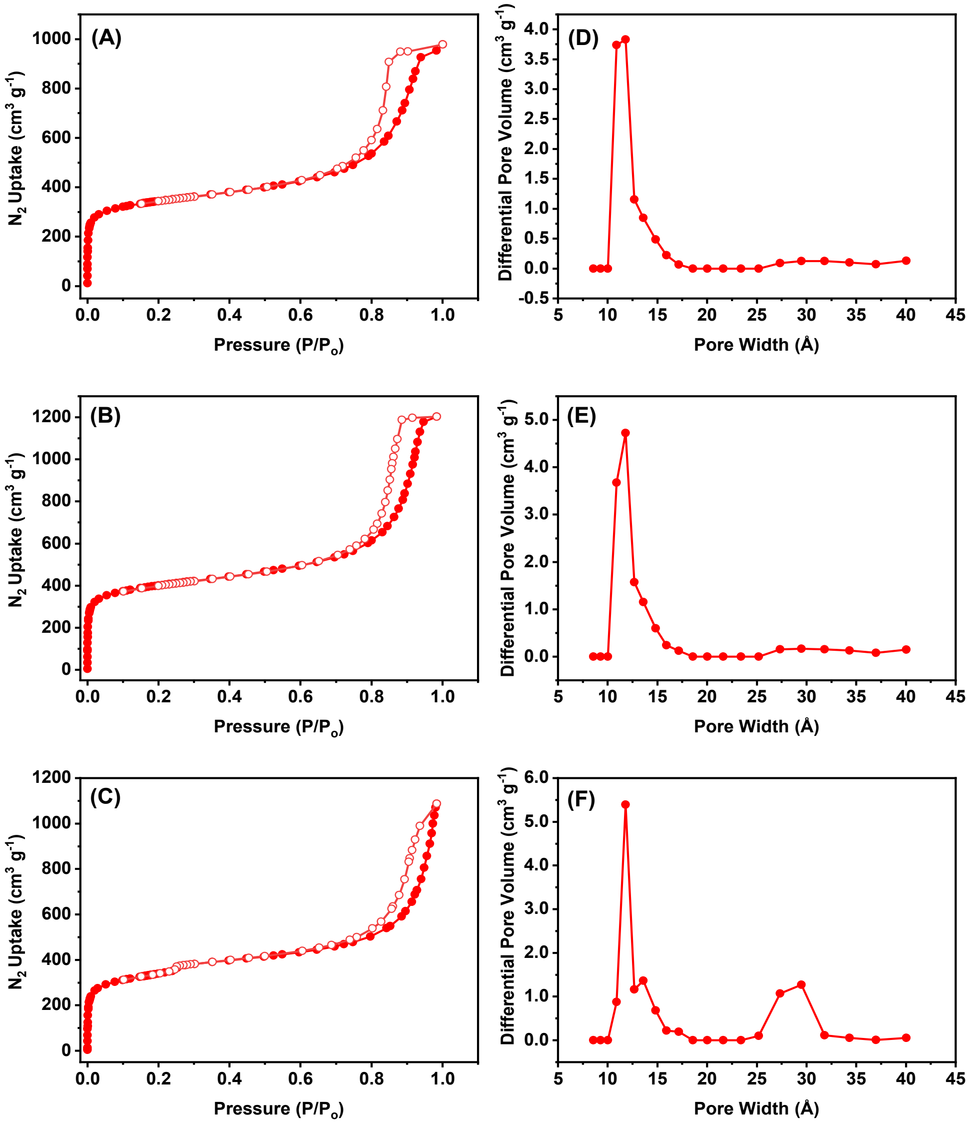

Figure 4.4 Nitrogen isotherms and pore size distributions of 70% **L1**: 30% **L2** (A/D); 50% **L1**: 50% **L2** (B/E); and 30% **L1**: 70% L2 (C/F).

Upon extensive characterization of material porosity, structural and elemental analyses are critical to discern the linker composition within the formed MOFs. ^{1}H NMR analysis of the dissolved MOFs show good agreement between initial and final synthetic ratios confirming the comparable pK_a of both linkers (**Table 4.1**). STEM-EDX indicates a uniform distribution of Br across the particle in the equimolar **L1**:**L2** system (**Figure 4.5**). While we cannot discern from the STEM images whether the sample is an aggregation of many small particles or one crystalline MOF particle, prior PXRD studies of this sample (**Figure 4.3**) indicate that only the **scu** topology is present. Thus, we conclude that both linkers are distributed throughout a **scu**

Table 4.1 Ratios of linkers according to (left) initial synthetic ratio and (right) integrations from ^{1}H NMR spectra of dissolved MOFs.

Initial **L1**: **L2** *in-situ*	^{1}H NMR Determined **L1**: **L2**
10% **L1**: 90% **L2**	17% **L1**: 83% **L2**
20% **L1**: 80% **L2**	27% **L1**: 73% **L2**
30% **L1**: 70% **L2**	35% **L1**: 65% **L2**
40% **L1**: 60% **L2**	40% **L1**: 60% **L2**
50% **L1**: 50% **L2**	51% **L1**: 49% **L2**
60% **L1**: 40% **L2**	54% **L1**: 46% **L2**
70% **L1**: 30% **L2**	75% **L1**: 25% **L2**
80% **L1**: 20% **L2**	86% **L1**: 14% **L2**
90% **L1**: 10% **L2**	96% **L1**: 4% **L2**

90% **L1**: 10% **L2** 96% **L1**: 4% **L2**

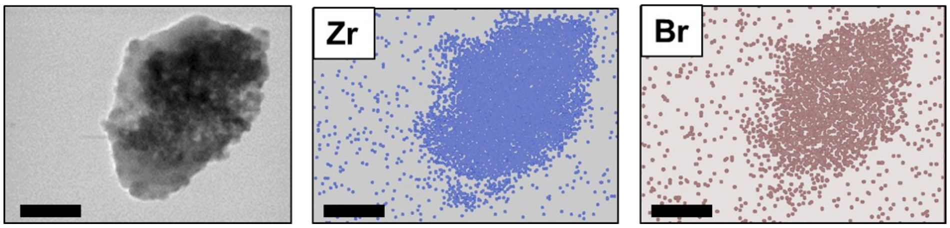

Figure 4.5 STEM-EDX images of MOF particle from 50% **L1**: 50% **L2** synthesis. Scale bar represents 250 nm.

system. Moreover, the successful introduction of a bulky functionality uniformly to the MOF while maintaining a **scu** topology, rather than undergoing a conformational change to the **csq** topology, can be of interest for future MOF design. In addition to the imaging insights from TEM, we explored SEM imaging to further characterize particle morphology. Distinct spherical particles were observed until an excess of **L2** (70%) was added to the system. An aggregation of small particles, ~50nm, were observed which made imaging unreliable (**Figures 4.31 and 4.32**) to detect the presence of rod-like particles that indicate **csq** topology.

4.4 Effect of Stepwise Linker Nucleation on a Zr_6O_8 Cluster and the MOF Topology

With the insights gained from a simultaneous nucleation system, we were motivated to explore the effects of seeding on linker competition between **L1** and **L2**. Therefore, we sought out to first determine if **L2** nucleation of the system prior to the addition of **L1** would now favor a **csq** topology product over **scu**. **L2** was first added to the system and was heated for 30 minutes at 100 °C. After this brief nucleation period, a cloudy solution indicating MOF precipitation was observed, before **L1** was added before 100 °C treatment for 16 hours. In **Figure 4.6A**, the overlapping **csq** and **scu** patterns unfortunately prevent greater insight into the dominant topology with **L2** prior nucleation. Nonetheless, we conclude that **L2** can successfully seed MOF growth to give a **csq** topology product in the presence of equimolar and even excess **L1**. These findings are in stark contrast to our earlier simultaneous nucleation studies in which we observed only **scu** topology until at least 70% **L2** was added.

Motivated to explore prior nucleation studies with **L1** now seeding the system, we predicted the facile formation of a **scu** topology MOF due to our prior observations that it is the kinetic product in this competing system. However, in **Figure 4.6B**, the 2.5 2θ peak indicative of the **csq** topology is clearly present in many of the samples. To rationalize these findings, we utilized ^{1}H NMR to probe the concentration of **L1** in solution after 30 minutes of nucleation upon observing extensive precipitate. Negligible **L1** remains in solution, indicating that it fully forms a MOF in solution within 30 minutes (**Figure 4.28**). Thus, **L2** can form a **csq** topology MOF with the remaining excess Zr_6 in solution because it acts as a pseudo-singular reagent upon its addition. Additionally, seeding within a heterogeneous system by either a substrate or pre-formed nuclei have been well-studied to indicate that the free energy of nucleation is lowered.[247,248] By circumventing the initial nucleation phase within our study's context, MOF formation can occur at a higher rate under less intensive thermodynamic requirements, in accordance to previous observations by Zhou and co-workers.[246]

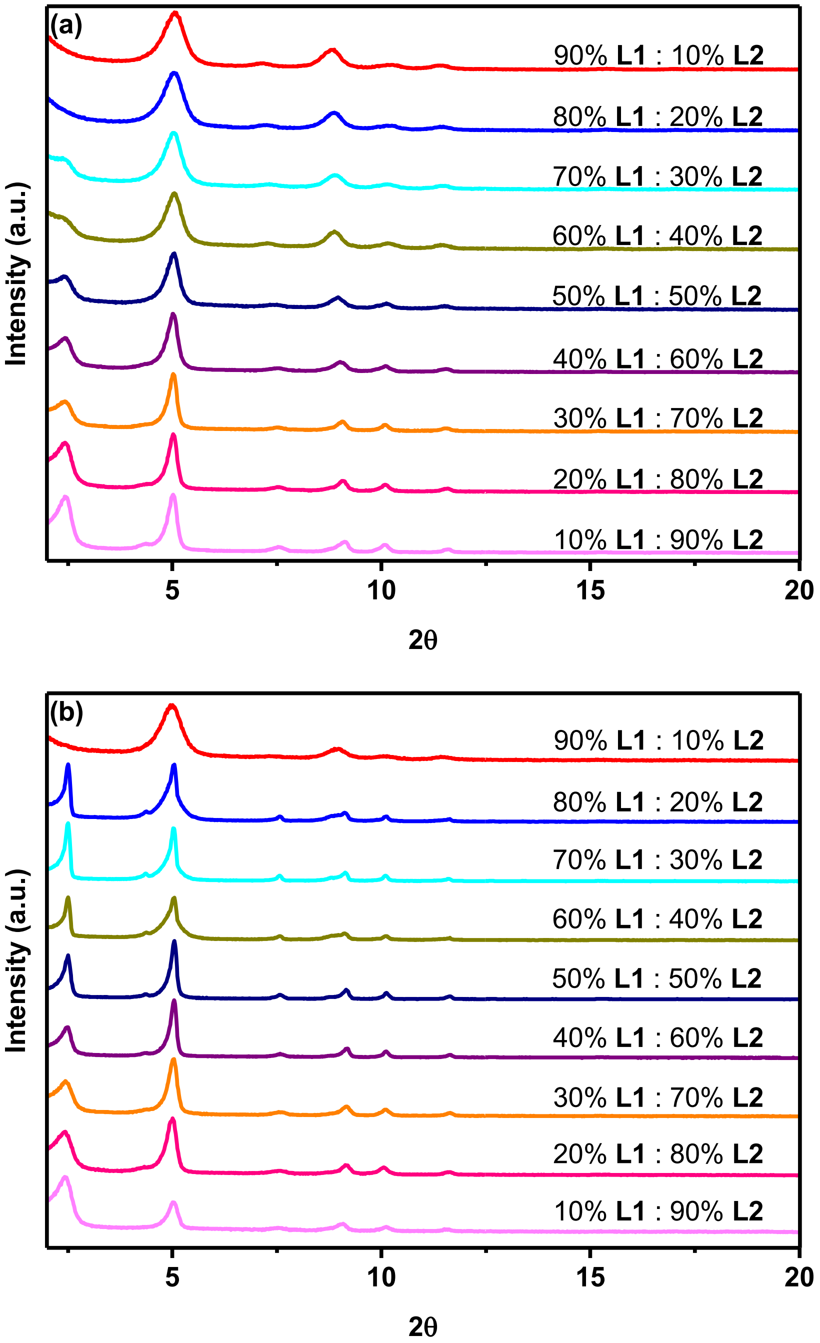

Figure 4.6 (a) PXRD patterns of MOFs synthesized with prior nucleation by **L2** (b) PXRD patterns of MOFs synthesized with prior nucleation by **L1**.

4.5 Conclusions

This study probed the competition of two linkers, **L1** and **L2**, in varying ratios during the simultaneous nucleation of a Zr_6 node to compare the kinetic and thermodynamic products between the **scu** and **csq** topologies that each linker respectively favors. Under equimolar conditions of **L1** and **L2** without prior seeding of the system, a clean **scu** topology MOF was observed and characterized, indicating that the **scu** determines the MOF growth process as the kinetic product. Elemental mapping analyses indicated an even distribution of both ligands throughout the system while ^{1}H NMR confirmed the ratios of the linkers within the dissolved MOF is in good agreement with the initial synthetic ratios. Through the strategic use of prior seeding of the system, we observed the thermodynamic **csq** product. While this inquiry examined the in-situ linker competition, careful synthetic tuning is necessary to afford these investigated systems in pure phase. This study provides some mechanistic insight into topology competition within a mixed phase MOF that can be used for future MOF design.

4.6 Additional Information

4.6.1 Materials

All chemicals and solvents were obtained from commercial suppliers and used without further purification. Zirconium(IV) oxynitrate hydrate (99%), formic acid (≥96%), 1,2,4,5-tetrakis(4-carboxyphenyl)benzene (TCPB) (≥98%), p-tolylmagnesium bromide solution (1.0 M in DMF), hexabromobenzene (98%), 1,2,4,5-tetrabromobenzene (97%), bromine (reagent grade), and carbon tetrachloride (99.9%), sulfuric acid-d_2 solution (96-98 wt. % in D_2O, 99.5 atom % D), and dimethyl sulfoxide-d_6 (99.9 atom % D) were purchased from Sigma-Aldrich. *N,N*-dimethylformamide (DMF) (99.9%), acetone (99.8%), hydrochloric acid (36.5−38%), nitric acid (67−70%), chloroform (99.8%), and hexane (98.5%) were purchased from Fisher Chemical.

Deionized water was used as the water source.

4.6.2 Linker Synthesis and Characterization

1,2,4,5-tetrakis(4-carboxyphenyl)benzene (**L1**) and 1,2,4,5-tetrakis(4-carboxyphenyl)-3,6-dibromobenzene (**L2**) were synthesized according to literature procedure.

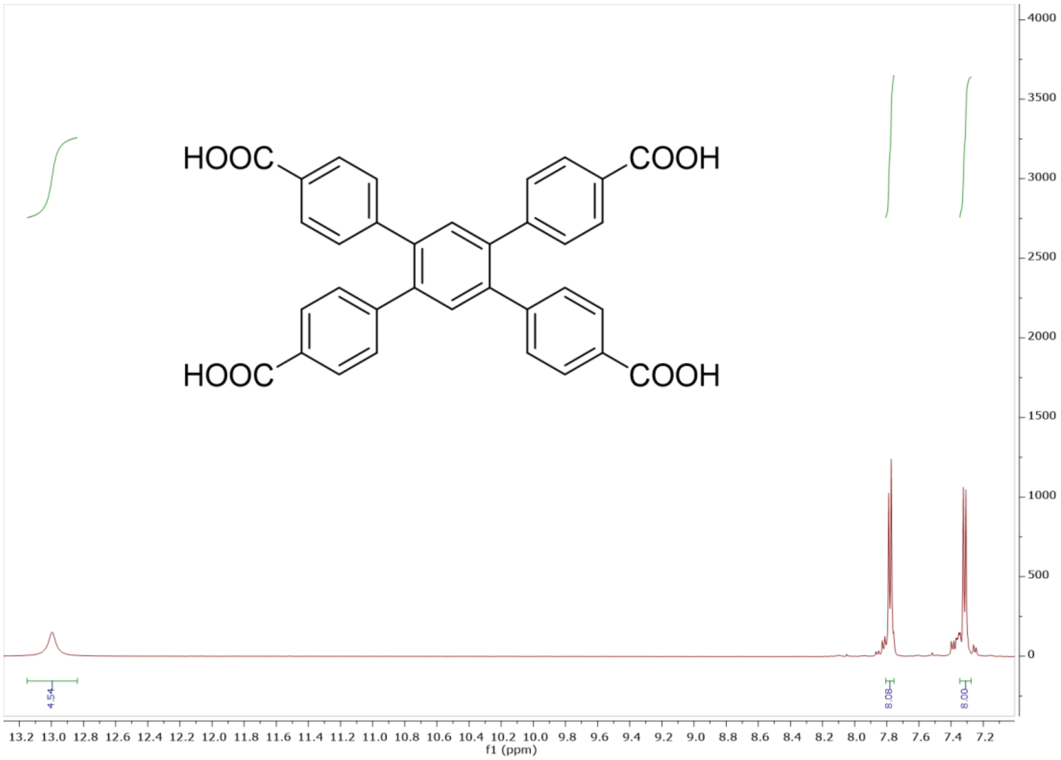

Figure 4.7 500 MHz ^{1}H spectrum of **L1** DMSO-d_6.

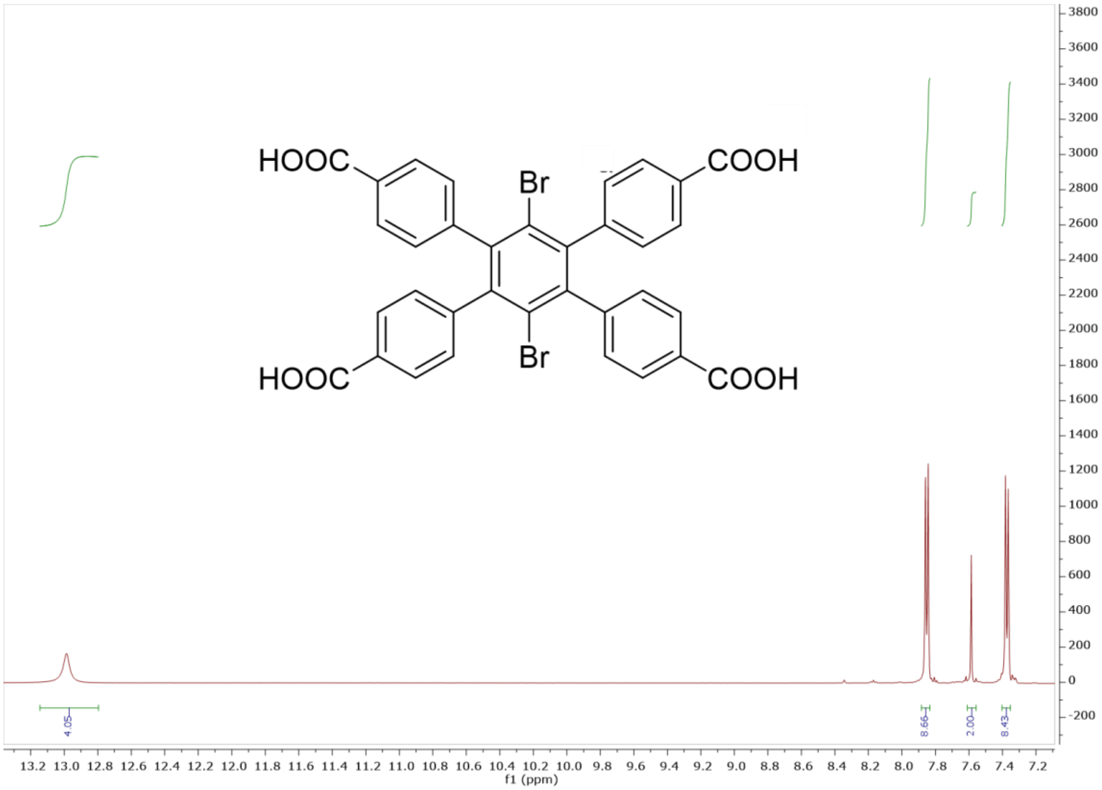

Figure 4.8 500 MHz ^{1}H spectrum of **L1** DMSO-d_6.

4.6.3 MOF Synthesis Protocols

*Competition Reaction for Simultaneous Nucleation of **L1** and **L2***: Zirconium oxynitrate hydrate (79.7 mg, 0.345 mmol) was placed in a 2-dram vial. 1 mL of *N,N*- dimethylformamide was added and the solution was sonicated until solubility was achieved. 1 mL of formic acid was added to the vial, which turned clear shortly thereafter. The Zr_6 node solution was sonicated if any remaining particles were not yet soluble. The vial was placed in an 80 °C oven for 1 hour. A **L1** solution was prepared by adding 14.9 mg (0.0267 mmol) of **L1** to 1 mL of *N,N*-dimethylformamide and was sonicated until soluble. A **L2** solution was prepared by adding 19.1 mg (0.0267 mmol) of **L2** to 1 mL of *N,N*- dimethylformamide and sonicated to ensure solubility. After the Zr_6 node solution was removed from the oven and cooled to room temperature, 200 µL aliquots of the solution were placed in nine separate 0.5 dram vials. The following amounts of **L1** and **L2** (in μL) were added to each of the nine vials: 20, 180; 40, 160; 60, 140; 80, 120; 100, 100; 120, 80; 140, 60; 160, 40; 180, 20. The vials were then placed in a 100 °C oven for 16 hours. Solutions were removed from the oven and cooled to room temperature. The mixtures were placed in 1.5 mL centrifuge tubes and centrifuged for five minutes to remove the supernatant. Then, the resultant white powder was washed with *N,N*-dimethylformamide (1.5 mL×2) and acetone (1.5 mL×2). The material was then dried in a vacuum oven at 80 °C for 1 hour.

To obtain adequate material for N_2 isotherm measurement of a specific ratio, the above procedure was repeated using the specific **L1**: **L2** ratio of interest on the same scale but repeated 10 times. The reacted solutions were then combined into a 15 mL centrifuge tube and washed with DMF (5 mL x 3) and acetone (5 mL x 3). The material soaked in acetone overnight, followed by washing with acetone (5 mL x 3). The material was then dried in the vacuum oven for 1 hour at 80 °C. The material was then activated by heating at 120 ˚C for overnight under high vacuum on a Micromeritics Smart Vacprep.

*Competition Reaction for Prior Seeding of **L1***: Zirconium oxynitrate hydrate (79.7 mg, 0.345 mmol) was placed in a 2-dram vial. 1 mL of *N,N*- dimethylformamide was added and the solution was sonicated until solubility was achieved. 1 mL of formic acid was added to the vial, which turned clear shortly thereafter. The Zr_6 node solution was sonicated if any remaining particles were not yet soluble. The vial was placed in an 80 °C oven for 1 hour. A **L1** solution was prepared by adding 14.9 mg (0.0267 mmol) of **L1** to 1 mL of *N,N*- dimethylformamide and was sonicated until soluble. After the Zr_6 node solution was removed from the oven and cooled to room temperature, 200 μL aliquots of the solution were placed in nine separate 0.5 dram vials. The following amounts of **L1** (in μL) were added to each of the nine vials: 20, 40, 60, 80, 100, 120, 140, 160, and 180. The vials were then placed in a 100 °C oven for 30 minutes. The vials were removed from the oven and cooled to room temperature. A **L2** solution was prepared by adding 19.1 mg (0.0267 mmol) of **L2** to 1 mL of *N,N*- dimethylformamide and sonicated to ensure solubility. The **L1** nucleated systems were removed from the oven and cooled to room temperature. Then, aliquots of **L2** (in μL) were added in the following order to the vials containing the above specific amounts of **L1** in solution: 180, 160, 140, 120, 100, 80, 60, 40, and 20. The vials were then placed in a 100 °C oven for 16 hours to react. Upon reaction completion, the vials were removed from the oven and cooled to room temperature. The mixtures were placed in 1.5 mL centrifuge tubes and centrifuged for five minutes to remove the supernatant. Then, the resultant white powder was washed with *N,N*-dimethylformamide (1.5 mL×2) and acetone (1.5 mL×2). The material was then dried in a vacuum oven at 80 °C for 1 hour.

To obtain adequate material for N_2 isotherm measurement of a specific ratio, the above procedure was repeated using the specific **L1**: **L2** ratio of interest on the same scale but repeated 10 times. The reacted solutions were then combined into a 15 mL centrifuge tube and washed with DMF (5 mL x 3) and acetone (5 mL x 3). The material soaked in acetone overnight, followed by washing with acetone (5 mL x 3). The material was then dried in the vacuum oven for 1 hour at 80 °C. The material was then activated by heating at 120 ˚C for overnight under high vacuum on a Micromeritics Smart Vacprep.

*Competition Reaction for Prior Seeding of **L2***: Zirconium oxynitrate hydrate (79.7 mg, 0.345 mmol) was placed in a 2-dram vial. 1 mL of *N,N*- dimethylformamide was added and the solution was sonicated until solubility was achieved. 1 mL of formic acid was added to the vial, which turned clear shortly thereafter. The Zr_6 node solution was sonicated if any remaining particles were not yet soluble. The vial was placed in an 80 °C oven for 1 hour. A **L2** solution was prepared by adding 19.1 mg (0.0267 mmol) of **L2** to 1 mL of *N,N*- dimethylformamide and was sonicated until soluble. After the Zr_6 node solution was removed from the oven and cooled to room temperature, 200 µL aliquots of the solution were placed in nine separate 0.5 dram vials. The following amounts of **L2** (in µL) were added to each of the nine vials: 20, 40, 60, 80, 100, 120, 140, 160, and 180. The vials were then placed in a 100 °C oven for 30 minutes. The vials were removed from the oven and cooled to room temperature. A **L1** solution was prepared by adding 19.1 mg (0.0267 mmol) of **L1** to 1 mL of *N,N*- dimethylformamide and sonicated to ensure solubility. The **L2** nucleated systems were removed from the oven and cooled to room temperature. Then, aliquots of **L1** (in µL) were added in the following order to the vials containing the above specific amounts of **L2** in solution: 180, 160, 140, 120, 100, 80, 60, 40, and 20. The vials were then placed in a 100 °C oven for 16 hours to react. Upon reaction completion, the vials were removed from the oven and cooled to room temperature. The mixtures were placed in 1.5 mL centrifuge tubes and centrifuged for five minutes to remove the supernatant. Then, the resultant white powder was washed with *N,N*-dimethylformamide (1.5 mL×2) and acetone (1.5 mL×2). The material was then dried in a vacuum oven at 80 °C for 1 hour.

To obtain adequate material for N_2 isotherm measurement of a specific ratio, the above procedure was repeated using the specific **L1**: **L2** ratio of interest on the same scale but repeated 10 times. The reacted solutions were then combined into a 15 mL centrifuge tube and washed with DMF (5 mL x 3) and acetone (5 mL x 3). The material soaked in acetone overnight, followed by washing with acetone (5 mL x 3). The material was then dried in the vacuum oven for 1 hour at 80 °C. The material was then activated by heating at 120 ˚C for overnight under high vacuum on a Micromeritics Smart Vacprep.

NU-903 and NU-1008 Syntheses: The pure phase synthesis of NU-903 and NU-1008 were preformed following published procedure.

4.6.4 Methods for Material Characterization

Powder X-ray Diffraction Analysis: Powder X-ray diffraction (PXRD) patterns of the samples were measured by a STOE-STADI MP powder diffractometer operating at 40 kV voltage and 40 mA current with Cu-Kα1 X-ray radiation ($\lambda = 0.154056$ nm) in transmission geometry.

N_2 Sorption Isotherm Measurements: N_2 adsorption and desorption isotherms on activated materials were measured on a Micromeritics Tristar (Micromeritics, Norcross, GA) instrument at 77 K. Around 20 mg of sample was used in each measurement and the specific surface areas were determined using the Brunauer−Emmett−Teller model from the N_2 sorption data in the region $P/P_0 = 0.005–0.05$. Pore size distributions were obtained using DFT calculations using a carbon slit-pore model with a N_2 kernel.

^1H Nuclear Magnetic Resonance Spectroscopy: MOF samples (1 mg) were digested with 8 drops of D_2SO_4. After sonication for 20 min, 600 μL of DMSO-d_6 was added into the mixture. Proton NMR spectra were collected on a Bruker Avance III 500 MHz system equipped with DCH CryoProbe and automated with a BACS-60 autosampler.

Transmission Electron Imaging: Transmission electron microscopy (TEM) images were collected at Northwestern University’s EPIC /NUANCE facility using a Hitachi HD2300 STEM using a standard copper mesh sample holder at 200 kV.

Scanning Electron Microscope Imaging: Prior to observation, the samples were coated with OsO_4 (~9 nm) in a Denton Desk III TSC Sputter Coater. Scanning electron microscopy (SEM) images were acquired from a Hitachi SU8030 scanning electron microscope.

4.6.5 N_2 Sorption Experiments

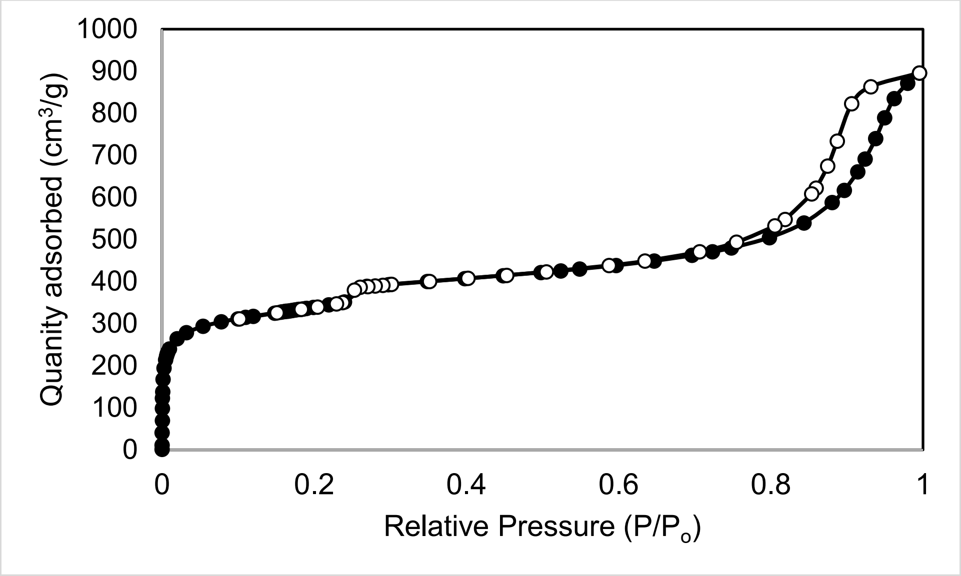

Figure 4.9 N_2 Isotherm of 30% **L2** prior nucleation followed by 70% **L1**. Reported BET surface area of 1245 m^2/g

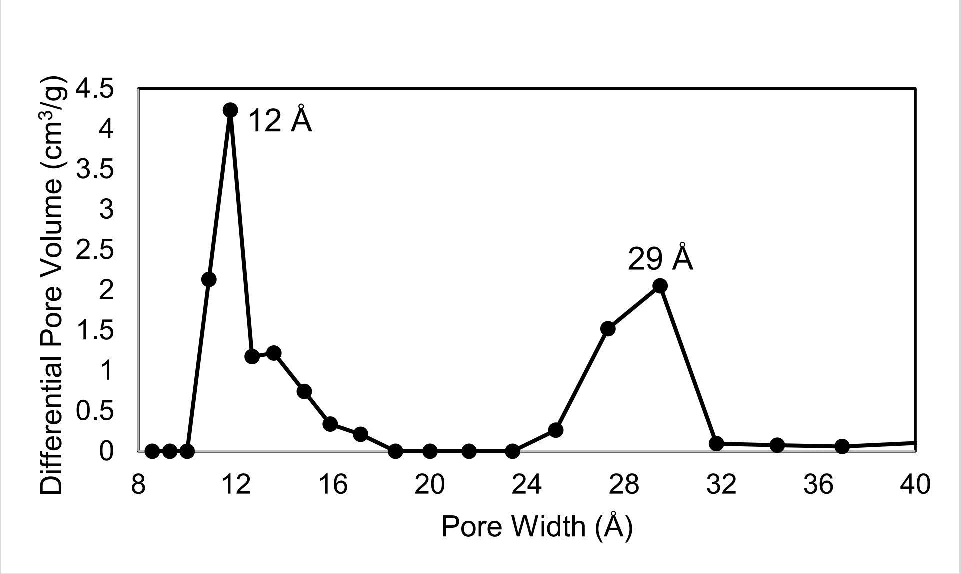

Figure 4.10 Pore Size Distribution of 30% **L2** prior nucleation followed by 70% **L1.**

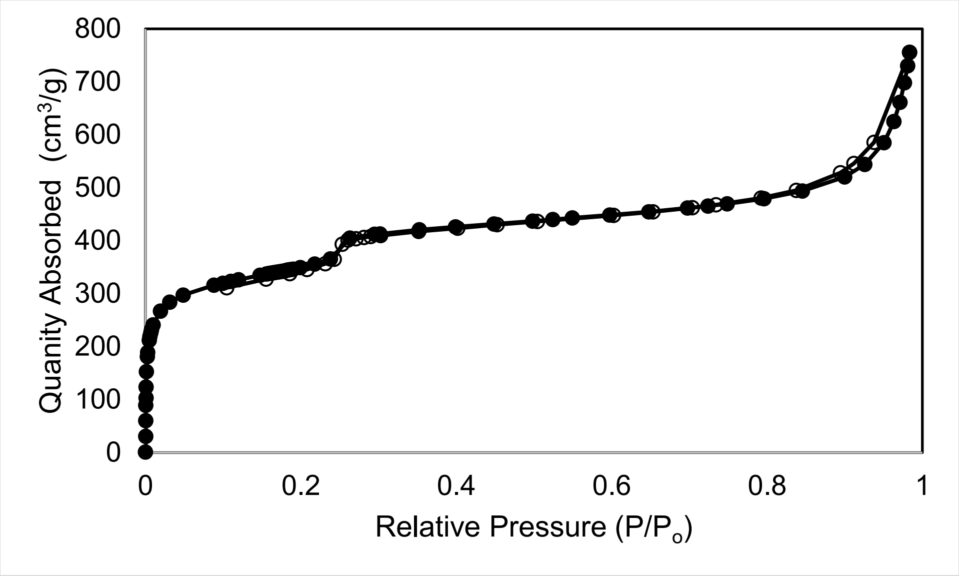

Figure 4.11 N_2 Isotherm of 30% **L1** prior nucleation followed by 70% **L2**. Reported BET surface area of 1280 m^2/g

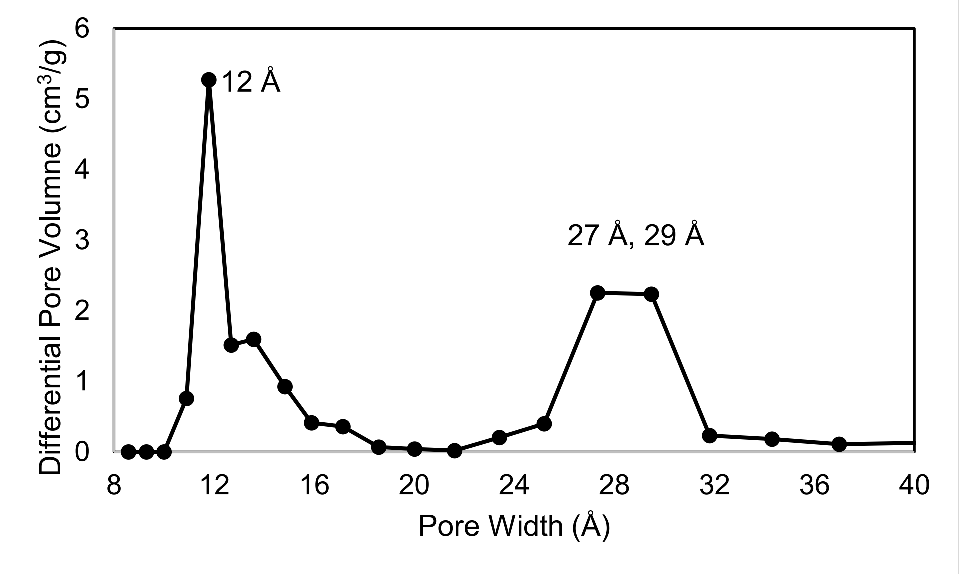

Figure 4.12 Pore Size Distribution of 30% **L1** prior nucleation followed by 70% **L2.**

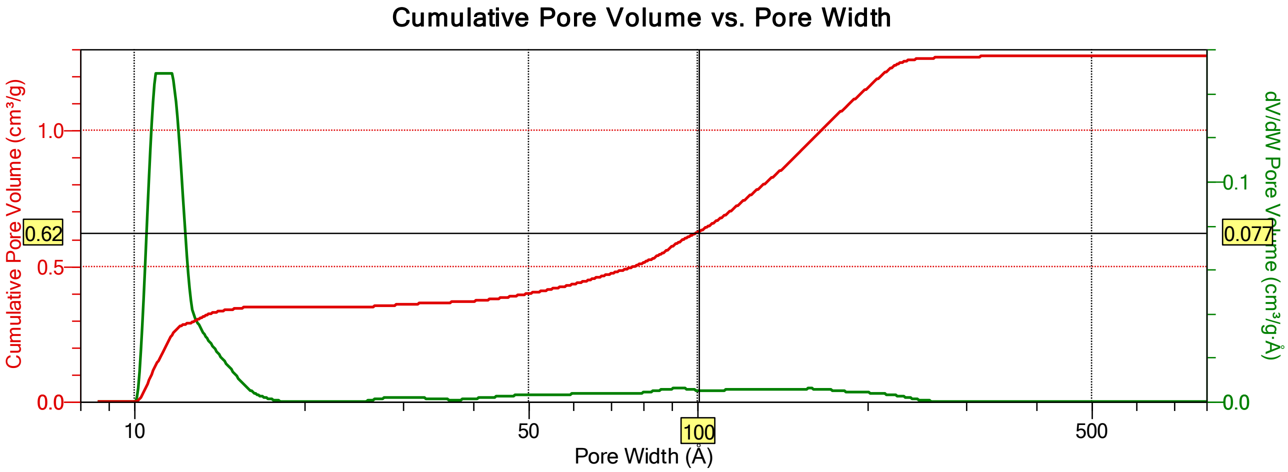

Figure 4.13: Cumulative pore volume and differential pore volume vs. pore width for simultaneous nucleation of 70% **L1**: 30% **L2**.

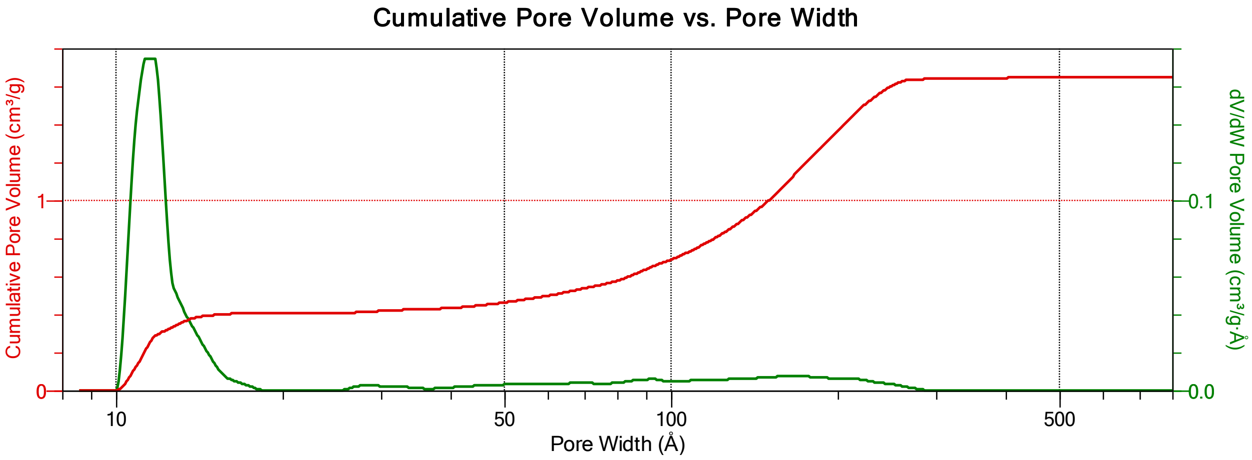

Figure 4.14 Cumulative pore volume and differential pore volume vs. pore width for simultaneous nucleation of 50% **L1**: 50% **L2**.

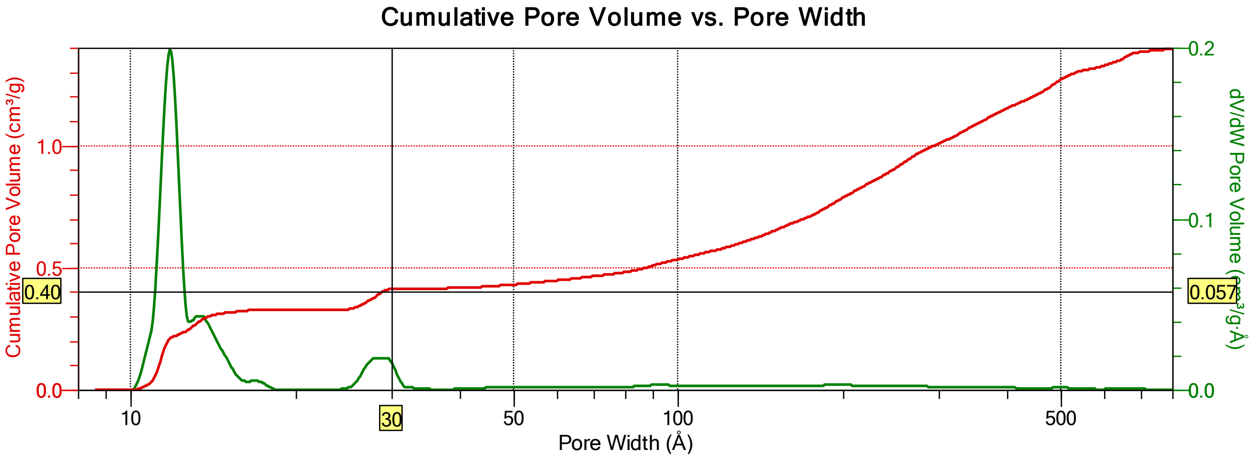

Figure 4.15 Cumulative pore volume and differential pore volume vs. pore width for simultaneous nucleation of 30% **L1**: 70% **L2**.

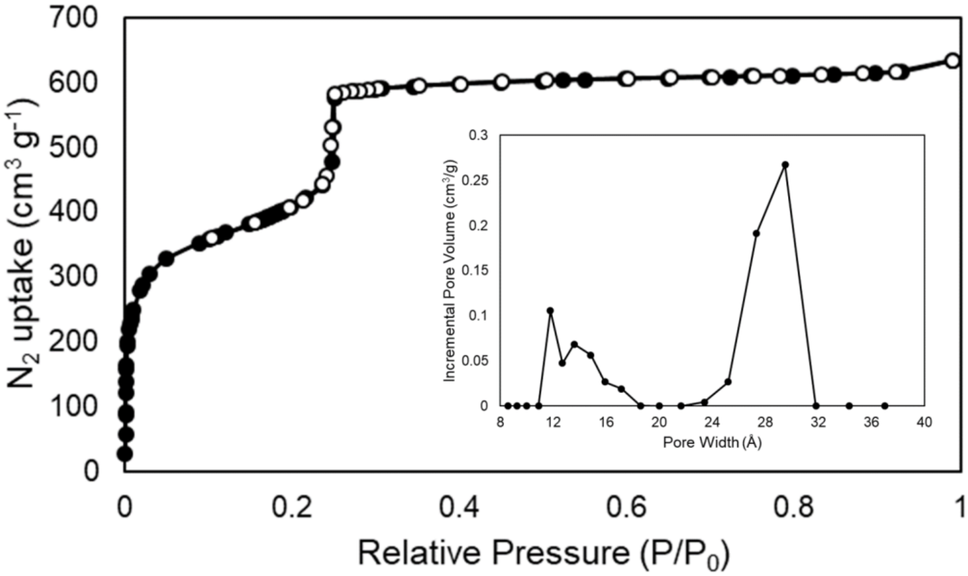

Figure 4.16 Isotherm and pore size distribution (inset) of NU-1008 with a BET surface area of 1420 m^2/g.

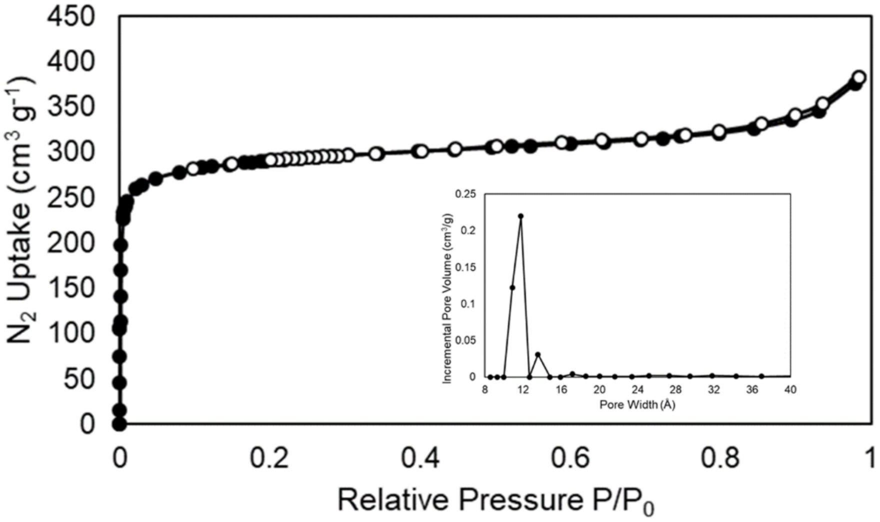

Figure 4.17 Isotherm and pore size distribution (inset) of NU-903 with a BET surface area of 1140 m^2/g

4.6.6 ^{1}H NMR Spectra

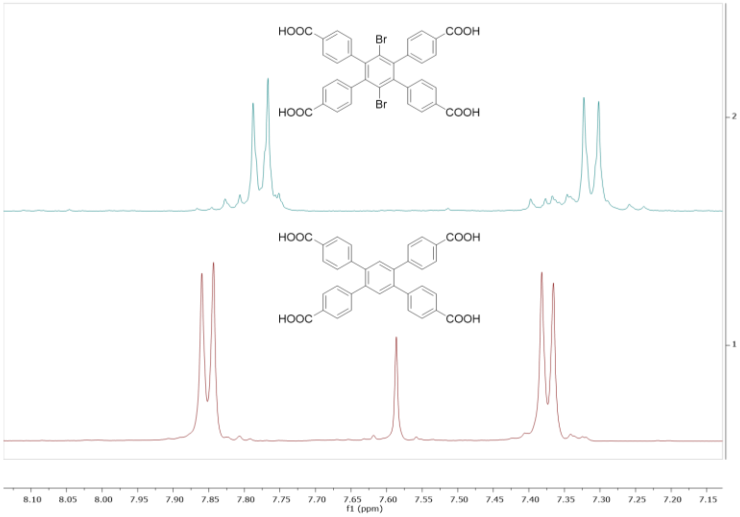

Figure 4.18 Stacked 500 MHz ^{1}H spectra of **L1** (bottom) and **L2** (top) in DMSO-d$_6$.

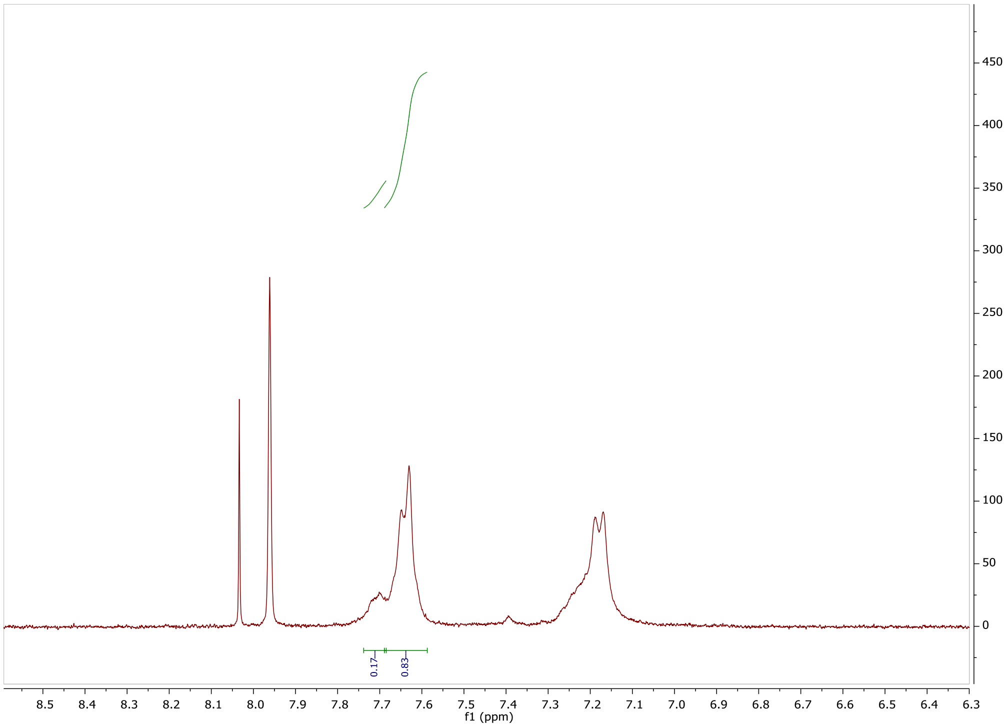

Figure 4.19 10% **L1**: 90% **L2** simultaneous nucleation MOF digested in D_2SO_4 / DMSO-d_6

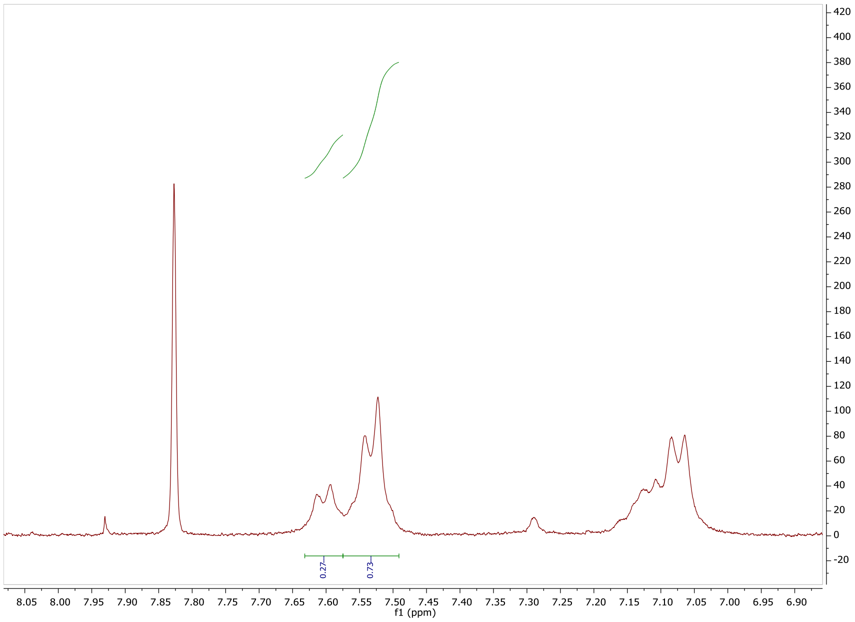

Figure 4.20 20% **L1**: 80% **L2** simultaneous nucleation MOF digested in D_2SO_4 / DMSO-d_6

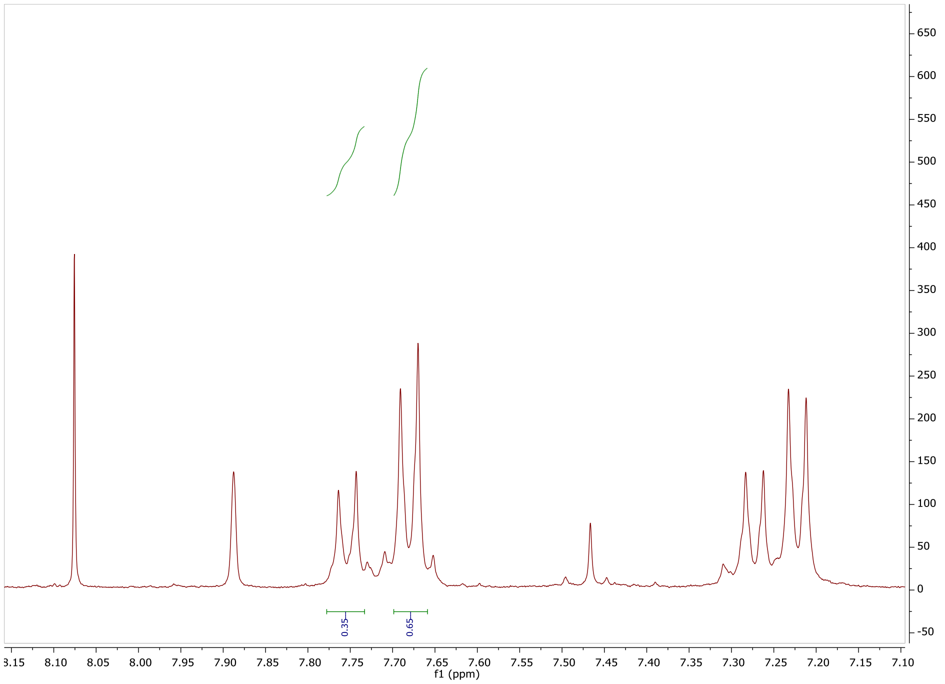

Figure 4.21 30% **L1** : 70% **L2** simultaneous nucleation MOF digested in D_2SO_4 / DMSO-d_6

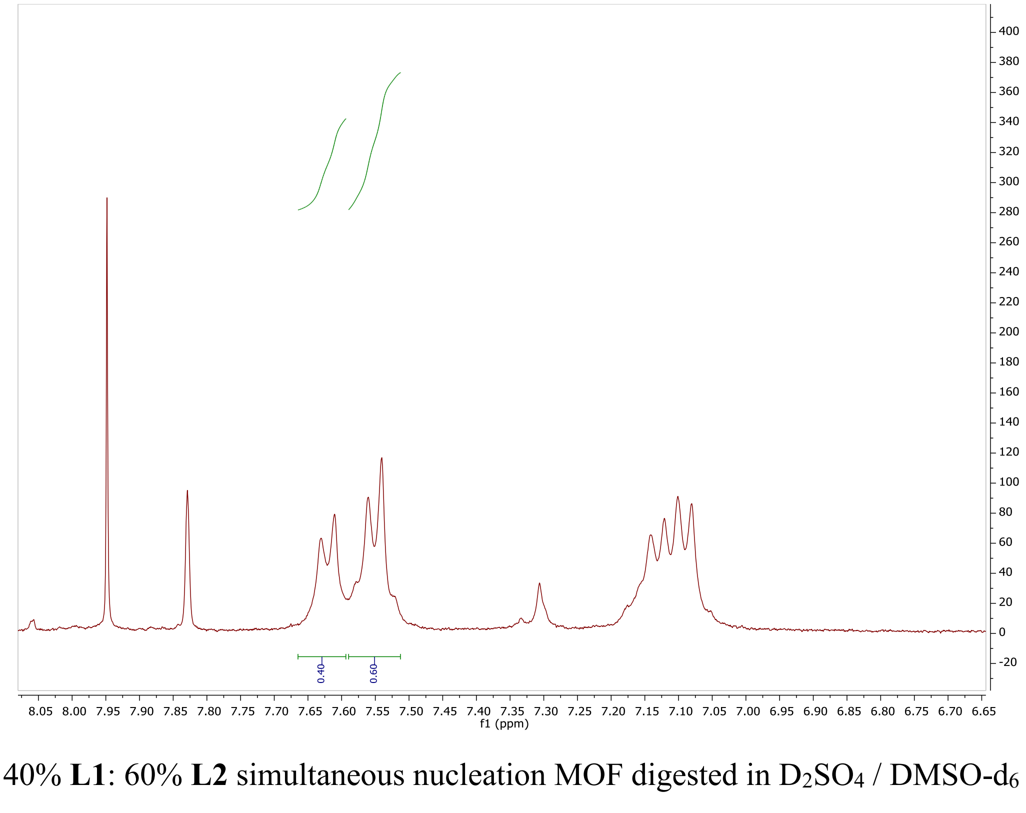

Figure 4.22 40% **L1**: 60% **L2** simultaneous nucleation MOF digested in D_2SO_4 / DMSO-d_6

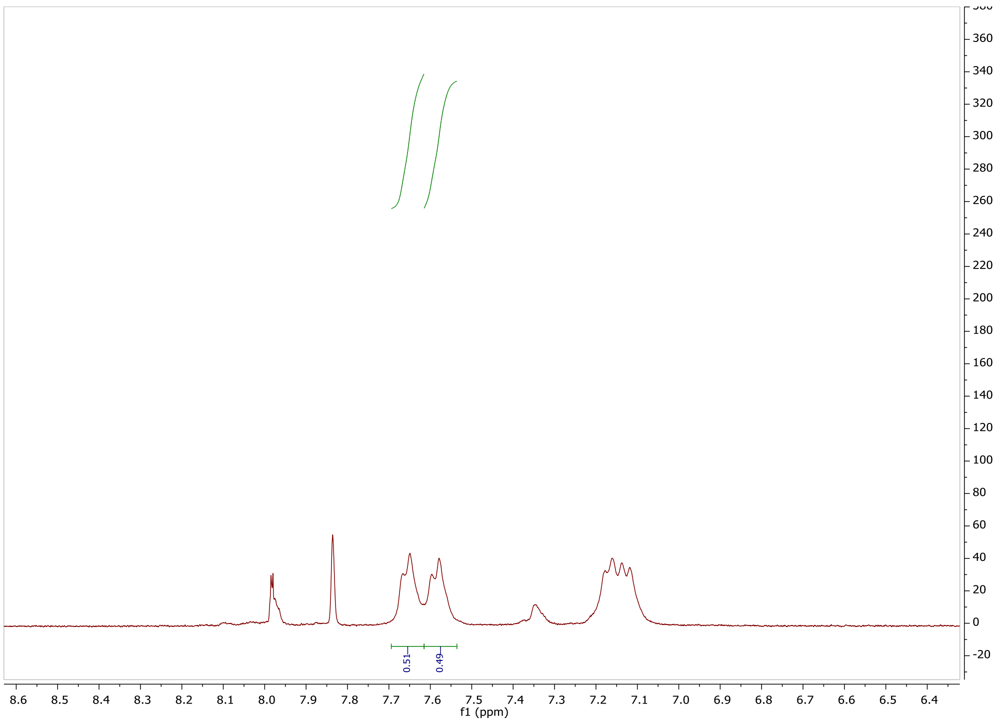

Figure 4.23 50% **L1**: 50% **L2** simultaneous nucleation MOF digested in D_2SO_4 / DMSO-d_6

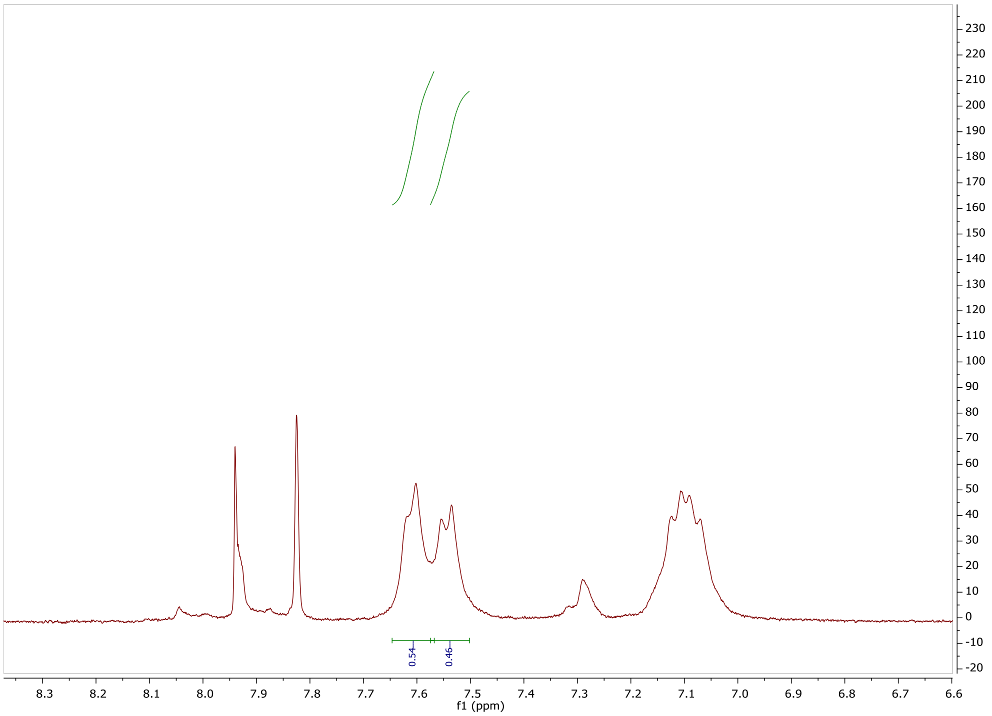

Figure 4.24 60% **L1**: 40% **L2** simultaneous nucleation MOF digested in D_2SO_4 / DMSO-d_6

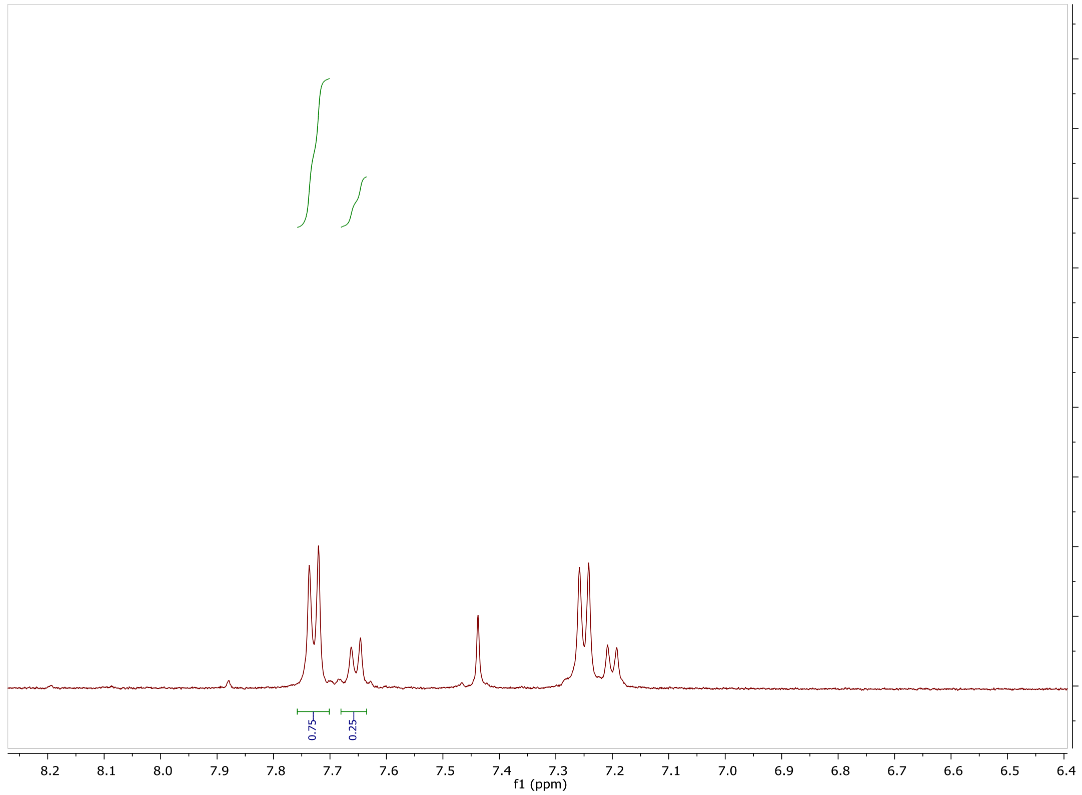

Figure 4.25 70% **L1**: 30% **L2** simultaneous nucleation MOF digested in D_2SO_4 / DMSO-d_6

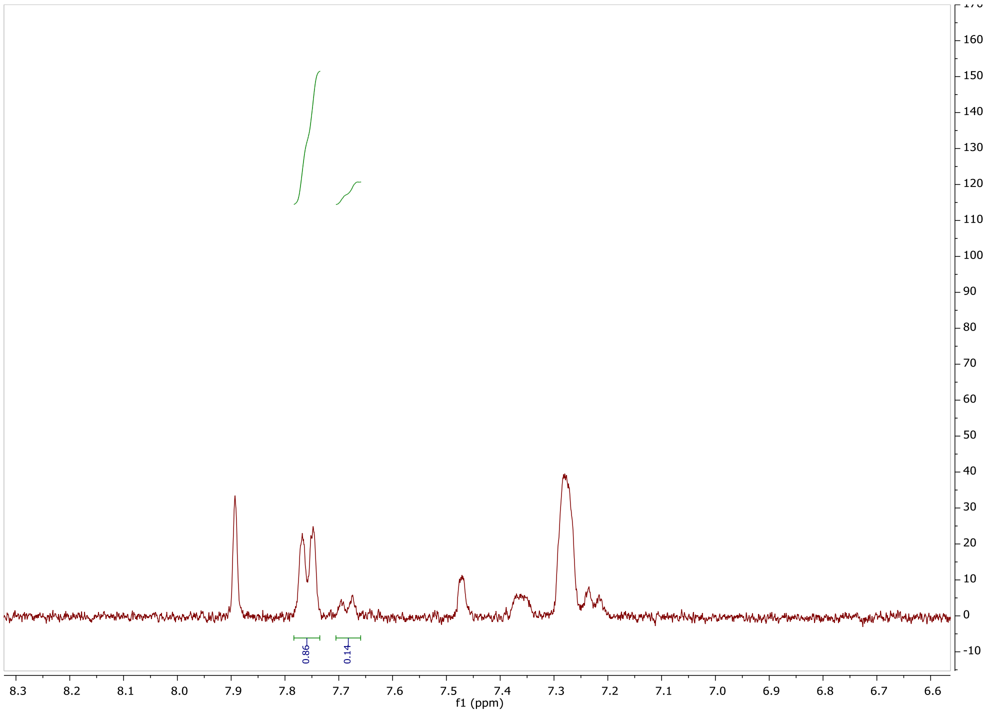

Figure 4.26 80% **L1**: 20% **L2** simultaneous nucleation MOF digested in D_2SO_4 / DMSO-d_6

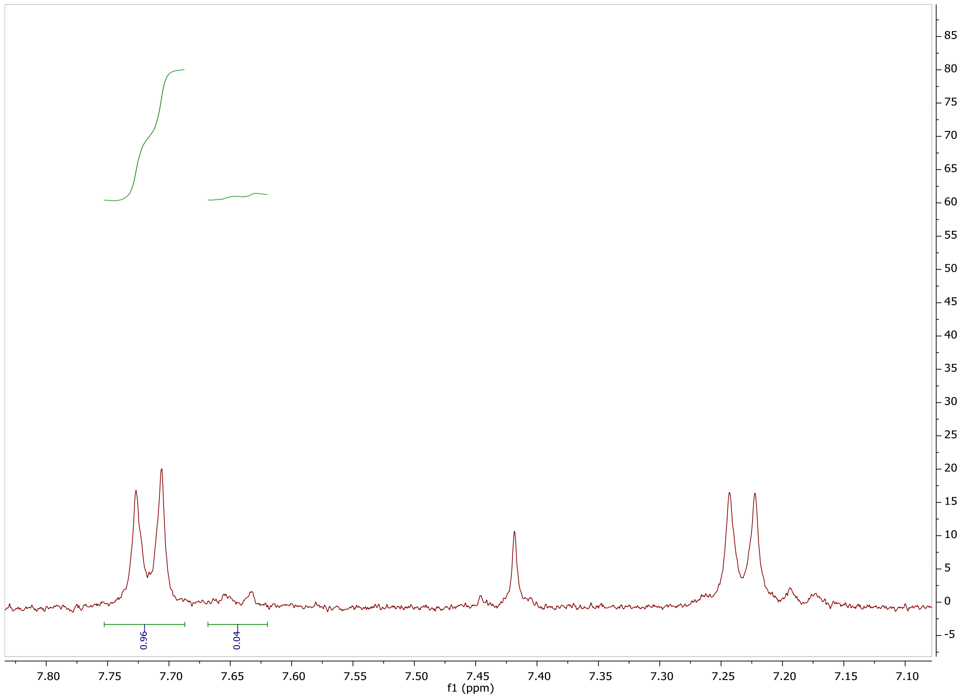

Figure 4.27 90% **L1**: 10% **L2** simultaneous nucleation MOF digested in D_2SO_4 / DMSO-d_6

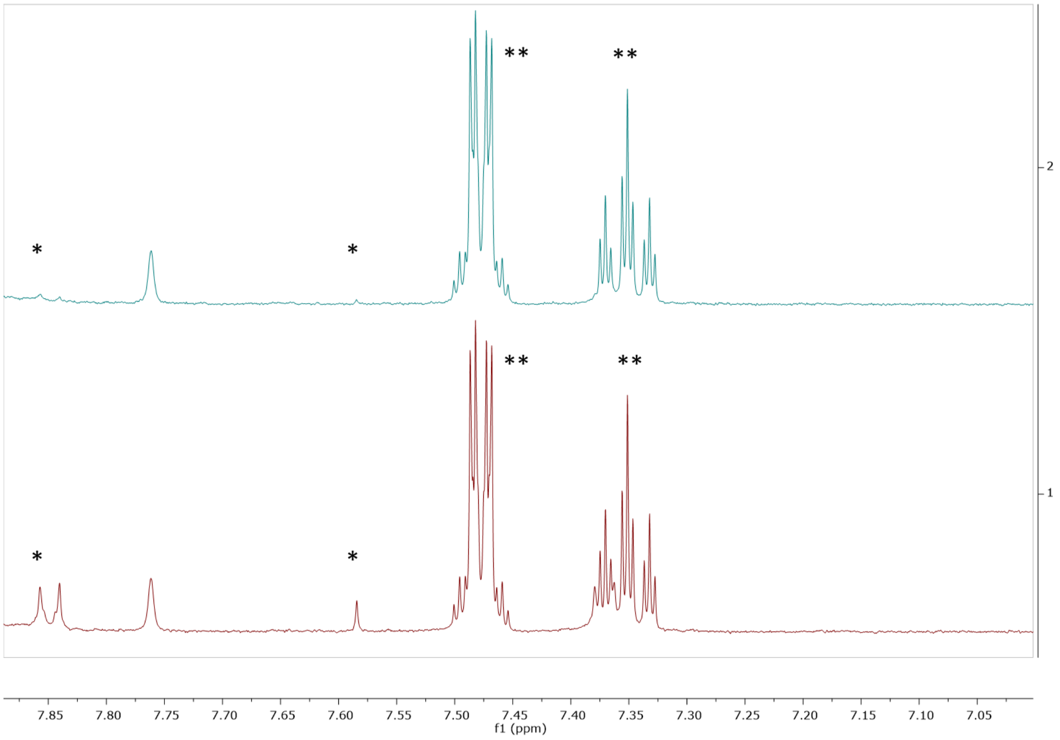

Figure 4.28 Stacked ^{1}H NMR spectra of time = 0 min (bottom) and time = 30 min (top) of 50% **L1** nucleation of Zr_6 node solution. (* refers to **L1** peaks, ** refers to internal standard 1-bromo-3,5-difluorobenzene)

4.6.7 PXRD Patterns

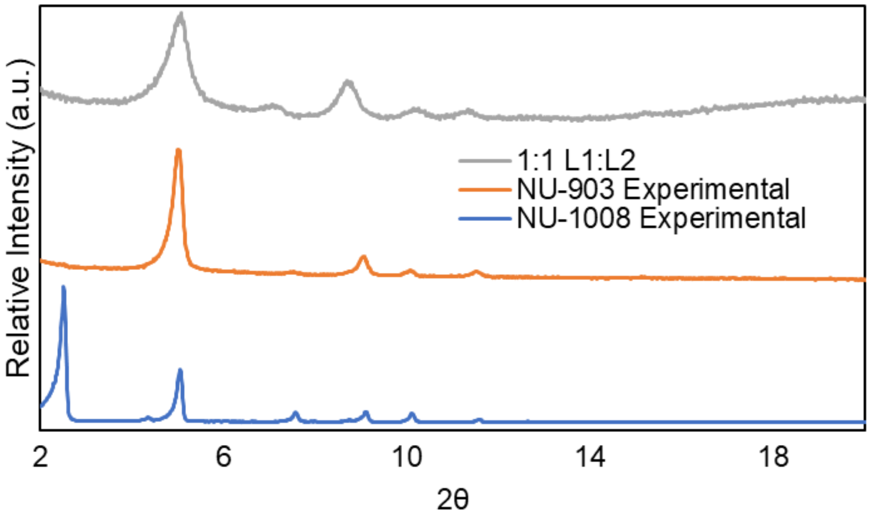

Figure 4.29 PXRD patterns of pure-phase NU-903, NU-1008, and 1:1 **L1**: **L2** under simultaneous nucleation.

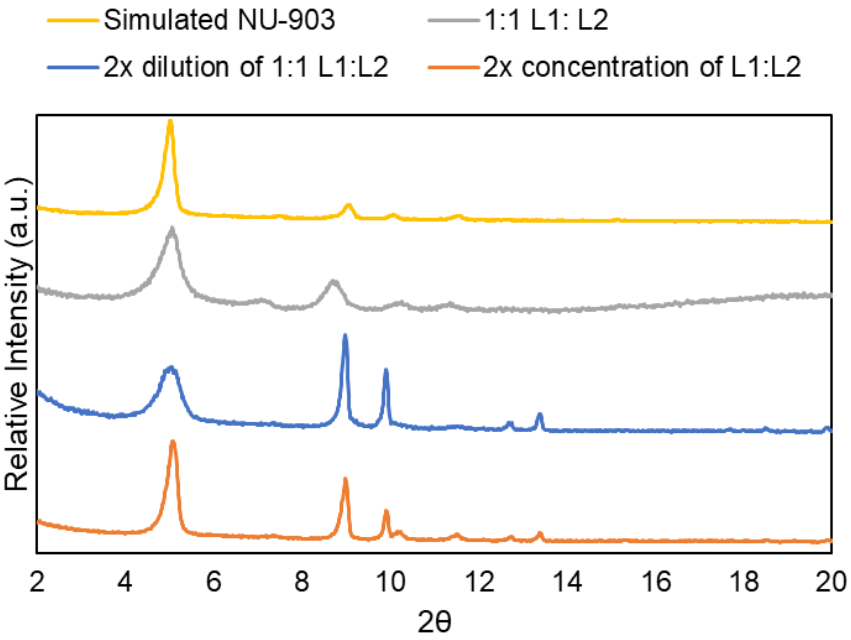

Figure 4.30 PXRD patterns examining the role of absolute concentration of the linker in solution to determine a possible change in kinetic product for the 1:1 **L1**: **L2** reaction conducted under simultaneous nucleation. While the 9, 10, 12.8, and 13.4 2θ peaks increase in intensity, the prediction of these shifts from the simulated pattern suggests that a change in the concentration of the system can slightly affect the crystallinity of the MOF particle, yet we did not observe a phase change.

4.6.8 SEM Images

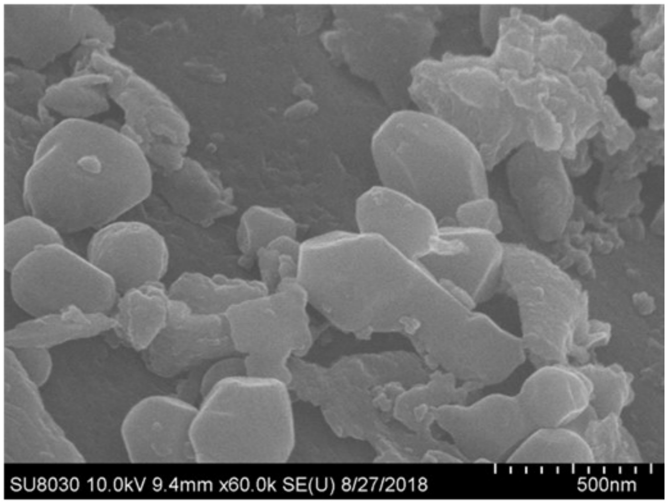

Figure 4.31 Image of simultaneous nucleation of 50% **L1**: 50% **L2**.

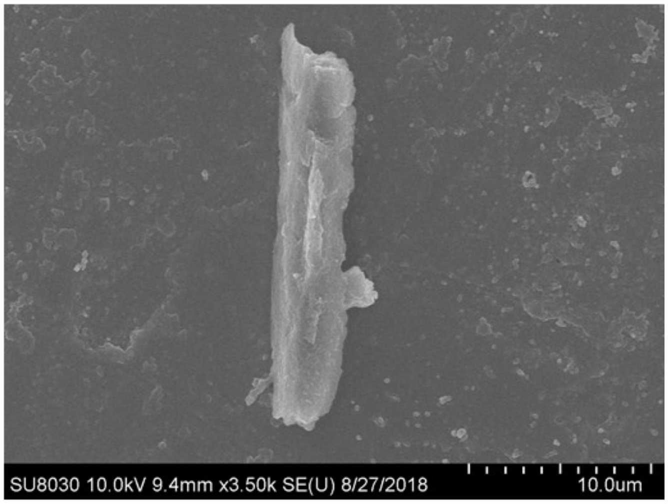

Figure 4.32 Image of simultaneous nucleation of 30% **L1**: 70% **L2.**

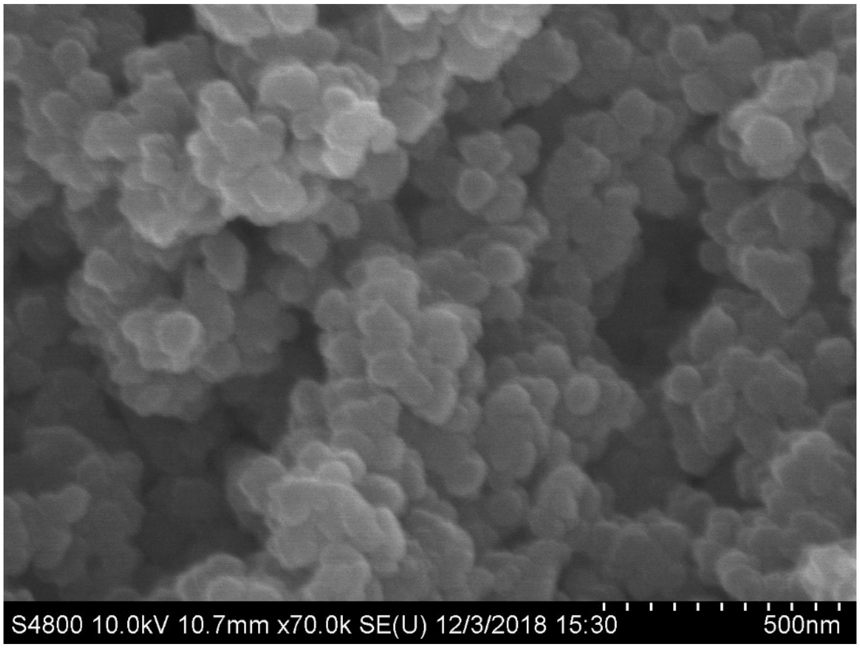

Figure 4.33 Image of simultaneous nucleation of 50% **L1**: 50% **L2** with 2x concentration of system**.**

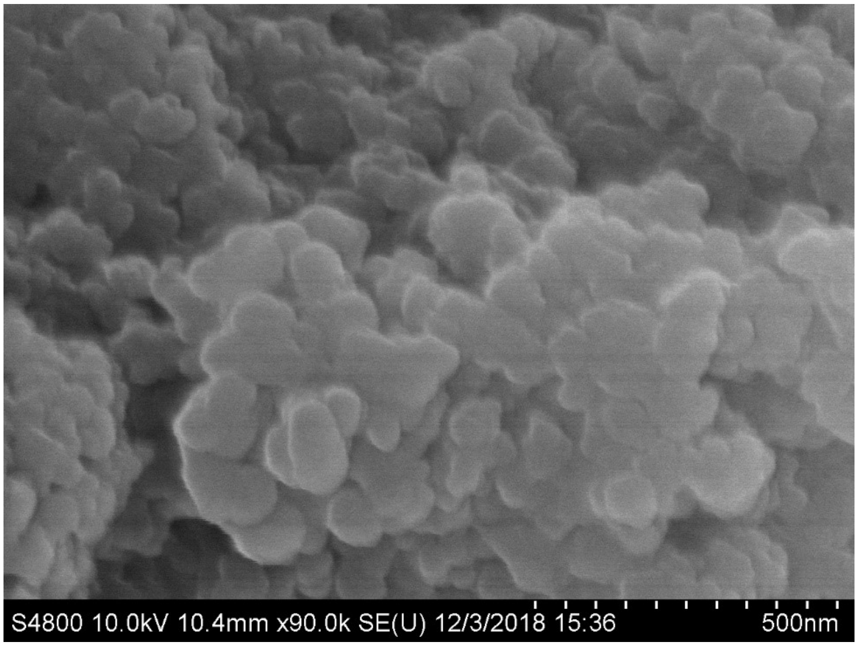

Figure 4.34 Image of simultaneous nucleation of 50% **L1**: 50% **L2** with 2x dilution of system**.**

Chapter 5. Modulation of Crystal Growth and Structure Within Cerium-Based Metal–Organic Frameworks

Portions of this chapter appear in the following manuscript:

Wasson, M. C.; Otake, K.; Gong, X.; Strathman, A. R.; Islamoglu, T.; Gianneschi, N. C.; Farha, O. K. *CrystEngComm* **2020**, *22* (47), 8182.

5.1 Chapter Summary

The intriguing catalytic properties of cerium-based materials has motivated the development of Ce-based metal–organic frameworks (MOFs). However, the controlled crystallization of Ce MOFs remains nascent due to complications with the high reductive potential of Ce^{4+} species. Modulators offer a route in other well-studied coordination networks to slow down crystallization processes to allow for corrective, uniform crystal growth. Herein, we report an investigation of modulator identity and concentration on the synthesis of a Ce-UiO-type MOF with 2,6-naphthalenedicarboxylic acid (NDC) as a linker. At low concentrations using both benzoic acid and trifluoroacetic acid, we observed a mononuclear Ce^{3+} MOF (NU-350) through single-crystal X-ray diffraction studies. Higher modulator concentrations yielded pure-phase Ce-UiO-NDC, with uniform particle sizes observed with utilizing benzoic acid as a modulator. Moreover, we demonstrated the transferability of this synthesis through the pure-phase synthesis of Ce-UiO-66 with benzoic acid as a modulator. High-resolution transmission electron microscopy observed a single crystalline domain within Ce-UiO-NDC.

5.2 Synthetic Strategies to Access Cerium-Based MOFs

The bottom up construction of sophisticated, uniform materials from simple nano-sized building blocks has received substantial attention of the past two decades.[38,249] As atomically precise, hybrid, nanoporous materials, metal–organic frameworks (MOFs) have emerged at the forefront of such impactful nanomaterials.[33] MOFs are composed of inorganic nodes and multidentate organic linkers that assemble into multidimensional lattices through coordination bonds.[37] As such, the frameworks access innumerable chemical functionalities to form highly tailorable structures. MOFs have been implemented in heterogeneous catalysis[32,41,250], water purification[251,252], drug delivery[56,253], gas capture/storage/separation[35–37,254], and chemical sensing[29,222,255,256] due to the high density of spatially isolated binding sites at nodes and linkers. MOFs have been exceptionally impactful as catalyst supports due to their crystallinity and uniformity, critical for precise identification of catalytic active sites to inform next-generation catalyst design.[23]

Earliest MOFs were based on divalent metals, namely, Zn^{2+} and Cu^{2+} and carboxylate linkers.[37,257] However, a higher charge density at the metal node was accessed with higher valent metals (Zr^{4+}, Hf^{4+}, Ce^{4+}) which subsequently increased the strength of the metal-carboxylate bond.[43–46] Of these metals, Zr^{4+}-O based frameworks have emerged as the most well-studied tetravalent species since their first inception in 2008.[43,75,121,227,228,242,258,259] However, strong Zr^{4+}-O bonds often yield polycrystalline materials rather than a single crystalline domain due to the fast precipitation events that occur. Additives, referred to as modulators, were discovered as a strategy to realize diffraction-quality crystals of a Zr^{4+} MOF.[234] Such modulators feature identical monotopic functionality to the multitopic linker in solution and subsequently compete with the linker through transient node binding to slow down coordination binding events.[53] Their role has been investigated throughout Zr-MOF syntheses, yet few generalizable modulation rules exist.[48,57,260–263]

Enabled by fundamental advancements in Zr^{4+} MOF syntheses, initial research toward the development of spatially isolated, periodic Ce^{4+} oxo frameworks emerged, partly inspired by the utility of its parent metal oxide within heterogeneous catalysis.[46,231,264] However, the high reductive potential of Ce^{4+} complicates the synthesis of crystalline cerium materials, including MOFs. MOF syntheses typically rely on high boiling point, formamide-based solvents, generally dimethylformamide (DMF), under high temperatures. The *in-situ* decomposition into formic acid and dimethylamine often enables the facile formation of $Ce(HCOO)_3$ rather than an assembly of hexanuclear Ce^{4+} nodes as observed by Reinsch and team.[46,265]

Stock and coworkers first synthesized Ce^{4+} MOFs through a clever, fast precipitation strategy to access the frameworks in less than 15 minutes, prior to formation of deleterious $Ce(HCOO)_3$.[46,264] However, such methodologies sacrifice control over defect concentration, crystallite morphology, or particle size. Inconsistent particle size imparts diffusion effects, indiscernible morphology complicates identification of pure-phase materials, and defective sites, or exposed open metal sites due to missing linkers or nodes, result in vast differences in framework reactivity.[266,267] Moreover, efforts to develop controlled crystal growth processes coincide with emerging structural and mechanical characterizations which require access to well-defined surface structures (facets and edges), such as high-resolution transmission electron microscopy (HRTEM) and nanoindentation studies.[268,269]

An environmentally friendly synthesis utilized solvent free conditions to synthesize an array of Ce-UiO type MOFs, yet the mechanochemistry crystallization process precluded the formation of the characteristic octahedral morphology.[270] Previously inaccessible redox active porphyrin and pyrene – based Ce MOFs were synthesized utilizing a glycine-capped Ce^{4+} cluster which lowered the Ce reductive potential.[103,135] However, this procedure still utilizes a rapid precipitation method that prevents a controlled crystallization process. Recent work utilized a syringe-pump to slowly introduce cerium ammonium nitrate in the presence of acetic acid as a modulator to form well defined Ce-UiO-66 particles.[271] However, the practical limitations of introducing additional equipment may limit the scale of this procedure. More recently, Huang and co-workers varied acetic acid modulator concentration and temperature to access uniform octahedral Ce-UiO-66 particles effective in the separation of CO_2 and CH_4.[272]

Toward developing Ce MOF syntheses, we elected to study the role of modulator identity and concentration on the crystal growth of Ce UiO-type frameworks. Well-reported examples within Zr MOFs include the modulator dependence on framework topology, beyond merely particle size or morphology, highlighting the potential influence these species can play in MOF syntheses.[48,273] We conducted a systematic study investigating two different modulators, benzoic acid and trifluoroacetic acid, on the controlled crystallization of a UiO Type MOF: Ce-UiO-NDC (NDC = 2,6-naphthalenedicarboxylic acid). We elected to study Ce-UiO-NDC given its higher porosity and stability toward activation procedures than the well-studied Ce-UiO-66.[274] Through varying modulator concentration, we identified two pure-phase products: Ce-UiO-NDC and NU-350, a mononuclear Ce chain MOF linked through NDC linkers. Specifically, an increase in modulator concentration resulted in both pure-phase Ce-UiO-NDC as well as large particle sizes, with benzoic acid providing high uniformity. Modulator trends developed within Ce-UiO-NDC were transferable for the synthesis of pure-phase octahedral Ce-UiO-66 particles. HRTEM identified a single crystalline domain within Ce-UiO-NDC.

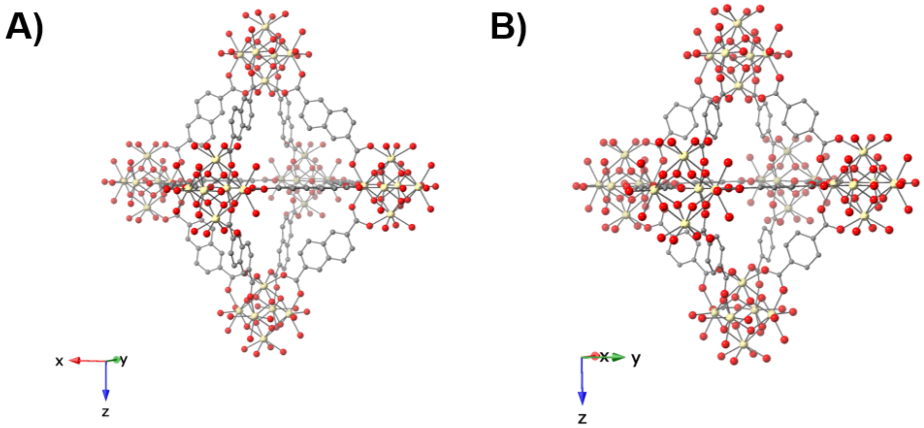

Figure 5.1 Structures of Ce-UiO-NDC (A) and Ce-UiO-66 (B). C, grey; O, red; Ce, pale yellow. H atoms are omitted for clarity.

5.3 Modulator Identity and Concentration Effect on Ce-MOF Structure

To probe the modulator effect on the synthesis of Ce-UiO-type frameworks, we selected benzoic acid and trifluoroacetic acid (TFA), species successfully employed as modulators in the synthesis of Zr-based MOFs. We elected to first investigate Ce-UiO-NDC, a 12-connected framework based on 2,6-naphthalenedicarboxylic acid linkers that crystallizes in **fcu** topology. We utilized the aforementioned glycine-capped hexanuclear Ce_6O_8 cluster instead of traditionally used cerium ammonium nitrate, given the cluster's lowered reduction potential which can circumvent the formation of $Ce(HCOO)_3$ in the DMF synthesis.[103,135,265] We introduced equivalencies of a targeted modulator in a solvothermal synthesis that reacted overnight and utilized powder X-ray diffraction (PXRD) for preliminary structural characterization. Through PXRD, we observed an

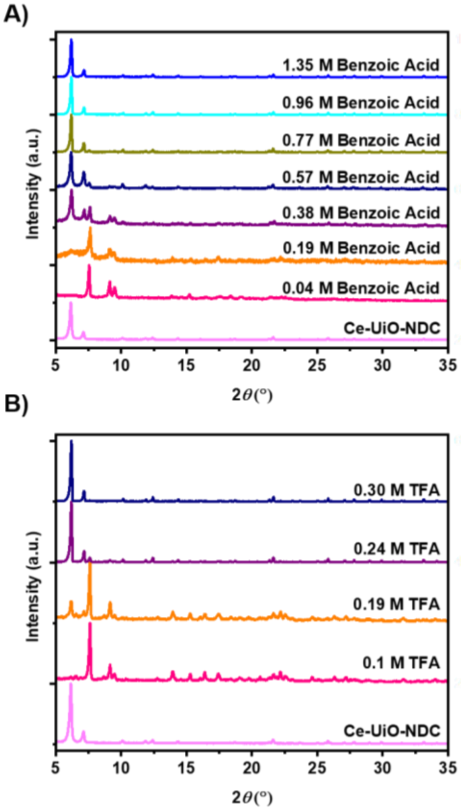

Figure 5.2 Stacked PXRD patterns of targeted synthesis of Ce-UiO-NDC using A) benzoic acid or B) trifluoroacetic acid. Bottom magenta trace labeled Ce-UiO-NDC corresponds to experimentally synthesized frameworks using the prior literature procedure from ref. 46.

alternate phase at lower concentrations of both modulators, tracked through the sharp peak appearing at 7.6 2θ (**Figure 5.2**). With increasing modulator concentrations, the characteristic Ce-UiO-NDC peaks become more prominent at 6.1 and 7.1 2θ (**Figure 5.2**). Pure-phase UiO-NDC was achieved with 1.35 M of benzoic acid as the modulator while the highly acidic TFA modulator yielded a pure phase material when present in only 0.30 M. At higher modulator conditions of TFA, we did not observe further product formation. Throughout the syntheses, the resulting PXRD patterns lacked peaks characteristic of $Ce(HCOO)_3$. SEM images (**Figure 5.6**) of these initial modulator investigations showed uniform clean octahedral particles of ~500 nm were achieved with benzoic acid as a modulator with a concentration of at least 1 M. However, at ~ 0.8 M, smaller octahedral particles of 200 nm were observed with several larger particles of about 500 nm interspersed (**Figure 5.6**). Alternatively, TFA modulated synthesis showed deformed octahedral particles of inconsistent size (**Figure 5.6**).

5.4 Structural Description of NU-350

Intrigued by the alternative phase detected in both modulated syntheses at low concentrations, we utilized single crystal X-ray diffraction (SC-XRD) to identify the alternative structure appearing at lower modulator concentrations. A novel mononuclear Ce^{III} chain MOF, comprised of 3 crystallographically distinct Ce atoms connected through naphthalene dicarboxylic acid was isolated, referred to as NU-350. NU-350 crystallized into the *P*-1 space group with a = 13.2389(6) Å, b = 13.3168(7) Å, c = 19.909(1) Å, α = 71. 557(4)°, β = 74.917(4)°, and γ = 75.843(3)°. Similar to a Ce^{III} chain MOF also based on naphthalene carboxylate reported by Bonino and co-workers (**Figure 5.10**), we observed the coordination of DMF to the framework.[275] Interestingly, a series of three crystallographically distinct nodes repeated throughout the framework. Ce1 features 2 DMF, 4 monodentate NDC, and 1 chelating NDC that altogether

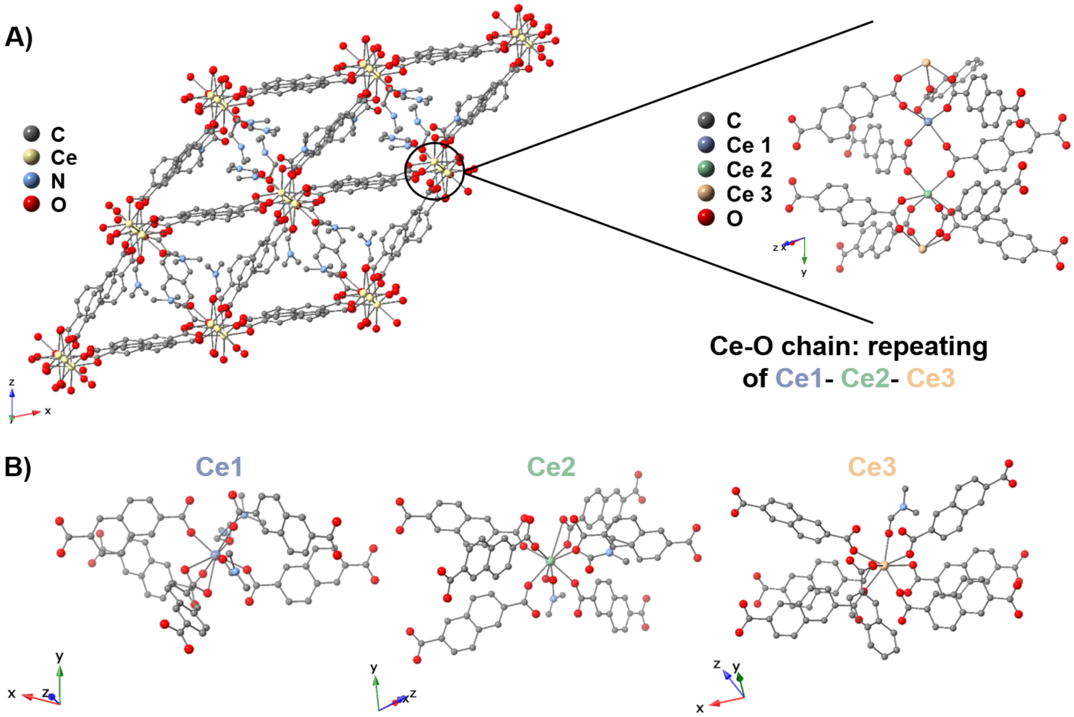

Figure 5.3 A) View of NU-350 viewed along crystallographic *b* axis with three crystallographically unique Ce nodes. B) Unique coordination of each Ce-based node.

comprise the CeO_8 polyhedron. Additionally, Ce2 contains 1.5 DMF, 4.5 monodentate NDC, 1 chelating NDC, and 1 OH/H_2O on the CeO_9 polyhedron. Lastly, the coordination of 1 DMF and 7 monodentate NDC moieties to Ce3 formed another CeO_8 polyhedron. X-ray photoelectron spectroscopy (XPS) confirmed the Ce^{III} oxidation state (**Figure 5.9**) Thus, in addition to prior work documenting deleterious formation of $Ce(HCOO)_3$ in solvothermal Ce_6- MOF syntheses, these findings demonstrate the favorability of Ce^{3+} extended networks when framework modulation is low. We infer that reaction conditions hydrolyzed the Ce_6 node to yield the individual Ce atoms in solution yet increasing monocarboxylate capping agents in solution stabilized the Ce_6 node. Thus, it is suggested that modulators limited the reduction of Ce^{4+} needed to access NU-350 which presents a new, intriguing role in modulating self-assembly for MOFs with highly redox active inorganic nodes.

5.5 Material Characterizations of Ce-UiO-66 and Ce-UiO-NDC

With insights gained from modulator concentration effects on structure and growth, we developed a finetuned Ce-UiO-NDC synthesis to probe bulk porosity utilizing benzoic acid as a modulator. To determine if our insights of controlled Ce-UiO-NDC MOF were transferable within the Ce-UiO MOF family, bulk procedures to synthesize Ce-UiO-66 were additionally developed. PXRD patterns overlaid with their simulated Zr analogues demonstrated good agreement in phase purity (**Figures 5.4A/B**). A likely increase in unit cell parameters is consistent with the shifting of

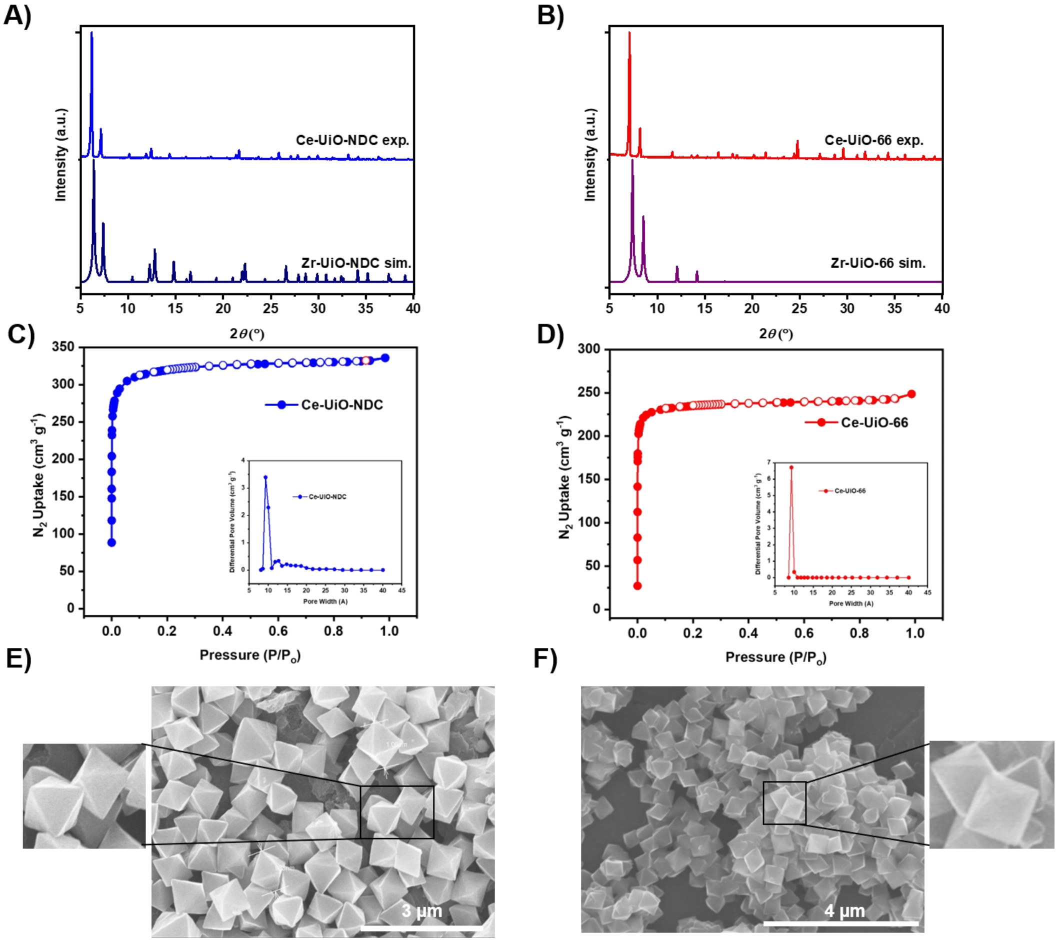

Figure 5.4 A/B) Experimental PXRDs of Ce-UiO-NDC and Ce-UiO-66 overlaid with simulated Zr-UiO-NDC and Zr-UiO-66, C/D) N_2 physisorption isotherms of Ce-UiO-NDC and Ce-UiO-66 with respective insets of NLDFT calculated pore size distributions. D/E) SEM images of Ce-UiO-NDC and Ce-UiO-66 respectively.

Ce experimental peaks to lower 2*θ*, attributed to the larger in lattice constants consistent with an anticipated larger unit cell of the Ce MOFs likely due to larger Ce-O bond distances as compared to Zr-O.[276] In addition to probing bulk crystallinity, N_2 physisorption isothermal measurements were conducted at 77 K and are consistent with a microporous material. BET area was calculated as 965 and 1265 m^2/g for Ce-UiO-66 and Ce-UiO-NDC, respectively (**Figures 5.4C/D**). Non-local density functional theory pore size distributions were calculated using a carbon-slit model and N_2 kernel to show pore sizes ~ 10 Å. Thermogravimetric analyses probed the defects present in the materials (**Figure 5.11**). Increasing modulator concentration to ~1.5 M under the fine-tuned bulk synthesis of Ce-UiO-NDC resulted in an increase of particle size to ~ 1 μm (**Figure 5.4E**) as compared to our preliminary modulation conditions. Pure octahedral morphology particles of ~600 nm Ce-UiO-66 were observed with SEM utilizing benzoic acid as a modulator (**Figure 5.4F**).

Beyond SEM imaging that provided critical insights of particle morphology and size

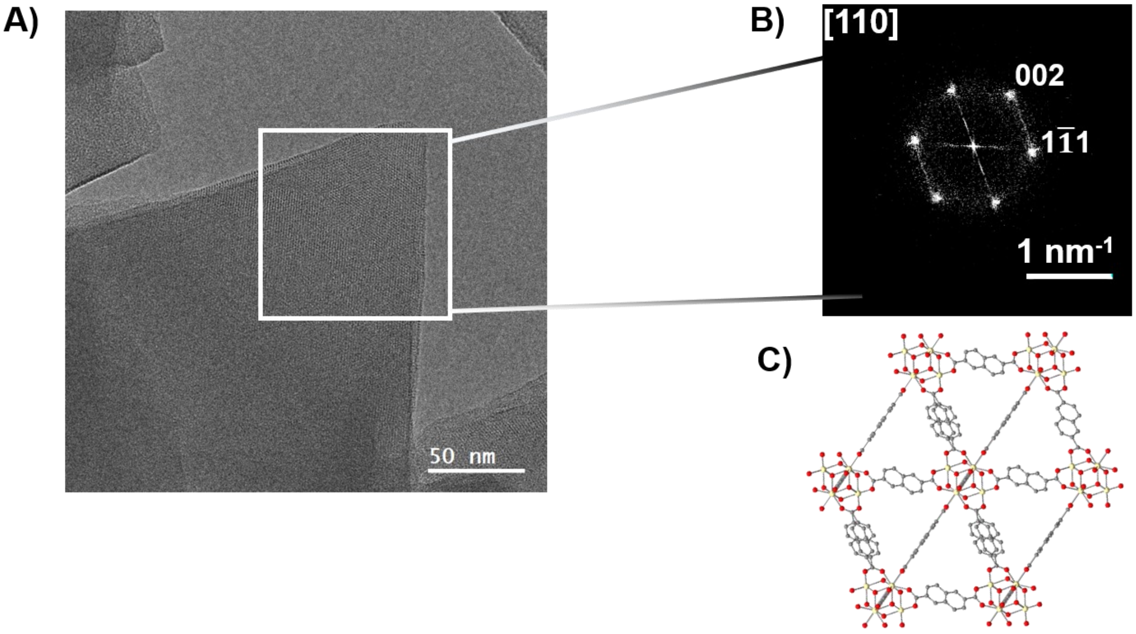

Figure 5.5. A) HRTEM image of Ce-UiO-NDC along [110] zone axis. B) FFT of the image inside the white square, cropped at the predominant lattice fringes. C) Simulated view of [110] plane of Ce-UiO-NDC. C, grey; O, red; Ce, pale yellow. H atoms are omitted for clarity.

uniformity, we utilized high-resolution transmission electron microscopy (HRTEM), a technique that allows for the direct visualization of crystalline structures and consequently provides direct proof of the structures. After exposure to low electron dose conditions, HRTEM can be utilized to specifically image smaller sized MOF particles within a few hundred nanometers, while confirming their crystallinity and nanostructures. Therefore, we elected to utilize HRTEM to directly probe the ~ 200 nm Ce-UiO-NDC particles synthesized in the initial modulator concentration screenings. For a particle tilted on its [110] zone axis, lattice fringes of (111) and (002) planes were identified from fast Fourier transform (FFT) (**Figure 5.5**).

5.6 Conclusions

In this work, we investigated two different modulators, benzoic acid and trifluoroacetic acid, on the crystal growth and structure of Ce-based MOFs. Through varying modulator concentration, we identified two pure-phase products: Ce-UiO-NDC and a mononuclear Ce chain MOF linked through NDC linkers (NU-350). Both modulators similarly affected MOF structure; specifically, an increase in modulator concentration resulted in both pure-phase Ce-UiO-NDC as compared to NU-350 accessed at lower modulator conditions. However, benzoic acid provided higher particle size uniformity and pure phase octahedral particles through SEM imaging. Modulator trends developed within Ce-UiO-NDC were transferable for the synthesis of pure-phase Ce-UiO-66 with octahedral particles. HRTEM imaging observed a single crystalline domain within Ce-UiO-NDC. This study provides mechanistic insights behind the formation of cerium MOFs while also providing a strategy for accessing highly controlled MOF particles useful for further MOF investigations. The specific observation of modulators preventing the reduction of the Ce node suggests a new role of modulators in the self-assembly of redox active metals in MOF syntheses.

5.7 Additional Information

5.7.1 Materials

All chemicals and solvents were obtained from commercial suppliers and used without further purification. Ammonium cerium nitrate (≥98.5%), glycine (≥99%), sodium chloride (≥99.5%), benzoic acid (≥99.5%), terephthalic acid (98%), 2,6-naphthalenedicarboxylic acid (99%), and N,N-dimethylformamide (99%) were purchased from Sigma-Aldrich. Acetone (99.8%) was purchased from Fischer Chemical. Deionized water was used as the water source.

5.7.2 Material Syntheses and Characterization

$[Ce_6(\mu_3\text{-}O)_4(\mu_3\text{-}OH)_4(NH_3CH_2COO)_8(NO_3)_4(H_2O)_6]Cl_8\cdot 8H_2O$ (**Ce_6 precursor**) was synthesized according to literature procedure.[103,135]

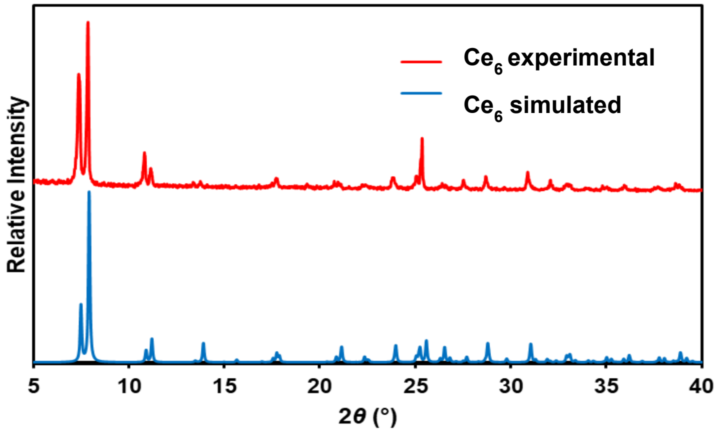

Figure 5.6 PXRD patterns (λ = 1.5406 Å) of experimentally synthesized and simulated patterns of **Ce_6 precursor**.

Ce-MOF Modulation Protocols with Benzoic Acid: 63 mg of **Ce_6 precursor** was placed in 3.5 mL of DMF and sonicated until dispersed. 500 µL of this solution was then placed in seven 1.5-dram vials. Next, the following amounts of benzoic acid were massed out and placed in the separate vials: 4.7 mg, 23.5 mg, 47 mg, 70.5 mg, 94 mg, 117.5 mg, 141 mg, 188 mg. Next, 70 mg of 2,6-naphthalenedicarboxylic acid was placed in 3.5 mL of DMF and sonicated. 500 µL of this solution was then placed in each of the vials. The vials were then placed in a 100 °C oven for 18 hours. Upon reaction completion, the vials were removed from the oven and cooled to room temperature. The mixtures were placed in 1.5 mL centrifuge tubes and centrifuged for five minutes to remove the supernatant. Then, the resultant product was washed with N,N-dimethylformamide (1.5 mL×2) and acetone (1.5 mL×2). The material was then dried in a vacuum oven at 80 °C for 1 hour.

Ce-MOF Modulation Protocols with Trifluoroacetic Acid: 81 mg of **Ce_6 precursor** was placed in 4.5 mL of DMF and sonicated until dispersed. 500 µL of this solution was then placed in nine 1.5-dram vials. Next, the following amounts of trifluoroacetic acid were added to the separate vials: 3 µL, 7.4 µL, 10.3 µL, 14.7 µL, 19.1 µL, 23.5 µL, 29.5 µL, 44.2 µL, and 58.9 µL. Next, 90 mg of 2,6-naphthalenedicarboxylic acid was placed in 4.5 mL of DMF and sonicated. 500 µL of this solution was then placed in each of the vials. The vials were then placed in a 100 °C oven for 18 hours. Upon reaction completion, the vials were removed from the oven and cooled to room temperature. The mixtures were placed in 1.5 mL centrifuge tubes and centrifuged for five minutes to remove the supernatant. Then, the resultant product was washed with N,N-dimethylformamide (1.5 mL×2) and acetone (1.5 mL×2). The material was then dried in a vacuum oven at 80 °C for 1 hour.

NU-350 Synthesis: 9 mg of **Ce_6 precursor** was placed in 0.5 mL of DMF inside a 1.5 dram vial and sonicated until dispersed. Next, 3 µL of trifluoroacetic acid was added. Lastly, 10 mg of 2,6-naphthalenedicarboxylic acid was solubilized in 0.5 mL of DMF which was then added to the Ce solution. The reaction was placed in a 100 °C oven for 18 hours. Upon reaction completion, the vial was removed from the oven and cooled to room temperature. The mixture was placed in 1.5

mL centrifuge tubes and centrifuged for five minutes to remove the supernatant. Then, the resultant product was washed with N,N-dimethylformamide (1.5 mL×2) and acetone (1.5 mL×2). The material was then dried in a vacuum oven at 80 °C for 1 hour.

Ce-UiO-NDC Bulk Synthesis: 70 mg of **Ce_6 precursor** was added to 3.5 mL of DMF in an 8-dram vial and sonicated until dispersed. Next, 1.5 g of benzoic acid was added to this vial which was then sonicated. Separately, 100 mg of 2,6-naphthalenedicarboxylic acid was added to 5 mL of DMF which was then sonicated. This 5 mL linker solution was then added to the starting node solution. The vial was then transferred to a 100 °C oven for 18 hours. Upon reaction completion, the vial was removed from the oven and cooled to room temperature. The resulting product was then into a 15 mL centrifuge tube and washed with DMF (5 mL x 3) and acetone (5 mL x 3). The material soaked in acetone overnight, followed by additional washing with acetone (5 mL x 3). The material was then dried in the vacuum oven for 1 hour at 80 °C. The material was then activated by heating at 100 ˚C for overnight under high vacuum on a Micromeritics Smart Vacprep.

Ce-UiO-66 Bulk Synthesis: 156 mg of **Ce_6 precursor** was added to 2 mL of water in a 100 mL VWR glass jar. Separately, 4 g of benzoic acid was sonicated in 9 mL of DMF which was then added to the VWR jar. 132 mg of terephthalic acid was added to 9 mL of DMF in a separate vial which was then sonicated. The resulting linker solution was then added to the glass jar. Then, the glass jar was transferred to a 100 °C oven for 18 hours. Upon reaction completion, the vial was removed from the oven and cooled to room temperature. The resulting product was then into a 15 mL centrifuge tube and washed with DMF (5 mL x 3) and acetone (5 mL x 3). The material soaked in acetone overnight, followed by additional washing with acetone (5 mL x 3). The material was then dried in the vacuum oven for 1 hour at 80 °C. The material was then activated by heating at 100 ˚C for overnight under high vacuum on a Micromeritics Smart Vacprep.

5.7.3 Methods for Material Characterization

Single Crystal X-Ray Diffraction Analysis and Refinement Details of NU-350: For single-crystal X-ray diffraction measurements, one crystal of NU-350 was mounted on MicroMesh (MiTeGen) in paratone oil and transferred to the cold gas stream (200 K) of a Bruker APEX II CCD area detector equipped with a Cu Kα (λ = 1.54178 Å) I µS micro-source with MX optics. Data integration and reduction were performed using Bruker SAINT program in APEX2. Absorption correction was performed by multi-scan method using SADABS.[277] Space groups were determined using XPREP program implemented in APEX2. The structure was determined by intrinsic phasing methods (SHELXT 2014/5)[278] and refined by full-matrix least-squares refinement on F^2 (SHELXL-2018/3)[279] using the Yadokari-XG software package.[280] Refinement results are summarized in **Table 5.1**. Crystallographic data in CIF format have been deposited in the Cambridge Crystallographic Data Centre (CCDC) under deposition number CCDC-2017725. The data can be obtained free of charge via www.ccdc.cam.ac.uk/data_request/cif (or from the Cambridge Crystallographic Data Centre, 12 Union Road, Cambridge CB2 1EZ, U.K.).

Responses to B level checkcif alert for NU-350 single crystal:

Alert level B

THETM01_ALERT_3_B The value of sine(theta_max)/wavelength is less than 0.575
Calculated sin(theta_max)/wavelength = 0.5577

Response: Diffraction spots from high angles were weak for this material despite several attempts at data collection. This may be because there is a large amount of disorder in the structure, especially for the coordinated solvent species.

PLAT220_ALERT_2_B NonSolvent Resd 1 C Ueq(max)/Ueq(min) Range 9.0 Ratio

Response: This may be because there is a large amount of disorder in the structure, especially for the coordinated solvent species.

Table 5.1 Crystallographic details of NU-350

Empirical formula	$C_{64.5}H_{59}Ce_{3}N_{4.5}O_{24.5}$
Formula weight	1709.52
Temperature/K	200
Crystal System	Triclinic
Space Group	*P*–1
***a*/Å**	13.2389 (6)
***b*/Å**	14.3168(7)
***c*/Å**	19.909(1)
***α*/°**	71.557(4)
***β*/°**	74.917(4)
***γ*/°**	75.843(3)
Volume/Å^3	3401.7(3)
Z	2
ρ_{calc}g/cm^3	1.669
μ/mm^{-1}	15.943
***F*(000)**	1665
Crystal size/mm^3	0.015×0.015×0.015
Radiation / Å	1.54178
2θ range for data collection/°	2.387–59.296
Index ranges	3.51–58.72
Reflections collected	18978
Independent reflections	9628
Data/restraints/parameters	9628/223/932
Goodness-of-fit on F^2	1.017 ($I \geq 2\sigma(I)$), 1.012 (all data)
Final *R* indexes [$I \geq 2\sigma(I)$]	$R_1 = 0.0527$, $wR_2 = 0.1235$
Final *R* indexes [all data]	$R_1 = 0.0729$, $wR_2 = 0.1338$
CCDC deposition number	2017725

Powder X-ray Diffraction Analysis: Powder X-ray diffraction (PXRD) patterns of the samples were measured by a STOE-STADI MP powder diffractometer operating at 40 kV voltage and 40 mA current with Cu-Kα1 X-ray radiation ($\lambda = 1.5406$ Å) in transmission geometry.

N_2 Sorption Isotherm Measurements: N_2 adsorption and desorption isotherms on activated materials were measured on a Micromeritics Tristar (Micromeritics, Norcross, GA) instrument at 77 K. Around 30 mg of sample was used in each measurement. Prior to N_2 isotherm measurements, the samples were placed under high vacuum at 100 °C on a Micromeritics Smart Vacprep for 18 h. The specific surface areas were determined using the Brunauer−Emmett−Teller model from the N_2 sorption data in the region $P/P_0 = 0.005$–0.05. Pore size distributions were obtained using DFT calculations using a carbon slit-pore model with a N_2 kernel.

X-ray Photoelectron Spectroscopy: X-ray photoelectron spectroscopy measurements were carried out on a Thermo Scientific ESCALAB 250 Xi equipped with an electron flood gun and a scanning ion gun. Analysis used the Thermo Scientific Avantage Data System software, and C1s peak (284.8 eV) peak was used as the reference. Oxidation states of Ce were assigned by comparison to previously published data.[133]

Scanning Electron Microscopy Imaging: Prior to observation, the samples were coated with OsO_4 (~9 nm) in a Denton Desk III TSC Sputter Coater. Scanning electron microscopy (SEM) images were acquired from a Hitachi SU8030 scanning electron microscope.

High Resolution Transmission Electron Microscopy Imaging: Transmission electron microscopy (TEM) images were collected at Northwestern University's EPIC/NUANCE facility using a TEM JEOL ARM300F equipped with a Gatan OneView-IS camera (CMOS electron sensor) at an acceleration voltage of 300 kV and an emission current of 15 μA. The samples were prepared with Lacey carbon copper mesh girds and loaded onto a single tilt TEM holder. The cumulative electron dose was around 5 $e^-/Å^2$.

Thermogravimetric Analysis: Sample weight loss data was measured on a Mettler Toledo TGA/DSC 1 Star System instrument. Samples were heated in air from 30°C to 600°C at a rate of 5°C/minute. The sample was held at 600°C for 60 minutes.

5.7.4 SEM Images

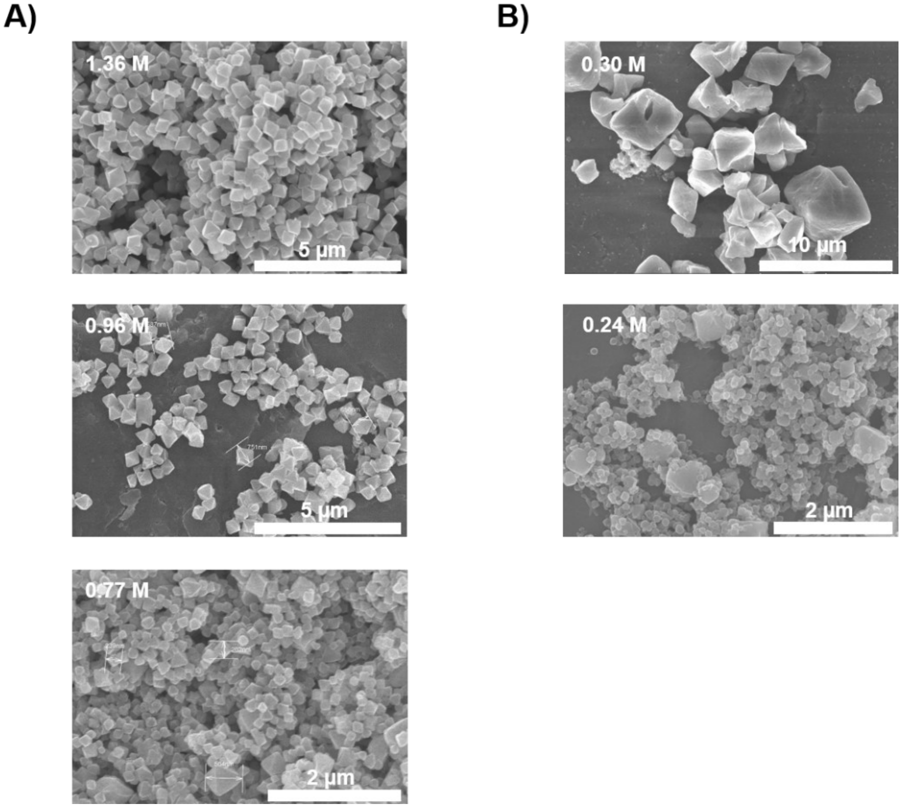

Figure 5.7 Scanning electron microscopy (SEM) images of Ce-UiO-NDC under specified concentrations of either (A) benzoic acid or (B) trifluoroacetic acid.

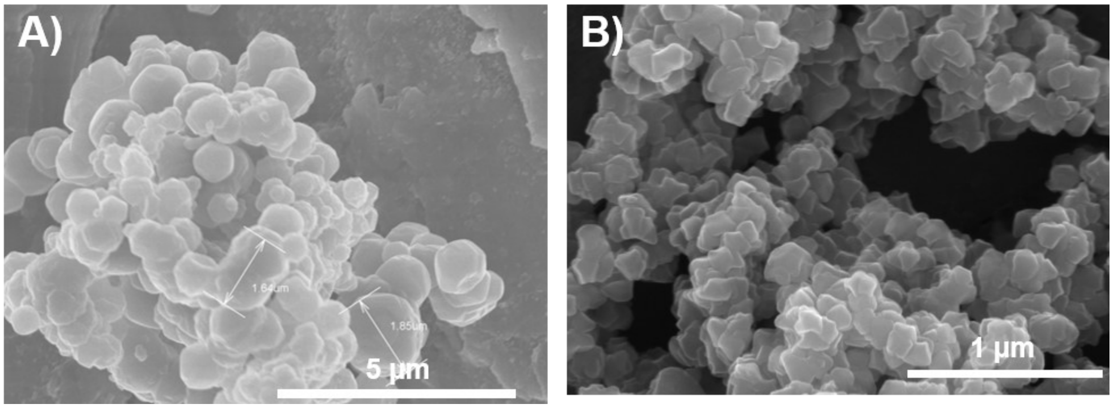

Figure 5.8 Scanning electron microscopy (SEM) images of (A) Ce-UiO-NDC and (B) Ce-UiO-66 following syntheses reported from previously reported protocols.[46]

5.7.5 XPS Data

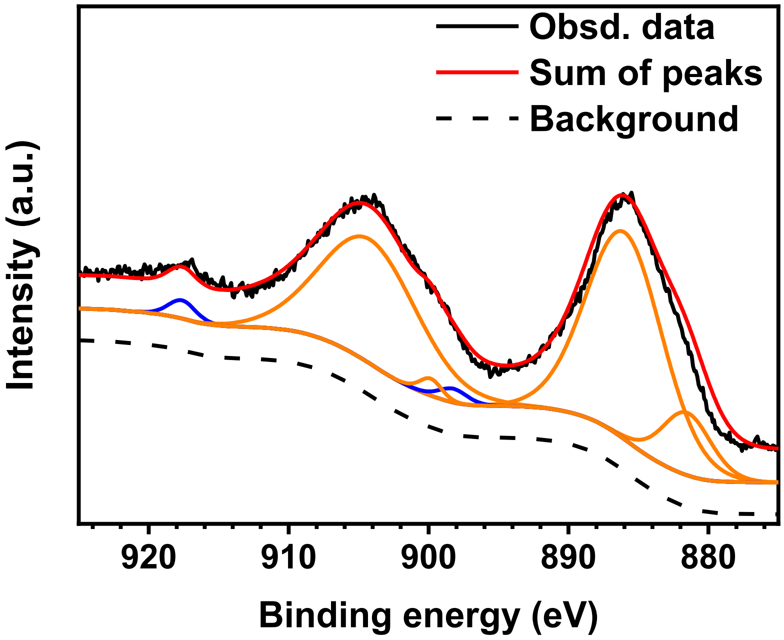

Figure 5.9 Observed Ce 3d XPS (solid black line) and sum of fitted data (red line) for NU-350. The observed data were fitted by Gaussian/Lorentzian functions with deconvoluted peaks in blue corresponding to Ce^{4+} and orange deconvoluted peaks corresponding to Ce^{3+}.

5.7.6 PXRD Patterns

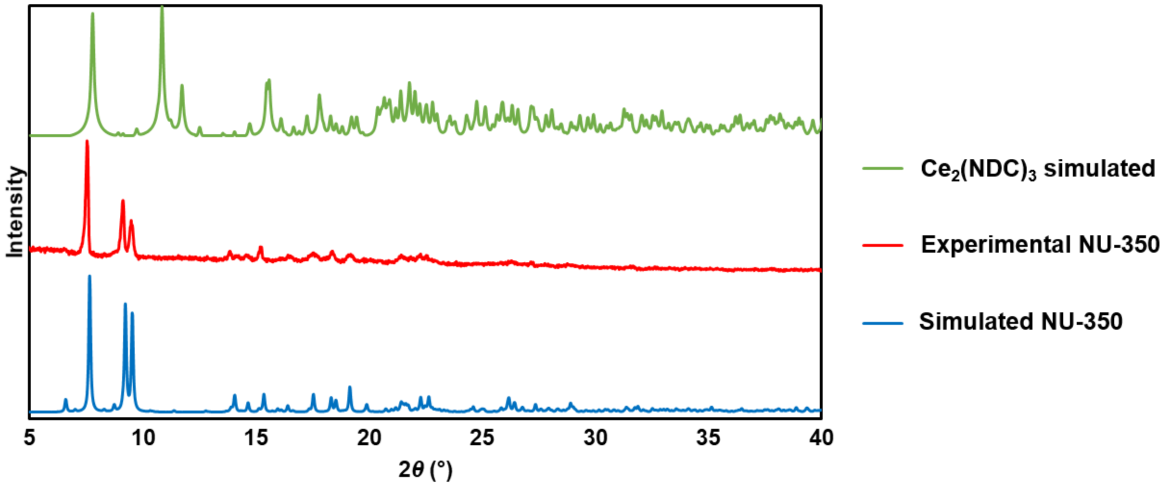

Figure 5.10 Overlaid PXRD patterns of simulated and experimentally observed NU-350 in this study as well as a simulated pattern of a similar $Ce_2(NDC)_3$ framework reported in literature.[275]

5.7.7 Thermogravimetric Analysis Data

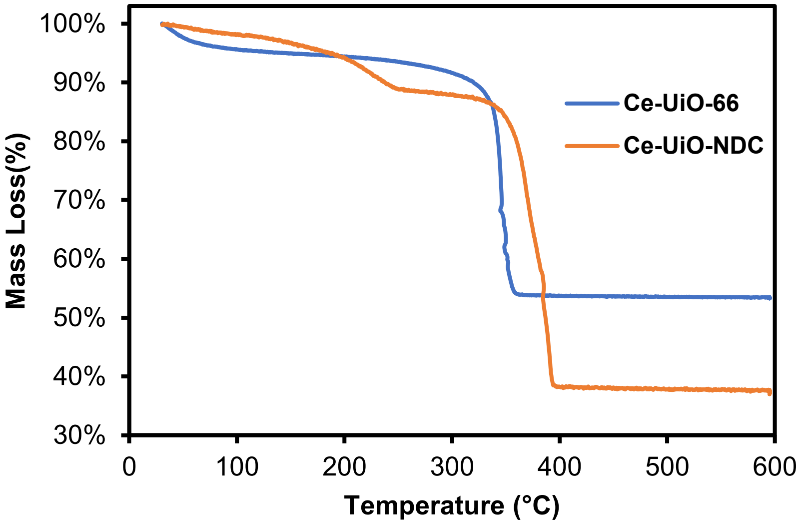

Figure 5.11 TGA data of Ce-UiO-66 and Ce-UiO-NDC large batch syntheses. The mass loss of ~39% corresponds to ~1.4 missing linkers per node in Ce-UiO-66. The mass loss of ~50% corresponds to ~0.8 missing linkers per node in Ce-UiO-NDC.

Chapter 6. Structural Transformation of Metal Oxo Species within UiO-66 Type Metal–Organic Frameworks

Portions of this chapter appear in the following manuscript:

Wasson, M.C.; Xie, H.; Wang, X.; Duncan, J.; Farha, O.K. *In Preparation.*

6.1 Chapter Summary

Studying the coordination of actinide-based metal oxo clusters can provide valuable insights for nuclear energy technologies and radioactive waste containment. Metal–organic frameworks serve as a platform to directly interrogate the structure and properties of understudied actinide elements, including thorium. Examples of structural evolutions within Th oxo species within MOFs are rare yet relevant for nuclear waste speciation in solution. Herein, we report the serendipitous discovery of the structural evolution of Th-UiO-66 containing a hexanuclear Th node to a mononuclear $Th(bdc)_2(dmf)_2$ upon the evaporation of solvent from the reaction. We observe a partial reversal of $Th(bdc)_2(dmf)_2$ back to Th-UiO-66 upon hydrothermal treatment, indicating the complex dynamics of Th oxo species in solution. We report that isolated Ce-UiO-66 similarly transforms to a newly isolated 1D Ce^{III} carboxylate chain MOF named NU-351 in the same conditions as Th-UiO-66, while Zr-UiO-66 and Hf-UiO-66 retain their structures.

6.2 Thorium–Based Metal-Organic Frameworks

Metal–organic frameworks (MOFs) are an emerging class of highly porous, well-defined crystalline materials that have attracted considerable interest for catalysis, gas storage/separation, toxic chemical sequestration, and chemical sensing, among other applications.[32–36] Inorganic nodes, comprised of either metal ions or metal clusters, form coordination bonds to multitopic organic linkers to produce a targeted MOF. Researchers can leverage this tunability to impart and study targeted chemical reactivity within the different building units. Moreover, the controlled self-assembly of the MOF building blocks can spatially isolate components to better study or harness their chemical properties.

Beyond the well-studied transition metal elements ubiquitous within MOF literature, recent reports of actinide-containing MOF nodes have accelerated the understanding of the elements' unique coordination chemistry which is pertinent for the nuclear waste storage and nuclear energy applications.[47,281–284] In particular, limited knowledge exists about that solid-state structural chemistry of thorium due to the uncontrolled growth of polynuclear Th species in solution.[285,286] Recent interest has surfaced to better understanding the structural behavior of thorium given surging interest in developing a more sustainable nuclear fuel process based on the ^{233}U–^{232}Th fuel cycle as opposed to the U^{235} fuel cycle.[287,288] Furthermore, Th^{IV} is largely considered a surrogate to study the coordination and behavior of more highly regulated Pu^{IV}.[289]

Approximately 60 thorium oxide-based coordination compounds have been reported in the Cambridge Structural Database, which appears miniscule as compared to the vast number of total coordination compounds deposited.[290] Therefore, a major impetus is directed at expanding the library of thorium-oxo based clusters and frameworks through systematically tuning solvent compositions and reagent ratios.[291,292] For example, modifying the concentration of selenic acid and water in the presence of thorium hydrates yielded 5 discrete Th clusters; lowered reaction temperature and acidity yielded higher nuclearity Th clusters.[290] Seminal work by Loiseau and co-workers further accessed Th oxo clusters installed within Th-based MOFs, including a Th analogue of the well-known Zr-MOF UiO-66,[44] through the modulation of temperature, Th: linker ratio, and water concentration.[293] Th-UiO-66 features a Th_6O_8 building block previously isolated as a discrete Th oxo cluster.[82,84,294] Alternatively, Th-based MOFs can stabilize unique cluster coordination elusive within discrete thorium clusters. For example, our group reported a hexanuclear secondary building unit comprised of $[Th_6(\mu_3\text{-}O)_2(HCOO)_4(H_2O)_6]$ self-assembled with tetrakis(4-carboxyphenyl)porphyrin linkers.[295] However, once Th-based frameworks are assembled, examples of structural evolution within Th-based MOFs are rare. In one recent study, a non-interpenetrated MOF dissolved and recrystallized into a 2-fold interpenetrated MOF, but the Th nuclearity of the node remained the same.[296] Therefore, it is imperative to study examples of Th-MOF based phase transformation with the evolution of the Th oxo species better understand the coordination chemistry of Th.

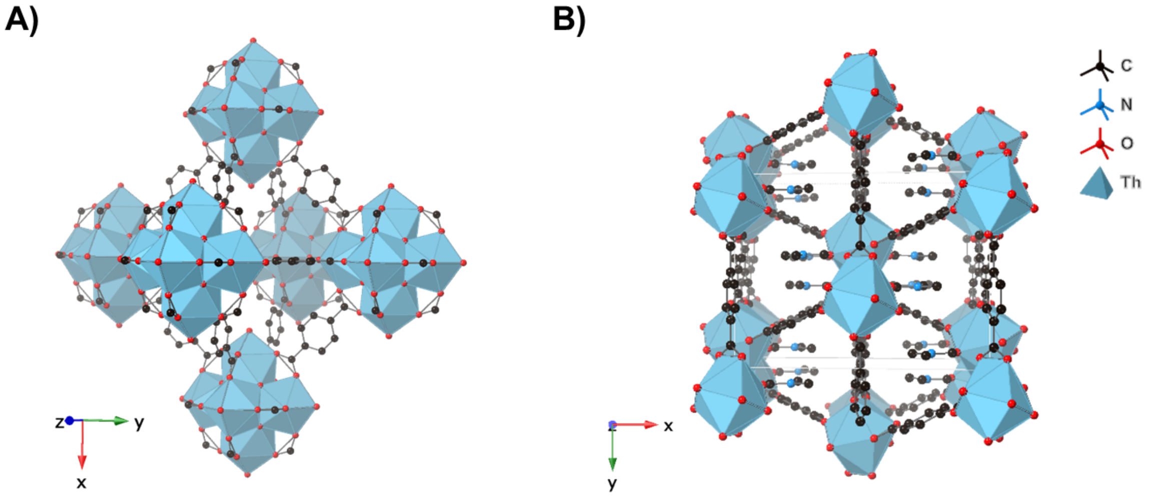

Figure 6.1 Structures of (A) Th-UiO-66 and (B) $Th(bdc)_2(dmf)_2$.

Herein, we report the discovery of a phase transition between Th-UiO-66 and $Th(bdc)_2(dmf)_2$ over time. This transition is accompanied by the hydrolysis of the Th_6O_8 node of Th-UiO-66 to a 10-coordinate $ThO_8(dmf)_2$ node. We monitored the process over 72 hr with powder X-ray diffraction (PXRD) and scanning electron microscopy (SEM) techniques. We postulate that that solvent evaporation and subsequent increased concentration of reagents in solution result in the phase transition. Moreover, the transition is suggested to be partially reversible upon the addition of heat and water to $Th(bdc)_2(dmf)_2$ to partially reform Th-UiO-66. Under the same conditions that Th-UiO-66 transitions, its isostructural Ce-UiO-66 analogue also transforms into a newly reported 1D Ce^{III} carboxylate MOF, NU-351, while Zr-UiO-66 and Hf-UiO-66 retain their structures.

6.3 Phase Transformations of Th-UiO-66

We serendipitously observed a phase transition of Th-UiO-66 to the reported $Th(bdc)_2(dmf)_2$ polymorph when the reaction time was increased from 24 hr to 72 hr (Figure 1). In 2 separate trials, identical solutions of 0.9 mmol 1,4 benzene dicarboxylic acid and 0.35 mmol $Th(NO_3)_4 \cdot 5H_2O$ were reacted for 24 hr and 72 hr in a 4:1 solution of DMF: water. The resulting PXRD patterns demonstrated good agreement of the 24 hr synthesis with the simulated Th-UiO-66 pattern while the 72 hr synthesis matched the simulated pattern of $Th(bdc)_2(dmf)_2$. and confirmed through PXRD identical patterns with the simulated structure (**Figure 6.2; Figure 6.8**). While the initial report of Th-UiO-66 included thorough synthetic screenings to yield the MOFs in pure-phase, a transition from one phase to another over time was not explored.[293] We were intrigued by the hydrolysis of the Th_6O_8 node of Th-UiO-66 to a 10-coordinate $ThO_8(DMF)_2$ node and further investigated the kinetic timescale of this transition.

PXRD patterns were collected of identical solutions and each vial was removed after 12 hours to monitor the crystalline phase formed. As shown in **Figure 6.2**, we observed PXRD patterns from 12-48 hr that are consistent with Th-UiO-66. After 60 hours, the growth of Th(bdc)$_2$(dmf)$_2$ peaks was indicated through the appearance of five new peaks at between 10-13 degrees 2*θ*, while the primary Th-UiO-66 peaks at 6.9 and 7.9 degrees 2*θ* are still visible. The PXRD pattern collected at 72 hours demonstrated a nearly complete conversion of Th-UiO-66 to the Th(bdc)$_2$(dmf)$_2$ framework. SEM images indicated the growth of Th(bdc)$_2$(dmf)$_2$ after 60 hours with the presence of large 100 µm size trapezoidal crystals appearing along size of smaller 1 µm sized Th-UiO-66 particles (**Figure 6.3**). The larger 100 µm trapezoidal crystals of Th(bdc)$_2$(dmf)$_2$ were only observed at 72 hr. After 72 hr, the reaction vials contained ~ 50% of the starting solvent amount, indicating solvent evaporation must have occurred during the solvothermal synthesis.

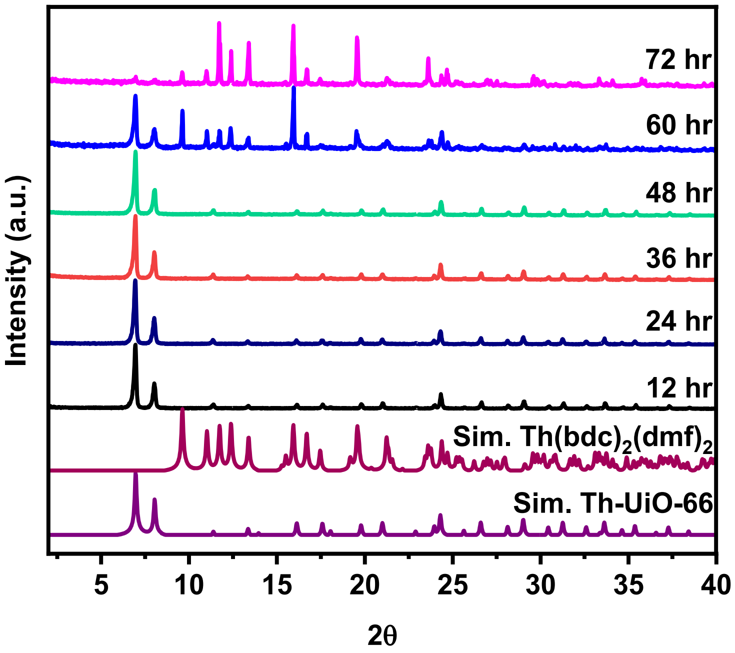

Figure 6.2 PXRD patterns of phase transition monitored of Th-UiO-66 to Th(bdc)$_2$(dmf)$_2$ at a designated time point of the reaction between 1,4 benzene dicarboxylic acid and Th(NO$_3$)$_4$·5H$_2$O.

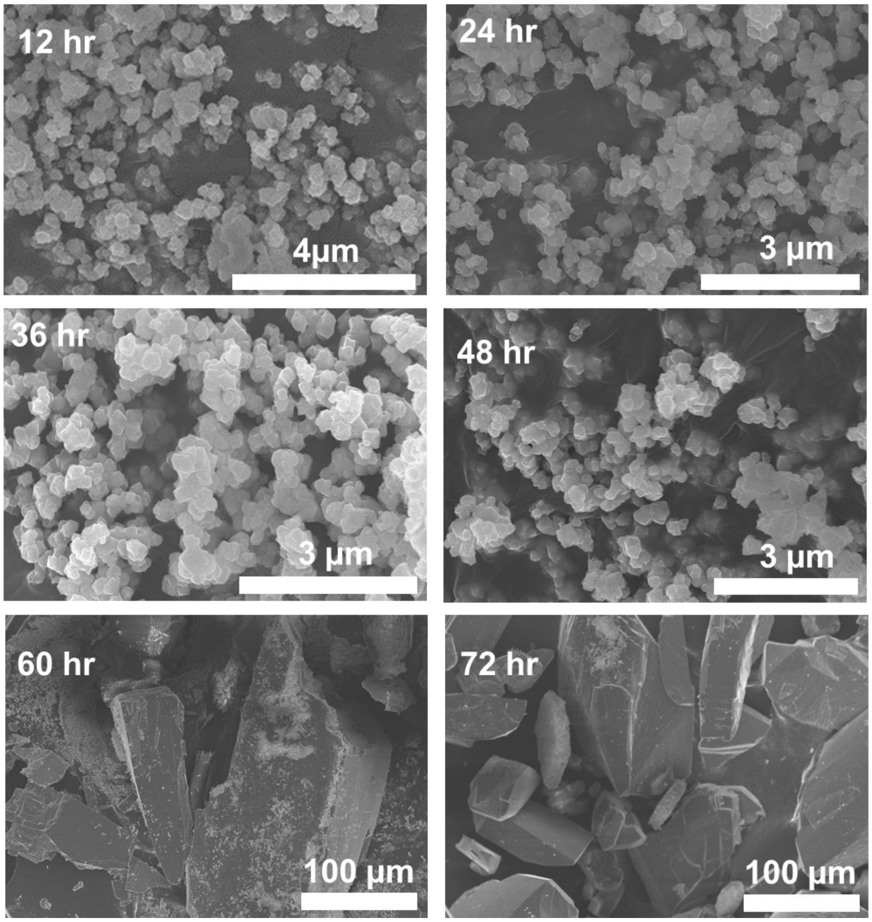

Figure 6.3 SEM images of resulting particles from the reaction between 1,4 benzene dicarboxylic acid and $Th(NO_3)_4 \cdot 5H_2O$ at designated time points.

Beyond the different node environments, the two MOFs have vastly different physical properties as evidenced through surface areas of 620 m^2/g for Th-UiO-66 compared to < 5 m^2/g for $Th(bdc)_2(dmf)_2$ (**Figures 6.13-6.14**). Thus, it is imperative to better understand the complexity of the phase transformation. We then sought to complete *in situ* investigations to monitor the phase transitions. Before observing the 72-hour process *in situ*, we first took an aliquot of the reaction mixture (see supporting information) and placed it in a borosilicate capillary that was flame sealed. We compared the PXRDs of the capillary heated in the oven concurrently with the mother reaction mixture in a vial reacting at the same time. After 72 hours, PXRDs demonstrated that the flame sealed system formed Th-UiO-66 while the mother solution in the vial formed $Th(bdc)_2(dmf)_2$ (**Figure 6.9**). Thus, we reasoned that the flame seal capillary must provide a better seal for our reactants than the polyvinyl capped vials our bulk syntheses were conducted in, which resulted in the aforementioned solvent evaporation over the reaction time. We conjectured that a higher concentration of reactants results in the formation of $Th(bdc)_2(dmf)_2$.

In our next set of experiments, we used vials with caps lined with polytetrafluoroethylene (PTFE) which features a higher melting point than polyvinyl, providing a more closed system and limiting solvent evaporation. We utilized the same amount of reagents and ratio of DMF: water in the solution as our prior experiments, but systematically decreased the total solvent amount to increase the overall concentration of both reactants in solution. The syntheses reacted again for 72 hr, and we utilized PXRD to investigate the resulting phases. We observed the most visible formation of $Th(bdc)_2(dmf)_2$ with the highest concentration (3x) of the reactants (pattern C in **Figure 6.4**) while we observe a slight formation of $Th(bdc)_2(dmf)_2$ in the 2x and regular concentrations in patterns B and A respectively. We determined that concentration is a critical factor in this phase transformation, but we did not observe the full conversion even in the 3x concentration vial to $Th(bdc)_2(dmf)_2$.

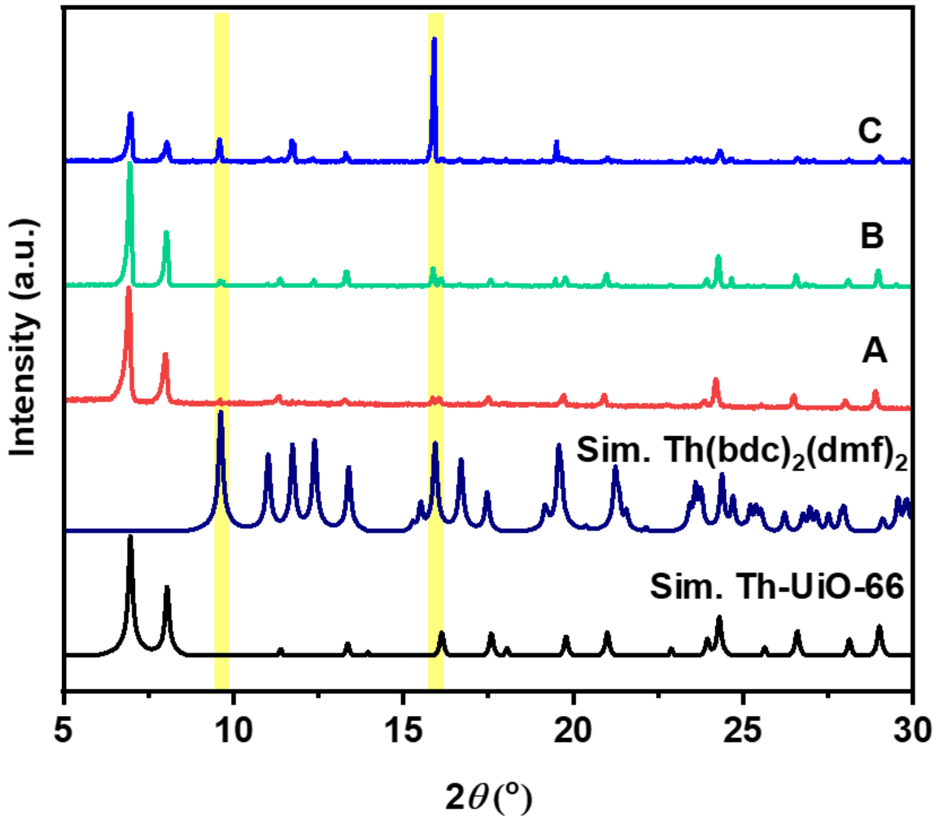

Figure 6.4 Overlaid PXRDs of A) 1X concentration B) 2X concentration and C) 3X concentration within PTFE-lined vials. Highlighted regions added to aid in monitoring the growth of Th(bdc)$_2$(dmf)$_2$ peaks.

Given prior reports of the role of formate concentration on Th oxo cluster size, we next explored the role of the decomposition products, formic acid and dimethylamine, on the phase transition. We added equivalents of lithium formate or a diethylamine (DEA) to isolated Th-UiO-66 added into the DMF/water solution which soaked for 48 hours at 130 °C. Through PXRDs of the resulting products, we observed only a slight formation of Th(bdc)$_2$(dmf)$_2$ upon the addition of DEA, even with as high of a ratio of 1:1 DMF: DEA (pattern H **Figure 6.10**). Furthermore, solutions containing Th-UiO-66 with added lithium formate did not exhibit a phase change. We thus determined that the concentration of the reactants greatly promotes the conversion of Th-UiO-66 to Th(bdc)$_2$(dmf)$_2$ as opposed to the decomposition products of DMF.

Previously, it was reported that water can stabilize the hexanuclear cluster of Th-UiO-66 by favoring olation and oxolation condensation processes.[293] Thus, we probed whether adding water to an isolated sample of $Th(bdc)_2(dmf)_2$ would prompt a phase transition back to Th-UiO-66. After heating at 80 °C at 24 hr, we observed the growth of peaks at 6.9 and 7.9 degrees 2θ, consistent with the Th-UiO-66 phase as well as sharp peaks still present at 9.5 degrees 2θ indicating residual $Th(bdc)_2(dmf)_2$ (**Figure 6.5**). We attempted longer reaction times of $Th(bdc)_2(dmf)_2$ in water in an attempt to fully convert the mononuclear MOF back to Th-UiO-66, but we were unable to achieve full conversion. Nonetheless, we learned that the phase change is partially reversible, highlighting the complexity of Th oxo species.

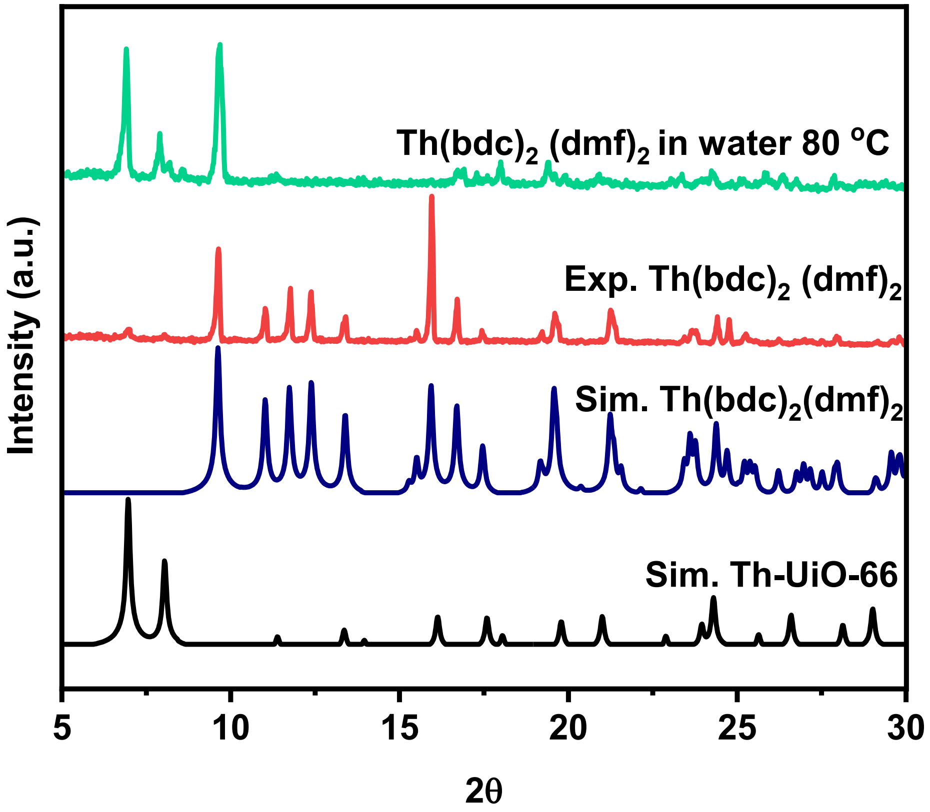

Figure 6.5 Overlaid PXRDs of $Th(bdc)_2(dmf)_2$ as synthesized and after exposure to water at 80 °C for 24 hr.

6.4 Phase Transitions within the Isostructural M-UiO-66 MOF Family

Inspired by the transition between MOFs containing Th and the BDC linker, we explored whether phase transformations in other M-UiO-66 type MOFs could occur under the same conditions that facilitated the phase transition of Th-UiO-66. For example, the Zr-carboxylate one-dimensional chain MOF MIL-140A can also be formed from $ZrCl_4$ and BDC linkers react as opposed to the much more well-known Zr-UiO-66 phase.[297] Our group recently observed the interconversion of UiO-66 to MIL-140A at high temperatures during the solid phase catalytic degradation of polyethylene terephthalate.[298] To compare the stabilities of the isostructural M_6O_8 clusters, we synthesized pure-phase Zr-UiO-66, Hf-UiO-66, and Ce-UiO-66. Each MOF was heated at 130 °C in a solution of 4:1 DMF/ H_2O for 48 hr to replicate the Th-UiO-66 to $Th(bdc)_2(dmf)_2$ phase transition conditions. After this treatment, the PXRD patterns of Zr-UiO-66 and Hf-UiO-66 were unchanged (**Figures 6.11-6.12**) indicating neither M_6O_8 node was hydrolyzed. However, after the treatment of Ce-UiO-66, the resulting PXRD indicated the formation of a new, crystalline phase (**Figure 6.6**). Through synthetic screenings of a Ce^{IV} source and the BDC linker, we generated single crystals of a new material called NU-351 (see NU-351 synthesis in Chapter *6.6.3*). The experimental PXRD of NU-351 aligns with the product of the Ce-UiO-66 phase transition (**Figure 6.6),** and we determined the structure of NU-351 through single-crystal X-ray diffraction. As shown in **Figure 6.7**, NU-351 is a MOF with a one-dimensional Ce^{III} chain with the formula of $(Ce^{III})_5(BDC)_{7.5}(DMF)_5$ comprised of 5 crystallographically unique Ce atoms. The Ce^{III} oxidation state was confirmed through X-ray photoelectron spectroscopy (Figure S9). Of note, NU-351 is structurally similar to NU-350, another one-dimensional Ce^{III}-MOF we previously reported that is favored over Ce-UiO-NDC (NDC = 2,6-napthalenedicarboxylic acid) in the presence of low amounts of carboxylate modulator.[171]

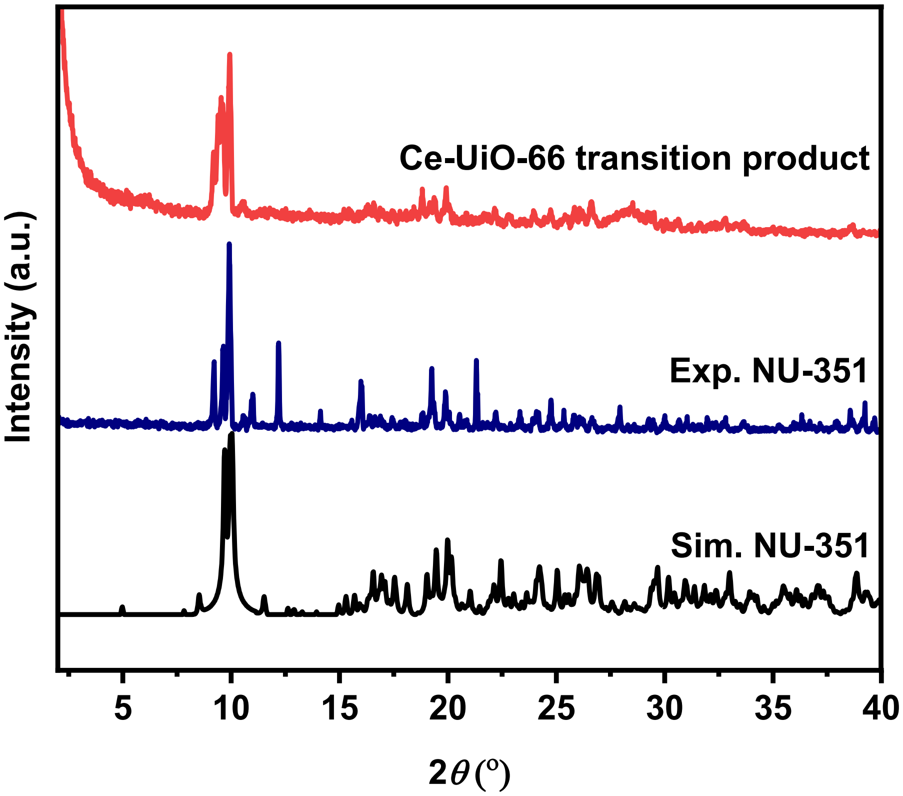

Figure 6.6 Overlaid PXRD patterns of the simulated and experimental NU-351 in agreements with the resulting phase transition of Ce-UiO-66 in 4:1 DMF/ water at 130 °C for 48 hr.

We postulate that MOFs with 1D metal-carboxylate chains formed from the transition of both Ce and Th-UiO-66 as opposed to Zr and Hf-UiO-66 result from several factors. Previous work from our group investigated the O-H stretching frequencies within M-UiO-66 (M= Zr, Hf, Ce, and Th) and determined that Ce and Th are less electronegative than Zr and Hf within the isostructural MOF family.[299] Thus, the Ce-O and Th-O bonds within the M_6O_8 clusters are weaker than Zr-O and Hf-O, rationalizing the susceptibility of the Ce and Th nodes to undergo hydrolysis and a subsequent phase transition. Additionally, Ce and Th have larger ionic radii and increased abilities to accommodate higher coordination numbers, likely facilitating the transition to the mononuclear MOFs with high Ce and Th coordination spheres. Lastly, Ce^{IV} has a high redox potential and can readily be reduced to Ce^{III} in DMF without sufficient modulator present.[103,171]

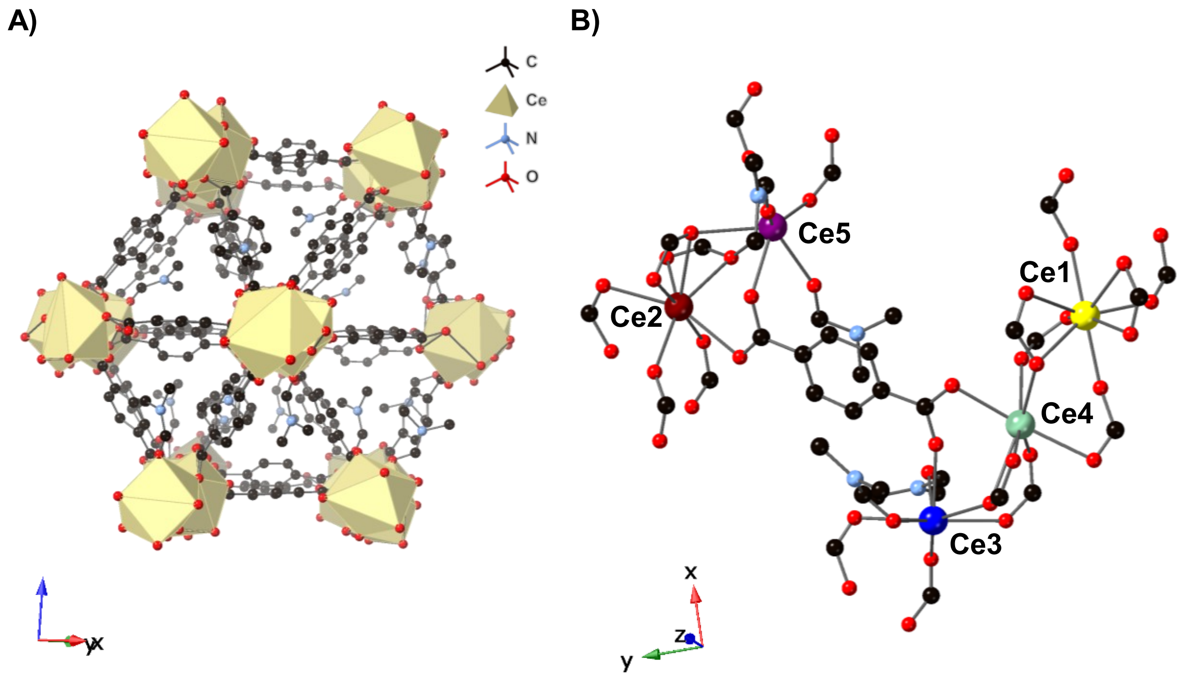

Figure 6.7 A) NU-351 structure with H atoms omitted for clarity and B) coordination environment of the 5 crystallographically distinct Ce atoms present. BDC linkers reduced to COO^- groups on node for visual clarity. Colors indicated in legend except Ce1 denoted as yellow, Ce2 denoted as dark red, Ce3 denoted as royal blue, Ce4 donated as light green, Ce5 denoted as purple.

6.5 Conclusions

We reported and monitored a serendipitous observation of a phase transition of Th-UiO-66 to $Th(bdc)_2(dmf)_2$ through PXRD and SEM imaging, attributed to a fluctuation in concentration dependent on the reaction vial used. Furthermore, we demonstrated that the partial reversibility of $Th(bdc)_2(dmf)_2$ converting back to Th-UiO-66. Under these conditions that facilitate the phase transformation of Th-UiO-66, we determined that Ce-UiO-66 also undergoes a phase transition to

NU-351 while both Zr and Hf-UiO-66 retain their structures. This work demonstrates the importance of studying the evolution of isolated metal oxo species within MOFs for both applied and fundamental perspectives; changes in Th speciation in solutions are relevant for long-term nuclear waste storage while analyzing transitions in isostructural MOFs can provide insights into overall metal oxo cluster strength and stability.

6.6 Additional Information

6.6.1 Materials

Caution! Thorium nitrate ($Th(NO_3)_4 \cdot 5H_2O$) is a radioactive and chemically toxic reactant. Thus, suitable care, precautions, and protection for handling such substances have been followed.

All chemicals and solvents were obtained from commercial suppliers and used without further purification. Thorium nitrate ($Th(NO_3)_4 \cdot 5H_2O$) ($\geq 98\%$, radiation clearance tested) was purchased from International Bio-Analytical Industries, Inc. Zirconium (IV) chloride, hafnium (IV) dichloride oxide octahydrate, cerium (IV) ammonium nitrate, terephthalic acid (BDC), glacial acetic acid, triethylamine, glycine, sodium chloride, benzoic acid, diethlyamine, lithium formate, and N,N-dimethylformamide were purchased from Sigma-Aldrich. Ethanol was purchased from Fischer Chemical. Deionized water was used as the water source. N_2 used for the adsorption and desorption measurements was Ultra High Purity Grade 5 and obtained from Airgas Specialty Gases (Chicago, IL).

6.6.2 Methods for Materials Characterization

Single Crystal X-Ray Diffraction Analysis and Refinement Details of NU-351: For single-crystal X-ray diffraction measurements, one crystal of NU-351 were collected at 100 K and the structure of **NU-351** at 100K, respectively, using a Rigaku Cu-Synergy diffractometer,equipped with shutter-less electronic-noise free Hybrid Photon Counting (HPC) detector and Cryostream 80-500K (Cryostream Oxford Cryosystems, Oxford, United Kingdom), CuKα (λ = 1.54184 Å) microfocus source with a beam size of ~110 μm and a 4-circle Kappa geometry goniometer. The single crystals were mounted on MicroMesh (MiTeGen) with paratone oil. The irradiation of crystals were done with the paratone oil for 20 min. The structures were determined by intrinsic phasing (SHELXT 2018/2) and refined by full-matrix least-squares refinement (SHELXL-2018/3) using the Olex2 software packages. Refinement results are summarized in Table S1. Crystallographic data in CIF format have been deposited in the Cambridge Crystallographic Data Centre (CCDC) under deposition number CCDC-2167180. The data can be obtained free of charge via www.ccdc.cam.ac.uk/data_request/cif (or from the Cambridge Crystallographic Data Centre, 12 Union Road, Cambridge CB2 1EZ, U.K.).

Table 6.1 Crystallographic details of NU-351

Empirical formula	**$C_{72}H_{60}Ce_5N_4O_{34}$**
Formula weight	2225.84
Temperature/K	100.02(10)
Crystal system	triclinic
Space group	P-1
a/Å	13.9994(2)
b/Å	15.2612(3)
c/Å	17.7824(3)
α/°	89.9738(15)
β/°	86.8717(14)
γ/°	89.3377(13)
Volume/Å^3	3793.24(11)

Z	2
ρ_{calc}g/cm^3	1.949
μ/mm^{-1}	23.518
F(000)	2164.0
Crystal size/mm^3	0.2 × 0.12 × 0.1
Radiation	Cu Kα (λ = 1.54184)
2Θ range for data collection/°	7.638 to 159.348
Index ranges	$-17 \le h \le 17$, $-19 \le k \le 19$, $-21 \le l \le 17$
Reflections collected	45422
Independent reflections	14925 [R_{int} = 0.0526, R_{sigma} = 0.0393]
Data/restraints/parameters	14925/174/1032
Goodness-of-fit on F^2	1.128
Final R indexes [I>=2σ (I)]	R_1 = 0.1205, wR_2 = 0.3275
Final R indexes [all data]	R_1 = 0.1231, wR_2 = 0.3285
Largest diff. peak/hole / e Å^{-3}	7.86/-5.86

Powder X-ray Diffraction Analysis: Powder X-ray diffraction (PXRD) patterns of the samples were measured by a STOE-STADI MP powder diffractometer operating at 40 kV voltage and 40 mA current with Cu-Kα1 X-ray radiation (λ = 1.5406 Å) in transmission geometry.

N_2 Sorption Isotherm Measurements: N_2 adsorption and desorption isotherms on activated materials were measured on a Micromeritics Tristar (Micromeritics, Norcross, GA) instrument at 77 K. Around 30 mg of sample was used in each measurement. Prior to N_2 isotherm measurements, the samples were placed under high vacuum at 100 °C on a Micromeritics Smart Vacprep for 18 h. The specific surface areas were determined using the Brunauer−Emmett−Teller model from the N_2 sorption data in the region P/P_0 = 0.005–0.05. Pore size distributions were obtained using DFT calculations using a carbon slit-pore model with a N_2 kernel.

X-ray Photoelectron Spectroscopy: X-ray photoelectron spectroscopy measurements were carried out on a Thermo Scientific ESCALAB 250 Xi equipped with an electron flood gun and a scanning ion gun. Analysis used the Thermo Scientific Avantage Data System software, and C1s peak (284.8 eV) peak was used as the reference. Oxidation states of Ce were assigned by comparison to previously published data.[133]

Scanning Electron Microscopy Imaging: Prior to observation, the samples were coated with OsO_4 (~9 nm) in a Denton Desk III TSC Sputter Coater. Scanning electron microscopy (SEM) images were acquired from a Hitachi SU8030 scanning electron microscope.

6.6.3 Materials Syntheses and Corresponding PXRD Characterizations

Phase Transition of Th-UiO-66 to Th(bdc)₂(dmf)₂

1,4 benzene dicarboxylic acid (150 mg, 0.9 mmol) and $Th(NO_3)_4 \cdot 5H_2O$ (200 mg, 0.35 mmol), 4 mL of DMF and 1 mL of H_2O were each placed a 2-dram DWK Life Sciences screw-thread vial lined with polyvinyl-faced pulp liners. A total of 4 identical vials were prepared. All vials were sonicated for approximately 10 minutes and then heated at 130 °C. 2 vials were left in the oven for 24 hr and contained a white powder corresponding to Th-UiO-66. The remaining 2 vials were removed after 72 hr and instead contained clear trapezoidal crystals. Each product was washed with DMF 3 times and then washed with ethanol 3 times prior to further characterization.

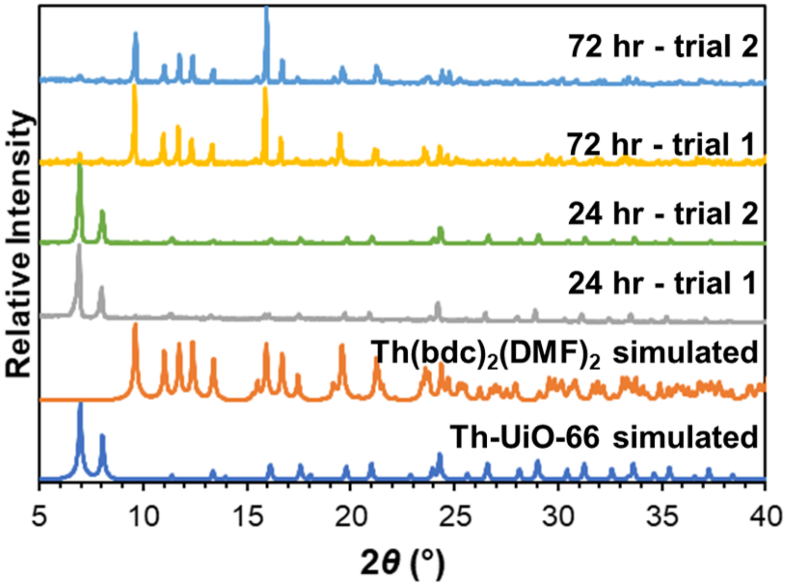

Figure 6.8: Overlaid PXRDs showing reaction time of identical vials and the evolution of the resulting products from Th-UiO-66 to $Th(bdc)_2(dmf)_2$.

Kinetic Monitoring of Phase Transition of Th-UiO-66 to Th(bdc)$_2$(dmf)$_2$

1,4 benzene dicarboxylic acid (37.5 mg, 0.225 mmol) and $Th(NO_3)_4 \cdot 5H_2O$ (50 mg, 0.0875 mmol), 1 mL of DMF and 0.25 mL of H_2O were each placed a 0.5-dram DWK Life Sciences screw-thread vial lined with polyvinyl-faced pulp liners. A total of 6 identical vials were prepared. All vials were sonicated for approximately 10 minutes and then heated at 130 °C. A vial was removed every 12 hours beginning at 12 hours and ending at a 72 hour time point. Each product was washed with DMF 3 times and then washed with ethanol 3 times prior to further characterization.

Phase Transition of Th(bdc)$_2$(dmf)$_2$ to Th-UiO-66

20 mg of Th(bdc)$_2$(dmf)$_2$ and 5 mL of water were added to a 2-dram DWK Life Sciences screw-thread vial lined with polyvinyl-faced pulp liners and heated for 80 °C for 24 hr.

Attempted Phase Transition of Th-UiO-66 to Th(bdc)$_2$(dmf)$_2$ in a Capillary

1,4 benzene dicarboxylic acid (150 mg, 0.9 mmol) and $Th(NO_3)_4 \cdot 5H_2O$ (200 mg, 0.35 mmol), 4 mL of DMF and 1 mL of H_2O were each placed a 2-dram DWK Life Sciences screw-thread vial lined with polyvinyl-faced pulp liners. The vial was sonicated for approximately 10 minutes. Approximately 100 µL aliquot of the reaction mixture was placed inside a 1.5 mm boron-rich capillary, which was then flame sealed. The capillary and then mother solution were left to in an oven at 130 C and taken out after 3 days. After a first PXRD measurement, the capillary was placed in the oven for an additional 7 days, before a second measurement.

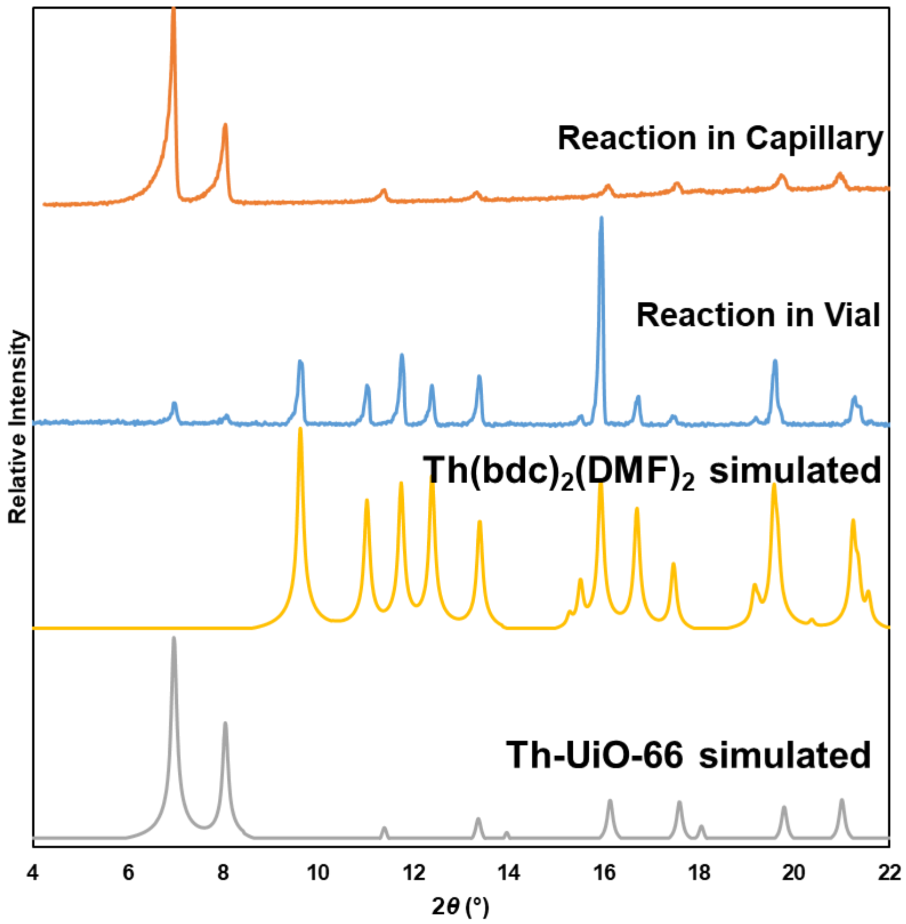

Figure 6.9 Comparing attempted phase transition of identical syntheses in a flame sealed capillary versus a polyvinyl-based vial.

Varying Concentration in Attempted Phase Transition of Th-UiO-66 to Th(bdc)$_2$(dmf)$_2$

1,4 benzene dicarboxylic acid (75 mg, 0.45 mmol) and Th(NO$_3$)$_4$·5H$_2$O (100 mg, 0.175 mmol) were each placed a 1-dram DWK Life Sciences screw-thread vial lined with PTFE/rubber. Vial A contained 2 mL DMF and 0.5 mL water (same concentration as original synthesis); vial B contained 1 mL DMF and 0.25 mL water (2x concentration of reactants as original synthesis); vial C contained 0.67 mL DMF and 0.17 mL water (3x concentration of reactants as original synthesis). The vials were sonicated for approximately 10 minutes and then were placed in an oven at 130 °C for 72 hr. Each product was washed with DMF 3 times and then washed with ethanol 3 times prior to further characterization.

Effect of Amine and Formate Additive in Attempted Phase Transition of Th-UiO-66 to $Th(bdc)_2(dmf)_2$

Pure phase Th-UiO-66 was synthesized first by reacting 1,4 benzene dicarboxylic acid (150 mg, 0.9 mmol) and $Th(NO_3)_4 \cdot 5H_2O$ (200 mg, 0.35 mmol), 4 mL of DMF and 1 mL of H2O in a 2-dram DWK Life Sciences screw-thread vial lined with polyvinyl-faced pulp liners. The vial was sonicated for approximately 10 minutes and then heated at 130 °C for 24 hours. The product was washed with DMF 3 times and then washed with ethanol 3 times before it was heated on a Smart Vac Prep instrument under vacuum for 18 hours at 100 °C.

20 mg of isolated Th-UiO-66 was placed in 2-dram DWK Life Sciences screw-thread vial lined with polyvinyl-faced pulp liners with the following solvent conditions:

A) 4 mL DMF

B) 4 mL DMF + 1 mL water

C) 4 mL DMF + 0.4 mL diethylamine (3.85 mmol)

D) 4 mL DMF + 1 mL water + 0.400 mL diethylamine (3.85 mmol)

E) 4 mL DMF + 200 mg lithium formate (3.85 mmol)

F) 4 mL DMF + 200 mg lithium formate (3.85 mmol) + 1 mL water

G) 2 mL DMF + 2 mL diethylamine

H) 4 mL DMF + 0.4 mL diethylamine (1 week)

The vials were sonicated for 10 minutes, and then the vials were placed in a 130 °C oven for 48 hours unless otherwise indicated

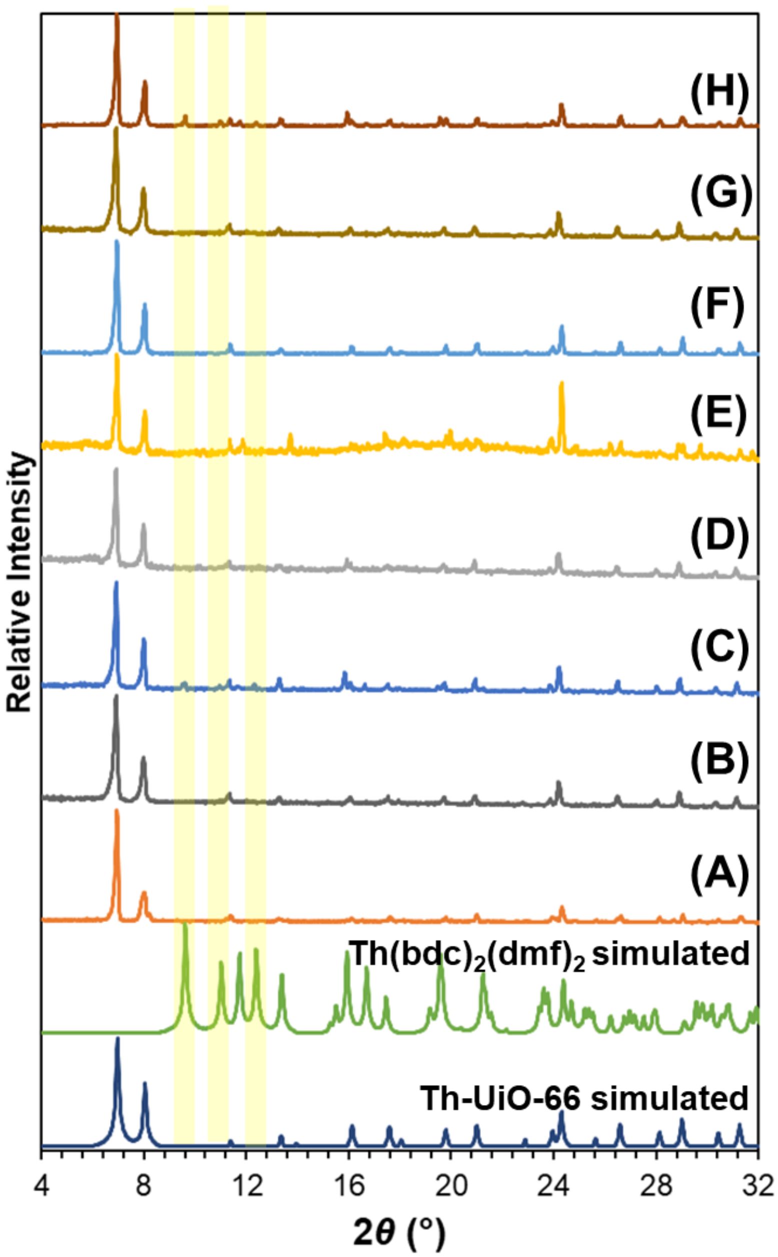

Figure 6.10 PXRD Patterns of Th-UiO-66 product exposed to: A) 4 mL DMF; B) 4 mL DMF + 1 mL water; C) 4 mL DMF + 0.4 mL diethylamine (3.85 mmol); D) 4 mL DMF + 1 mL water + 0.400 mL diethylamine (3.85 mmol); E) 4 mL DMF + 200 mg lithium formate (3.85 mmol); F) 4 mL DMF + 200 mg lithium formate (3.85 mmol) + 1 mL water; G) 4 mL DMF + 0.4 mL diethylamine (1 week); H) 2 mL DMF + 2 mL diethylamine

Attempted Phase Transition of Zr-UiO-66, Hf-UiO-66, and Ce-UiO-66

Zr, Hf, and Ce-UiO-66 were synthesized according to literature procedure.[6,7] 20 mg of a selected MOF, 4 mL of DMF, and 1 mL of water were placed in a 2 dram DWK Life Sciences screw-thread vial lined with polyvinyl-faced pulp liners and reacted for 48 hours at 130 °C. Each product was washed with DMF 3 times and then washed with ethanol 3 times prior to further characterization.

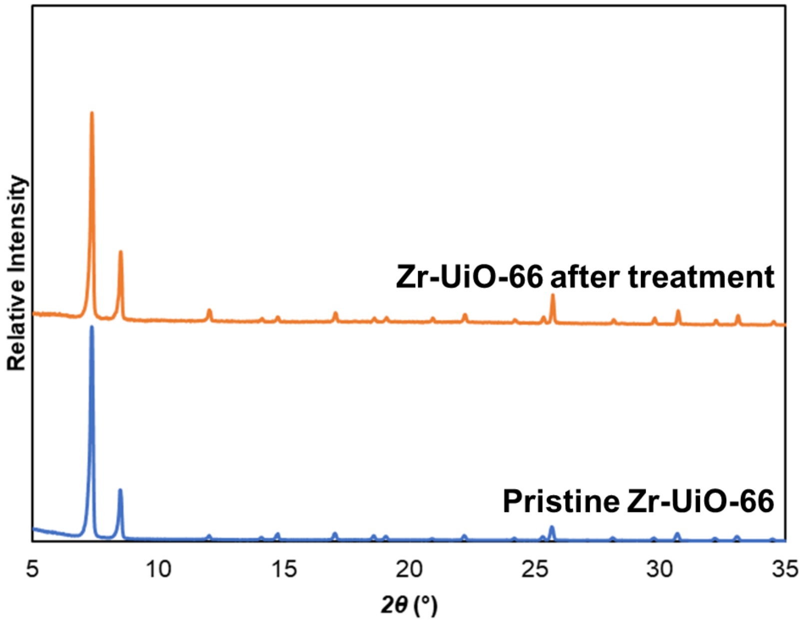

Figure 6.11 Zr-UiO-66 (top) after heating in 4:1 DMF : water at 130 °C for 48 hr stacked over as-synthesized Zr-UiO-66.

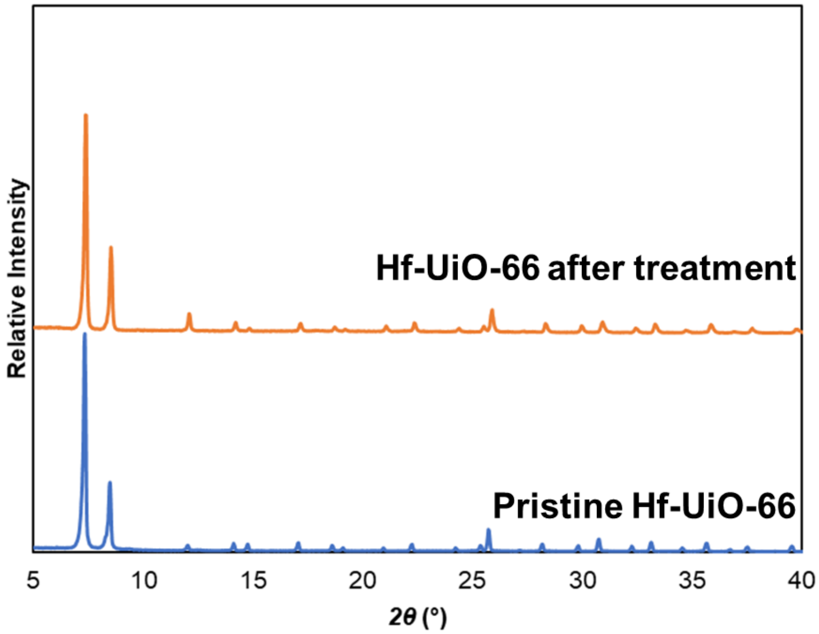

Figure 6.12: Hf-UiO-66 (top) after heating in 4:1 DMF : water at 130 °C for 48 hr stacked over as-synthesized Hf-UiO-66.

NU-351 Single Crystal Synthesis

352 mg of a Ce_6 precursor (0.15 mmol), which was synthesized according to literature procedures[8], 150 mg of 1,4 benzene dicarboxylic acid (0.90 mmol), 4 mL of DMF, and 1 mL of water were added to a 2 dram DWK Life Sciences screw-thread vial lined with polyvinyl-faced pulp liners. The vial was sonicated for 10 minutes and was placed in a 130 °C oven for 72 hours. The clear rod-shaped crystals were washed with DMF 3 times and then washed with ethanol 3 times prior to further characterization.

6.6.4 N_2 Physisorption Isotherms

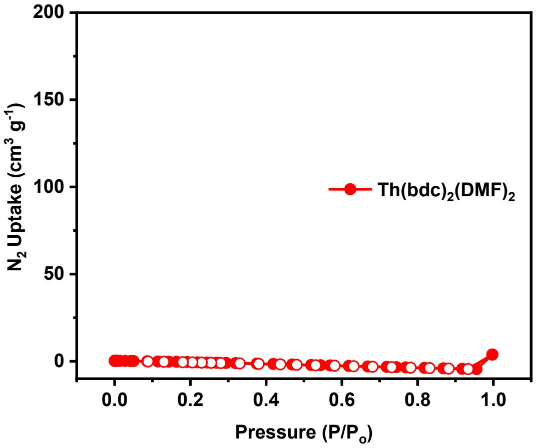

Figure 6.13 N_2 physisorption isotherm collected at 77 K. Apparent BET area was < 5 m^2/g.

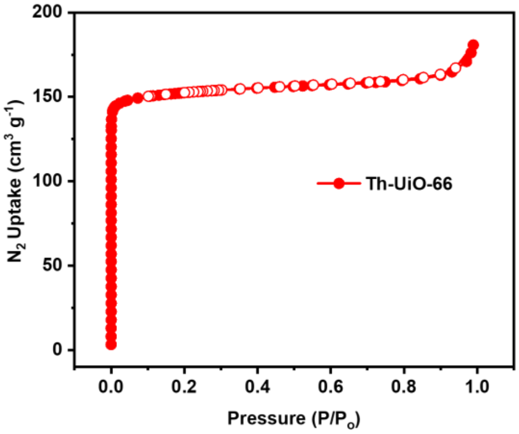

Figure 6.14 N_2 physisorption isotherm collected at 77 K. Apparent BET area was 620 m^2/g.

6.6.5 XPS Data

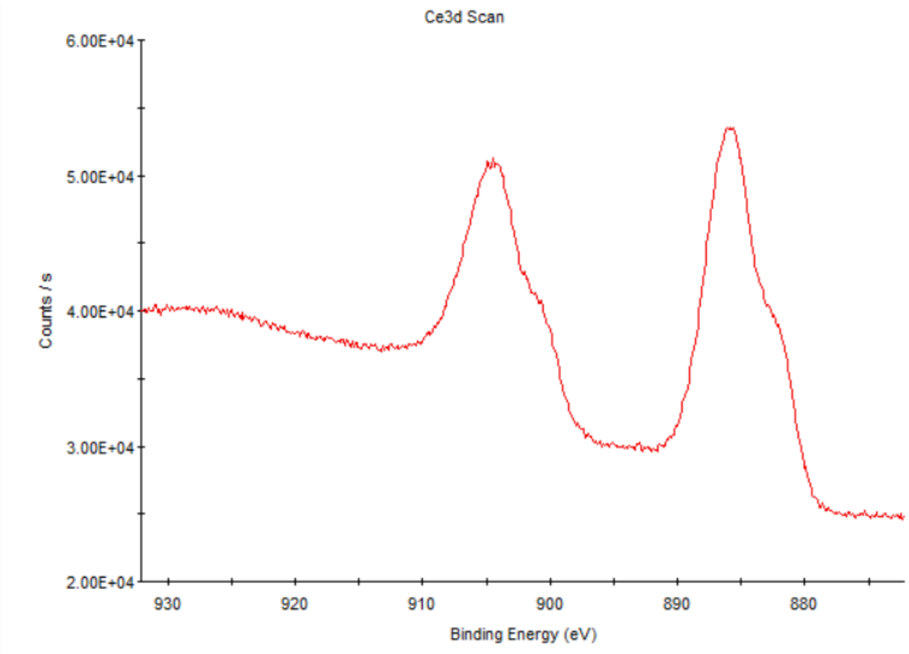

Figure 6.15 XPS spectrum of NU-351 showing characteristic Ce^{III} peaks.

Concluding Thoughts

Porous metal oxo cluster assemblies or metal oxo based MOFs demonstrate precise uniformity and tunabilty absent in metal oxides or other solid supports. MOFs synthesized to date are often limited to low nuclearity inorganic nodes (i.e. 10 metal ions or less); the installation of higher nuclearity metal oxo clusters as MOF building nodes can expand the functionality available for MOF applications such as catalysis while expanding the fundamental discoveries within reticular chemistry via unique molecular building blocks. To facilitate the installation of higher nuclearity metal oxo clusters as MOF building blocks, these clusters must have accessible surfaces that can accommodate the diffusion of larger MOF linkers as well as sufficient lability in the coordinated capping ligands to later be exchanged. I propose several guidelines to consider for future work on these systems:

- Capping ligands with extended length and aromaticity can induce higher porosity within the discrete Ce_{38} clusters of Chapter 2.
- The bridging units linking the MCe70 clusters in Chapter 3 were limited to sulfate and monocationic sites. However, bulkier organic-based cationic bridging units should be investigating as a way to further dictate and arrange the 1-D ring channels to enhance porosity.
- Chapter 5 demonstrated the importance of modulator pK_a on Ce oxo node stability. Similarly, the pK_a of each capping agent can be varied to tune the lability of the coordination bonds to determine optimal bond strength for post-synthetic ligand exchange with a multitopic MOF linker while still retaining the original size of the parent cluster.

References

(1) Liu, L.; Corma, A. Metal Catalysts for Heterogeneous Catalysis: From Single Atoms to Nanoclusters and Nanoparticles. *Chem Rev*. **2018**, *118*(10),4981–5079.

(2) Jose, R.; Thavasi, V.; Ramakrishna, S. Metal Oxides for Dye-Sensitized Solar Cells. *J. Am. Ceram. Soc.* **2009**, *92* (2), 289–301.

(3) Nikolova, M. P.; Chavali, M. S. Metal Oxide Nanoparticles as Biomedical Materials. *Biomimetics* **2020**, *5* (2), 27.

(4) Védrine, J. C. Metal Oxides in Heterogeneous Oxidation Catalysis: State of the Art and Challenges for a More Sustainable World. *ChemSusChem* **2019**, *12* (3), 577–588.

(5) Wachs, I. E.; Chen, Y.; Jehng, J. M.; Briand, L. E.; Tanaka, T. Molecular Structure and Reactivity of the Group V Metal Oxides. *Catal. Today* **2003**, *78* (1–4), 13–24.

(6) Höcker, J.; Krisponeit, J.-O.; Schmidt, T.; Falta, J.; Flege, J. I. The Cubic-to-Hexagonal Phase Transition of Cerium Oxide Particles: Dynamics and Structure. *Nanoscale* **2017**, *9* (27), 9352–9358.

(7) Ha, H.; Yoon, S.; An, K.; Kim, H. Y. Catalytic CO Oxidation over Au Nanoparticles Supported on CeO2 Nanocrystals: Effect of the Au–CeO2 Interface. *ACS Catal.* **2018**, *8* (12), 11491–11501.

(8) Nolan, M.; Watson, G. W. The Surface Dependence of CO Adsorption on Ceria. *J. Phys. Chem. B* **2006**, *110* (33), 16600–16606.

(9) Chizallet, C.; Costentin, G.; Che, M.; Delbecq, F.; Sautet, P. Revisiting Acido-Basicity of the MgO Surface by Periodic Density Functional Theory Calculations: Role of Surface Topology and Ion Coordination on Water Dissociation. *J. Phys. Chem. B* **2006**, *110* (32), 15878–15886.

(10) Pacchioni, G. Oxygen Vacancy: The Invisible Agent on Oxide Surfaces. *ChemPhysChem* **2003**, *4* (10), 1041–1047.

(11) Xu, J.; Harmer, J.; Li, G.; Chapman, T.; Collier, P.; Longworth, S.; Tsang, S. C. Size Dependent Oxygen Buffering Capacity of Ceria Nanocrystals. *Chem. Commun.* **2010**, *46* (11), 1887–1889.

(12) Huang, X.; Beck, M. J. Size-Dependent Appearance of Intrinsic O Xq Activated Oxygen Molecules on Ceria Nanoparticles. *Chem. Mater.* **2015**, *27* (17), 5840–5844.

(13) Mueller, D. N.; MacHala, M. L.; Bluhm, H.; Chueh, W. C. Redox Activity of Surface Oxygen Anions in Oxygen-Deficient Perovskite Oxides during Electrochemical Reactions. *Nat. Commun. 2015 61* **2015**, *6* (1), 1–8.

(14) Corby, S.; Francàs, L.; Kafizas, A.; Durrant, J. R. Determining the Role of Oxygen Vacancies in the Photoelectrocatalytic Performance of WO3 for Water Oxidation. *Chem. Sci.* **2020**, *11* (11), 2907–2914.

(15) Tsai, Y. Y.; Oca-Cossio, J.; Lin, S. M.; Woan, K.; Yu, P. C.; Sigmund, W. Reactive

Oxygen Species Scavenging Properties of ZrO2–CeO2 Solid Solution Nanoparticles. *Nanomed. J.* **2008**, *3* (5), 637–645.

(16) Wu, X.; Selloni, A.; Nayak, S. K. First Principles Study of CO Oxidation on TiO2(110): The Role of Surface Oxygen Vacancies. *J. Chem. Phys.* **2004**, *120* (9), 4512.

(17) Sun, S.; Zeng, H.; Robinson, D. B.; Raoux, S.; Rice, P. M.; Wang, S. X.; Li, G. Monodisperse MFe2O4 (M = Fe, Co, Mn) Nanoparticles. *J. Am. Chem. Soc.* **2004**, *126* (1), 273–279.

(18) Jana, N. R.; Chen, Y.; Peng, X. Size- and Shape-Controlled Magnetic (Cr, Mn, Fe, Co, Ni) Oxide Nanocrystals via a Simple and General Approach. *Chem. Mater.* **2004**, *16* (20), 3931–3935.

(19) Kim, T. K.; Lee, K. J.; Cheon, J. Y.; Lee, J. H.; Joo, S. H.; Moon, H. R. Nanoporous Metal Oxides with Tunable and Nanocrystalline Frameworks via Conversion of Metal-Organic Frameworks. *J. Am. Chem. Soc.* **2013**, *135* (24), 8940–8946.

(20) Du, J. S.; eng-Cheng Chen, P.; rian Meckes, B.; huang Xie, Z.; Zhu, J.; Liu, Y.; Dravid, V. P.; Mirkin, C. A.; Du, S.; Chen, P.; Zhu, J.; Dravid, V. P.; Mirkin, C. A.; Meckes, D.; Liu, Y.; Du, J. S. The Structural Fate of Individual Multicomponent Metal-Oxide Nanoparticles in Polymer Nanoreactors. *Angew. Chem. Int. Ed.* **2017**, *56* (26), 7625–7629.

(21) Hausmann, D. M.; Gordon, R. G. Surface Morphology and Crystallinity Control in the Atomic Layer Deposition (ALD) of Hafnium and Zirconium Oxide Thin Films. *J. Cryst. Growth* **2003**, *249* (1–2), 251–261.

(22) Blasco, T.; López Nieto, J. M. Oxidative Dyhydrogenation of Short Chain Alkanes on Supported Vanadium Oxide Catalysts. *Appl. Catal. A Gen.* **1997**, *157* (1–2), 117–142.

(23) **Wasson, M. C.**; Buru, C. T.; Chen, Z.; Islamoglu, T.; Farha, O. K. Metal–Organic Frameworks: A Tunable Platform to Access Single-Site Heterogeneous Catalysts. *Appl. Catal A.: Gen.* **2019**, *586*, 117214.

(24) Jena, P.; Castleman, A. W. Introduction to Atomic Clusters. *Sci. Technol. At. Mol. Condens. Matter Biol. Syst.* **2010**, *1* (1 D), 1–36.

(25) Schubert, U. Inorganic-Organic Hybrid Polymers Based on Surface-Modified Metal Oxide Clusters. *Macromol. Symp.* **2008**, *267* (1), 1–8.

(26) Zhang, Y.; Holm, R. H. Synthesis of a Molecular Mo2Fe6S9 Cluster with the Topology of the PN Cluster of Nitrogenase by Rearrangement of an Edge-Bridged Mo2Fe6S8 Double Cubane. *J. Am. Chem. Soc.* **2003**, *125* (13), 3910–3920.

(27) Zhu, M.; Eckenhoff, W. T.; Pintauer, T.; Jin, R. Conversion of Anionic [Au25(SCH2CH 2Ph)18]- Cluster to Charge Neutral Cluster via Air Oxidation. *J. Phys. Chem. C* **2008**, *112* (37), 14221–14224.

(28) Zhang, Y.; de Azambuja, F.; Parac-Vogt, T. N. The Forgotten Chemistry of Group(IV) Metals: A Survey on the Synthesis, Structure, and Properties of Discrete Zr(IV), Hf(IV), and Ti(IV) Oxo Clusters. *Coord. Chem. Rev.* **2021**, *438*, 213886.

(29) Jin, R.; Zeng, C.; Zhou, M.; Chen, Y. Atomically Precise Colloidal Metal Nanoclusters and Nanoparticles: Fundamentals and Opportunities. *Chem. Rev.* **2016**, *116*(18), 10346–10413.

(30) Pinkard, A.; Champsaur, A. M.; Roy, X. Molecular Clusters: Nanoscale Building Blocks for Solid-State Materials. *Acc. Chem. Res.* **2018**, *51* (4), 919–929.

(31) Mitchell, K. J.; Abboud, K. A.; Christou, G. Atomically-Precise Colloidal Nanoparticles of Cerium Dioxide. *Nat. Commun.* **2017**, *8* (1), 1445.

(32) Lee, J.; Farha, O. K.; Roberts, J.; Scheidt, K. A.; Nguyen, S. T.; Hupp, J. T. Metal–Organic Framework Materials as Catalysts. *Chem. Soc. Rev.* **2009**, *38* (5), 1450–1459.

(33) Zhou, H.-C.; Long, J. R.; Yaghi, O. M. Introduction to Metal–Organic Frameworks. *Chem. Rev.* **2012**, *112* (2), 673–674.

(34) Lin, R.-B.; Li, L.; Zhou, H.-L.; Wu, H.; He, C.; Li, S.; Krishna, R.; Li, J.; Zhou, W.; Chen, B. Molecular Sieving of Ethylene from Ethane Using a Rigid Metal–Organic Framework. *Nat. Mater.* **2018**, *17* (12), 1128–1133.

(35) Cui, X.; Chen, K.; Xing, H.; Yang, Q.; Krishna, R.; Bao, Z.; Wu, H.; Zhou, W.; Dong, X.; Han, Y.; Li, B.; Ren, Q.; Zaworotko, M. J.; Chen, B. Pore Chemistry and Size Control in Hybrid Porous Materials for Acetylene Capture from Ethylene. *Science.* **2016**, *353* (6295), 141–144.

(36) Mason, J. A.; Oktawiec, J.; Taylor, M. K.; Hudson, M. R.; Rodriguez, J.; Bachman, J. E.; Gonzalez, M. I.; Cervellino, A.; Guagliardi, A.; Brown, C. M.; Llewellyn, P. L.; Masciocchi, N.; Long, J. R. Methane Storage in Flexible Metal–Organic Frameworks with Intrinsic Thermal Management. *Nature* **2015**, *527*, 357.

(37) Li, H.; Eddaoudi, M.; O'Keeffe, M.; Yaghi, O. M. Design and Synthesis of an Exceptionally Stable and Highly Porous Metal-Organic Framework. *Nature* **1999**, *402*, 276.

(38) Yaghi, O. M.; O'Keeffe, M.; Ockwig, N. W.; Chae, H. K.; Eddaoudi, M.; Kim, J. Reticular Synthesis and the Design of New Materials. *Nature* **2003**, *423* (6941), 705–714.

(39) Chen, Z.; Weseliński, Ł. J.; Adil, K.; Belmabkhout, Y.; Shkurenko, A.; Jiang, H.; Bhatt, P. M.; Guillerm, V.; Dauzon, E.; Xue, D.-X.; O'Keeffe, M.; Eddaoudi, M. Applying the Power of Reticular Chemistry to Finding the Missing Alb-MOF Platform Based on the (6,12)-Coordinated Edge-Transitive Net. *J. Am. Chem. Soc.* **2017**, *139* (8), 3265–3274.

(40) Yuan, S.; Qin, J.-S.; Li, J.; Huang, L.; Feng, L.; Fang, Y.; Lollar, C.; Pang, J.; Zhang, L.; Sun, D.; Alsalme, A.; Cagin, T.; Zhou, H.-C. Retrosynthesis of Multi-Component Metal−organic Frameworks. *Nat. Commun.* **2018**, *9* (1), 808.

(41) Yang, D.; Gates, B. C. Catalysis by Metal Organic Frameworks: Perspective and Suggestions for Future Research. *ACS Catal.* **2019**, *9* (3), 1779–1798.

(42) Chui, S. S.-Y.; Lo, S. M.-F.; Charmant, J. P. H.; Orpen, A. G.; Williams, I. D. A Chemically Functionalizable Nanoporous Material [Cu3(TMA)2(H2O)3]N. *Science.* **1999**, *283* (5405), 1148–1150.

(43) Yuan, S.; Qin, J.-S.; Lollar, C. T.; Zhou, H.-C. Stable Metal–Organic Frameworks with Group 4 Metals: Current Status and Trends. *ACS Cent. Sci.* **2018**, *4* (4), 440–450.

(44) Cavka, J. H.; Jakobsen, S.; Olsbye, U.; Guillou, N.; Lamberti, C.; Bordiga, S.; Lillerud, K. P. A New Zirconium Inorganic Building Brick Forming Metal Organic Frameworks with Exceptional Stability. *J. Am. Chem. Soc.* **2008**, *130* (42), 13850–13851.

(45) Beyzavi, M. H.; Vermeulen, N. A.; Howarth, A. J.; Tussupbayev, S.; League, A. B.; Schweitzer, N. M.; Gallagher, J. R.; Platero-Prats, A. E.; Hafezi, N.; Sarjeant, A. A.; Miller, J. T.; Chapman, K. W.; Stoddart, J. F.; Cramer, C. J.; Hupp, J. T.; Farha, O. K. A Hafnium-Based Metal–Organic Framework as a Nature-Inspired Tandem Reaction Catalyst. *J. Am. Chem. Soc.* **2015**, *137* (42), 13624–13631.

(46) Lammert, M.; Wharmby, M. T.; Smolders, S.; Bueken, B.; Lieb, A.; Lomachenko, K. A.; Vos, D. De; Stock, N. Cerium-Based Metal Organic Frameworks with UiO-66 Architecture: Synthesis, Properties and Redox Catalytic Activity. *Chem. Commun.* **2015**, *51* (63), 12578–12581.

(47) Martin, C. R.; Leith, G. A.; Shustova, N. B. Beyond Structural Motifs: The Frontier of Actinide-Containing Metal–Organic Frameworks. *Chem. Sci.* **2021**, *12* (21), 7214–7230.

(48) Islamoglu, T.; Otake, K.; Li, P.; Buru, C. T.; Peters, A. W.; Akpinar, I.; Garibay, S. J.; Farha, O. K. Revisiting the Structural Homogeneity of NU-1000, a Zr-Based Metal–Organic Framework. *CrystEngComm* **2018**, *20*, 5913-5918.

(49) Ma, J.; Tran, L. D.; Matzger, A. J. Toward Topology Prediction in Zr-Based Microporous Coordination Polymers: The Role of Linker Geometry and Flexibility. *Cryst. Growth Des.* **2016**, *16* (7), 4148–4153.

(50) Gong, X.; Noh, H.; Gianneschi, N. C.; Farha, O. K. Interrogating Kinetic versus Thermodynamic Topologies of Metal–Organic Frameworks via Combined Transmission Electron Microscopy and X-Ray Diffraction Analysis. *J. Am. Chem. Soc.* **2019**, *141* (15), 6146–6151.

(51) Gándara, F.; Bennett, T. D. Crystallography of Metal–Organic Frameworks. *IUCrJ.* **2014**, *1* (6), 563–570.

(52) Huang, Z.; Grape, E. S.; Li, J.; Inge, A. K.; Zou, X. 3D Electron Diffraction as an Important Technique for Structure Elucidation of Metal-Organic Frameworks and Covalent Organic Frameworks. *Coord. Chem. Rev.* **2021**, *427*, 213583.

(53) Tsuruoka, T.; Furukawa, S.; Takashima, Y.; Yoshida, K.; Isoda, S.; Kitagawa, S. Nanoporous Nanorods Fabricated by Coordination Modulation and Oriented Attachment Growth. *Angew. Chem. Int. Ed.* **2009**, *48* (26), 4739–4743.

(54) Li, R.; Alomari, S.; Stanton, R.; **Wasson, M. C.**; Islamoglu, T.; Farha, O. K.; Holsen, T. M.; Thagard, S. M.; Trivedi, D. J.; Wriedt, M. Efficient Removal of Per- And Polyfluoroalkyl Substances from Water with Zirconium-Based Metal-Organic Frameworks. *Chem. Mater.* **2021**, *33* (9), 3276–3285.

(55) Mondloch, J. E.; Katz, M. J.; Isley III, W. C.; Ghosh, P.; Liao, P.; Bury, W.; Wagner, G. W.; Hall, M. G.; DeCoste, J. B.; Peterson, G. W.; Snurr, R. Q.; Cramer, C. J.; Hupp, J. T.;

Farha, O. K. Destruction of Chemical Warfare Agents Using Metal-Organic Frameworks. *Nat. Mater.* **2015**, *14*, 512–516.

(56) Chen, Y.; Li, P.; Modica, J. A.; Drout, R. J.; Farha, O. K. Acid-Resistant Mesoporous Metal-Organic Framework toward Oral Insulin Delivery: Protein Encapsulation, Protection, and Release. *J. Am. Chem. Soc.* **2018**, *140* (17), 5678–5681.

(57) Morris, W.; Wang, S.; Cho, D.; Auyeung, E.; Li, P.; Farha, O. K.; Mirkin, C. A. Role of Modulators in Controlling the Colloidal Stability and Polydispersity of the UiO-66 Metal–Organic Framework. *ACS Appl. Mater. Interfaces* **2017**, *9* (39), 33413–33418.

(58) Chen, Z.; Hanna, S. L.; Redfern, L. R.; Alezi, D.; Islamoglu, T.; Farha, O. K. Reticular Chemistry in the Rational Synthesis of Functional Zirconium Cluster-Based MOFs. *Coord. Chem. Rev.* **2019**, *386*, 32–49.

(59) Farha, O. K.; Eryazici, I.; Jeong, N. C.; Hauser, B. G.; Wilmer, C. E.; Sarjeant, A. A.; Snurr, R. Q.; Nguyen, S. T.; Yazaydin, A. Ö.; Hupp, J. T. Metal-Organic Framework Materials with Ultrahigh Surface Areas: Is the Sky the Limit? *J. Am. Chem. Soc.* **2012**, *134* (36), 15016–15021.

(60) Chen, Z.; Li, P.; Anderson, R.; Wang, X.; Zhang, X.; Robison, L.; Redfern, L. R.; Moribe, S.; Islamoglu, T.; Gómez-Gualdrón, D. A.; Yildirim, T.; Stoddart, J. F.; Farha, O. K. Balancing Volumetric and Gravimetric Uptake in Highly Porous Materials for Clean Energy. *Science.* **2020**, *368* (6488), 297–303.

(61) Morris, R. E.; Brammer, L. Coordination Change, Lability and Hemilability in Metal-Organic Frameworks. *Chem. Soc. Rev.* **2017**, *46* (17), 5444–5462.

(62) Jiang, H.; Alezi, D.; Eddaoudi, M. A Reticular Chemistry Guide for the Design of Periodic Solids. *Nat. Rev. Mater. 2021 66* **2021**, *6* (6), 466–487.

(63) Kelly, K. L.; Coronado, E.; Zhao, L. L.; Schatz, G. C. The Optical Properties of Metal Nanoparticles: The Influence of Size, Shape, and Dielectric Environment. *J. Phys. Chem. B* **2003**, *107* (3), 668–677.

(64) Jiang, L.; Fan, Z. Design of Advanced Porous Graphene Materials: From Graphene Nanomesh to 3D Architectures. *Nanoscale.* **2014**, *6*, 1922–1945.

(65) Long, D.-L.; Tsunashima, R.; Cronin, L. Polyoxometalates: Building Blocks for Functional Nanoscale Systems. *Angew. Chem. Int. Ed.* **2010**, *49* (10), 1736–1758.

(66) Bury, W.; Walczak, A. M.; Leszczyński, M. K.; Navarro, J. A. R. Rational Design of Noncovalent Diamondoid Microporous Materials for Low-Energy Separation of C6-Hydrocarbons. *J. Am. Chem. Soc.* **2018**, *140* (44), 15031–15037.

(67) Cui, P. F.; Lin, Y. J.; Li, Z. H.; Jin, G. X. Dihydrogen Bond Interaction Induced Separation of Hexane Isomers by Self-Assembled Carborane Metallacycles. *J. Am. Chem. Soc.* **2020**, *142* (18), 8532–8538.

(68) Vu, T. T.; Marbán, G. Sacrificial Template Synthesis of High Surface Area Metal Oxides. Example: An Excellent Structured Fenton-like Catalyst. *Appl. Catal. B Environ.* **2014**, *152–153*, 51–58.

(69) Bluthardt, C.; Fink, C.; Flick, K.; Hagemeyer, A.; Schlichter, M.; Volpe, A. Aqueous Synthesis of High Surface Area Metal Oxides. *Catal. Today* **2008**, *137* (1), 132–143.

(70) Fuertes, A. B. A General and Low-Cost Synthetic Route to High-Surface Area Metal Oxides through a Silica Xerogel Template. *J. Phys. Chem. Solids* **2005**, *66* (5), 741–747.

(71) Perego, C.; Millini, R. Porous Materials in Catalysis: Challenges for Mesoporous Materials. *Chem. Soc. Rev.* **2013**, *42* (9), 3956–3976.

(72) Yilmaz, B.; Müller, U. Catalytic Applications of Zeolites in Chemical Industry. *Topics in Catalysis*. **2009**, *52*, 888–895.

(73) Corma, A. From Microporous to Mesoporous Molecular Sieve Materials and Their Use in Catalysis. *Chem. Rev.* **1997**, *97* (6), 2373–2419.

(74) Li, H.; Moler, D. B.; O'Keeffe, M.; Yaghi, O. M.; Chen, B.; Reineke, T. M.; Eddaoudi, M. Modular Chemistry: Secondary Building Units as a Basis for the Design of Highly Porous and Robust Metal−Organic Carboxylate Frameworks. *Acc. Chem. Res.* **2002**, *34* (4), 319–330.

(75) Chen, Z.; Hanna, S. L.; Redfern, L. R.; Alezi, D.; Islamoglu, T.; Farha, O. K. Reticular Chemistry in the Rational Synthesis of Functional Zirconium Cluster-Based MOFs. *Coord. Chem. Rev.* **2019**, *386*, 32–49.

(76) Langille, M. R.; Personick, M. L.; Zhang, J.; Mirkin, C. A. Defining Rules for the Shape Evolution of Gold Nanoparticles. *J. Am. Chem. Soc.* **2012**, *134* (35), 14542–14554.

(77) Serpone, N.; Lawless, D.; Khairutdinov, R. Size Effects on the Photophysical Properties of Colloidal Anatase TiO2 Particles: Size Quantization or Direct Transitions in This Indirect Semiconductor? *J. Phys. Chem.* **1995**, *99* (45), 16646–16654.

(78) Narayanan, R.; El-Sayed, M. A. Catalysis with Transition Metal Nanoparticles in Colloidal Solution: Nanoparticle Shape Dependence and Stability. *J. Phys. Chem. B* **2005**, *109* (26), 12663–12676.

(79) Qian, H.; Eckenhoff, W. T.; Zhu, Y.; Pintauer, T.; Jin, R. Total Structure Determination of Thiolate-Protected Au38 Nanoparticles. *J. Am. Chem. Soc.* **2010**, *132* (24), 8280–8281.

(80) Chen, Y.; Liu, C.; Tang, Q.; Zeng, C.; Higaki, T.; Das, A.; Jiang, D. E.; Rosi, N. L.; Jin, R. Isomerism in Au28(SR)20 Nanocluster and Stable Structures. *J. Am. Chem. Soc.* **2016**, *138* (5), 1482–1485.

(81) Pan, L.; Heddy, R.; Li, J.; Zheng, C.; Huang, X. Y.; Tang, X.; Kilpatrick, L. Synthesis and Structural Determination of a Hexanuclear Zirconium Glycine Compound Formed in Aqueous Solution. *Inorg. Chem.* **2008**, *47* (13), 5537–5539.

(82) Hennig, C.; Takao, S.; Takao, K.; Weiss, S.; Kraus, W.; Emmerling, F.; Scheinost, A. C. Structure and Stability Range of a Hexanuclear Th(Iv)-Glycine Complex. *Dalt. Trans.* **2012**, *41* (41), 12818–12823.

(83) Knope, K. E.; Wilson, R. E.; Vasiliu, M.; Dixon, D. A.; Soderholm, L. Thorium(IV) Molecular Clusters with a Hexanuclear Th Core. *Inorg. Chem.* **2011**, *50* (19), 9696–9704.

(84) Takao, S.; Takao, K.; Kraus, W.; Emmerling, F.; Scheinost, A. C.; Bernhard, G.; Hennig, C. First Hexanuclear U ^{IV} and Th ^{IV} Formate Complexes - Structure and Stability Range in Aqueous Solution. *Eur. J. Inorg. Chem.* **2009**, *2009* (32), 4771–4775.

(85) Takao, K.; Takao, S.; Scheinost, A. C.; Bernhard, G.; Hennig, C. Formation of Soluble Hexanuclear Neptunium(IV) Nanoclusters in Aqueous Solution: Growth Termination of Actinide(IV) Hydrous Oxides by Carboxylates. *Inorg. Chem.* **2012**, *51* (3), 1336–1344.

(86) Knope, K. E.; Soderholm, L. Plutonium(IV) Cluster with a Hexanuclear [Pu6(OH) 4O4]12+ Core. *Inorg. Chem.* **2013**, *52* (12), 6770–6772.

(87) Soderholm, L.; Almond, P. M.; Skanthakumar, S.; Wilson, R. E.; Burns, P. C. The Structure of the Plutonium Oxide Nanocluster [Pu38O56Cl54(H2O)8]14−. *Angew. Chem. Int. Ed.* **2008**, *47* (2), 298–302.

(88) Falaise, C.; Volkringer, C.; Vigier, J.-F.; Beaurain, A.; Roussel, P.; Rabu, P.; Loiseau, T. Isolation of the Large $\{\text{Actinide}\}_{38}$ Poly-Oxo Cluster with Uranium. *J. Am. Chem. Soc.* **2013**, *135* (42), 15678–15681.

(89) Chatelain, L.; Faizova, R.; Fadaei-Tirani, F.; Pécaut, J.; Mazzanti, M. Structural Snapshots of Cluster Growth from $\{U_6\}$ to $\{U_{38}\}$ During the Hydrolysis of UCl_4. *Angew. Chem. Int. Ed.* **2019**, *58* (10), 3021–3026.

(90) Carrettin, S.; Concepción, P.; Corma, A.; López Nieto, J. M.; Puntes, V. F. Nanocrystalline CeO2 Increases the Activity of Au for CO Oxidation by Two Orders of Magnitude. *Angew. Chemie Int. Ed.* **2004**, *43* (19), 2538–2540.

(91) Ganduglia-Pirovano, M. V.; Da Silva, J. L. F.; Sauer, J. Density-Functional Calculations of the Structure of Near-Surface Oxygen Vacancies and Electron Localization on CeO 2 (111). *Phys. Rev. Lett.* **2009**, *102* (2), 026101.

(92) Zhou, K.; Wang, X.; Sun, X.; Peng, Q.; Li, Y. Enhanced Catalytic Activity of Ceria Nanorods from Well-Defined Reactive Crystal Planes. *J. Catal.* **2005**, *229* (1), 206–212.

(93) Gorte, R. J. Ceria in Catalysis: From Automotive Applications to the Water-Gas Shift Reaction. *AIChE J.* **2010**, *56* (5), 1126-1135.

(94) Montini, T.; Melchionna, M.; Monai, M.; Fornasiero, P. Fundamentals and Catalytic Applications of CeO2-Based Materials. *Chem. Rev.* **2016**, *116* (10), 5987–6041.

(95) Abanades, S.; Flamant, G. Thermochemical Hydrogen Production from a Two-Step Solar-Driven Water-Splitting Cycle Based on Cerium Oxides. *Sol. Energy* **2006**, *80* (12), 1611–1623.

(96) Tanaka, A.; Hashimoto, K.; Kominami, H. Preparation of Au/CeO 2 Exhibiting Strong Surface Plasmon Resonance Effective for Selective or Chemoselective Oxidation of Alcohols to Aldehydes or Ketones in Aqueous Suspensions under Irradiation by Green Light. *J. Am. Chem. Soc.* **2012**, *134* (35), 14526–14533.

(97) Paier, J.; Penschke, C.; Sauer, J. Oxygen Defects and Surface Chemistry of Ceria: Quantum Chemical Studies Compared to Experiment. *Chem. Rev.* **2013**, *113* (6), 3949–3985.

(98) Nolan, M.; Parker, S. C.; Watson, G. W. The Electronic Structure of Oxygen Vacancy Defects at the Low Index Surfaces of Ceria. *Surf. Sci.* **2005**, *595* (1), 223–232.

(99) Cargnello, M.; Doan-Nguyen, V. V. T.; Gordon, T. R.; Diaz, R. E.; Stach, E. A.; Gorte, R. J.; Fornasiero, P.; Murray, C. B. Control of Metal Nanocrystal Size Reveals Metal-Support Interface Role for Ceria Catalysts. *Science.* **2013**, *341* (6147), 771–773.

(100) Mars, P.; van Krevelen, D. W. Oxidations Carried out by Means of Vanadium Oxide Catalysts. *Chem. Eng. Sci.* **1954**, *3*, 41–59.

(101) Huang, X.-S.; Sun, H.; Wang, L.-C.; Liu, Y.-M.; Fan, K.-N.; Cao, Y. Morphology Effects of Nanoscale Ceria on the Activity of Au/CeO2 Catalysts for Low-Temperature CO Oxidation. *Appl. Catal. B Environ.* **2009**, *90* (1), 224–232.

(102) Esch, F.; Fabris, S.; Zhou, L.; Montini, T.; Africh, C.; Fornasiero, P.; Comelli, G.; Rosei, R. Chemistry: Electron Localization Determines Defect Formation on Ceria Substrates. *Science.* **2005**, *309* (5735), 752–755.

(103) Estes, S. L.; Antonio, M. R.; Soderholm, L. Tetravalent Ce in the Nitrate-Decorated Hexanuclear Cluster [Ce6(M3-O)4(M3-OH)4]12+: A Structural End Point for Ceria Nanoparticles. *J. Phys. Chem. C* **2016**, *120* (10), 5810–5818.

(104) Mathey, L.; Paul, M.; Copéret, C.; Tsurugi, H.; Mashima, K. Cerium(IV) Hexanuclear Clusters from Cerium(III) Precursors: Molecular Models for Oxidative Growth of Ceria Nanoparticles. *Chem. - A Eur. J.* **2015**, *21* (38), 13454–13461.

(105) Malaestean, I. L.; Ellern, A.; Baca, S.; Kögerler, P. Cerium Oxide Nanoclusters: Commensurate with Concepts of Polyoxometalate Chemistry? *Chem. Commun.* **2012**, *48* (10), 1499–1501.

(106) Mullins, D. R. The Surface Chemistry of Cerium Oxide. *Surf. Sci. Rep.* **2015**, *70* (1), 42–85.

(107) Shirase, S.; Tamaki, S.; Shinohara, K.; Hirosawa, K.; Tsurugi, H.; Satoh, T.; Mashima, K. Cerium(IV) Carboxylate Photocatalyst for Catalytic Radical Formation from Carboxylic Acids: Decarboxylative Oxygenation of Aliphatic Carboxylic Acids and Lactonization of Aromatic Carboxylic Acids. *J. Am. Chem. Soc.* **2020**. *142*(12), 5668-5675.

(108) Arunan, E.; Gutowsky, H. S. The Rotational Spectrum, Structure and Dynamics of a Benzene Dimer. *J. Chem. Phys.* **1993**, *98* (5), 4294–4296.

(109) Sinnokrot, M. O.; Valeev, E. F.; Sherrill, C. D. Estimates of the Ab Initio Limit for π-π Interactions: The Benzene Dimer. *J. Am. Chem. Soc.* **2002**, *124* (36), 10887–10893.

(110) Hamada, I. Van Der Waals Density Functional Made Accurate. *Phys. Rev. B - Condens. Matter Mater. Phys.* **2014**, *89* (12), 121103.

(111) Klimeš, J.; Bowler, D. R.; Michaelides, A. Chemical Accuracy for the van Der Waals Density Functional. *J. Phys. Condens. Matter* **2010**, *22* (2), 022201.

(112) Klimeš, J.; Bowler, D. R.; Michaelides, A. Van Der Waals Density Functionals Applied to Solids. *Phys. Rev. B - Condens. Matter Mater. Phys.* **2011**, *83* (19), 195131.

(113) Kresse, G.; Furthmüller, J. Efficiency of Ab-Initio Total Energy Calculations for Metals and Semiconductors Using a Plane-Wave Basis Set. *Comput. Mater. Sci.* **1996**, *6* (1), 15–50.

(114) Kresse, G.; Furthmüller, J. Efficient Iterative Schemes for Ab Initio Total-Energy Calculations Using a Plane-Wave Basis Set. *Phys. Rev. B - Condens. Matter Mater. Phys.* **1996**, *54* (16), 11169–11186.

(115) The theoretical pore volume of Ce38-BA was calculated from NLDFT as 0.376 cm^3/g, lower than the experimental pore volume of 0.04 cm^3/g.

(116) Colligan, M.; Forster, P. M.; Cheetham, A. K.; Lee, Y.; Vogt, T.; Hriljac, J. A. Synchrotron X-Ray Powder Diffraction and Computational Investigation of Purely Siliceous Zeolite Y under Pressure. *J. Am. Chem. Soc.* **2004**, *126* (38), 12015–12022.

(117) Hriljac, J. A. High-Pressure Synchrotron X-Ray Powder Diffraction Studies of Zeolites. *Crystallogr. Rev.* **2006**, *12* (2), 181–193.

(118) Redfern, L. R.; Farha, O. K. Mechanical Properties of Metal-Organic Frameworks. *Chem. Sci*. **2019**, *10*, 10666–10679.

(119) Robison, L.; Drout, R. J.; Redfern, L. R.; Son, F. A.; **Wasson, M. C.**; Goswami, S.; Chen, Z.; Olszewski, A.; Idrees, K. B.; Islamoglu, T.; Farha, O. K. Designing Porous Materials to Resist Compression: Mechanical Reinforcement of a Zr-MOF with Structural Linkers. *Chem. Mater.* **2020**, *32*(8), 3545-3552.

(120) Chapman, K. W.; Halder, G. J.; Chupas, P. J. Pressure-Induced Amorphization and Porosity Modification in a Metal-Organic Framework. *J. Am. Chem. Soc.* **2009**, *131* (48), 17546–17547.

(121) Redfern, L. R.; Robison, L.; **Wasson, M. C.**; Goswami, S.; Lyu, J.; Islamoglu, T.; Chapman, K. W.; Farha, O. K. Porosity Dependence of Compression and Lattice Rigidity in Metal–Organic Framework Series. *J. Am. Chem. Soc.* **2019**, *141* (10), 4365–4371.

(122) Vanorio, T.; Prasad, M.; Nur, A. Elastic Properties of Dry Clay Mineral Aggregates, Suspensions and Sandstones. *Geophys. J. Int.* **2003**, *155* (1), 319–326.

(123) Kosacki, I.; Suzuki, T.; Anderson, H. U.; Colomban, P. Raman Scattering and Lattice Defects in Nanocrystalline CeO2 Thin Films. *Solid State Ionics* **2002**, *149* (1–2), 99–105.

(124) Joubert, D. From Ultrasoft Pseudopotentials to the Projector Augmented-Wave Method. *Phys. Rev. B - Condens. Matter Mater. Phys.* **1999**, *59* (3), 1758–1775.

(125) Rosen, A. S.; Notestein, J. M.; Snurr, R. Q. Identifying Promising Metal–Organic Frameworks for Heterogeneous Catalysis via High-throughput Periodic Density Functional Theory. *J. Comput. Chem.* **2019**, *40* (12), 1305–1318.

(126) Hjorth Larsen, A.; JØrgen Mortensen, J.; Blomqvist, J.; Castelli, I. E.; Christensen, R.; Dułak, M.; Friis, J.; Groves, M. N.; Hammer, B.; Hargus, C.; Hermes, E. D.; Jennings, P. C.; Bjerre Jensen, P.; Kermode, J.; Kitchin, J. R.; Leonhard Kolsbjerg, E.; Kubal, J.; Kaasbjerg, K.; Lysgaard, S.; Bergmann Maronsson, J.; Maxson, T.; Olsen, T.; Pastewka, L.; Peterson, A.; Rostgaard, C.; SchiØtz, J.; Schütt, O.; Strange, M.; Thygesen, K. S.;

Vegge, T.; Vilhelmsen, L.; Walter, M.; Zeng, Z.; Jacobsen, K. W. The Atomic Simulation Environment - A Python Library for Working with Atoms. *Journal of Physics Condensed Matter*. Institute of Physics Publishing June 7, 2017.

(127) Ong, S. P.; Richards, W. D.; Jain, A.; Hautier, G.; Kocher, M.; Cholia, S.; Gunter, D.; Chevrier, V. L.; Persson, K. A.; Ceder, G. Python Materials Genomics (Pymatgen): A Robust, Open-Source Python Library for Materials Analysis. *Comput. Mater. Sci.* **2013**, *68*, 314–319.

(128) Rappé, A. K.; Casewit, C. J.; Colwell, K. S.; Goddard, W. A.; Skiff, W. M. UFF, a Full Periodic Table Force Field for Molecular Mechanics and Molecular Dynamics Simulations. *J. Am. Chem. Soc.* **1992**, *114* (25), 10024–10035.

(129) Hammersley, A. P.; Svensson, S. O.; Hanfland, M.; Fitch, A. N.; Häusermann, D. Two-Dimensional Detector Software: From Real Detector to Idealised Image or Two-Theta Scan. *High Press. Res.* **1996**, *14* (4–5), 235–248.

(130) Toby, B. H.; Von Dreele, R. B. GSAS-II: The Genesis of a Modern Open-Source All Purpose Crystallography Software Package. *J. Appl. Crystallogr.* **2013**, *46* (2), 544–549.

(131) Angel, R. J.; Alvaro, M.; Gonzalez-Platas, J. EosFit7c and a Fortran Module (Library) for Equation of State Calculations. *Zeitschrift für Krist. - Cryst. Mater.* **2014**, *229* (5), 405–419.

(132) Gonzalez-Platas, J.; Alvaro, M.; Nestola, F.; Angel, R. EosFit7-GUI: A New Graphical User Interface for Equation of State Calculations, Analyses and Teaching. *J. Appl. Crystallogr.* **2016**, *49* (4), 1377–1382.

(133) Bêche, E.; Charvin, P.; Perarnau, D.; Abanades, S.; Flamant, G. Ce 3d XPS Investigation of Cerium Oxides and Mixed Cerium Oxide (Ce XTiyOz). *Surf. Interface Anal.* **2008**, *40*, 264–267.

(134) Nelson, A. P.; Farha, O. K.; Mulfort, K. L.; Hupp, J. T. Supercritical Processing as a Route to High Internal Surface Areas and Permanent Microporosity in Metal#organic Framework Materials. *J. Am. Chem. Soc.* **2009**, *131* (2), 458–460.

(135) Smolders, S.; Struyf, A.; Reinsch, H.; Bueken, B.; Rhauderwiek, T.; Mintrop, L.; Kurz, P.; Stock, N.; De Vos, D. E. A Precursor Method for the Synthesis of New Ce(IV) MOFs with ReactIVe Tetracarboxylate Linkers. *Chem. Commun.* **2018**, *54* (8), 876–879.

(136) Somorjai, G. A.; Li, Y. Impact of Surface Chemistry. *Proc. Natl. Acad. Sci.* **2011**, *108* (3), 917–924.

(137) Zhou, Z. Y.; Tian, N.; Li, J. T.; Broadwell, I.; Sun, S. G. Nanomaterials of High Surface Energy with Exceptional Properties in Catalysis and Energy Storage. *Chem. Soc. Rev.* **2011**, *40* (7), 4167–4185.

(138) Tian, N.; Zhou, Z. Y.; Sun, S. G.; Ding, Y.; Zhong, L. W. Synthesis of Tetrahexahedral Platinum Nanocrystals with High-Index Facets and High Electro-Oxidation Activity. *Science.* **2007**, *316* (5825), 732–735.

(139) Jiao, K.; Zhang, B.; Yue, B.; Ren, Y.; Liu, S.; Yan, S.; Dickinson, C.; Zhou, W.; He, H.

Growth of Porous Single-Crystal Cr2O3 in a 3-D Mesopore System. *Chem. Commun.* **2005**, No. 45, 5618–5620.

(140) Shi, Y.; Lee, S. C.; Monti, M.; Wang, C.; Feng, Z. A.; Nix, W. D.; Toney, M. F.; Sinclair, R.; Chueh, W. C. Growth of Highly Strained CeO2 Ultrathin Films. *ACS Nano* **2016**, *10* (11), 9938–9947.

(141) Jin, R.; Li, G.; Sharma, S.; Li, Y.; Du, X. Toward Active-Site Tailoring in Heterogeneous Catalysis by Atomically Precise Metal Nanoclusters with Crystallographic Structures. *Chem. Rev.* **2020**, *121* (2), 567–648.

(142) Reidy, R. F.; Swider, K. E. Determination of the Cerium Oxidation State in Cerium Vanadate. *J. Am. Ceram. Soc.* **1995**, *78* (4), 1121–1122.

(143) Stubenrauch, J.; Vohs, J. M. Interaction of CO with Rh Supported on Stoichiometric and Reduced CeO2(111) and CeO2(100) Surfaces. *J. Catal.* **1996**, *159* (1), 50–57.

(144) Trovarelli, A. Catalytic Properties of Ceria and CeO2-Containing Materials. *Catal. Rev.* **2006**, *38* (4), 439–520.

(145) Mathey, L.; Paul, M.; Copéret, C.; Tsurugi, H.; Mashima, K. Cerium(IV) Hexanuclear Clusters from Cerium(III) Precursors: Molecular Models for Oxidative Growth of Ceria Nanoparticles. *Chem. – A Eur. J.* **2015**, *21* (38), 13454–13461.

(146) Malaestean, I. L.; Ellern, A.; Baca, S.; Kögerler, P. Cerium Oxide Nanoclusters: Commensurate with Concepts of Polyoxometalate Chemistry? *Chem. Commun.* **2012**, *48* (10), 1499–1501.

(147) **Wasson, M. C.**; Zhang, X.; Otake, K.-I.; Rosen, A. S.; Alayoglu, S.; Krzyaniak, M. D.; Chen, Z.; Redfern, L. R.; Robison, L.; Son, F. A.; Chen, Y.; Islamoglu, T.; Notestein, J. M.; Snurr, R. Q.; Wasielewski, M. R.; Farha, O. K. Supramolecular Porous Assemblies of Atomically Precise Catalytically Active Cerium-Based Clusters. *Chem. Mater.* **2020**.

(148) Russell-Webster, B.; Lopez-Nieto, J.; Abboud, K. A.; Christou, G. Truly Monodisperse Molecular Nanoparticles of Cerium Dioxide of 2.4 Nm Dimensions: A {Ce100O167} Cluster. *Angew. Chem. Int. Ed.* **2021**, *60* (22), 12591–12596.

(149) Colliard, I.; Morrison, G.; Zur Loye, H. C.; Nyman, M. Supramolecular Assembly of U(IV) Clusters and Superatoms with Unconventional Countercations. *J. Am. Chem. Soc.* **2020**, *142* (19), 9039–9047.

(150) Øien-Ødegaard, S.; Bazioti, C.; Redekop, E. A.; Prytz, Ø.; Petter Lillerud, K.; Olsbye, U.; Øien-Ødegaard, S.; Redekop, E. A.; Lillerud, K. P.; Olsbye, U.; Bazioti, C.; Prytz, Ø. A Toroidal Zr70 Oxysulfate Cluster and Its Diverse Packing Structures. *Angew. Chemie Int. Ed.* **2020**, *59* (48), 21397–21402.

(151) Colliard, I.; Nyman, M. CeIV70 Oxosulfate Rings, Frameworks, Supramolecular Assembly, and Redox Activity. *Angew. Chem. Int. Ed.* **2021**, *60* (13), 7308–7315.

(152) Colliard, I.; Brown, J. C.; Fast, D. B.; Sockwell, A. K.; Hixon, A. E.; Nyman, M. Snapshots of Ce70Toroid Assembly from Solids and Solution. *J. Am. Chem. Soc.* **2021**, *143* (25), 9612–9621.

(153) Wang, X.; Xie, H.; Knapp, J.G.; **Wasson, M.C.**; Wu, Y.; Ma, K; Krzyaniak, M.D.; Chen, Y.; Zhang, X.; Wasielewski, M. R.; Farha, O. K. Mechanistic Investigation of Enhanced Catalytic Selectivity toward Alcohol Oxidation with Ce-Oxysulfate Clusters. *submitted*.

(154) Chang, K.; Zhang, H.; Cheng, M. J.; Lu, Q. Application of Ceria in CO2 Conversion Catalysis. *ACS Catal.* **2019**, *10* (1), 613–631.

(155) Kacimi, S.; Barbier, J.; Taha, R.; Duprez, D. Oxygen Storage Capacity of Promoted Rh/CeC2 Catalysts. Exceptional Behavior of RhCu/CeO2. *Catal. Lett.* **1993**, *22* (4), 343–350.

(156) Binet, C.; Daturi, M.; Lavalley, J. C. IR Study of Polycrystalline Ceria Properties in Oxidised and Reduced States. *Catal. Today* **1999**, *50* (2), 207–225.

(157) Binet, C.; Badri, A.; Lavalley, J. C. A Spectroscopic Characterization of the Reduction of Ceria from Electronic Transitions of Intrinsic Point Defects. *J. Phys. Chem.* **2002**, *98* (25), 6392–6398.

(158) Wu, W.; Savereide, L. M.; Notestein, J.; Weitz, E. In-Situ IR Spectroscopy as a Probe of Oxidation/Reduction of Ce in Nanostructured CeO 2. *Appl. Surf. Sci.* **2018**, *445*, 548–554.

(159) Luo, L.; Hua, Q.; Jiang, Z.; Huang, W. A Pulse Chemisorption/Reaction System for in Situ and Time-Resolved DRIFTS Studies of Catalytic Reactions on Solid Surfaces. *Rev. Sci. Instrum.* **2014**, *85* (6), 064103.

(160) Mina-Camilde, N.; Manzanares I., C.; Caballero, J. F. Molecular Constants of Carbon Monoxide at v = 0, 1, 2, and 3: A Vibrational Spectroscopy Experiment in Physical Chemistry. *J. Chem. Educ.* **1996**, *73* (8), 804–807.

(161) Hadjiivanov, K.; Knözinger, H. FTIR Study of CO and NO Adsorption and Coadsorption on a Cu/SiO2 Catalyst: Probing the Oxidation State of Copper. *Phys. Chem. Chem. Phys.* **2001**, *3* (6), 1132–1137.

(162) Aubke, F.; Wang, C. Carbon Monoxide as a σ-Donor Ligand in Coordination Chemistry. *Coord. Chem. Rev.* **1994**, *137* (C), 483–524.

(163) Persson, B. N. J.; Tüshaus, M.; Bradshaw, A. M. On the Nature of Dense CO Adlayers. *J. Chem. Phys.* **1990**, *92* (8), 5034–5046.

(164) Schilling, C.; Hofmann, A.; Hess, C.; Ganduglia-Pirovano, M. V. Raman Spectra of Polycrystalline CeO2: A Density Functional Theory Study. *J. Phys. Chem. C* **2017**, *121* (38), 20834–20849.

(165) Spanier, J. E.; Robinson, R. D.; Zhang, F.; Chan, S. W.; Herman, I. P. Size-Dependent Properties of CeO2−y Nanoparticles as Studied by Raman Scattering. *Phys. Rev. B* **2001**, *64* (24), 245407.

(166) Sartoretti, E.; Novara, C.; Giorgis, F.; Piumetti, M.; Bensaid, S.; Russo, N.; Fino, D. In Situ Raman Analyses of the Soot Oxidation Reaction over Nanostructured Ceria-Based Catalysts. *Sci. Reports.* **2019**, *9* (1), 1–14.

(167) Gendron, F.; Autschbach, J.; Malrieu, J. P.; Bolvin, H. Magnetic Coupling in the Ce(III)

Dimer Ce 2 (COT) 3. *Inorg. Chem.* **2019**, *58* (1), 581–593.

(168) Yang, Z.; Woo, T. K.; Baudin, M.; Hermansson, K. Atomic and Electronic Structure of Unreduced and Reduced CeO2 Surfaces: A First-Principles Study. *J. Chem. Phys.* **2004**, *120* (16), 7741.

(169) Loschen, C.; Migani, A.; Bromley, S. T.; Illas, F.; Neyman, K. M. Density Functional Studies of Model Cerium Oxide Nanoparticles. *Phys. Chem. Chem. Phys.* **2008**, *10* (37), 5730–5738.

(170) Skorodumova, N. V.; Simak, S. I.; Lundqvist, B. I.; Abrikosov, I. A.; Johansson, B. Quantum Origin of the Oxygen Storage Capability of Ceria. *Phys. Rev. Lett.* **2002**, *89* (16), 166601/1-166601/4.

(171) **Wasson, M. C.**; Otake, K.; Gong, X.; Strathman, A. R.; Islamoglu, T.; Gianneschi, N. C.; Farha, O. K. Modulation of Crystal Growth and Structure within Cerium-Based Metal–Organic Frameworks. *CrystEngComm* **2020**, *22* (47), 8182.

(172) Chiang, Y. M.; Lavik, E. B.; Blom, D. A. Defect Thermodynamics and Electrical Properties of Nanocrystalline Oxides: Pure and Doped CeO2. *Nanostructured Mater.* **1997**, *9* (1–8), 633–642.

(173) Nagata, T.; Miyajima, K.; Hardy, R. A.; Metha, G. F.; Mafuné, F. Reactivity of Oxygen Deficient Cerium Oxide Clusters with Small Gaseous Molecules. *J. Phys. Chem. A* **2015**, *119* (22), 5545–5552.

(174) Chen, H. T.; Chang, J. G. Oxygen Vacancy Formation and Migration in Ce1−xZrxO2 Catalyst: A DFT+U Calculation. *J. Chem. Phys.* **2010**, *132* (21), 214702.

(175) Ziemba, M.; Hess, C. Influence of Gold on the Reactivity Behaviour of Ceria Nanorods in CO Oxidation: Combining Operando Spectroscopies and DFT Calculations. *Catal. Sci. Technol.* **2020**, *10* (11), 3720–3730.

(176) Ziemba, M.; Ganduglia-Pirovano, M. V.; Hess, C. Elucidating the Oxygen Storage-Release Dynamics in Ceria Nanorods by Combined Multi-Wavelength Raman Spectroscopy and DFT. *J. Phys. Chem. Lett.* **2020**, *11* (20), 8554–8559.

(177) MacIel, C. G.; Silva, T. D. F.; Profeti, L. P. R.; Assaf, E. M.; Assaf, J. M. Study of CuO/CeO2 Catalyst with for Preferential CO Oxidation Reaction in Hydrogen-Rich Feed (PROX-CO). *Appl. Catal. A Gen.* **2012**, *431–432*, 25–32.

(178) Mosrati, J.; Abdel-Mageed, A. M.; Vuong, T. H.; Grauke, R.; Bartling, S.; Rockstroh, N.; Atia, H.; Armbruster, U.; Wohlrab, S.; Rabeah, J.; Brückner, A. Tiny Species with Big Impact: High Activity of Cu Single Atoms on CeO2-TiO2Deciphered ByOperandoSpectroscopy. *ACS Catal.* **2021**, *11* (17), 10933–10949.

(179) Muravev, V.; Spezzati, G.; Su, Y. Q.; Parastaev, A.; Chiang, F. K.; Longo, A.; Escudero, C.; Kosinov, N.; Hensen, E. J. M. Interface Dynamics of Pd–CeO2 Single-Atom Catalysts during CO Oxidation. *Nat. Catal. 2021 46* **2021**, *4* (6), 469–478.

(180) Biesinger, M. C.; Lau, L. W. M.; Gerson, A. R.; Smart, R. S. C. Resolving Surface Chemical States in XPS Analysis of First Row Transition Metals, Oxides and Hydroxides:

Sc, Ti, V, Cu and Zn. *Appl. Surf. Sci.* **2010**, *257* (3), 887–898.

(181) O'Haver, T. peakfit.m - File Exchange - MATLAB Central https://www.mathworks.com/matlabcentral/fileexchange/23611-peakfit-m.

(182) Wu, W.; Savereide, L. M.; Notestein, J.; Weitz, E. In-Situ IR Spectroscopy as a Probe of Oxidation/Reduction of Ce in Nanostructured CeO2. *Appl. Surf. Sci.* **2018**, *445*, 548–554.

(183) Jin, T.; Zhou, Y.; Mains, G. J.; White, J. M. Infrared and X-Ray Photoelectron Spectroscopy Study of Carbon Monoxide and Carbon Dioxide on Platinum/Ceria. *J. Phys. Chem.* **2002**, *91* (23), 5931–5937.

(184) Melix, P. Dataset for "Structural Linkage Unit-Dependent Catalytic Activity for CO Oxidation Within Cerium Oxysulfate Cluster Assemblies." **2021**.

(185) Hunter, J. D. Matplotlib: A 2D Graphics Environment. *Comput. Sci. Eng.* **2007**, *9* (3), 90–95.

(186) Humphrey, W.; Dalke, A.; Schulten, K. VMD: Visual Molecular Dynamics. *J. Mol. Graph.* **1996**, *14* (1), 33–38.

(187) PLAMS, SCM, Theoretical Chemistry, Vrijie Universiteit, Amsterdam, The Netherlands.

(188) Perdew, J. P.; Burke, K.; Ernzerhof, M. Generalized Gradient Approximation Made Simple. *Phys. Rev. Lett.* **1996**, *77* (18), 3865.

(189) Grimme, S.; Antony, J.; Ehrlich, S.; Krieg, H. A Consistent and Accurate Ab Initio Parametrization of Density Functional Dispersion Correction (DFT-D) for the 94 Elements H-Pu. *J. Chem. Phys.* **2010**, *132* (15), 154104.

(190) Grimme, S.; Ehrlich, S.; Goerigk, L. Effect of the Damping Function in Dispersion Corrected Density Functional Theory. *J. Comput. Chem.* **2011**, *32* (7), 1456–1465.

(191) Kühne, T. D.; Iannuzzi, M.; Del Ben, M.; Rybkin, V. V.; Seewald, P.; Stein, F.; Laino, T.; Khaliullin, R. Z.; Schütt, O.; Schiffmann, F.; Golze, D.; Wilhelm, J.; Chulkov, S.; Bani-Hashemian, M. H.; Weber, V.; Borštnik, U.; Taillefumier, M.; Jakobovits, A. S.; Lazzaro, A.; Pabst, H.; Müller, T.; Schade, R.; Guidon, M.; Andermatt, S.; Holmberg, N.; Schenter, G. K.; Hehn, A.; Bussy, A.; Belleflamme, F.; Tabacchi, G.; Glöß, A.; Lass, M.; Bethune, I.; Mundy, C. J.; Plessl, C.; Watkins, M.; VandeVondele, J.; Krack, M.; Hutter, J. CP2K: An Electronic Structure and Molecular Dynamics Software Package - Quickstep: Efficient and Accurate Electronic Structure Calculations. *J. Chem. Phys.* **2020**, *152* (19), 194103.

(192) Goerigk, L.; Hansen, A.; Bauer, C.; Ehrlich, S.; Najibi, A.; Grimme, S. A Look at the Density Functional Theory Zoo with the Advanced GMTKN55 Database for General Main Group Thermochemistry, Kinetics and Noncovalent Interactions. *Phys. Chem. Chem. Phys.* **2017**, *19* (48), 32184–32215.

(193) Schütt, O.; Messmer, P.; Hutter, J.; VandeVondele, J. GPU-Accelerated Sparse Matrix–Matrix Multiplication for Linear Scaling Density Functional Theory. *Electron. Struct. Calc. Graph. Process. Units From Quantum Chem. to Condens. Matter Phys.* **2016**, 173–190.

(194) Borštnik, U.; Vandevondele, J.; Weber, V.; Hutter, J. Sparse Matrix Multiplication: The Distributed Block-Compressed Sparse Row Library. *Parallel Comput.* **2014**, *40* (5–6), 47–58.

(195) Kühne, T. D.; Krack, M.; Mohamed, F. R.; Parrinello, M. Efficient and Accurate Car-Parrinello-like Approach to Born-Oppenheimer Molecular Dynamics. *Phys. Rev. Lett.* **2007**, *98* (6), 066401.

(196) Vandevondele, J.; Krack, M.; Mohamed, F.; Parrinello, M.; Chassaing, T.; Hutter, J. Quickstep: Fast and Accurate Density Functional Calculations Using a Mixed Gaussian and Plane Waves Approach. *Comput. Phys. Commun.* **2005**, *167* (2), 103–128.

(197) Frigo, M.; Johnson, S. G. The Design and Implementation of FFTW3. *Proc. IEEE* **2005**, *93* (2), 216–231.

(198) Kolafa, J. Time-Reversible Always Stable Predictor–Corrector Method for Molecular Dynamics of Polarizable Molecules. *J. Comput. Chem.* **2004**, *25* (3), 335–342.

(199) Lippert, G.; Hutter, J.; Parrinello, M. A Hybrid Gaussian and Plane Wave Density Functional Scheme. *Mol. Phys.* **2010**, *92* (3), 477–488.

(200) VandeVondele, J.; Hutter, J. Gaussian Basis Sets for Accurate Calculations on Molecular Systems in Gas and Condensed Phases. *J. Chem. Phys.* **2007**, *127* (11), 114105.

(201) Hutter, J.; Iannuzzi, M.; Schiffmann, F.; Vandevondele, J. Cp2k: Atomistic Simulations of Condensed Matter Systems. *Wiley Interdiscip. Rev. Comput. Mol. Sci.* **2014**, *4* (1), 15–25.

(202) Krack, M. Pseudopotentials for H to Kr Optimized for Gradient-Corrected Exchange-Correlation Functionals. *Theor. Chem. Acc.* **2005**, *114* (1), 145–152.

(203) Hartwigsen, C.; Goedecker, S.; Hutter, J. Relativistic Separable Dual-Space Gaussian Pseudopotentials from H to Rn. *Phys. Rev. B* **1998**, *58* (7), 3641.

(204) Lu, J. B.; Cantu, D. C.; Nguyen, M. T.; Li, J.; Glezakou, V. A.; Rousseau, R. Norm-Conserving Pseudopotentials and Basis Sets to Explore Lanthanide Chemistry in Complex Environments. *J. Chem. Theory Comput.* **2019**, *15* (11), 5987–5997.

(205) Martyna, G. J.; Tuckerman, M. E. A Reciprocal Space Based Method for Treating Long Range Interactions in Ab Initio and Force-Field-Based Calculations in Clusters. *J. Chem. Phys.* **1999**, *110* (6), 2810.

(206) Dudarev, S. L.; Botton, G. A.; Savrasov, S. Y.; Humphreys, C. J.; Sutton, A. P. Electron-Energy-Loss Spectra and the Structural Stability of Nickel Oxide: An LSDA U Study. *Phys. Rev. B* **1998**, *57* (3), 1505.

(207) Dudarev, S. L.; Manh, D. N.; Sutton, A. P. Effect of Mott-Hubbard Correlations on the Electronic Structure and Structural Stability of Uranium Dioxide. *Philos. Mag. B* **2006**, *75* (5), 613–628.

(208) Fabris, S.; De Gironcoli, S.; Baroni, S.; Vicario, G.; Balducci, G. Reply to "Comment on 'Taming Multiple Valency with Density Functionals: A Case Study of Defective Ceria.'" *Phys. Rev. B - Condens. Matter Mater. Phys.* **2005**, *72* (23), 237102.

(209) Da Silva, J. L. F. Stability of the Ce2 O3 Phases: A DFT+U Investigation. *Phys. Rev. B - Condens. Matter Mater. Phys.* **2007**, *76* (19), 193108.

(210) Mishra, A. K.; Roldan, A.; De Leeuw, N. H. CuO Surfaces and CO2 Activation: A Dispersion-Corrected DFT+U Study. *J. Phys. Chem. C* **2016**, *120* (4), 2198–2214.

(211) AMS 2020, SCM, Theoretical Chemistry, Vrije Universiteit, Amsterdam, The Netherlands http://www.scm.com.

(212) GaussView, Version 6, Dennington, Roy; Keith, Todd A.; Millam, John M. Semichem Inc., Shawnee Mission, KS, 2016.

(213) Thielsch, R.; Böhme, T.; Reiche, R.; Schläfer, D.; Bauer, H. D.; Böttcher, H. Quantum-Size Effects of PbS Nanocrystallites in Evaporated Composite Films. *Nanostructured Mater.* **1998**, *10* (2), 131–149.

(214) Wang, L.; Maxisch, T.; Ceder, G. Oxidation Energies of Transition Metal Oxides within the GGA+U Framework. *Phys. Rev. B - Condens. Matter Mater. Phys.* **2006**, *73* (19), 195107.

(215) Mann, G. W.; Lee, K.; Cococcioni, M.; Smit, B.; Neaton, J. B. First-Principles Hubbard U Approach for Small Molecule Binding in Metal-Organic Frameworks. *J. Chem. Phys.* **2016**, *144* (17), 174104.

(216) Furukawa, H.; Cordova, K. E.; O'Keeffe, M.; Yaghi, O. M. The Chemistry and Applications of Metal-Organic Frameworks. *Science.* **2013**, *341* (6149).

(217) Li, J.-R.; Kuppler, R. J.; Zhou, H.-C. Selective Gas Adsorption and Separation in Metal-Organic Frameworks. *Chem. Soc. Rev.* **2009**, *38* (5), 1477–1504.

(218) Murray, L. J.; Dinca, M.; Long, J. R. Hydrogen Storage in Metal-Organic Frameworks. *Chem. Soc. Rev.* **2009**, *38* (5), 1294–1314.

(219) Eddaoudi, M.; Kim, J.; Rosi, N.; Vodak, D.; Wachter, J.; O'Keeffe, M.; Yaghi, O. M. Systematic Design of Pore Size and Functionality in Isoreticular MOFs and Their Application in Methane Storage. *Science.* **2002**, *295* (5554), 469–472.

(220) Ryan, P.; Farha, O. K.; Broadbelt, L. J.; Snurr, R. Q. Computational Screening of Metal-Organic Frameworks for Xenon/Krypton Separation. *AIChE J.* **2011**, *57* (7), 1759–1766.

(221) Zhang, S.-Y.; Yang, C.-X.; Shi, W.; Yan, X.-P.; Cheng, P.; Wojtas, L.; Zaworotko, M. J. A Chiral Metal-Organic Material That Enables Enantiomeric Identification and Purification. *Chem* **2017**, *3* (2), 281–289.

(222) Kreno, L. E.; Leong, K.; Farha, O. K.; Allendorf, M.; Van Duyne, R. P.; Hupp, J. T. Metal-Organic Framework Materials as Chemical Sensors. *Chem. Rev.* **2012**, *112* (2), 1105–1125.

(223) Zhang, S.-Y.; Shi, W.; Cheng, P.; Zaworotko, M. J. A Mixed-Crystal Lanthanide Zeolite-like Metal–Organic Framework as a Fluorescent Indicator for Lysophosphatidic Acid, a Cancer Biomarker. *J. Am. Chem. Soc.* **2015**, *137* (38), 12203–12206.

(224) Horcajada, P.; Gref, R.; Baati, T.; Allan, P. K.; Maurin, G.; Couvreur, P.; Ferey, G.;

Morris, R. E.; Serre, C. Metal-Organic Frameworks in Biomedicine. *Chem. Rev.* **2012**, *112* (2), 1232–1268.

(225) Liu, J.; Chen, L.; Cui, H.; Zhang, J.; Zhang, L.; Su, C.-Y. Applications of Metal-Organic Frameworks in Heterogeneous Supramolecular Catalysis. *Chem. Soc. Rev.* **2014**, *43* (16), 6011–6061.

(226) Shultz, A. M.; Farha, O. K.; Adhikari, D.; Sarjeant, A. A.; Hupp, J. T.; Nguyen, S. T. Selective Surface and Near-Surface Modification of a Noncatenated, Catalytically Active Metal-Organic Framework Material Based on Mn(Salen) Struts. *Inorg. Chem.* **2011**, *50* (8), 3174–3176.

(227) Furukawa, H.; Gandara, F.; Zhang, Y.-B.; Jiang, J.; Queen, W. L.; Hudson, M. R.; Yaghi, O. M. Water Adsorption in Porous Metal−Organic Frameworks and Related Materials. *J. Am. Chem. Soc.* **2014**, *136*, 4369–4381.

(228) Mondloch, J. E.; Bury, W.; Fairen-Jimenez, D.; Kwon, S.; DeMarco, E. J.; Weston, M. H.; Sarjeant, A. A.; Nguyen, S. T.; Stair, P. C.; Snurr, R. Q.; Farha, O. K.; Hupp, J. T. Vapor-Phase Metalation by Atomic Layer Deposition in a Metal–Organic Framework. *J. Am. Chem. Soc.* **2013**, *135* (28), 10294–10297.

(229) Zhang, Y.; Zhang, X.; Lyu, J.; Otake, K. I.; Wang, X.; Redfern, L. R.; Malliakas, C. D.; Li, Z.; Islamoglu, T.; Wang, B.; Farha, O. K. A Flexible Metal-Organic Framework with 4-Connected Zr 6 Nodes. *J. Am. Chem. Soc.* **2018**, *140* (36), 11179–11183.

(230) Bon, V.; Senkovska, I.; Baburin, I. A.; Kaskel, S. Zr- and Hf-Based Metal–Organic Frameworks: Tracking Down the Polymorphism. *Cryst. Growth Des.* **2013**, *13* (3), 1231–1237.

(231) Lammert, M.; Reinsch, H.; Murray, C. A.; Wharmby, M. T.; Terraschke, H.; Stock, N. Synthesis and Structure of Zr(Iv)- and Ce(Iv)-Based CAU-24 with 1,2,4,5-Tetrakis(4-Carboxyphenyl)Benzene. *Dalt. Trans.* **2016**, *45* (47), 18822–18826.

(232) Yuan, S.; Qin, J. S.; Lollar, C. T.; Zhou, H. C. Stable Metal-Organic Frameworks with Group 4 Metals: Current Status and Trends. *ACS Cent. Sci.* **2018**, *4* (4), 440–450.

(233) Deria, P.; Gomez-Gualdron, D. A.; Hod, I.; Snurr, R. Q.; Hupp, J. T.; Farha, O. K. Framework-Topology-Dependent Catalytic Activity of Zirconium-Based (Porphinato)Zinc(II) MOFs. *J. Am. Chem. Soc.* **2016**, *138* (43), 14449–14457.

(234) Schaate, A.; Roy, P.; Godt, A.; Lippke, J.; Waltz, F.; Wiebcke, M.; Behrens, P. Modulated Synthesis of Zr-Based Metal–Organic Frameworks: From Nano to Single Crystals. *Chem. – A Eur. J.* **2011**, *17* (24), 6643–6651.

(235) Gomez-Gualdron, D. A.; Gutov, O. V; Krungleviciute, V.; Borah, B.; Mondloch, J. E.; Hupp, J. T.; Yildirim, T.; Farha, O. K.; Snurr, R. Q. Computational Design of Metal–Organic Frameworks Based on Stable Zirconium Building Units for Storage and Delivery of Methane. *Chem. Mater.* **2014**, *26* (19), 5632–5639.

(236) Pang, J.; Liu, C.; Wu, M.; Yuan, D.; Hong, M.; Pang, J.; Yuan, S.; Qin, J.; Lollar, C.; Zhou, H.-C.; Pang, J. Control the Structure of Zr-Tetracarboxylate Frameworks through Steric Tuning. *J. Am. Chem. Soc.* **2017**, *139* (46), 16939–16945.

(237) Lyu, J.; Zhang, X.; Otake, K.-I.; Wang, X.; Li, P.; Li, Z.; Chen, Z.; Zhang, Y.; **Wasson, M. C.**; Yang, Y.; Bai, P.; Guo, X.; Islamoglu, T.; Farha, O. K. Topology and Porosity Control of Metal-Organic Frameworks through Linker Functionalization. *Chem. Sci.* **2019**, *10* (4), 1186-1192.

(238) Morris, W.; Volosskiy, B.; Demir, S.; Gándara, F.; McGrier, P. L.; Furukawa, H.; Cascio, D.; Stoddart, J. F.; Yaghi, O. M. Synthesis, Structure, and Metalation of Two New Highly Porous Zirconium Metal–Organic Frameworks. *Inorg. Chem.* **2012**, *51* (12), 6443–6445.

(239) Feng, D.; Gu, Z.-Y.; Li, J.-R.; Jiang, H.-L.; Wei, Z.; Zhou, H.-C. Zirconium-Metalloporphyrin PCN-222: Mesoporous Metal-Organic Frameworks with Ultrahigh Stability as Biomimetic Catalysts. *Angew. Chem. Int. Ed.* **2012**, *51* (41), 10307–10310.

(240) Feng, D.; Gu, Z.-Y.; Chen, Y.-P.; Park, J.; Wei, Z.; Sun, Y.; Bosch, M.; Yuan, S.; Zhou, H.-C. A Highly Stable Porphyrinic Zirconium Metal–Organic Framework with Shp-a Topology. *J. Am. Chem. Soc.* **2014**, *136* (51), 17714–17717.

(241) Feng, D.; Chung, W.-C.; Wei, Z.; Gu, Z.-Y.; Jiang, H.-L.; Chen, Y.-P.; Darensbourg, D. J.; Zhou, H.-C. Construction of Ultrastable Porphyrin Zr Metal-Organic Frameworks through Linker Elimination. *J. Am. Chem. Soc.* **2013**, *135* (45), 17105–17110.

(242) Jiang, H.-L.; Feng, D.; Wang, K.; Gu, Z.-Y.; Wei, Z.; Chen, Y.-P.; Zhou, H.-C. An Exceptionally Stable, Porphyrinic Zr Metal-Organic Framework Exhibiting PH-Dependent Fluorescence. *J. Am. Chem. Soc.* **2013**, *135* (37), 13934–13938.

(243) Kung, C.-W.; Wang, T. C.; Mondloch, J. E.; Fairen-Jimenez, D.; Gardner, D. M.; Bury, W.; Klingsporn, J. M.; Barnes, J. C.; Van Duyne, R.; Stoddart, J. F.; Wasielewski, M. R.; Farha, O. K.; Hupp, J. T. Metal-Organic Framework Thin Films Composed of Free-Standing Acicular Nanorods Exhibiting Reversible Electrochromism. *Chem. Mater.* **2013**, *25* (24), 5012–5017.

(244) Webber, T. E.; Liu, W.-G.; Desai, S. P.; Lu, C. C.; Truhlar, D. G.; Penn, R. L. Role of a Modulator in the Synthesis of Phase-Pure NU-1000. *ACS Appl. Mater. Interfaces* **2017**, *9* (45), 39342–39346.

(245) Liu, W.-G.; Truhlar, D. G. Computational Linker Design for Highly Crystalline Metal–Organic Framework NU-1000. *Chem. Mater.* **2017**, *29* (19), 8073–8081.

(246) Xu, H.-Q.; Wang, K.; Ding, M.; Feng, D.; Jiang, H.-L.; Zhou, H.-C. Seed-Mediated Synthesis of Metal-Organic Frameworks. *J. Am. Chem. Soc.* **2016**, *138* (16), 5316–5320.

(247) Sosso, G. C.; Chen, J.; Cox, S. J.; Fitzner, M.; Pedevilla, P.; Zen, A.; Michaelides, A. Crystal Nucleation in Liquids: Open Questions and Future Challenges in Molecular Dynamics Simulations. *Chem. Rev.* **2016**, *116* (12), 7078–7116.

(248) Van Vleet, M. J.; Weng, T.; Li, X.; Schmidt, J. R. In Situ, Time-Resolved, and Mechanistic Studies of Metal–Organic Framework Nucleation and Growth. *Chem. Rev.* **2018**, *118* (7), 3681–3721.

(249) Akiyama, G.; Matsuda, R.; Sato, H.; Takata, M.; Kitagawa, S. Cellulose Hydrolysis by a New Porous Coordination Polymer Decorated with Sulfonic Acid Functional Groups. *Adv. Mater.* **2011**, *23*, 3294–3297.

(250) Wang, C.; An, B.; Lin, W. Metal–Organic Frameworks in Solid–Gas Phase Catalysis. *ACS Catal.* **2019**, *9* (1), 130–146.

(251) Audu, C. O.; Nguyen, H. G. T.; Chang, C. Y.; Katz, M. J.; Mao, L.; Farha, O. K.; Hupp, J. T.; Nguyen, S. T. The Dual Capture of AsV and AsIII by UiO-66 and Analogues. *Chem. Sci.* **2016**, *7* (10), 6492–6498.

(252) Drout, R. J.; Otake, K.; Howarth, A. J.; Islamoglu, T.; Zhu, L.; Xiao, C.; Wang, S.; Farha, O. K. Efficient Capture of Perrhenate and Pertechnetate by a Mesoporous Zr Metal-Organic Framework and Examination of Anion Binding Motifs. *Chem. Mater.* **2018**, *30* (4), 1277–1284.

(253) Abánades Lázaro, I.; Haddad, S.; Sacca, S.; Orellana-Tavra, C.; Fairen-Jimenez, D.; Forgan, R. S. Selective Surface PEGylation of UiO-66 Nanoparticles for Enhanced Stability, Cell Uptake, and PH-Responsive Drug Delivery. *Chem* **2017**, *2* (4), 561–578.

(254) Islamoglu, T.; Chen, Z.; **Wasson, M. C.**; Buru, C. T.; Kirlikovali, K. O.; Afrin, U.; Mian, M. R.; Farha, O. K. Metal-Organic Frameworks against Toxic Chemicals. *Chem. Rev.* **2020**.

(255) Hu, Z.; Deibert, B. J.; Li, J. Luminescent Metal–Organic Frameworks for Chemical Sensing and Explosive Detection. *Chem. Soc. Rev.* **2014**, *43* (16), 5815–5840.

(256) Nickerl, G.; Senkovska, I.; Kaskel, S. Tetrazine Functionalized Zirconium MOF as an Optical Sensor for Oxidizing Gases. *Chem. Commun.* **2015**, *51* (12), 2280–2282.

(257) Yaghi, O. M. Reticular Chemistry in All Dimensions. *ACS Cent. Sci*. **2019**, *5*(8), 1295–1300.

(258) Mondloch, J. E.; Katz, M. J.; Isley III, W. C.; Ghosh, P.; Liao, P.; Bury, W.; Wagner, G. W.; Hall, M. G.; DeCoste, J. B.; Peterson, G. W.; Snurr, R. Q.; Cramer, C. J.; Hupp, J. T.; Farha, O. K. Destruction of Chemical Warfare Agents Using Metal–Organic Frameworks. *Nat. Mater.* **2015**, *14*, 512.

(259) Krause, S.; Bon, V.; Stoeck, U.; Senkovska, I.; Többens, D. M.; Wallacher, D.; Kaskel, S. A Stimuli-Responsive Zirconium Metal-Organic Framework Based on Supermolecular Design. *Angew. Chemie Int. Ed.* **2017**, *56* (36), 10676–10680.

(260) Griffin, S. L.; Briuglia, M. L.; ter Horst, J. H.; Forgan, R. S. Assessing Crystallisation Kinetics of Zr Metal–Organic Frameworks through Turbidity Measurements to Inform Rapid Microwave-Assisted Synthesis. *Chem. – A Eur. J.* **2020**, *26* (30), 6910–6918.

(261) Marshall, R. J.; Hobday, C. L.; Murphie, C. F.; Griffin, S. L.; Morrison, C. A.; Moggach, S. A.; Forgan, R. S. Amino Acids as Highly Efficient Modulators for Single Crystals of Zirconium and Hafnium Metal–Organic Frameworks. *J. Mater. Chem. A* **2016**, *4* (18), 6955–6963.

(262) Zahn, G.; Zerner, P.; Lippke, J.; Kempf, F. L.; Lilienthal, S.; Schröder, C. A.; Schneider, A. M.; Behrens, P. Insight into the Mechanism of Modulated Syntheses: In Situ Synchrotron Diffraction Studies on the Formation of Zr-Fumarate MOF. *CrystEngComm* **2014**, *16* (39), 9198–9207.

(263) Forgan, R. S. Modulated Self-Assembly of Metal-Organic Frameworks. *Chem. Sci.* **2020**, 11, 4546–4562.

(264) Islamoglu, T.; Atilgan, A.; Moon, S.-Y.; Peterson, G. W.; DeCoste, J. B.; Hall, M.; Hupp, J. T.; Farha, O. K. Cerium(IV) vs Zirconium(IV) Based Metal–Organic Frameworks for Detoxification of a Nerve Agent. *Chem. Mater.* **2017**, *29* (7), 2672–2675.

(265) Heidenreich, N.; Waitschat, S.; Reinsch, H. Investigation of the Kinetic Stabilization of a Ce4+-Based MOF by in-Situ Powder X-Ray Diffraction. *Zeitschrift für Anorg. und Allg. Chemie* **2018**, *644* (24), 1826–1831.

(266) Wang, B.; Liu, W.; Zhang, W.; Liu, J. Nanoparticles@nanoscale Metal-Organic Framework Composites as Highly Efficient Heterogeneous Catalysts for Size- and Shape-Selective Reactions. *Nano Res.* **2017**, *10* (11), 3826–3835.

(267) Shearer, G. C.; Chavan, S.; Bordiga, S.; Svelle, S.; Olsbye, U.; Lillerud, K. P. Defect Engineering: Tuning the Porosity and Composition of the Metal–Organic Framework UiO-66 via Modulated Synthesis. *Chem. Mater.* **2016**, *28* (11), 3749–3761.

(268) Zhou, W.; Greer, H. F. What Can Electron Microscopy Tell Us Beyond Crystal Structures? *Eur. J. Inorg. Chem.* **2016**, *2016* (7), 941–950.

(269) Ramamurty, U.; Jang, J. Il. Nanoindentation for Probing the Mechanical Behavior of Molecular Crystals-a Review of the Technique and How to Use It. *CrystEngComm* **2014**, *16* (1), 12–23.

(270) Campanelli, M.; Del Giacco, T.; De Angelis, F.; Mosconi, E.; Taddei, M.; Marmottini, F.; D'Amato, R.; Costantino, F. Solvent-Free Synthetic Route for Cerium(IV) Metal–Organic Frameworks with UiO-66 Architecture and Their Photocatalytic Applications. *ACS Appl. Mater. Interfaces* **2019**, *11* (48), 45031–45037.

(271) Zhao, P.; Qin, F.; Huang, Z.; Sun, C.; Shen, W.; Xu, H. MOF-Derived Hollow Porous Ni/CeO2 Octahedron with High Efficiency for N2O Decomposition. *Chem. Eng. J.* **2018**, *349*, 72–81.

(272) Zhou, J.; Liu, H.; Lin, Y.; Zhou, C.; Huang, A. Synthesis of Well-Shaped and High-Crystalline Ce-Based Metal Organic Framework for CO2/CH4 Separation. *Microporous Mesoporous Mater.* **2020**, *302*, 110224.

(273) Lyu, J.; Gong, X.; Lee, S. J.; Gnanasekaran, K.; Zhang, X.; **Wasson, M. C.**; Wang, X.; Bai, P.; Guo, X.; Gianneschi, N. C.; Farha, O. K. Phase Transitions in Metal-Organic Frameworks Directly Monitored through in Situ Variable Temperature Liquid-Cell Transmission Electron Microscopy and in Situ X-Ray Diffraction. *J. Am. Chem. Soc.* **2020**, *142* (10), 4609–4615.

(274) Ayoub, G.; Islamoglu, T.; Goswami, S.; Friščić, T.; Farha, O. K. Torsion Angle Effect on the Activation of UiO Metal-Organic Frameworks. *ACS Appl. Mater. Interfaces* **2019**, *11* (17), 15788–15794.

(275) Atzori, C.; Lomachenko, K. A.; Øien-ØDegaard, S.; Lamberti, C.; Stock, N.; Barolo, C.; Bonino, F. Disclosing the Properties of a New Ce(III)-Based MOF: Ce 2 (NDC) 3 (DMF) 2. *Cryst. Growth Des.* **2019**, *19* (2), 787–796.

(276) Nagai, Y.; Yamamoto, T.; Tanaka, T.; Yoshida, S.; Nonaka, T.; Okamoto, T.; Suda, A.; Sugiura, M. XAFS and XRD Analysis of Ceria-Zirconia Oxygen Storage Promoters for Automotive Catalysts. In *Topics in Catalysis*; Springer, 2008; Vol. 47, pp 137–147.

(277) Krause, L.; Herbst-Irmer, R.; Sheldrick, G. M.; Stalke, D. Comparison of Silver and Molybdenum Microfocus X-Ray Sources for Single-Crystal Structure Determination. *J. Appl. Crystallogr.* **2015**, *48* (1), 3–10.

(278) Sheldrick, G. M. Crystal Structure Refinement with SHELXL. *Acta Crystallogr. Sect. C Struct. Chem.* **2015**, *71* (1), 3–8.

(279) Sheldrick, G. M. SHELX2017, Programs for Crystal Structure Determination. *Univ. Göttingen, Ger.* **2017**.

(280) Kabuto, C.; Akine, S.; Nemoto, T.; Kwon, E. *Nihon Kessho Gakkaishi* **2009**, *51* (3), 218–224.

(281) Hanna, S. L.; Chheda, S.; Anderson, R.; Ray, D.; Malliakas, C. D.; Knapp, J. G.; Otake, K. ichi; Li, P.; Li, P.; Wang, X.; **Wasson, M. C.**; Zosel, K.; Evans, A. M.; Robison, L.; Islamoglu, T.; Zhang, X.; Dichtel, W. R.; Stoddart, J. F.; Gomez-Gualdron, D. A.; Gagliardi, L.; Farha, O. K. Discovery of Spontaneous De-Interpenetration through Charged Point-Point Repulsions. *Chem* **2022**, *8* (1), 225–242.

(282) Hastings, A. M.; Ray, D.; Jeong, W.; Gagliardi, L.; Farha, O. K.; Hixon, A. E. Advancement of Actinide Metal-Organic Framework Chemistry via Synthesis of Pu-UiO-66. *J. Am. Chem. Soc.* **2020**, *142* (20), 9363–9371.

(283) Gilson, S. E.; Li, P.; Szymanowski, J. E. S.; White, J.; Ray, D.; Gagliardi, L.; Farha, O. K.; Burns, P. C. In Situ Formation of Unprecedented Neptunium-Oxide Wheel Clusters Stabilized in a Metal-Organic Framework. *J. Am. Chem. Soc.* **2019**, *141* (30), 11842–11846.

(284) Gilson, S. E.; Fairley, M.; Hanna, S. L.; Szymanowski, J. E. S.; Julien, P.; Chen, Z.; Farha, O. K.; Laverne, J. A.; Burns, P. C. Unusual Metal-Organic Framework Topology and Radiation Resistance through Neptunyl Coordination Chemistry. *J. Am. Chem. Soc.* **2021**, *143* (42), 17354–17359.

(285) Baes, C. F.; Meyer, N. J.; Roberts, C. E. The Hydrolysis of Thorium(IV) at 0 and 95°. *Inorg. Chem.* **2002**, *4* (4), 518–527.

(286) Ekberg, C.; Albinsson, Y.; Comarmond, M. J.; Brown, P. L. Studies on the Complexation Behavior of Thorium(IV). 1. Hydrolysis Equilibria. *J. Solut. Chem. 2000 291* **2000**, *29* (1), 63–86.

(287) *Thoria-Based Nuclear Fuels*; Das, D., Bharadwaj, S. R., Eds.; Green Energy and Technology; Springer London: London, 2013.

(288) Serp, J.; Allibert, M.; Beneš, O.; Delpech, S.; Feynberg, O.; Ghetta, V.; Heuer, D.; Holcomb, D.; Ignatiev, V.; Kloosterman, J. L.; Luzzi, L.; Merle-Lucotte, E.; Uhlíř, J.; Yoshioka, R.; Zhimin, D. The Molten Salt Reactor (MSR) in Generation IV: Overview and Perspectives. *Prog. Nucl. Energy* **2014**, *77*, 308–319.

(289) Lin, J.; Cross, J. N.; Diwu, J.; Meredith, N. A.; Albrecht-Schmitt, T. E. Comparisons of Plutonium, Thorium, and Cerium Tellurite Sulfates. *Inorg. Chem.* **2013**, *52* (8), 4277–4281.

(290) Lin, J.; Qie, M.; Zhang, L.; Wang, X.; Lin, Y.; Liu, W.; Bao, H.; Wang, J. Probing the Influence of Acidity and Temperature to Th(IV) on Hydrolysis, Nucleation, and Structural Topology. *Inorg. Chem.* **2017**, *56* (22), 14198–14205.

(291) Li, Z. J.; Guo, S.; Lu, H.; Xu, Y.; Yue, Z.; Weng, L.; Guo, X.; Lin, J.; Wang, J. Q. Unexpected Structural Complexity of Thorium Coordination Polymers and Polyoxo Cluster Built from Simple Formate Ligands. *Inorg. Chem. Front.* **2019**, *7* (1), 260–269.

(292) Li, P.; Wang, X.; Otake, K. I.; Lyu, J.; Hanna, S. L.; Islamoglu, T.; Farha, O. K. Synthetic Control of Thorium Polyoxo-Clusters in Metal-Organic Frameworks toward New Thorium-Based Materials. *ACS Appl. Nano Mater.* **2019**, *2* (4), 2260–2265.

(293) Falaise, C.; Charles, J. S.; Volkringer, C.; Loiseau, T. Thorium Terephthalates Coordination Polymers Synthesized in Solvothermal DMF/H2O System. *Inorg. Chem.* **2015**, *54* (5), 2235–2242.

(294) Knope, K. E.; Wilson, R. E.; Vasiliu, M.; Dixon, D. A.; Soderholm, L. Thorium(IV) Molecular Clusters with a Hexanuclear Th Core. *Inorg. Chem.* **2011**, *50* (19), 9696–9704.

(295) Li, P.; Goswami, S.; Otake, K. I.; Wang, X.; Chen, Z.; Hanna, S. L.; Farha, O. K. Stabilization of an Unprecedented Hexanuclear Secondary Building Unit in a Thorium-Based Metal-Organic Framework. *Inorg. Chem.* **2019**, *58* (6), 3586–3590.

(296) Wu, Y. B.; Xiong, C.; Liu, Q. Y.; Ma, J. G.; Luo, F.; Wang, Y. L. Structural Evolution from Noninterpenetrated to Interpenetrated Thorium-Organic Frameworks Exhibiting High Propyne Storage. *Inorg. Chem.* **2021**, *60* (9), 6472–6479.

(297) Butova, V. V.; Budnyk, A. P.; Charykov, K. M.; Vetlitsyna-Novikova, K. S.; Lamberti, C.; Soldatov, A. V. Water as a Structure-Driving Agent between the UiO-66 and MIL-140A Metal–Organic Frameworks. *Chem. Commun.* **2019**, *55* (7), 901–904.

(298) Wu, Y.; Wang, X.; Kirlikovali, K. O.; Gong, X.; Atilgan, A.; Ma, K.; Schweitzer, N. M.; Gianneschi, N. C.; Li, Z.; Zhang, X.; Farha, O. K. Catalytic Degradation of Polyethylene Terephthalate Using a Phase-Transitional Zirconium-Based Metal-Organic Framework. *Angew. Chem. Int. Ed.* **2022**.

(299) Islamoglu, T.; Ray, D.; Li, P.; Majewski, M. B.; Akpinar, I.; Zhang, X.; Cramer, C. J.; Gagliardi, L.; Farha, O. K. From Transition Metals to Lanthanides to Actinides: Metal-Mediated Tuning of Electronic Properties of Isostructural Metal-Organic Frameworks. *Inorg. Chem.* **2018**, *57* (21), 13246–13251.